LesionAir: A low-cost tool for automated skin cancer diagnosis and mapping
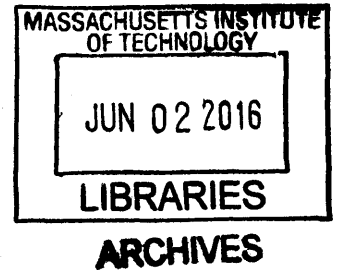
by

Tyler David Wortman

M.S., University of Nebraska - Lincoln (2011)
B.S., University of Nebraska - Lincoln (2009)

Submitted to the Department of Mechanical Engineering
in partial fulfillment of the requirements for the degree of

Doctor of Philosophy in Mechanical Engineering

at the

MASSACHUSETTS INSTITUTE OF TECHNOLOGY

June 2016

Signature redacted

Author . . . .
Department of Mechanical Engineering
May 16, 2016

Signature redacted

Certified by . . . .
Alexander H. Slocum
Pappalardo Professor of Mechanical Engineering
Thesis Supervisor

Signature redacted

Accepted by . . . .
Rohan Abeyaratne
Chairman, Department Committee on Graduate Theses

LesionAir: A low-cost tool for automated skin cancer diagnosis and mapping

by

Tyler David Wortman

Abstract

Skin cancer is the most common form of cancer in the United States; one out of every five Americans develops skin cancer at some point in their lifetime. Diagnosing cancerous lesions early is critical as it significantly increases the chance of survival. However, current techniques for diagnosing skin cancer lack specificity and sensitivity, resulting in many unnecessary biopsies and missed diagnoses. Although some researchers have increased diagnostic efficacy by quantitatively diagnosing skin cancer in an automated fashion, these methods require extremely bulky, expensive, and complicated equipment.

This thesis presents the design and testing of LesionAir, a small, low-cost skin cancer diagnostic tool that measures the full-field compliance of the skin — which is well known to correlate strongly with skin cancer — by applying a vacuum force to the tissue and measuring precise deflection using structured light 3D reconstruction. Image processing algorithms determine additional morphological information about the potentially cancerous lesion.

A pilot study of ten patients with suspect lesions validated LesionAir's effectiveness. After biopsy and analysis, a dermatopathologist confirmed the diagnosis of skin cancer in tissue that LesionAir identified as noticeably stiffer, and the regions of this stiffened tissue aligned nearly perfectly with the bounds established by the histological tests, which showed the method determines the precise coordinates that must be excised to safely remove all cancerous tissue. This technology can thus enable patients, primary care physicians, and dermatologists to rapidly identify and diagnose skin cancer with diagnostic quality not seen before from any equipment in this class.

Thesis Supervisor: Alexander H. Slocum
Title: Pappalardo Professor of Mechanical Engineering

Doctoral Committee

Alexander Slocum, Ph.D.
Thesis Supervisor and Committee Chair
Pappalardo Professor of Mechanical Engineering
Massachusetts Institute of Technology

Roger Kamm, Ph.D.
Professor of Biological and Mechanical Engineering
Massachusetts Institute of Technology

Peter So, Ph.D.
Professor of Mechanical Engineering
Massachusetts Institute of Technology

Edward Perez, M.D., Ph.D.
Dermatologist
Dermatology Skin Laser Center

William Plummer, Ph.D.
President
WTP Optics, Inc.

Acknowledgments

First and foremost, I would like to thank my parents. I cannot thank you enough for everything you have done for me. You inspired a young kid from rural Nebraska to dream big and shoot for the stars. You were with me every step of the way providing love and support. I dedicate this work to you.

I am immensely grateful to my thesis advisor, Prof. Alex Slocum, for providing me with the opportunity to work on this project, for being a tremendous and brilliant mentor, and for helping me through some really tough spots in my research. You are one of a kind and a pleasure to work for.

I would also like to thank the rest of my committee — Prof. Roger Kamm, Prof. Peter So, Dr. Ed Perez, and Dr. Bill Plummer — for devoting time and providing insightful comments and suggestions. Additional thanks to Dr. Perez for generating the initial problem statement and allowing me to validate my research in a clinical setting.

I owe a debt of gratitude to the Precision Engineering Research group – I would especially like to thank Megan O'Brien, David Taylor, Kevin Simon, Douglas Jonart, Maha Haji, Jocie Kluger, Felicia Hsu, Nick Sondej, Nikolai Begg, Anthony Wong, and Nevan Hanumara. You all were involved in brainstorming sessions that contributed to my research, but more importantly, you were all great friends who helped keep me sane throughout my research.

There are several other friends and colleagues from the MIT community who provided help along the way. I would especially like to thank Dr. Marianna Helin and Dr. Allison Larson from MIT Medical as well as Susan Conover. The MIT network is truly powerful and I am glad I had the opportunity to experience it firsthand.

Last but certainly not least, I would like to thank Jay Carlson. Your friendship, advice, and teaching has made me a better person. You put in significant time and effort towards this project and it would not have been so successful without you. I look forward to our continued friendship and future collaborations.

Contents

List of Figures

14

15

List of Tables

Chapter 1

Introduction

1.1 Motivation

More than 3 million non-melanoma skin cancers [1] and 140,000 melanoma skin cancers [2] afflict people every year in the United States; this translates to one out of every three cancers [3]. One out of five Americans will develop skin cancer at some point in their life [4].

There are three primary types of skin cancer based on the type of skin cells that are affected: basal cell carcinoma, squamous cell carcinoma, and melanoma. Melanoma, while only accounting for 1% of skin cancer cases, is much more deadly, causing more than 75% of skin cancer deaths [5]. There were 10,130 estimated melanoma deaths in 2016 [2]. The non-melanoma cancer types are more frequent, but highly curable as they are less likely to metastasize. The presented research focuses primarily on melanoma as it is significantly more dangerous; however, additional details on non-melanoma cancers will be briefly discussed.

Skin cancer is the only form of cancer that has seen a steady increase in incidence and mortality rates during the past 30 years. [2]. Out of the seven most common cancers in the United States, melanoma is the only one whose incidence is increasing [5, 6], causing some to claim that skin cancer has reached epidemic proportions [7, 8]. Others attribute increases in incidence to expanded skin screenings [9] and the increased detection of tumors with low metastatic potential [10]. However, most

researchers contest this argument by showing that not only is there an increased diagnosis in thinner tumors, but there is also a continued increase in the diagnosis of more fatal, thick tumors [11], demonstrating an all-around increase in incidence.

Identifying early-stage skin cancer before it has metastasized is critical, as prompt excision of the lesion nearly guarantees the patient's recovery [12]. A tumor will grow horizontally in the skin before penetrating deeper into the tissue where cancer cells can be dispersed to other areas of the body via the underlying vasculature. Three out of every four melanomas are diagnosed while the melanoma is still thin and localized [6]. If the tumor is less than 0.76 mm, there is a 99% chance for ten-year survival, however this survival percentage drops to less than 50% for a tumor thickness greater than 3 mm [12]. Tumor thickness is statistically the most important indicator of survival [13].

It is clear that the single most promising strategy to reduce the mortality rate of skin cancer is early detection [14]. Fortunately, skin cancer generally develops in the outermost layers of skin, making a possible malignant tumor visible in the early stage when treatment is likely to be most successful.

Although early diagnosis almost guarantees survival, the U.S. Preventive Services Task Force concluded there wasn't enough evidence to support routine screening by primary care physicians [15]. This is partially because there is a considerable debate on who should be screened, who should do the screening, and how often the screening should occur [16]. There are also millions of high-risk melanoma patients with several abnormally appearing lesions. It is impossible to predict which lesions will become cancerous and the excision of all is not practical, requires unnecessary surgery, and does not completely prevent the chance of skin cancer [17].

Tissue differentiation is critical for identifying cancerous tissue; however, without performing a biopsy, it is challenging to characterize tissue types within the same tissue structure . In most clinical settings, practitioners analyze tissue using nothing more than sight and touch. Fidelity is limited, due to resolution and sensitivity constraints of the practitioner; this method is only effective when performed by experienced dermatologists [18].

24

Because of these limitations, the gold standard for diagnosis has been invasive biopsy and excision, followed by histological and pathological examination. Studies have found that the ratio of biopsies of benign lesions to malignant ones can be as high as 500 to one [19], while at the same time, one-third of skin cancers are missed [20]; this shows current practices have neither specificity nor sensitivity, and a better approach is required.

To make matters worse, when a lesion is determined to be cancerous via biopsy, the physician typically determines the boundaries for excision using a completely subjective visual observation; the only way to verify that the entire lesion was excised is by performing a time-consuming pathology test on the tissue after it has been excised. This guess-and-check method can result in repeat procedures to remove a single lesion, which is inefficient, risks infection, and is cosmetically unappealing.

To this end, there is both a need and a significant market for low-cost tools that enable dermatologists and non-specialists to identify high-probability cancerous lesions in vivo and in any setting. This research focuses on developing a method to conduct fully-automated, non-invasive tissue characterization and diagnosis, which provide an objective process to rapidly assess the skin and subsequently map the tumor border for excision.

1.2   Goals of Research

Research in this area has focused on developing optical technologies to automate and assist the dermatologist in diagnosing skin lesions; however, current devices are complex, expensive, and designed to be used by a trained dermatologist only as a means of verifying the initial diagnosis. Most methods focus on measuring optical responses, which vary with stimulation and rely on ad-hoc heuristic metrics, which have limited reliability and may not work across all clinical populations. Technology adoption has thus been slow due to these issues.

Instead of relying on heuristic methods to gauge cancerous tissue, emerging attempts have been made to accurately measure skin stiffness, which is an intrinsic

property that changes when tissue becomes cancerous. Stiffness quantification, commonly referred to as *elastography*, has been performed manually via palpation to detect various types of cancers for decades. While effective, manual human palpation cannot detect very small changes or anomalies of the skin. These changes must be so large compared to normal skin tissue that the difference can be detected by touch of a finger. Automating stiffness measurement has the potential to increase sensitivity and consistency over current methods, turning a subjective test into a repeatable, objective test. This results in cancer being diagnosed sooner and a greater chance of survival.

While stiffness is a simple mechanical property that can be calculated from force and deflection, applying a known force to viscoelastic tissue and measuring deflection accurately is challenging. To obtain deflection, a 3D model of the scene is required. Researchers generally use ultrasound or MRI to quantifiably map the elastic properties of tissue, and while proven to be effective, the equipment costs and size prevent these methods from being adopted in clinical environments.

One low-cost way to create a 3D model of the scene is to perform 3D reconstruction using stereo image processing; two ways this is commonly done is by stereo matching or structured light [21]. Stereo matching algorithmically matches up content in a left and right view of a scene, similar to how human depth perception works. By looking at the displacement of content in the left and right view, depth information can be recovered. This process requires a highly textured scene to accurately match content, so it is not suitable for skin imaging.

Structured light is an alternative technique for 3D reconstruction that replaces one of the cameras with a projector that casts an image of known geometry onto the scene. The algorithm combines the apparent view from the camera with the known geometry of the projected pattern to obtain depth information from the scene. By actively projecting an illumination pattern on the region of interest, there is no longer a need to rely on features inherent to the scene, so long as the camera can see the projected pattern.

Unfortunately, structured light systems have traditionally used a video projector to illuminate the skin, which adds cost and complexity. This research replaces a video projector with a fixed projection pattern placed between an LED and projection optic, which dramatically reduces costs and complexity, and ultimately enables a smartphone to perform the same tasks as an MRI or ultrasound machine in this scenario. It is hypothesized that a smartphone form factor, combined with cost effective hardware and consumer friendly software will greatly increase technology adoption for dermatology applications.

The primary goals of this research were to develop a method and instrument with both diagnostic and therapeutic applications. As a diagnostic tool, this research provides the means to objectively and quantitatively map the stiffness and morphology of a suspect lesion, typically observed through visual observation and palpation. This is relevant in the tracking and diagnosis of suspect skin cancer moles, reducing the need for biopsies. As a surgical tool the surgeon could be given an augmented vision of the surgical landscape, enabling real-time, in-situ identification of margins, thus providing smaller and more accurate margins while simultaneously reducing the need for revisions. Realization of these goals will allow dermatologists, primary care physicians, and patients to more effectively monitor and diagnose suspect lesions.

The auxiliary technology developed during this research also has a broad impact outside the application; a low-cost structured light system will provide an avenue for smartphone developers to add depth-sensing to many medical and non-medical applications.

1.3   Thesis Organization

This thesis is structured as seven chapters and three appendices.

- Chapter 1 provides an insight into the motivations and objectives to this research.

- Chapter 2 provides a high level overview of healthy human skin, skin cancer, as well as the theory behind the optical measurement techniques used.

- Chapter 3 details the various types of technology that are available or being developed for skin cancer detection.

- Chapter 4 explains the design process, discussing the strategies and concepts that were developed to meet the functional requirements of the project.

- Chapter 5 extensively details the design of the prototype system that was developed to validate the research.

- Chapter 6 shows benchtop testing results along with initial results from a small clinical trial.

- Chapter 7 summarizes the research, explores other applications of the technology, and identifies areas where future work is necessary.

- Appendix A illustrates the camera and projector calibration process and results.

- Appendix B provides details on the Institutional Review Board (IRB) protocol and approval.

- Appendix C details the comprehensive clinical trial results.

Chapter 2

Clinical Background

Understanding the composition of healthy skin and how its properties change when cancer invades is critical when trying to detect cancer in its earliest stages. This chapter provides a background on skin, its structure and function, and the diseases that can affect it.

2.1 Human Skin

Skin is an intricate organ that covers the entire surface of the human body and accounts for approximately 15% of the total adult body weight, making it the largest human organ [22]. Skin is comprised of all tissue types — epithelial, connective, vascular, muscular and nervous — allowing it to perform multiple functions. The primary function is to act as the body's shield against mechanical, chemical, or biological stresses from harsh environments [23]. Secondary functions include temperature regulation and vitamin D synthesis [24, 25].

Properties of skin vary due to its complexity. Skin is non-linear, anisotropic, and inhomogeneous; it evolves over time and has inconsistent boundary conditions [26]. Compounding these local inconsistencies with the person-to-person variability necessitates relative evaluation versus absolute.

Skin color is determined by the composition of chromophores within the tissue, which reflect or absorb certain wavelengths of light. The primary chromophores in
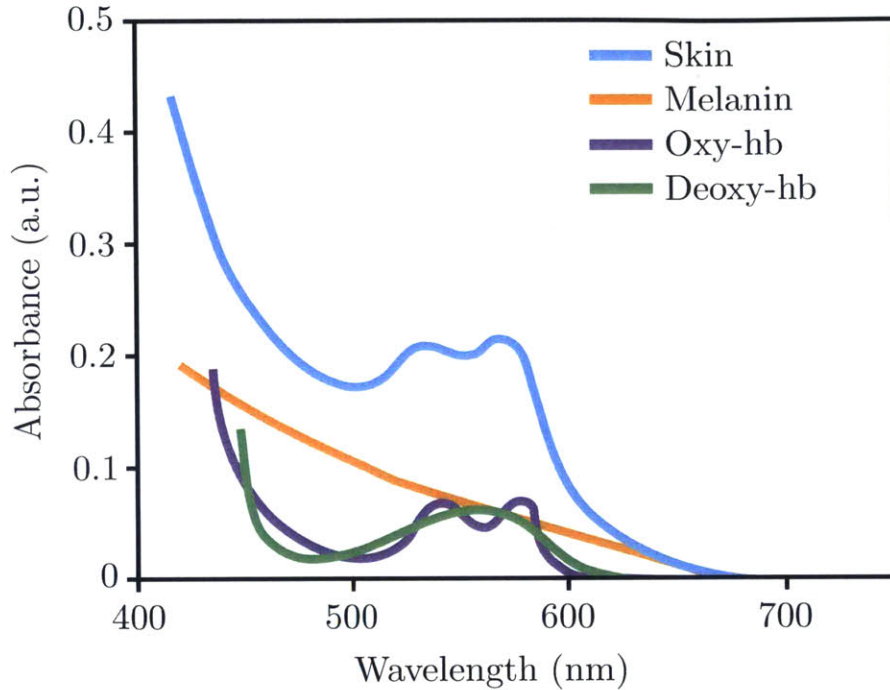
Figure 2-1: Typical absorbance spectrum of skin [27]

skin are melanin, oxy-hemoglobin, and deoxy-hemoglobin [27]. A typical human skin absorbance spectrum can be seen in Fig. 2-1. All three chromophores reflect the red region (>600 nm) of the visible light spectrum, causing skin to have a reddish hue.

The Fitzpatrick scale is used to classify skin based on color [29]. It was developed as a way to estimate the response of different types of skin to ultraviolet light. The Fitzpatrick scale is shown in Table 2.1.

Table 2.1: Fitzpatrick scale, a classification scheme for human skin color

Type	Skin Color	UV Response
I	Very fair	Always burns, never tans
II	Fair	Usually burns, sometimes tans
III	Medium	Sometimes burns, usually tans
IV	Olive	Rarely burns, always tans
V	Brown	Very rarely burns, tans very easily
VI	Black	Never burns, never tans
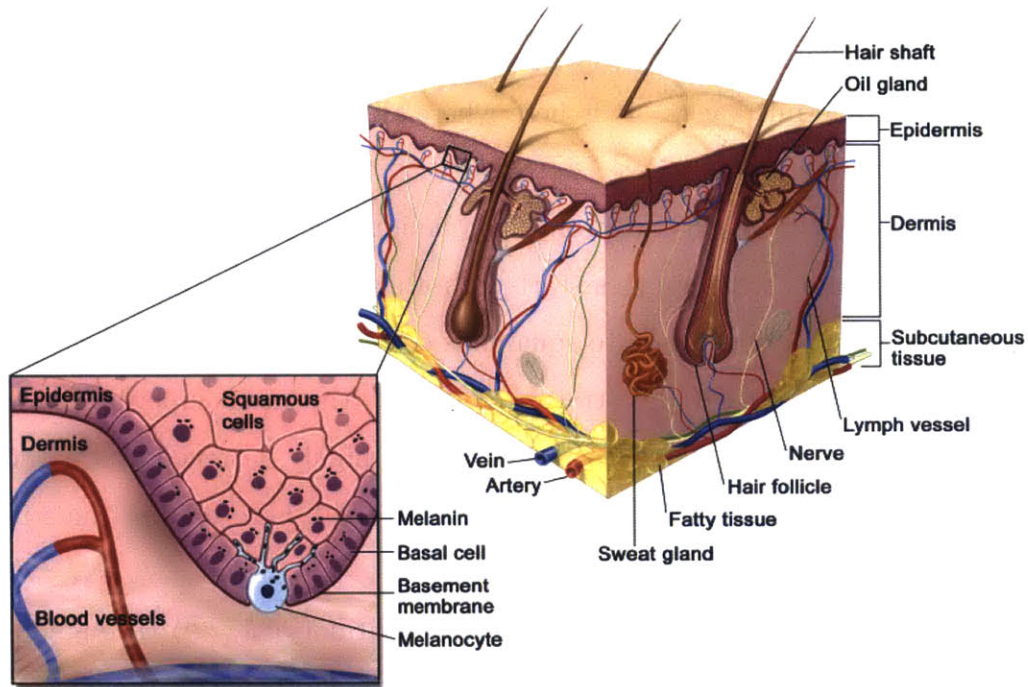
Figure 2-2: Schematic representation of normal human skin [28]

Human skin is made of 3 layers, shown in Fig. 2-2. The epidermis is a thin layer that provides a tough, waterproof barrier to the external environment. The dermis is a network of elastic collagen fibers and lymphatic elements that contributes the most to stiffness as it acts as a place of resistance for external stress [30]. The hypodermis is a viscous and soft layer composed primarily of fat that acts as a cushion and provides insulation. The thickness and elasticity of each layer, varies significantly based on several factors, including age, body site, and hydration [31–33].

2.1.1 Epidermis

The epidermis is a layer of partially keratinized cells that progressively dehydrate as they migrate to outer surface, eventually shedding in approximately 30 days [23]. This results in a constant renewal of the skin. The average layer thickness is approximately 0.1 mm, but this is highly dependent on body location. This thickness can be as low as 0.05 mm for the eyelids and as large as 1 mm for the palms and soles [22].

31

The epidermis is comprised of primarily (90–95%) keratinocyte cells [23]. Basal keratinocytes line the dermal-epidermal junction, a single cell delineation between the dermis and epidermis layers. It is here where all epidermal cells originate from mitotic divisions of stem cells.

Keratinocyte cells move outward from the junction and progressively differentiate before shedding. Basal keratinocytes start with a columnar or cubical shape and a large nucleus. As they differentiate to squamous cells they become long and spindly. Once the keratinocytes reach the stratum corneum (the most superficial layer of the epidermis) they are considered dead, as they are highly flattened and without a nucleus or other cytoplasmic organelle [23, 34]. The dried, hard cells in the stratum corneum act as a shell.

Also sparsely spread (one for every ten basal keratinocytes [22]) throughout the dermal-epidermal junction are melanocytes, dendritic cells that look similar to basal cells. Melanocytes produce melanin, a pigmented molecule that gives skin it's color. Melanin acts as a filter by using its darker color to absorb UV light from the sun and other sources, protecting the internal organs from dangerous radiation [25]. The number of melanocyte cells is consistent across different ethnicities, however, the activity of the melanocytes varies giving different pigmentation [22].

Other cells within the epidermis include: Langerhans cells, responsible for immune responses, and Merkel cells, sensory receptors for touch [34].

2.1.2 Dermis

Whereas the epidermis is made up of mostly keratinocytes, the dermis is primarily collagen and elastin, fibrous molecules that provide support as an elastic and compressible connective tissue structure that is interwoven with vasculature, nerves, and other cells. 98% of the total mass of the dermis is collagen [23].

Collagen and elastin are fibrous proteins that give skin its non-linear mechanical resistance [36]. This non-linear relationship can be seen in the stress-strain plot shown in Fig. 2-3. Elastin, the protein that allows skin to snap back to its original shape, resists initial stresses, providing an initially low, linear elastic modulus. Collagen,
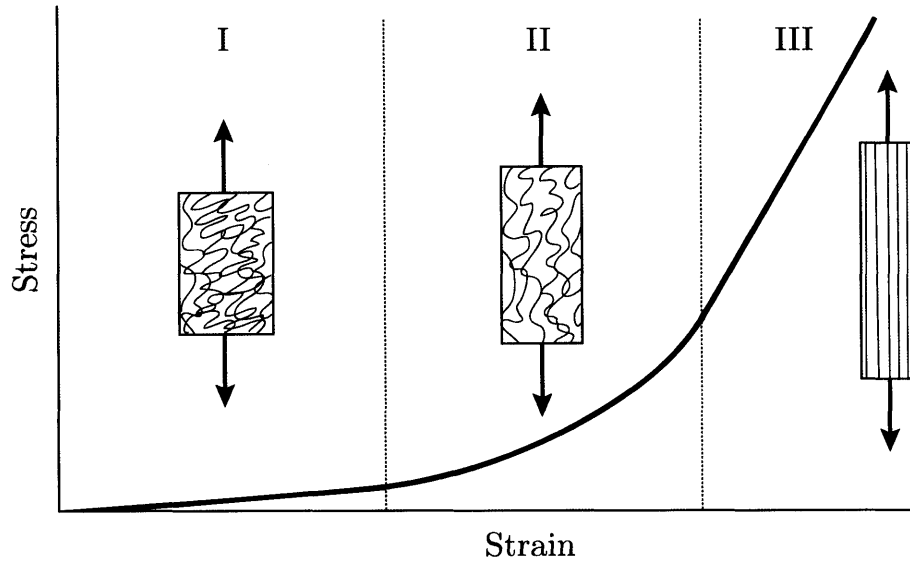
Figure 2-3: Stress-strain plot illustrating the non-linear elastic response of human skin [35]

when unstressed, looks like a long, thin squiggly coiled fibers. As the stress increases, the fibers that were initially randomly oriented start to straighten and align with the load direction. The Young's modulus is non-linear as the fibers are partially straightened. Once fully stretched straight, the elastic modulus again becomes linear, although it is significantly larger than it was at low stresses. Most soft tissues behave this way due to the presence of collagen.

Langer's lines can be useful in describing the patterns of biomechanical anisotropy. These lines are topological lines that can be drawn on the human body to theoretically map the natural orientation of collagen fibers in the dermis. Along these lines, the skin has the least flexibility and the highest stiffness.

The thickness of the dermis ranges from 0.5–2 mm [37, 38].

2.1.3   Hypodermis

The hypodermis, or subcutaneous fat layer, is made up of a loose connective adipose tissue. This layer provides thermal insulation, cushioning from mechanical stresses,

and a method of energy storage [34]. The thickness of the hypodermis varies significantly, ranging from 1 mm to 5 cm in healthy adults [30].

2.2 Skin Lesions

It is common for people to have one or more lesions on the body; most of the time, these are harmless and benign, however, these lesions can become malignant. It is helpful to understand the morphological and functional differences between lesion types so they can be diagnosed properly. The textbooks by Burns [34], Soutor [25], and Rigel [39] provide an excellent overview of lesion types which are summarized below. This review is not exhaustive and only presents the types of lesions that are related to this research.

2.2.1 Benign Skin Lesions

Non-cancerous skin lesions can be separated into two groups — melanocytic lesions, or those that originate from melanocytes, and non-melanocytic, or those that arise from other cells or vasculature.

2.2.1.1 Melanocytic Lesions

Melanocytic nevi, most often referred to as moles, are among the most common benign tumors in humans. Benign nevi are typically small, circular macules, papules, or nodules. Macular is just a flat change in color of the skin. Papular and nodular are solid raised lesions that are less than and greater than 1 cm in diameter, respectively. The most common presentations of nevi are junctional, intradermal, and compound nevi. Other nevi are congenital, dysplastic, halo, blue, and spitz nevi.

Junctional Nevi As their name suggests, junctional nevi lie within the dermal-epidermal junction and are macular. They can be found anywhere on the body and are typically less than 1 cm.

Intradermal Nevi Intradermal nevi are nested in the dermis and are papular. They commonly appear on the face and have little pigment.

Compound Nevi Compound nevi have both junctional and dermal components resulting in a raised papular bump surrounded by a flat pigmented area.

Congenital Nevi Congenital nevi are those that are present at birth and not acquired, occurring in approximately 1–6% of newborns. The size can vary significantly, ranging from less than 1 cm to covering an entire portion of the body, and they will enlarge proportional to the child's growth.

Dysplastic Nevi Dysplastic, or atypical, nevi are common macular or papular lesions that are benign but appear with variable colors and irregular borders, sharing similarities with malignant melanoma. It is controversial whether dysplastic nevi are precursors to malignant melanoma. These lesions are typically removed due to their ambiguity.

Other Types of Nevi Halo nevi are pigmented melanocytic nevi surrounded by a halo of depigmented skin. Melanoma occasionally looks similar to halo nevi so if the nevus looks suspect at all, a dermatologist will typically remove it.

Blue nevi range in color from blue to black and are most common in Asians. Like halo nevi, melanoma sometimes appears comparable to blue nevi, so it will be biopsied if there are any atypical features.

Spitz nevi are pink or brown lesions that are most common in children. Occasionally they will grow quite rapidly and then remain unchanged for years.

2.2.1.2 Non-melanocytic Lesions

The most common non-melanocytic lesions are seborrheic keratosis, lentigo, dermatofibromas, and acrochorda. Less common are haemangiomas. Not mentioned but also included in this class are keloid scars and cysts.

Seborrheic Keratosis   Seborrheic keratosis appears as a flat or raised papule with a smooth, waxy surface caused by the overgrowth of keratinocytes in the epidermis. Color ranges from yellowish-brown to dark brown and black. This type of lesion is extremely common in those over sixty and typically appears in grouped formations on the trunk.

Lentigo   Lentigines are small, flat, pigmented spots on the skin that result from an increased number of melanocytes in the dermal-epidermal junction. The additional melanocytes differentiate a lentigo from a freckle, which in contrast, is just an increase in melanin. A lentigo is typically acquired but can be congenital. Color is light to dark brown as they ordinarily appear in sun exposed skin areas.

Dermatofibromas   A dermatofibroma is a firm papule or nodule. The stiffer lesion is caused by a fibrotic healing response to a minor trauma. Dermatofibromas are generally small with light to dark brown pigmentation.

Acrochorda   Acrochorda are generally referred to as skin tags, occurring often in adults along sites of friction, like the armpit or groin. These papules have a thin stalk and their color usually matches the surrounding skin.

Hemangiomas   Hemangioma describes a class of vascular lesions that can present as a melanoma due to it's coloration and assymmetry. The deep red and purple color is typically used to distinguish it from othe lesions. Some hemangiomas are acquired and will disappear, while others are congenital and permanent.

2.2.2   Malignant Skin Lesions

Cancer develops when DNA within the cells becomes damaged and the body is unable to repair the damage. These damaged cells begin to grow, divide uncontrollably, and override their programmed cell death. As the damaged cells multiply, they form a neoplasm or tumor and start to restructure the surrounding tissue. At some point
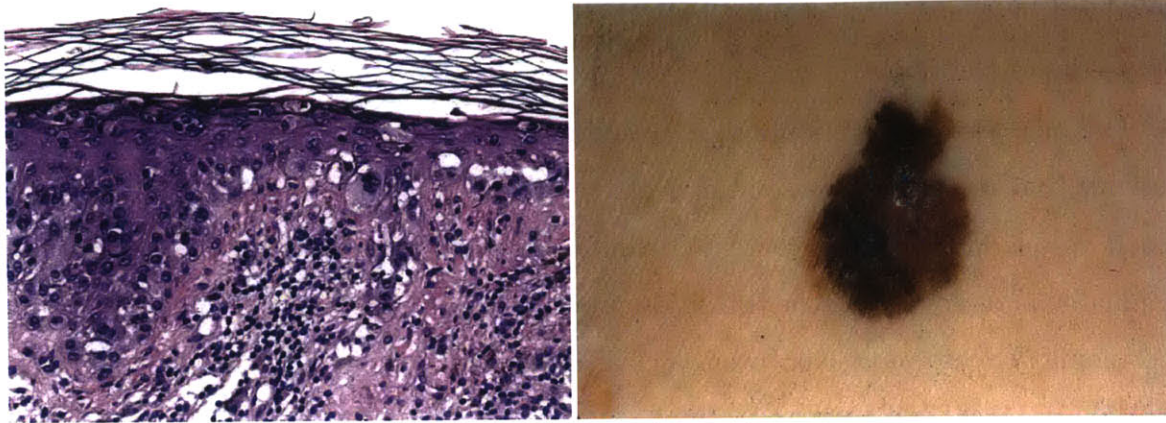
Figure 2-4: Photograph of malignant melanoma next to histological section [39]

the cells start to diffuse to other parts of the body. The abnormal cancer cells will start to inhibit the function of vital organs and death will occur.

The most common types of skin cancer are melanoma, basal cell carcinoma, and squamous cell carcinoma. The details of these will now be discussed, with primary focus on melanoma.

2.2.2.1 Melanoma

Pathophysiology Melanoma is a cancer of the melanocytes. Some malignant melanomas develop from preexisting benign nevi, but most arise *de novo*, or from no existing lesion. The genetic mutations that occur are complex and dependent on the melanoma subtype. A malignant melanoma and its histological cross-section are shown in Fig. 2-4. The groupings of dark purple dots are nests of malignant melanocytes surrounded by a pink to red extracellular matrix of collagen. Melanoma grows radially first before vertically invading the dermis.

The presence of melanin in the dermis is the most significant sign of melanoma, but cannot be used as sole diagnosis criterion because the earliest stage of melanoma, *in situ*, is located only in the epidermis. Other signs of melanoma are the thickening of collagen fibers in papillary dermis (fibrosis), increased blood supply at the lesion periphery (erythematic reaction), and lack of blood within the lesion in the areas

destroyed by cancer. All of these indications result in detectable changes within the properties of the skin.

The increased blood supply to a cancerous lesion is due to the elevated metabolic activity that requires increased nutrients to survive. The development of additional blood vessels facilitates an increased tumor mass [40]. Blood vessel vascularization gradually increases during the transition process from benign nevi to dysplastic nevi to melanoma. Excessive vasculature is a clear indication of a high chance of malignancy [41, 42].

The rate of melanoma growth is difficult to quantify as it is dependent on several factors. One study found that one-third of the melanomas grew vertically into the dermis by 0.5 mm per month or more with a median monthly growth rate of 0.12 mm for superficial spreading melanomas, 0.13 mm for lentigo maligna melanomas, and 0.49 mm for nodular melanomas [43]. As mentioned in Section 1.1, survival is nearly guaranteed if the thickness of a cancerous tumor is less than 0.76 mm, but drops to less than 50% when the tumor exceeds 3 mm in depth. This provides further evidence that delaying diagnosis and treatment for just a short amount of time can rapidly decrease the probability of survival.

Clinical Presentation The morphological features of malignant melanoma are used to distinguish it from a benign lesion. Melanoma appears abnormal, with asymmetric and irregular borders, and a mix of colors, ranging from red and blue to brown and black. Late-stage melanomas will ulcerate or bleed. Melanoma constantly changes, whereas benign lesions remain consistent in appearance. A changing mole has a 400 times higher relative risk factor for the development of melanoma [45].

Subtypes of Melanoma Location, morphological appearance, and histological presentation are used to classify malignant melanoma into different subtypes.

Superficial Spreading Melanoma Superficial spreading melanoma is the earliest stage and most common type of melanoma, accounting for approximately 70%
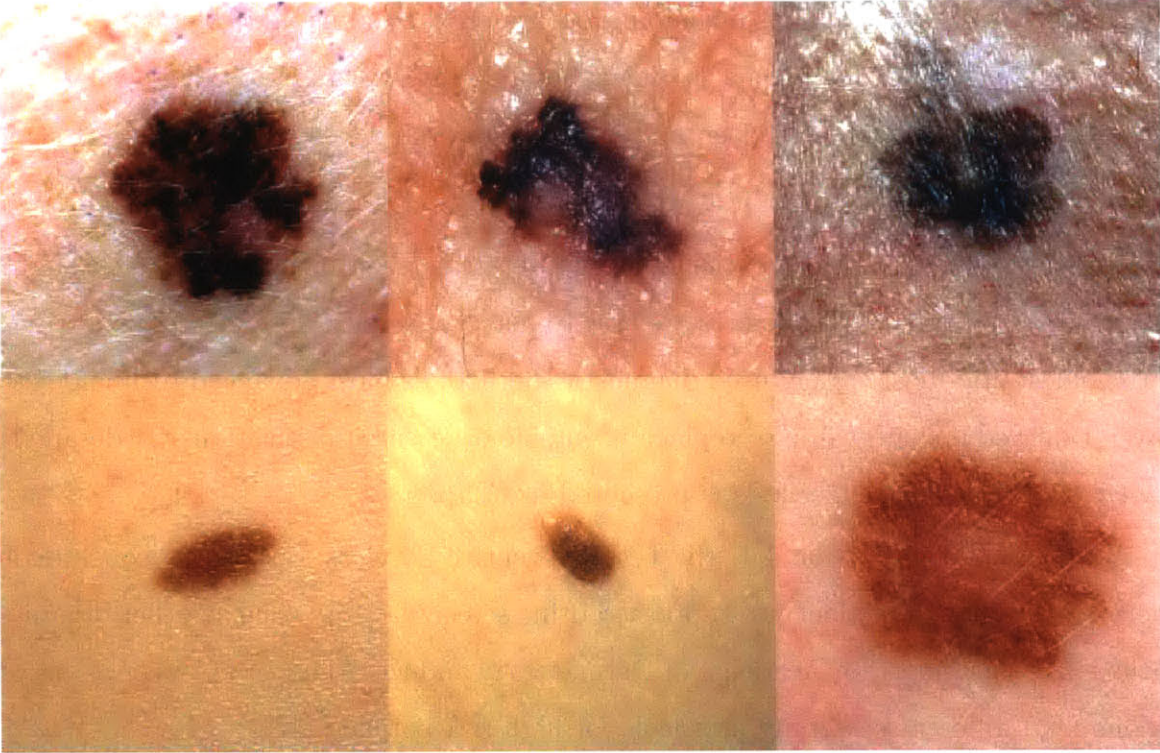
Figure 2-5: Malignant melanoma (top) compared with benign nevi (bottom) [44]

of all malignant melanoma cases. This type of melanoma is a superficial lesion that is confined to the dermis as it spreads radially.

Lentigo Melanoma   Lentigo melanoma is caused by sun damage and occurs most often in the face and neck of elderly patients. These lesions are characteristically flat, with an large irregular shape and mixed pigmentation. This is a type of slow growing melanoma that has a reduced chance of becoming invasive.

Nodular Melanoma   Nodular melanoma makes up around 15% of all melanomas cases but is considered to be extremely dangerous as it grows quite rapidly into the dermis without growing radially first. The lesion will present as a papule or nodule with dark blue and black colors. Nodular melanomas are the most difficult to diagnose as their shape is usually regular and symmetrical.

Acral Melanoma   Acral melanoma occurs on the palms and soles and is the most common type of melanoma in Asians and Blacks. It can evade diagnosis as it appears in areas that are not often noticed and can even develop under the nails.

Diagnosis   The majority of patients end up detecting their own melanoma through self-diagnosis, while dermatologists are able to detect it sooner [46]. Visual inspection is the oldest and most widely used diagnostic method, as most advanced technologies haven't offered enough value to replace it outside of research institutions. A detailed review of all diagnostic methods is presented in Chapter 3.

As mentioned in Section 1.1, the U.S. Preventive Services Task Force concluded there wasn't enough evidence to support routine screening [15], whereas other organizations like the American Academy of Dermatology and the American Cancer Society recommend different screening protocols for high risk patients [47].

Schleswig-Holstein, Germany, implemented a one-year pilot skin cancer screening program from 2003 to 2004 that resulted in decreased mortality rates [48]. Due to these successful results, more research groups are starting to advocate for targeted screening programs, while even suggesting methods to make this process more efficient [49].

Prognosis   Breslow's depth was one of the first metrics used to prognostically evaluate a lesion [50]. It was reasoned that a thicker lesion was invasive and therefore dangerous. The Breslow's depth staging is shown in Table 2.2.

Table 2.2: Melanoma staging based on Breslow's depth

Stage	Depth
I	less than or equal to 0.75mm
II	0.76 mm – 1.50 mm
III	1.51 mm – 2.25 mm
IV	2.26 mm – 3.0 mm
V	greater than 3.0 mm

The American Joint Committee on Cancer uses the more involved TMN staging system to describe how far a cancer has spread [51]. Staging requires a lesion to be biopsied and reviewed by a pathologist. The TMN system is based on three parts. The T portion describes the tumor with a number from 0 to 4 with larger numbers corresponding to an increased thickness. T can also be assigned a letter to designate that the lesion is bleeding or growing rapidly. The N classification designates if the cancer has spread to nearby lymph nodes. An N ranking requires a lymph node biopsy to be performed in addition to the lesion biospy. The M ranking denotes if the cancer has metastasized to other organs. Lactate dehydrogenase (LDH), an enzyme used for cellular respiration, is also evaluated for the M class. Table 2.3 details the staging criteria.

Treatment The gold standard for treatment of a suspected melanoma is a biopsy to confirm the diagnosis through histopathological analysis. Once the lesion is confirmed to be malignant it is surgically excised. Surgical margins, or the excision of additional healthy tissue around the lesion, helps increase the probability that all cancerous cells are removed, decreasing the chance for a recurrent tumor. The recommended surgical margins for melanoma are 0.5 cm to 2 cm depending on Breslow depth [52]. Pathologists will evaluate the excised tissue to verify that there are no cancerous cells close to the periphery. If cancerous cells are found on or near the edge, additional surgery will be required.

Advanced stages of melanoma require a sentinel node biopsy. A radioactive dye is injected into the lesion and then traced to the first lymph node that it drains to. The sentinel lymph node is biopsied to determine if the cancer has started to metastasize. If cancer is found in the lymph nodes, more advanced, holistic treatment methods required.

There is a specialized method of skin surgery, called *Mohs micrographic surgery,* that is considered state-of-the-art for malignant skin lesion removal [53]. Mohs is named after Frederic E. Mohs, a general surgeon who developed the procedure in 1938. The technique is more commonly used for basal and squamous cell carcinoma,

Table 2.3: TMN Staging for Melanoma

T Classification	Thickness	Ulceration
TX	Tumor cannot be assessed	N/A
T0	No evidence of a tumor	N/A
Tis	Melanoma in situ	N/A
T1	Less than or equal 1.00mm	a: no ulceration b: ulceration
T2	1.01 mm – 2.00 mm	a: no ulceration b: ulceration
T3	2.01 mm – 3.00 mm	a: no ulceration b: ulceration
T4	Greater than 4.0 mm	a: no ulceration b: ulceration

N Classification	# of Cancerous Lymph Nodes
NX	Lymph nodes cannot be assessed
N0	0
N1	1
N2	2 – 3
N3	4 or more

M Classification	Site	LDH Level
M0	No distant metastasis	N/A
M1a	Metastasis to skin, subcutaneous tissue or lymph nodes	Normal
M1b	Metastasis to lungs	Normal
M1c	Metastasis to any other organs	Elevated

but more recently applied to melanoma. Mohs surgery attempts to utilize in situ microscope stained sections to evaluate where cancer has been removed and where it still exists at the edges of the excision.

Immediately after tissue is removed, it is processed and placed on microscope slides. The surgeon then maps out where the cancer has been removed and where more cancer needs to be excised. This iterative process is continued until the entire lesion is removed, resulting in a very time-consuming and labor-intensive process. Specialized equipment and training is required, and each excision can take 45 minutes or more to process [54], all while the patient waits under local anesthesia. Mohs is most frequently done on the face and neck to reduce excessive tissue removal and provide a better cosmetic outcome than the traditional surgical method.

Other types of treatment for melanoma include cryotherapy, immunotherapy, chemotherapy, and radiation therapy [55]. Patients with a history of melanoma will be followed closely after treatment as they are at higher risk to develop additional malignancies.

Epidemiology The common causes of skin cancer are a combination of genetic and environmental factors [45]. Ultraviolet (UV) radiation is a carcinogen linked to skin cancer [56] that humans are exposed to daily, through natural (sunlight) and synthetic (tanning beds) sources. More than 400,000 cases of skin cancer are caused each year from commercial indoor tanning beds [57].

The incidence and mortality rates for melanoma have a strong correlation with age, are higher for non-Hispanic white males, and most often occur on the trunk and upper extremities [58].

Multivariate analysis shows that there are six risk factors that independently influence the chances of developing malignant melanoma [59]. People with one or two of these risk factors have 3.5 times increased risk, and those with three or more factors have an approximate 20 times increased risk to develop malignant melanoma.

The risk factors are:

- Family history of malignant melanoma
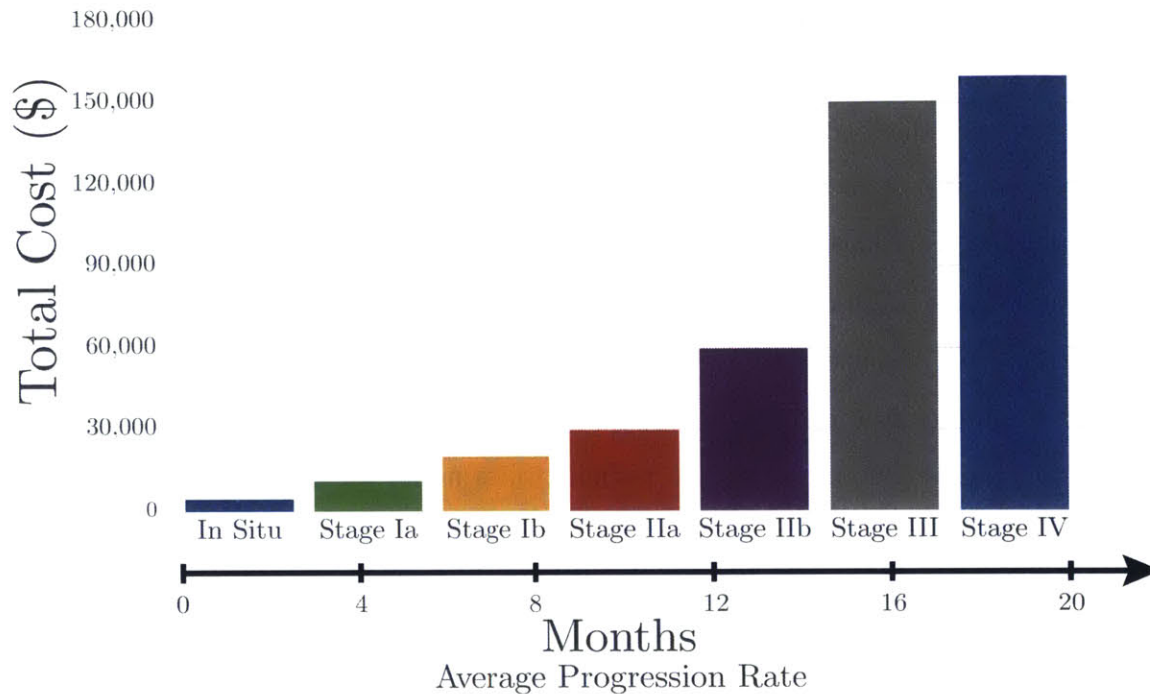
Figure 2-6: Average treatment costs for each stage of melanoma

- Presence of red or blonde hair

- Presence of marked freckling on the upper back

- History of three or more blistering sunburns prior to age 20

- History of three or more years of an outdoor summer job as a teenager

- Presence of actinic keratosis (scaly or crusty skin lesions)

Economic Impact   The cost of melanoma to the healthcare system is significant. The annual cost of treating skin cancers in the U.S. is estimated at a staggering $8.1 billion — $4.8 billion for nonmelanoma skin cancers and $3.3 billion for melanoma [60]. The costs to treat melanoma increase exponentially as it progresses. Late stage melanoma is approximately 32 times more expensive than early stage tumors [61]. A plot of the treatment costs for each stage of melanoma with the average rate of progression is shown in Fig. 2-6. The substantial cost of diagnosing and treating melanoma make it one of the most expensive cancers.

Figure 2-7: Nodular basal cell carcinoma with ulcerating center [39]

The non-monetary costs of skin cancer are also quite large. The average number of years of potential life lost per death was approximately 15 for melanoma [62]. These high costs provide added justification of the development of effective strategies for early diagnosis.

2.2.2.2 Basal Cell Carcinoma

Basal cell carcinoma (BCC) is the most prevalent form of skin cancer with more than three million new cases diagnosed every year in the United States [63]. Fortunately, these common lesions are slow-growing and rarely metastasize. If untreated, BCC will invade locally and start to degrade the skin around it causing it to become cosmetically disfiguring.

As the name suggests, BCC arises from the basal cells lining the dermal-epidermal junction. This causes BCC to appear as a slightly raised, pink, waxy or translucent bump. Late-stage lesions will bleed, especially if irritated. BCC is most common in the sun damaged skin of elderly caucasian patients.
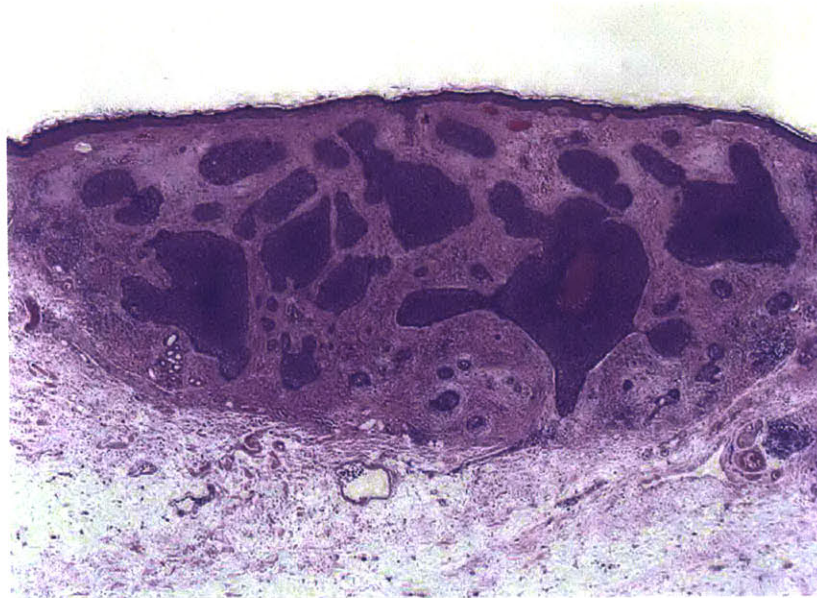
Figure 2-8: Histology section of a large basal cell carcinoma tumor [39]

Fig. 2-7 shows a nodular BCC with red rolling borders and an ulcerating center that has started to form a crater. Fig. 2-8 is a histological section of a large BCC tumor. The large purple masses are clumps of malignant basophilic cells.

Like melanoma, there are several subtypes of BCC, classified based on the clinical presentation and history of the lesion.

Nodular Basal Cell Carcinoma Nodular BCC is the most common type of BCC that appears like a pimple that bleeds often and never seems to heal. The ulcerating center will start to form a pit over time while the border will stay translucent and pearl colored. Tissue destruction becomes quite severe as the lesion grows.

Superficial Basal Cell Carcinoma Superficial BCC is often confused with psoriasis or eczema as it appears like a patch of pink or red scaly skin. It rarely bleeds and lacks the typical translucency but still has the prototypical raised borders.

Morpheaform Basal Cell Carcinoma Morpheaform BCC is a subtype that resembles the plaque of scleroderma or a scar and is quite aggressive, occurring anywhere on the body. The lesion will have an ivory white appearance with ill-defined borders.
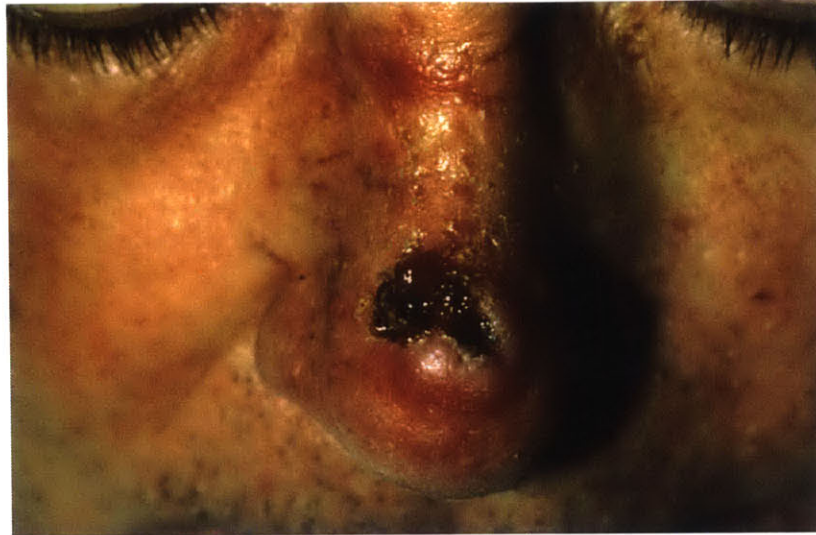
Figure 2-9: Ulcerating squamous cell carcinoma [64]

Infiltrative Basal Cell Carcinoma This variation of BCC is extremely aggressive and destructive. These lesions are usually flat or slightly raised, irregular in shape, and have a high rate of recurrance.

2.2.2.3 Squamous Cell Carcinoma

Squamous cell carcinoma (SCC) is the second most common form of skin cancer occurring in over 700,000 new patients every year [65]. Compared to BCC, it is much more rough and scaly with a dull red color. SCC is most common in elderly patients on chronic sun-exposed areas such as the head, neck, and extremities. SCC is extremely common in solid organ transplant patients.

Fig. 2-9 shows a bleeding SCC on the nose of a patient. Fig. 2-10 is a histological section of invasive SCC, characterized by atypical keratinocytes that are disorganized in structure as they extend from the epidermis deeper into the dermis.

Actinic Keratosis Actinic Keratosis (AK) is the precursor to SCC. AKs are rough, scaly, red or pink circumscribed patches of skin that appear on areas of the skin that have been chronically exposed to the sun. They are usually less than half a centimeter

47
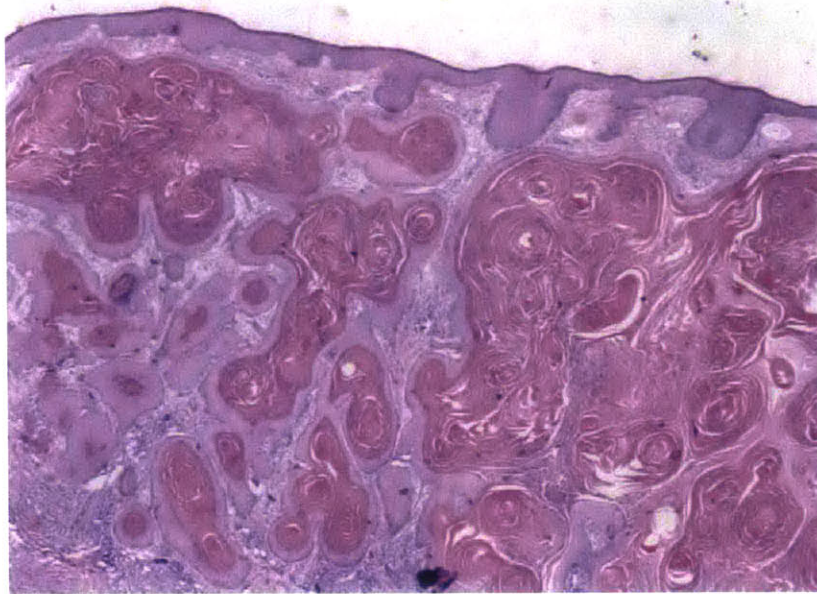
Figure 2-10: Histology section of invasive squamous cell carcinoma [39]

in diameter and feel like sandpaper. Cryotherapy is most often the treatment method for AKs.

Bowen's Disease Bowen's disease is a type of SCC in situ that appears as a red, scaly patch of skin. The lesion is usually slow growing and rarely invades deeper into the dermis.

Invasive Squamous Cell Carcinoma Invasive SCC has a spreading dermal component that has a risk for metastasis. This type of lesion appears clinically as a raised, firm, pink papule or nodule.

2.3   Tissue Mechanics

The mechanical properties of skin are some of the most useful tissue characteristics that can aid in medical diagnosis of various conditions. Cancer causes noticeable variations in the elastic properties or thickness of tissue. Palpation (shown in Fig.
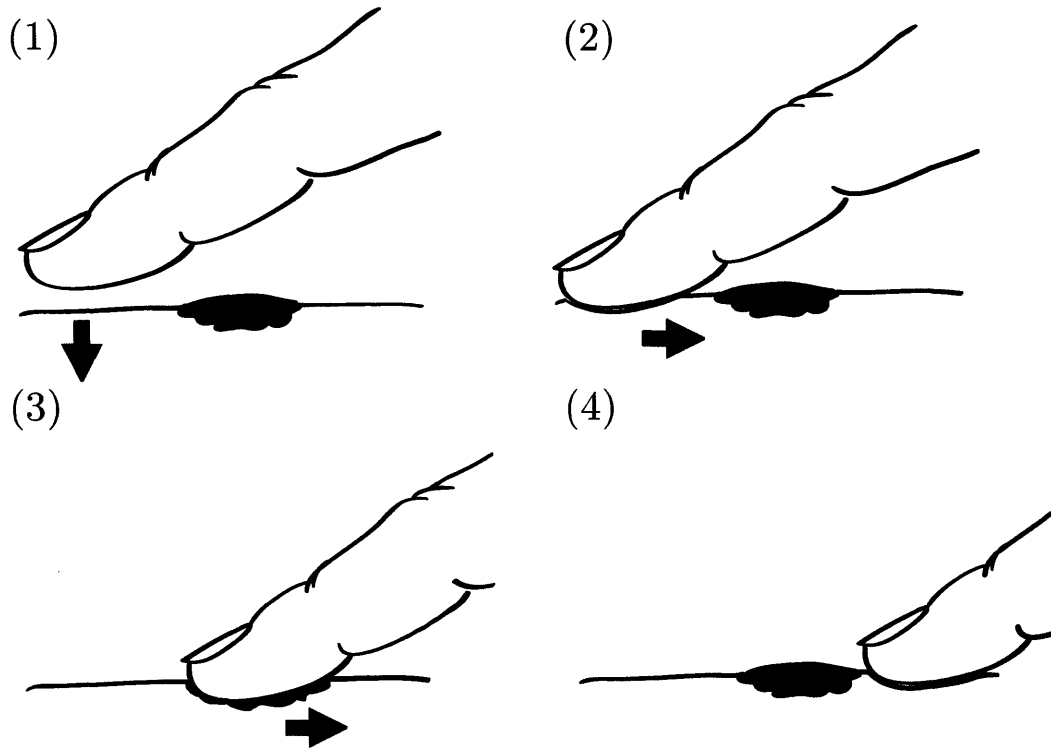
Figure 2-11: Example of palpation

2-11) of hard masses is a primary screening technique for several types of malignant tumors including breast, thyroid, and prostate.

Palpation is highly effective due to the modulation of tissue mechanical properties caused by disease. In addition to visual evaluation, digital palpation is used by dermatologists to detect skin cancer by sensing changes in the stiffness of a tumor compared with its surrounding tissue.

The research in this dissertation focuses primarily on the mechanical characteristics of tissue, therefore, a brief overview of fundamental tissue mechanics principles and models will now be presented, followed by the quantification of healthy tissue stiffness and an explanation of the change in stiffness that occurs when cancer occurs.

2.3.1 Elasticity

In mechanics, constitutive equations relate a material's response to mechanical loading using the intrinsic material properties. Hooke's law, used as a model to describe

an ideal linear elastic solid, states that stress is linearly proportional to strain [66]. This physical relationship is due to the materials ability to store potential energy. Hooke's law is only used as a first order approximation because it breaks down for large deformations and is only applied to time-independent cases as dynamic effects are not considered.

Hooke's law can be written in different forms. The one-dimensional case relates a force, F, to displacement, δ, by the spring constant, or stiffness, k:

$$F = k\delta \tag{2.1}$$

This can be rewritten for all three dimensions as:

$$\sigma = E\varepsilon \tag{2.2}$$

Stress, σ, is related to strain, ε, by the elastic modulus, E, also referred to as Young's modulus. Young's modulus is for axially-loaded conditions. When a material is loaded transversely, or in shear, the shear modulus is used. Shear modulus, G, and elastic modulus, E, have the following relationship:

$$E = 2G(1 + v) \tag{2.3}$$

Poisson's ratio, v, is the ratio of transverse to axial strain. Tissue, like rubber, is incompressible and conserves volume when deformed, so Poisson's ratio is 0.5, simplifying Eqn. 2.3 to:

$$E = 3G \tag{2.4}$$

One method for determining shear modulus is to apply a loading to a material and then measure the shear wave's speed of propagation. The relationship of shear modulus to density, ρ, and wave velocity, v, is:

$$G = \rho v^2 \tag{2.5}$$

Elastic modulus is not always the same as stiffness. Stiffness can vary based on structure geometry, whereas elastic modulus is an intrinsic property of the material. However, for a uniaxial load such as tension or compression, stiffness and elastic modulus can be used interchangeably. In this work, the primary loading type used is uniaxial, so stiffness, elastic modulus, and Young's modulus will be used as synonyms.

Tissue, similar to rubber, is highly compliant relative to other solids and therefore undergoes large strain when deformed, causing it to quickly diverge from the linear elastic model. Nonlinear elastic materials are classified as hyperelastic. Hyperelastic models are derived from the strain energy density function [67]. The general polynomial model for an incompressible hyperelastic material is:

$$U = \sum_{i,j=0}^{n} C_{ij}(I_1 - 3)^i (I_2 - 3)^j \tag{2.6}$$

where U is the strain energy density, C_{ij} are experimentally determined material constants, and I_1 and I_2 are invariants of the deformation tensor.

While there are several variations to the general polynomial hyperelastic model, the Neo-Hookean, Mooney-Rivlin, and Ogden variants are most often applied to tissue. The Neo-Hookean model [68] is the simplest as it determines strain energy from a single material property constant, C_{10}, and the first deviatoric strain invariant, I_1:

$$U = C_{10}(I_1 - 3) \tag{2.7}$$

The simple Neo-Hookean model does not fully capture the non-linear effects that happen at large strain. The Mooney-Rivlin model [69] addresses this by taking into account additional strain invariant terms:

$$U = C_{10}(I_1 - 3) + C_{01}(I_2 - 3) \tag{2.8}$$

For an incompressible material:

$$C_{10} = \frac{G}{2} = \frac{E}{6} \tag{2.9}$$

51

The Ogden model [70] is the most sophisticated, using experimentally-determined material parameters, μ_p and α_p, and the principle stretches, λ_i:

$$U = \sum_{i=1}^{N} \frac{\mu_p}{\alpha_p}(\lambda_1^\alpha + \lambda_2^\alpha + \lambda_3^\alpha - 3) \tag{2.10}$$

μ_p and α_p share the following relationship with the material's shear modulus:

$$G = \frac{\sum_{p=1}^{N} \mu_p \alpha_p}{2} \tag{2.11}$$

When loaded dynamically, the elastic relationships presented will not fully describe how tissue will respond. Tissue has a large fluid component that gives it viscous properties, affecting how the tissue respond to different strain rates. Viscoelastic effects can be seen when plotting stress and strain as a function of time and viewing the stress relaxation, creep, and hysteresis that occurs. For simplicity, this thesis ignores viscoelastic effects by assuming that all loading is done quasi-statically.

2.3.2   Tissue Stiffness

The literature on the elasticity of healthy tissue varies significantly and is extremely limited for abnormal tissue. It is clear that there is a differentiation in the stiffness of healthy tissue versus cancerous tissue [71], however, it is quite difficult to determine the absolute stiffness values.

Various techniques have been used to quantify the mechanical properties of skin in vivo. These include: compression or indentation, suction, torsion, wave propagation, tension from an extensometer, and impact from a ballistometer [72, 73].

Because skin is a viscoelastic material, meaningful deviation in skin stiffness values can occur. Repeatedly stretching the skin alters the mechanical properties as the tissue takes time to recover to its original state. Posture can also affect amount of slack in skin, resulting in significant deviations in measured values. Measurements using torsion, suction, or speed of shear wave propagation are all influenced by posture [74].

Table 2.4: Tissue elasticity parameters for the three layers of human skin

	Young's Modulus (kPa)	Mooney-Rivlin C_{10} (kPa)	Mooney-Rivlin C_{11} (kPa)	Ogden μ (kPa)	Ogden α
Epidermis	1,000	9.4×10^3	8.2×10^4	8.2×10^4	2.98
Dermis	35 – 300	9.4	82	22.6	3.29
Hypodermis	2 – 35	3	0	10.4	13.6
Lesion	50 – 400	N/A	N/A	N/A	N/A

Studies have shown that in vivo estimation of the skin's Young's modulus, a measure of stiffness, shows a range of values covering four orders of magnitude (10^4 to 10^8 Pa) [26]. Most research puts this value at approximately 10 kPa, but the results are highly dependent on measurement method [75]. This value has been shown to decrease with age, as the skin begins to lose its elastic properties [76]. Cancer, on the other hand, increases the Young's Modulus. One study found the average Young's Modulus of cancerous skin to be 52 kPa, however, these measurements were taken in vitro [77]. Another group found melanomas to be up to six times stiffer than normal surrounding skin [78].

Different models have been used to estimate the Young's Modulus of the individual skin layers. The Young's Modulus of the epidermis, the thin layer of dehydrated skin cells, is typically found to be 1 MPa [79, 80]. The value for the dermis is much less, ranging from 35–300 kPa [31, 80]. The hypodermis, composed of mostly fat, is even lower, with values of 2–35 kPa [31, 80]. The coefficients for the hyperelastic Mooney-Rivlin [81, 82] and Ogden [83] models of human tissue have also been experimentally determined. The coefficients can be found in Table 2.4.

Most tissue models disregard the hypodermis layer, however, since it is a compliant link between the upper skin layers and the much stiffer muscle and bone, it was included in all analysis. The boundary conditions under the skin can dominate the

resultant mechanical response when a force is being transmitted through the thickness of skin.

2.3.3 Tissue Stiffness Modulation Induced by Skin Cancer

Tissue stiffness is not static, but changes during different physiological processes. Examples include tissue development (aging), tissue remodeling during wound healing (scars), and tumor formation (cancer) [40].

Research has shown that while cancer cells are actually more compliant than healthy cells, cancer tissue as a whole is actually stiffer than healthy tissue. Individual cancer cells, independent of cancer type, are far less stiff than normal cells, due to the reorganization of the cell cytoskeleton or inner-cellular scaffolding [84, 85]. The ability of a cell to deform, flow, remodel, and contract allows metastasis as the cell can escape the tumor and migrate by way of the blood or lymph vessels to form tumors at multiple, distant sites [85–87]. Cancer cells with the highest invasive potential are five times less stiff than healthy cells [88].

Cancer tissue becomes stiffer on a macroscopic scale because the extracellular matrix (ECM) or stroma remodels and stiffens so that the architecture and physical properties become fundamentally different [89, 90]. Part of the increase in stiffness can be attributed to excess activities of lysyl oxidase, which cross-links collagen fibers and other ECM components [90]. Collagen metabolism is also deregulated in cancer, causing increased expression, elevated deposition, and altered organization [40, 89]. Collagen is the primary component contributing to the tensile strength of tissue. Increases in ECM stiffness enable cells to generate increased traction forces on their surroundings, which enhance growth, survival, and invasion to other parts of the body [91].

Chapter 3

Technology Background

It is clear that early diagnosis is the key to increasing the survival rate of patients with skin cancer. Minimizing the time before detection is critical when every additional day increases the potential for metastasis. A growing workforce shortage of dermatologists causes a long wait time for patients seeking evaluation of concerning moles. The average wait time to see a dermatologist is almost 30 days, with a high of 72 days in Boston and a low of 16 days in Miami [92]. Even worse, patients with changing lesions are forced to wait just as long as those patients with routine cosmetic complaints [93]. Significant research and development has went into various technologies to improve the efficacy of the screening process so that cancerous lesions can be caught sooner.

Prior to the 1980s, skin cancer was diagnosed only when the lesion started bleeding or ulcerating — too late for any effective intervention. Non-invasive melanoma diagnosis techniques have seen significant evolution since then, focusing primarily on visual or optical-based methods. This led to the development of visual screening techniques that relied heavily on the identification of morphologic clinical features. The most widely known and used of these techniques was the ABCD acronym; representing Asymmetry, Border irregularity, Color variation, and Diameter. These criteria were simple and effective but rather technologically primitive.

During the 1990s, a specialized microscope called a dermoscope was developed to enable dermatologists to see subsurface features. More recently, several variations of digital vision techniques and tools with sub-cellular resolution have been developed.

Some methods incorporate multispectral imaging and leverage the chromophores to quantify melanin, blood, and collagen content within a lesion. While most of these new technologies have proven to assist in the diagnosis of skin cancer, initial diagnosis is still always performed visually first.

The diagnostic ability of all new technology is quantified and compared using the sensitivity and specificity measures. Sensitivity, or the true positive case, is the probability that a patient tests positive for cancer and actually has cancer. Biopsy ratio is an important measure of sensitivity. Biopsy ratio is the number of biopsies of benign lesions to make a diagnosis of one skin cancer and this value varies from 5:1 to 500:1 [19]. Specificity, or the true negative case, is the probability that a patient tests negative for cancer and actually doesn't have cancer. False negatives are considered the worst type of diagnosis as this delays treatment and puts the patient at high risk.

The following review on non-invasive skin cancer detection methods will start with traditional detection methods that are most commonly found in practice today. Then, the most promising new technologies will be discussed. Table 3.3 is a comprehensive list of the technologies for comparison. Finally, because skin stiffness is an important metric for this research, methods to quantifiably measure the stiffness of skin will also be discussed.

3.1 Established Methods

The current gold standard in melanoma diagnosis is visual inspection of the skin by the naked eye [94]. This typically involves a trained physician examining a skin lesion. If the lesion is worrisome, an invasive biopsy will be performed, followed by histological examination of the skin specimen. The biggest challenge is identifying which lesion has the highest probability for being cancerous.

In 1985, the ABCD system was presented to assist dermatologists in visual diagnosis of melanoma by establishing metrics for evaluating four parameters — asymmetry, border irregularity, color variation, and diameter [95]. Since then, E has been added to the list, reminding physicians to look for evolving or changing lesions. Studies have

Table 3.1: Sensitivity and specificity of individual ABCDE criteria [98]

Metric	Sensitivity (%)	Specificity (%)
Asymmetry	57	72
Border Irregularity	57	71
Color Variation	65	59
Diameter	90	63
Evolution	84	90

Table 3.2: Sensitivity and specificity based on the number of ABCDE criteria present [98]

Criteria present	Sensitivity (%)	Specificity (%)
One	97	36
Two	89	65
Three	66	80
Four	54	64
All five	43	99

shown up to 35% of prospectively diagnosed melanomas were identified based solely on the basis of change [96, 97].

Several other similar checklists have also been proposed that vary in complexity. The sensitivity and specificity for these visual checklist techniques ranges from 57–90% and 59–90%, respectively [44].

Table 3.1 shows a break down of the sensitivity and specificity of the individual ABCDE criteria. As demonstrated by Table 3.2, sensitivity is decreased and specificity is increased when more criteria are present.

Along with guidelines, different lighting conditions have been used to improve visual diagnosis by creating increased contrast between the lesion and healthy skin

surrounding it. A Wood's lamp, similar to a black light, emits light in the UV spectrum (~360 nm wavelength). Melanin absorbs this spectrum and collagen reflects it, making it easier to distinguish between the two [99].

All dermatologists use visual inspection to detect cancerous lesions; however, it has been proven to vary in effectiveness and is highly dependent on the type of lesion [100] and who is performing the diagnosis [101]. The ability to accurately diagnose melanoma varies significantly between specialists (dermatologists) and non-specialists (primary care physicians, patients) with more experience leading to higher diagnostic accuracy. Dermatologists diagnostic accuracy ranges from 25% [102] to 89% [103], whereas non-specialists accuracy ranges from 4% to 80% [18, 102, 103]. This is worrisome as the majority of patients with suspicious skin lesions typically visit their primary care physician before seeing a dermatologist.

Due to these facts, visual diagnosis is commonly associated with a risk of missed melanomas (false-negative) and unnecessary biopsies (false-positive).

3.2 Research and Commercial Technology

Several research and commercial entities have developed imaging systems using various modalities to aid in diagnosing melanoma and other skin cancers. These devices range from simple tools to advanced solid-state or opto-electrical imaging probes that are able to give a range of views (full body, clinical, dermoscopic, histopathologic) with a range of resolutions (millimeters to submicrometers).

3.2.1 Total Body Photography

An extension of visual inspection uses high definition photographic imaging to track changes in lesions over time. The entire body is photographed in a standardized method and then software is used to compare potential lesions in follow-up sessions. This is a proven method for high-risk patients with several lesions that need to be tracked [104].
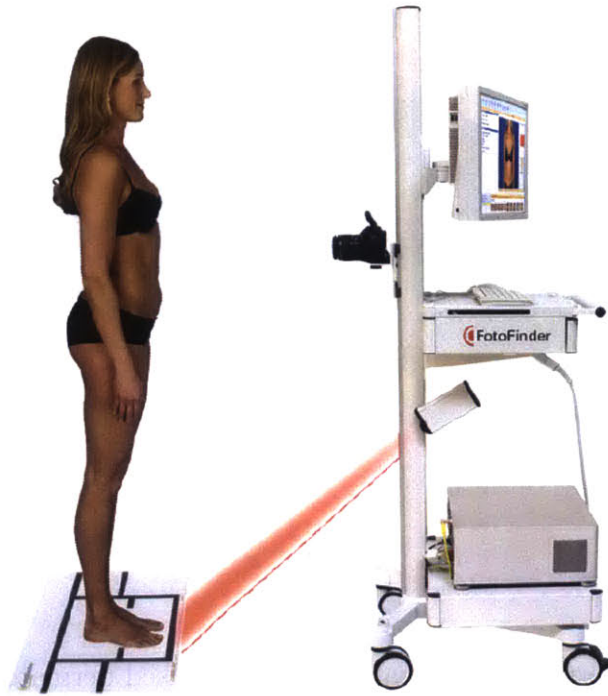
Figure 3-1: FotoFinder Bodystudio – an automated total body mapping system [105]

Total body photography is the only method that helps clinicians detect new lesions of concern. All other methods that will be discussed only help clinicians further evaluate lesions that are already deemed suspicious by visual inspection. Total body photography provides a history of the entire body, allowing clinicians to determine when new lesions appear. However, the technique is quite time consuming and laborious. Costs can also be very high at $500 per person and are not typically covered by insurance [19]. An entire total body photography system can cost $3,000–30,000.

The photographs are primarily used to detect changes over time. This relies on the premise that relative change is a sensitive marker for early melanoma and can lead to the excision of thinner, earlier stage melanomas.

Several commercially available, computer-aided total body-imaging systems exist. Examples include the FotoFinder Bodystudio [105] and Constellation [106]. All are computerized total body photography systems that help the clinician more rapidly and efficiently perform tasks by creating a digital mole map of skin. Full body scans take anywhere from a minute to several minutes to complete.

Figure 3-2: Dermlite DL1 – a smartphone based dermatoscope [109]

3.2.2 Dermoscopy

Dermoscopy, also known as dermatoscopy or epiluminescence microscopy, is the most popular method after traditional visual inspection. It consists of viewing pigmented skin lesions through a handheld magnifying lens or imaging system and using a fluid or polarized lens to absorb scattered light and prevent unwanted reflections. Non-polarizing and polarizing methods do not produce equivalent results — different colors or structures are better seen dependent on the method [107].

All methods of dermoscopy allow for improved visualization of the morphologic structures in the epidermis and dermal-epidermal junction [107, 108]. Dermoscopes typically come as standalone tools; however, products such as the DL1 [109] act as a modular hardware attachment that integrates the dermoscope with a smartphone for increased portability and convenience.

A classification system has been developed to help clinician identify lesions when using a dermoscope. Healthy nevi are symmetric, uniform, fewer than three colors, and orderly architecture. Melanomas generally have an atypical network, peripheral streaks, atypical dots or globules, negative pigment network, off-center pig-

mented blotches, a blue-white veil, atypical vascular structure, and peripheral brown structure-less areas [110, 111]. Diagnosis is dependent on the appearance of these classic features; therefore, the dermoscope is limited in the diagnosis of early and/or featureless melanomas [112]. Additionally, classifying characteristics is very complex and subjective to the user [113].

Dermoscopy has been shown to improve diagnostic accuracy over the unaided eye [114], but the accuracy is highly dependent on degree of experience of the examiners. Dermatologists with 5 years experience or more using dermoscopy had 92% sensitivity and 99% specificity, while inexperienced users had 69% sensitivity and 94% specificity [115,116]. Only 60% of dermatologists in the United States are trained in dermoscopy and fewer than half use it regularly [19].

3.2.3   Computer-aided Image Analysis

Standard clinical and dermoscopic images can be acquired using a digital camera and examined with image analysis algorithms for automated diagnosis. The goal of computer-aided image analysis techniques is to provide repeatable, objective metrics with which to evaluate lesions [113]. This process is typically broken up into the following three stages: image segmentation, feature extraction, and classification. Several types of algorithms exist for each stage.

Image Segmentation   Image segmentation is used to identify the border of the lesion so it can be differentiated from healthy tissue. Pigmented lesions are much easier to segment than non-pigmented lesions, due to the color difference. Segmentation techniques are usually based on differences in intensity, optical flow or gradient-based mapping, or color clustering [117, 118]. Prior to segmentation, the image is pre-processed to remove any lighting artifacts or hairs.

Feature Extraction   Once the lesion is identified in the image, algorithms are used to extract the morphological features, such as geometry, color, patterns, and textures.

61

Similar to visual inspection, feature extraction quantifies the ABCDs along with other metrics.

The symmetry of a lesion is usually determined by bisecting through the center of mass, or centroid, and comparing the areas [119]. Orientation is adjusted until the difference in area is maximized. Symmetric lesions will have a smaller area difference.

Border irregularity is not as straight forward, such that several methods have been shown to be effective, including bulkiness index [120], border irregularity index [121], compactness index [118], and fractal dimensions [120]. All evaluate the border shape based on it's efficiency.

Bulkiness index is the relationship between the area of an equivalent ellipse and the actual area of the lesion. Fractal dimensions characterize the plane filling ability of a curve. Border irregularity index compares the perimeter of a convex hull around the lesion to the actual perimeter of the border of the lesion. Compactness index is a comparison of the perimeter of a lesion to it's area.

Color variation is examined by identifying the range of colors within a lesion. Different color spaces are used based on the color channels of interest, such as red, green, blue (RGB), cyan, magenta, yellow (CMY), hue, saturation, value (HSV), or Y-luminance, UV (YUV) [119].

Diameter can only be determined if the system knows the relationship between pixel locations and real world coordinates.

Classification   After the features are quantified, the results are compared to an empirical database of benign and malignant lesions. Some classification techniques rely on classic statistical methods, whereas othere leverage machine learning techniques, such as neural networks [119]. The results are also usually recorded so that changes can be identified in future evaluations.

Computer-aided analysis software for skin cancer diagnosis has been commercially available for several years, but more recently there has been increased motivation to port the software over to smartphone applications [122].

3.2.4 Smartphone Applications

Within the last few years, smartphones have become increasingly capable and are owned and used daily by a large portion of the population. Various companies have attempted to use the smartphone's functionality by creating applications to help detect cancerous lesions. Several of these non-FDA approved smartphone applications exist on the market. All applications use the phone's built-in camera to take an image of the lesion. The lesions are then analyzed using an on-board image-processing algorithm (automated analysis) or the images are sent to an actual dermatologist for review (teledermatology).

There are no widely-used, commercially-available automated analysis smartphone apps; instead, app stores are full of diagnostic apps that disappear as quickly as they appear. Telederm apps are more prevalent, with some requiring just an image [123] and others requiring additional hardware to improve the image [124, 125].

A study was performed in 2013 to measure the performance of four of the most popular apps available and the results varied significantly. Sensitivity varied from 6.8–98.1% and specificity ranged from 30.4–93.7%, with tele-derm apps [126]. The Federal Trade Commission has confronted marketers of skin cancer detection apps who made false claims about their tool's diagnostic abilities, forcing them to pay fines or cease selling until they become compliant [127]. Technology that improves self-detection of melanoma is beneficial, but extreme caution must be used to avoid harming patients in the process because delaying diagnosis causes the greatest harm to the user.

3.2.5 Multispectral Imaging

Several commercially available devices use the fundamental characteristic that the depth of penetration of light into skin is directly related to wavelength. Lesion reflectance also varies with wavelength. Images are darker at short wavelengths where light penetrates less deep and is absorbed primarily by melanin in the epidermis. Longer wavelengths penetrate deeper into dermis and backscattering from collagen
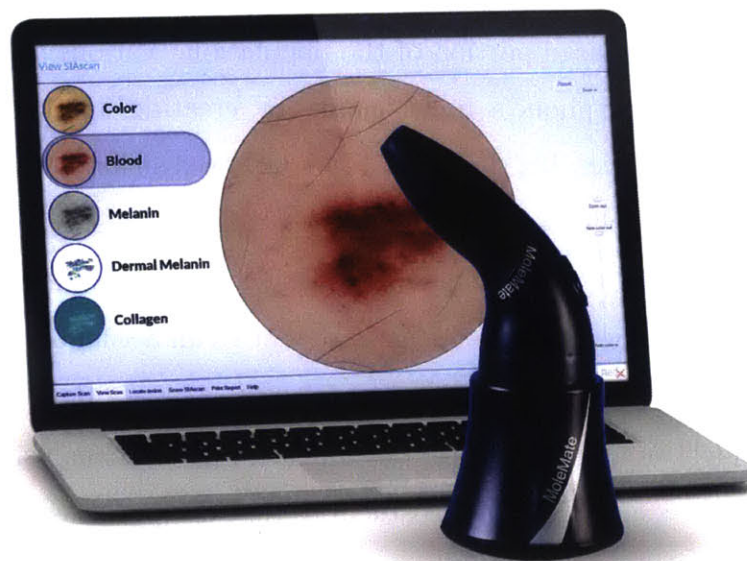
Figure 3-3: MoleMate – a multi-spectral imaging system that quantifies chromophores in skin [128]

is stronger. Two of the most popular devices utilizing these characteristics will be discussed.

MoleMate [128], first released in the early 2000s as SIAscope, relies on the spectrophotometric intracutaneous analysis (SIA) technique. MoleMate records the position of a lesion and then analyzes the distribution of the lesion's chromophores — including melanin, blood, and collagen — in the dermis. The chromophores are differentiated and quantified by producing eight narrow band spectrally filtered images with wavelengths varying from 400–1000 nm [129].

The original SIAscope algorithm had difficulty differentiating sebhorric keratosis and hemangiomas from melanoma so a new scoring algorithm, named MoleMate, was developed. The device's efficacy is highly user dependent [19], resulting in a sensitivity and specificity range of 80–100% and 59–91%, respectively [130]. SIAscopy was FDA approved in 2011 and costs $6000–8000.

Figure 3-4: MelaFind – a multi-spectral imaging system for melanoma diagnosis [131]

MelaFind [131] works similar to the MoleMate by illuminating the skin with light in ten narrow spectral bands ranging from 430–950 nm. White light is emitted through interference filters placed on rotating wheel. A CCD camera detects the reflected light in each band and records the image in gray scale with a 1024-level intensity resolution. The camera has a field of view of 2×2 cm and a pixel width of 20 μm. All ten images are taken in less than three seconds.

Automated image analysis then uses an image segmentation mask to define which pixels are part of the lesion. The lesion area and perimeter are then computed. Additional feature extraction determines asymmetry, blotchiness, and wavelet maxima (texture). Linear classifiers, trained on a proprietary database of thousands of lesions, then give each of the feature parameters a score. Thresholding determines if the lesion is classified as melanoma or not. Images are also stored so they can be used to compare changes over time [132, 133].

The MelaFind device was designed to provide a dermatologist with an objective second opinion. It is intended for use on borderline lesions, or those that dermatologist is considering for biopsy but unsure. The tool was approved by the FDA and European Union in 2011 after a failed initial FDA approval for not adequately comparing device to dermatologists [134]. MelaFind is a very sensitive tool but, similar to dermatologists, trades a high sensitivity for a lower specificity, resulting in biopsy recommendations for many benign lesions [135]. The sensitivity is almost perfect at 95–98% while the specificity range is 8–68% [130], resulting in a biopsy ratio of 10.8:1 [136].

There are a few downsides to the MelaFind device. First, it was designed as an aid for lesions that have historical characteristics of melanoma, meaning a clinician has to first identify lesion as suspicious and then examine it. Additionally, the device is only to be used to give additional information but not confirm the diagnosis.

MelaFind can only be used by a trained professional and has very specific usage criteria. The lesion must be accessible by the tool, have a diameter within 2–22 mm, have sufficient pigmentation, have no scarring or fibrosis, be non-ulcerous and non-bleeding, and not located on acral, palmar, plantar, mucosal, subungual areas or close to eyes. MelaFind can be leased for $10,000 with an annual renewal fee of $2000 plus additional patient costs at $25–175 per use [130]. Most insurance programs do not cover these costs [137].

Studies have concluded that MelaFind increases melanoma detection rates but is unlikely to decrease number of unnecessary biopsies. The device was also found to have a small number of false-negative results. This means that clinicians relying too heavily on the device will miss melanomas. Diffusion of MelaFind has been slow given competition from several other available dermoscopic devices [138].

3.2.6 Optical Coherence Tomography

Optical coherence tomography (OCT) uses light to produce an image based on the optical scattering of different structures within tissue. A laser illuminates the skin and the light is either absorbed or reflected depending on the type of cells within the tissue.

Light travels too fast to measure the time delay of the reflection so interferometry is used. Interferometry is accomplished by selectively detecting light that has travelled the same distance as light to and back from a reference mirror. The laser beam is initially split so half of the beam is sent to specimen, and half to a scanning reference mirror. The interference pattern is then measured to determine position within tissue where light was reflected.

Axial resolution is determined by coherence length of light source, lateral resolution is determined by spot size of incident beam, and penetration depth is dependent on the wavelength of light source. Due to these limitations, lateral resolution is insufficient for cellular resolution and penetration depth is only 1–2 mm [139, 140]. OCT has a 79–94% sensitivity and 85–96% specificity. VivoSight [141] is a commercially available OCT system for skin cancer diagnosis.

3.2.7 Confocal Microscopy

Confocal microscopy is similar to OCT and works by focusing a low-power laser beam on the skin. The laser power is less than 20 mW to prevent tissue damage and is typically at a near infrared wavelength. The light reflected from the tissue passes through a pinhole aperture, allowing only light from the focal plane of interest to pass to the detector, thereby increasing the resolution of the system. A scanner allows multiple images to be compiled and a large horizontal section is built.

Because of the complexity, a confocal microscope is relatively expensive but has a high enough resolution to provide a virtual biopsy. Imaging of the nuclear, cellular, and tissue architecture of the epidermis and other structures within the tissue can be seen. The lateral resolution of the device is approximately 1–2 μm and the axial resolution is 3–5 μm but confocal microscopy has a limited depth of less than 0.2 mm. The entire imaging process requires five to fifteen minutes per lesion [142].

Melanin has high refractive index so it appears brighter and causes increased back scattering in confocal imaging. Melanomas are typically differentiated by identifying polymorphic and irregularly shaped cells with coarse branching dendritic processes [142].

Figure 3-5: Vivascope 3000 – a confocal microscope for skin cancer detection [145]

Confocal Microscopy has shown a 91.9% sensitivity and 69.3% specificity. Studies found that it is best used as a second level examination of lesions selected by clinical and dermoscopic evaluation, with the goal of reducing the number of unnecessary excisions without reducing sensitivity [143]. Additional research demonstrated that combining confocal microscopy with dermoscopy increases sensitivity to 98% while reducing excisions by 23% [144].

Using a single optical fiber to both illuminate and detect laser light has miniaturized the device to a handheld version with a very high sensitivity and specificity [19]. The Vivascope 3000 [145] is an example of a commercially available, handheld confocal microscope for dermoscopic use. The Vivascope costs approximately $50,000 and sensitivity and specificity for the device are 90% and 86%, respectively [142].

3.2.8 Raman Spectroscopy

When light strikes a molecule, an energy transfer occurs that changes the vibrational mode of the bonds between the atoms. This reaction causes the energy of the scattered light to change. Raman spectroscopy measures the energy shift and uses it to identify the types and concentrations of molecules within a sample. Determining the biochemical composition of skin has proven to be effective in differentiating be-

nign and malignant skin lesions, with a sensitivity of 90–100% and a specificity of 54–95% [146].

The Verisante Aura [147] is one of the earliest commercially available skin diagnostic devices using Raman spectroscopy. In the research setting, Raman spectroscopy is being paired with other spectroscopic methods to evaluate the potential for increased efficacy [148].

3.2.9 Laser Doppler Perfusion Imaging

Malignant tumors are metabolically more active than healthy tissue and therefore, require an increase in vascularity and blood perfusion. Laser Doppler perfusion imaging (LDPI) takes advantage of this characteristic to differentiate between malignant melanoma and benign lesions. The technique moves a helium-neon laser at 633 nm wavelength over the skin surface. Erythrocytes in the blood reflect the laser, which is recorded by a scanner and turned into an electrical impulse. The ratio of the mean blood flow between tumors and surrounding healthy tissue can be quantified and then compared [149]. Studies have shown that false negative results prevent LDPI from being sufficient for diagnostic use [150].

Similar to LDPI, vascularity has also been quantified by exploiting the absorption of UV light by hemoglobin in the blood [151]. When a low power, 400 nm light is shone on the skin and then imaged, the blood vessels will look black with no light reflection. Vascularity is inferred by measuring the intensity distribution on the image.

3.2.10 Magnetic Resonance Imaging

Magnetic resonance imaging (MRI) has been used extensively in radiology to view detailed images of a patient's internal organs. MRI works based on absorption and re-emission of radio waves from tissue protons exposed to strong magnetic field. The technique is able to successfully differentiate between malignant melanoma and benign skin tumors [152] but is limited due to high costs, duration of evaluation, large size, need for specialized training, and limitations in patients with metal implants [94,113].

3.2.11 Ultrasound

The technology of ultrasound has been around for several decades but has only more recently been applied to skin cancer detection. The principle behind ultrasound is similar to OCT but uses sound instead of light. A transducer directs high frequency sound waves into skin and then detects the returned echo. Based on the speed of sound through a specified material, a time delay window is used to determine when to receive the signal. Images based on reflections are then created due to different acoustic properties within the tissue. Echoes carry information on the absorption and reflective properties of the tissue.

There are two primary modes of ultrasound scanning. A-mode (amplitude) creates a 1D graph that shows the intensity of reflections. B-mode (brightness) uses multiple A-mode scans to build a 2D image. The strength of the returned signal is dependent on strength of incident signal, depth from skin surface, scatter properties, and absorption characteristics of the lesion. Higher frequencies provide better resolution but limited depth in the skin. 20 MHz penetrates 1.5 cm while 100 MHz only penetrates 1.5 mm [113].

Ultrasound images have been used to discriminate between lesion types by measuring the quantitative mean echo strength between a lesion and the surrounding normal tissue. Melanoma has been found to be less attenuating to the signal than benign lesions [153]. The sensitivity and specificity of ultrasound are 81% and 76%, respectively [154]. Ultrasound can be combined with externally applied compression to quantify tissue stiffness, commonly referred to as elastography.

Ultrasound was the only technology found that has been used to map the size of tumors for surgical excision [155].

3.2.12 Infrared Thermal Imaging

As mentioned in Section 3.2.9, cancerous lesions are metabolically hyperactive and have an increased blood supply. Both of these characteristics cause a cancerous

lesion to be significantly warmer than healthy tissue. Research has shown that this temperature difference can be detected using infrared imaging.

Infrared (IR) imaging can be done passively or actively, but external forcing is faster and more robust. The skin is cooled and then the dynamic thermal response of the structure is captured using IR imaging. Movement can affect the readings, so motion-tracking methods have been developed [156, 157]. Further clinical studies are needed to determine the efficacy of this method for skin cancer detection. This technique is used commercially for breast cancer detection [158], however, no product specific to skin cancer exists on the market yet.

3.2.13 Bioimpedance

Morphological changes that are characteristic to cancerous skin lesions cause the conductivity and capacitance of the lesion to increase as the lesion size grows. Bioimpedance, like other skin properties, varies significantly depending on the person's age, skin location, hydration level, etc., and therefore a threshold value cannot be used, but instead changes over time must be monitored.

An array of electrode pins penetrating the top layers of the skin are used to induce an electric current and then measure the trans-impedance between the pins. Contrary to visual inspection, where the sensitivity increases for thick, mature tumors; electrical impedance counterintuitively detects early tumors with a better accuracy. Therefore, in order to detect all cases, electrical impedance is most effective when used in combination with visual inspection. The sensitivity is 91–100% and the specificity is 24–80% [130], with the highest sensitivity on the trunk and extremities but reduced sensitivity on the head and neck [159]. Nevisense [160] is a bioimpedance device that is commercially available in Europe and Australia.

3.2.14 Positron Emission Tomography

Positron Emission Tomography (PET) scans are used to image functional processes in the body. The system creates an image by detecting emitted gamma rays from tracer

particles that have been introduced in the body. Tumor cells consume a larger amount of glucose compared to healthy cells in order to sustain a high proliferation rate and increased need for macromolecular synthesis. PET scans detecting 18-Fluroscence can be used to see the increased glucose consumption in tumor cells. This method is cheaper than MRI but still suffers from similar limitations [94].

3.2.15 mRNA Tape Stripping

Tape stripping is considered a non-invasive method for detecting skin cancer because only a small number of cells are removed from the skin. Adhesive tape is applied to the lesion and the border is then marked on the tape. The tape is then removed which takes superficial cells from the epidermis. A ribonuclease protection assay analyzes these cells to differentiate melanoma from benign lesions. Epidermal Genetic Information Retrieval [161] is a commercialized form of this technology [94]. The sensitivity and specificity are 98% and 73%, respectively [162].

3.3 Elasticity Quantification

Simple mechanical methods for quantifying the elasticity of tissue have been used for several years to objectively assess scars and evaluate cosmetic products. A static force is applied to tissue and the resulting deformation is measured. Viscoelastic effects are ignored and the tissue is assumed to be linearly elastic, allowing for Young's modulus to be determined using Hooke's law.

Examples of devices include the tonometer [175], which drops a weighted piston onto tissue and measures the resulting deformation, extensometer [176], which pulls on two loci of skin with a constant force spring and measures the tissue deformation with a strain gauge, and the cutometer [177], which applies suction to tissue and uses an optical system to measure displacement as a function of time. These devices all have poor lateral resolution (1–6 mm) since they evaluate the elastic modulus of tissue as a whole, resulting in the lack of ability to differentiate spatial variations [178].

Table 3.3: Skin Cancer Diagnostic Technologies

Technique	Mode	Product Examples	Estimated Device Cost ($)	Sensitivity (%)	Specificity (%)
Visual Inspection	Optical (Visible)	N/A	0 – 250	25 – 100	26 – 95 [103]
Total Body Photography	Optical (Visible)	FotoFinder Bodystudio, [105] Constellation [106]	2,500 – 30,000 [19]	100	41 [163]
Dermoscopy	Optical (Visible)	Dermlite [109]	300 – 1,100 [94]	79 – 100	69 – 100 [114]
Computer-aided Image Analysis	Optical (Visible)	MoleExpertMicro [164]	Unknown	74 – 100	64 – 93 [119]
Smartphone Applications	Optical (Visible)	FirstDerm, [123] 3Derm, [124] MoleScope [125]	5 – 250 [130]	7 – 100	30 – 97 [130]
Multispectral Imaging	Optical (near-IR, Visible, near-UV)	MoleMate, [128] MelaFind [131]	5,000 – 10,000 [130]	80 – 100	8 – 91 [130]
Optical Coherence Tomography	Optical (near-IR)	VivoSight [141]	70,000 – 150,000 [165]	79 – 94	85 – 96 [166]
Confocal Microscopy	Optical (near-IR)	Vivascope [145]	50,000 – 100,000 [167]	90 – 92	69 – 86 [142,143]
Raman Spectroscopy	Optical (near-IR, Visible, near-UV)	Verisante Aura [147]	15,000 – 50,000 [168]	90 – 100	54 – 95 [146]
Laser Doppler Perfusion Imaging	Optical (near-IR, near-UV)	FluxEXPLORER [169]	Unknown	42	91 [150]
Magnetic Resonance Imaging	Optical (RF)	MAGNETOM (Siemens) [170]	150,000 – 3,000,000 [170]	Unknown	Unknown
Ultrasound	Acoustic	Dermascan C [171]	10,000 – 200,000 [172]	81	76 [154]
Infrared Imaging	Thermal	N/A	Unknown	Unknown	Unknown
Bioimpedence	Electrical	Nevisense [160]	Unknown	91 – 100	24 – 80 [130]
Positron Emission Tomography	Chemical	Biograph TruePoint PET/CT (Siemens) [173]	125,000 – 600,000 [173]	13 – 100	33 – 100 [94]
mRNA Tape Stripping	Chemical	Dermtech Adhesive Skin Biopsy Collection [161]	400 [161]	98	73 [162]
Elastography	Mechanical	GE Logiq E9 [174]	10,000 – 200,000 [172]	91	76 [154]

Elastography is an advancement of these techniques that employs different imaging modalities to map out the elastic properties of tissue. The tissue stiffness maps, or elastograms, are most often constructed using acousto-optics, ultrasonics, or magnetic resonance. Elastography relies on the differences in local mechanical properties as contrast agent to form images. Several elasticity imaging methods have been demonstrated, but they all work differently. The overall principle is the same, apply a mechanical stimulus and measure the response, but the type of stimulus and measurement method varies.

The mechanical stimulus type can be divided into two basic groups: static and dynamic. Static, or quasi-static, methods slowly compress the tissue and measure the resulting strain, whereas dynamic methods apply an oscillating force and measure the speed of the shear wave as it propagates. As previously shown with Eqns. 2.3–2.5, shear wave velocity can be used to determine the shear modulus and Young's modulus.

Both methods have downsides; static methods require knowledge of boundary conditions, whereas dynamic methods are unable to measure deeper in the body due to the attenuation of shear waves.

It is interesting to note that most often static methods will evaluate on strain alone, since it is considered linearly proportional to stiffness. Strain based images typically have a higher spatial resolution, whereas elastic modulus images have a lower spatial resolution but reduced artifacts from boundary effects [179].

Traditional elastography measurement techniques that are most often found in clinical practice use ultrasound or MRI machines. However, these machines are often inaccessible, due to their size and cost, so a lot of early stage research has looked into an assortment of other imaging modalities to form elastograms.

Ultrasound elastography is the method most often found in practice and it works by measuring the contrast in reflections of ultrasonic waves based on local variations of tissue acoustic impedance. In ultrasound elastography the probe is used to compress the tissue. If the probe has a load cell or other mechanism to determine the applied force, then the absolute stiffness can be inferred, otherwise only a relative strain map can be created [154].

MRI and OCT elastography measures tissue mechanical properties by imaging the velocity of the shear wave propagation created by a mechanical vibration source [80, 180].

Some elastography variations use optical measurement techniques like optical flow [181] or digital image correlation [182] on a set of images to map the surface displacement caused by an applied force. Both optical flow and digital image correlation track the movement of features within an image, and therefore are highly dependent on the scene. For digital image correlation, tissue texture is often not sufficient so a unique pattern is applied to the surface of the region of interest, which can be inconvenient in the clinical setting.

Other variations have coupled a compliant material between the tissue and measurement device. When compressed, the compliant material will deform dependent on the stiffness of the tissue; this full-field thickness of the material can be measured using OCT [178] or other optical methods [183]. Piezoelectric sensor arrays [184] and laser speckle shift [78] has also shown promise.

Additionally, elastography is useful in surgical settings as it can provide the surgeon with haptic feedback. Surgeons often manually palpate tissue with gloves or tools to diagnose or identify different anatomical features, especially when their view is obstructed by other organs. Open surgical procedures make this easy, as the surgeon can make the incision large enough such that the entire workspace can be directly touched. Direct tactile feedback is muted during minimally invasive surgery where surgeons have to rely on force feedback through the long, compliant tools in standard laparoscopic procedures, and completely removed during robotic minimally invasive surgery.

Elastography methods are starting to be used in the research setting to inform surgeons how much force they are applying and to characterize the tissue properties. One group measures differential stiffness by automatically moving a probe tip across a tissue surface and measuring the tip deflection wit a Hall effect sensor [185]. Another group uses the known position of a surgical robot end effector with a force torque sensor to quantify stiffness [186].

3.4 Tissue Substitutes for Design Verification

While research progresses towards new skin cancer detection devices, successful adoption of these technologies requires a robust, repeatable method for validation prior to comparative medicine or clinical trials. Skin tissue mimicking phantoms are widely used to validate diagnostic devices as they are able to accurately model the mechanical, optical, and acoustic properties of skin. In addition to validating models or simulations, phantoms provide a way to optimize, calibrate, and standardize the device [187].

Most commercially available phantoms cost thousands of dollars and are not customizable, making them not always suitable for new technologies or tests with variable configurations [188]. An ideal phantom should replicate the tissue properties of interest, be cost-effective, be easy to manufacture so parameters of the design can be modified if necessary.

To adequately mimic the properties of skin tissue, it is important that phantom tissue models be composed of layers that represent the three different layers of the skin: epidermis, dermis and hypodermis. The epidermis layer can be the most difficult to model because it is so thin [189].

Several types of bio-based and synthetic materials are used to simulate tissue. Agar-based tissue phantoms at different concentrations are the most widely used and well characterized [190–193]. Conveniently, the Young's Modulus of 1, 2, and 3% agar is nearly equivalent to the hypodermis, dermis, and epidermis, respectively [80]. Similar to agar, gelatin [182,188] and pig skin [182,194] are also often used materials.

Other groups have utilized Polydimethylsiloxane (PDMS) in combination with Titanium Oxide and nanorose particles to mimic both the biochemistry and optical properties of skin with incorporated lesions [195]. Additional materials, such as collagen, lipid scattering particles, polyacrylamide gels, and epoxy resins have also been used to simulate skin tissue for optical spectroscopy and imaging [187,188].

3.5 Technology Gap

Nearly all of the available diagnostic technologies suffer from the same fundamental problems. These devices are all relatively cumbersome, expensive, and require special training to use. There needs to be a shift in the paradigm used to develop diagnostic devices.

PSFK, a market intelligence company, suggests that healthcare is trending towards empowering the patient by giving them tools for knowledge and incentivizing proactive management of their health while making the doctor more efficient through the use of data driven treatments and visual tools that augment procedures [196].

The technologies discussed in this Chapter are progressing in this direction, but still have a long ways to go.

3.5.1 Ideal Diagnostic Tool

Researchers agree that the three main barriers that must be overcome for technology adoption in dermatology are time, training, and experience [19]. In doing so, the device must remain accurate and reliable, in order to yield objective and quantitative results.

One researcher suggests the ideal instrument for melanoma detection must have the following key requirements. The measurement should be relative comparing the properties of the lesion and healthy tissue of the same subject rather than comparing the responses of different individuals. The device should not require perfect contact with the skin or use of immersion fluid. Finally, the device must be non-invasive, reliable, small, low cost, sensitive, robust, and have strong support for manufacturing, customer support, and repair [197].

Another group claims the ideal tool should be easily available to any doctor or patient, fully automated with no expertise, have a high diagnostic accuracy, and be affordable for use [198]. This perfect tool would have the following design parameters: a large field of view (1.5–2 cm), cellular resolution (1 µm lateral resolution), good

penetrance depth (4 mm), and quick/easy to navigate. However, this group then concluded that this is not possible in the near future.

It is hypothesized that the ideal form factor for a skin cancer diagnostic device should be structured as hardware and software for a mobile smartphone. This is optimal because it provides a small, portable solution with extremely powerful computational abilities — capable of performing complex operations in real-time with a built-in connection to the cloud where networked information can be taken advantage of. Additionally, smartphones have become common tools that nearly every doctor uses. Surveys show that 90% of physicians use smartphones or tablets in their day-to-day professional activities [199].

Several biomedical diagnostic and monitoring devices outside the field of dermatology are currently being developed based around a smartphone. These include tools for heart rate and oxygen saturation [200], blood pressure monitoring [201], electrocardiogram readings [202], and eye exams [203].

The ideal device should be easy enough for a patient to use, while being accurate and reliable enough for a general practitioner to use in making a initial diagnosis, and advanced enough to aid a dermatologist in mapping out a cancerous lesion for precision excision as well as diagnosing highly-specialized instances.

Chapter 4

Design Process

The primary goal of this research is to automatically diagnose skin cancer through tissue characterization. An auxiliary mission, that is directly related to diagnosis, is to map out the cancerous lesion so that it can be precisely excised. Accomplishing these two tasks will increase accuracy over traditional methods by removing complexity and subjectivity, thereby improving survival rates, reducing the number of unnecessary biopsies, and reducing overall costs to the healthcare system.

The development of a device to meet this goal utilized a coarse-to-fine design process that is fully described in [204]. This began by precisely identifying the problem and reviewing the prior art. Design requirements were identified by formulating broad constraints that framed the solution along with specific functional requirements necessary to accomplish the research goals. Creative brainstorming sessions were used to generate high level strategies, which were then filtered down to potential conceptual solutions. The concepts were evaluated with respect to the functional requirements and constraints to determine the optimal solution. This systematic process efficiently ensured that the design space was fully explored and an optimized solution was selected.

Table 4.1: Design Constraints

Constraint	Action	Description
Cost	Minimize	Cost effective for purchasers, including hospitals, purchasing organizations, insurance companies, consumers
Size	Minimize	Portable and able to access hard-to-reach areas of the body
Ease of use	Maximize	No specialized training required and no long setup time
Repeatability	Maximize	Device should produce the same results when measuring under identical conditions
Objective	Maximize	Device relies on observable and measurable data only
Non-invasive	Maximize	No bodily penetration, as by incision or injection
Safety	Maximize	Device failure cannot cause bodily harm
Biocompatibiliity	Maximize	Device meets the guidelines for FDA biocompatibility

4.1 Design Constraints

The constraints shown in Table 4.1 were used to guide the design, with the most important being cost, size, and ease of use since these were identified as the primary barriers to the adoption of new technology by the dermatologic community, as determined from reviewing the prior art.

The technology should be inexpensive so that it is widely accessible to anyone. As Section 3.2 illustrated, several highly effective diagnostic technologies exist, however, at this point they are far too expensive to see use outside of research. The objective is to optimize the balance between cost and performance to maximize impact. An ideal device should be less than $100 if tailored to patients and $500 if geared towards physicians.

The second critical constraint is size. The device should be handheld and wireless, making it ultra-portable so that it is versatile enough to be used in a clinical exam room or out in the field. The other primary constraint is ease-of-use, with a focus on automation to reduce user error. It is critical that the device is intuitive, such that no special training is required and even a layperson can use it. In order to achieve high throughput for screening and surveillance, the data collection and analysis process should be quick and provide a clear, visual description of all key results.

4.2 Functional Requirements

The specific functional requirements guided the design within the constraints and served as evaluation metrics.

The following functional requirements must be met:
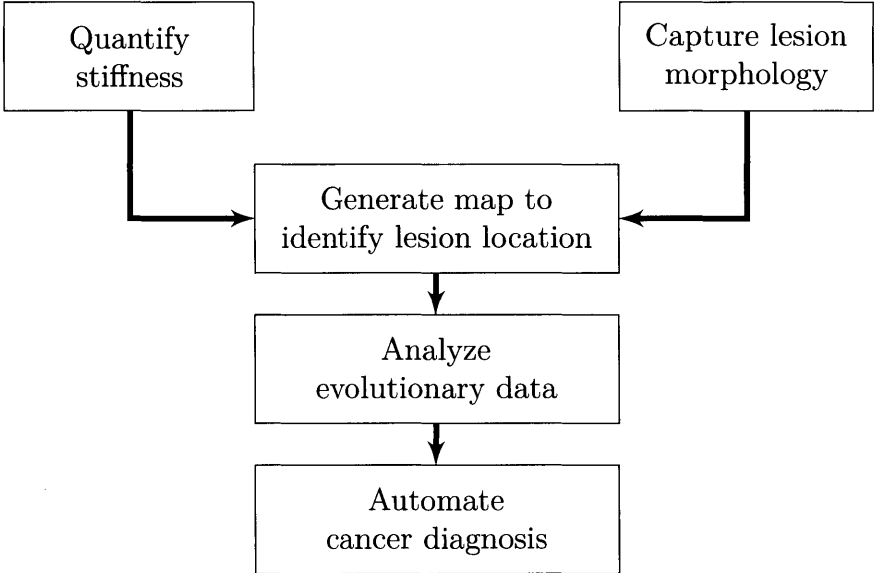
Figure 4-1: Structured list of the functional requirements

The primary functional requirement is the ability to quantify the stiffness of a potentially cancerous lesion and the healthy tissue surrounding it, characterizing the tissue similar to other elastography methods, emulating the manual palpation that clinicians use for diagnosis. The human finger is limited in fidelity and cannot detect

81

very small changes or anomalies of the skin. Automating this process produces greater sensitivity and consistency, turning a traditional subjective test into an objective test.

The device must also capture information about the lesion morphology. The size, shape, color, and texture of a lesion can be defined using the ABCD checklist. The combination of the stiffness with the morphology information provides both intrinsic and extrinsic information about the lesion and thus, can be used to map out the lesion boundaries.

It is extremely difficult to use absolute threshold values as a means to detect cancer, so the key is to continually monitor the skin and provide alerts when any changes occur. Monitoring lesions over time exploits the fact that changing lesions are highly correlated with cancer.

Finally, all of this information must be processed automatically. The device can present meaningful data to the user to assist with diagnosis, but to meet the primary constraint of ease-of-use, the technology must be able to make its own inferences.

4.3   Design Filtering

4.3.1   Strategies

Several high level strategies were generated to meet the primary functional requirement of quantifying stiffness. A straightforward solution would be to apply a force and measure the resulting displacement, or using reciprocity, measure the amount of force to deform tissue a specified amount. A more indirect solution would be to quantify the amount of collagen in tissue, since an over-expression of collagen results in an increase in stiffness.

It is very difficult to apply a known displacement to tissue due to the reference ground, in this case the human body, not being stable; therefore, measuring force as a function of displacement was ruled out. Collagen can be quantified using spectroscopic methods or with a biopsy, but these concepts also violate the design constraints. Spectroscopic methods are typically quite expensive and large, while a biopsy is invasive

and time consuming. Applying a mechanical stimulus and measuring the resulting deformation is the most fitting path forward.

4.3.2 Concepts

Next, using the coarse-to-fine design methodology, concepts were developed to accomplish the strategy of applying a specified force and measuring displacement. There are many different ways to apply a force — these can be broken down into several categories, including type, frequency, direction, and location.

A force can be applied through either contact or non-contact means. Non-contact forces include pneumatic or acoustic, gravitational, electrical, and magnetic. Examples of contact forces include indentation, tension, torsion, impact, vibration and wave propagation. All of these force types can be applied directly to the region of interest or remotely. Because tissue is a continuous elastic body, a remote force that is within three to five characteristic distances away from the region of interest will still cause a strain.

The possible force directions are axial or normal, radial, and tangential. The frequency of the force can be very low, such that the force is considered static or constant, or it can be high, as in an oscillating dynamic force. A dynamic force would require the amplitude of the deformation to be measured so that the dissipation of energy through damping could be determined.

Possible displacement measurement methods can also be classified as contact or non-contact methods. A high level taxonomy of the various spatial measurement techniques is shown in Fig. 4-2. A classic contact measurement method is an encoder — where the position of a mechanism is encoded using optical, magnetic, inductive, capacitive, resistive or eddy current technologies.

Non-contact methods are typically based on light. Ultrasound and Infrared rangefinders, time-of-flight cameras, interferometers, and LIDAR are all light-based methods that are used to measure the shape of a surface. Other non-contact 3D reconstruction techniques based on triangulation exist and are capable of providing high-resolution measurements. These methods are classified as passive or active, depending on the

Spatial
Measurement

Contact   Non-contact

Non-destructive   Destructive   Reflective   Transmissive
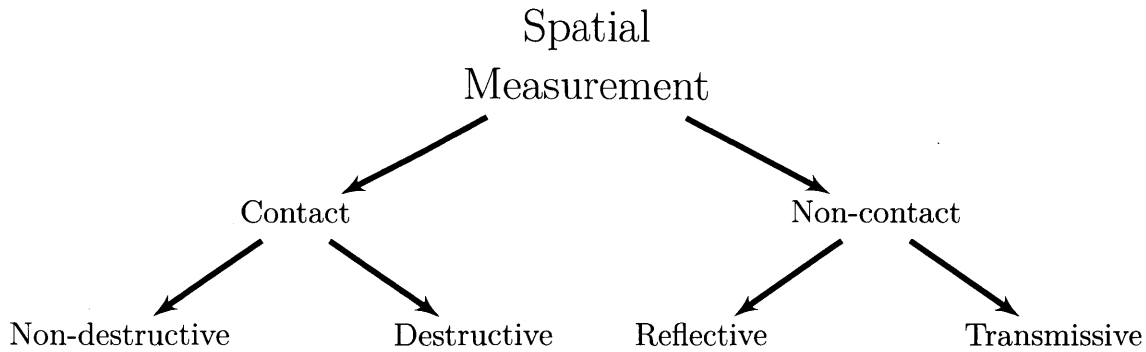
Figure 4-2: Classification of spatial measurement methods

amount of controlled illumination required. Passive scanners rely solely on ambient light whereas active methods will project controlled light onto the scene.

The measurement techniques can be further categorized into instantaneous, full-field and point-wise scanning methods. An instantaneous, full-field approach is able to measure the entire region of interest at once, providing the possibility to capture dynamic scenes, whereas point-wise methods measure the scene serially, or one point at a time. Several point-wise techniques can be combined in a physical array to create instantaneous, full-field measurements. These physical arrays commonly rely on capacitive, piezo, or magnetostrictive properties to measure displacement or pressure. The resolution of these arrays has been increasing [205], and they are now able to bend to contour to any surface shape [206].

Two specific contact measurement concepts that were appealing were the vibrating stylus and rebound tonometer. A stylus could be preloaded into the skin and then vibrated at a specified frequency as it scanned across the tissue. A cancerous lesion could be identified by monitoring the change in amplitude as the stylus touched a stiffer region. A rebound tonometer is often used by ophthalmologists to determine intraocular pressure. This mechanism would bounce a mass off the lesion and measure the distance and speed that it rebounds. Both of these concepts were rejected because they are point-wise scanning methods that would take too long to operate.

When evaluating these concepts against the functional requirements and constraints, as well as weighing the pros and cons of each, the non-contact reconstruction methods using triangulation rose to the top. Structured light and stereo vision are

both fast, full-field measurement techniques that are able to provide non-contact, *in vivo* measurements.

Stereoscopic imaging is a widely used passive triangulation technique for 3D imaging systems. Stereoscopy, similar to human depth perception, uses two or more cameras to capture different views of an object, and then uses a feature matching, or correspondence, algorithm to match up content from each of the views. The amount of offset, or disparity, of features is used to determine their depth.

Feature-matching provides a sparse reconstruction, while stereo matching creates a dense reconstruction. Dense reconstruction provides depth information for every pixel of the camera, whereas sparse reconstruction only provides depth information for a sample of pixels. Robust feature matching can be difficult and remains a challenging problem in stereoscopy, as flat or repeated textures prevent accurate matching. This means that tissue, due to its unpredictable texture and generally low contrast, is difficult for passive stereoscopic methods to measure. Stereoscopy is also challenging to implement on a small, portable platform like a smartphone, due to the processing demands and difficulty in connecting multiple cameras to the phone.

Active optical scanners overcome the correspondence problem by controlling the illumination of the scene. Structured lighting is a common active scanning approach that projects a pattern on the scene. Classic structured light methods utilize a video projector that scans a visible, UV, or IR wavelength structured pattern through the scene.

Various pattern encodings have been used in structured light methods, including points, lines, coded binary patterns, color coded stripes, random texture, and more [207,208]. These patterns can be encoded within one frame (spatially) or across multiple frames (temporally). Spatial encoding uses a single static pattern that allows for dynamic scenes to be captured, but only provides sparse reconstruction. Temporal encoding has the advantage of redundancy and the ability to acquire dense reconstructions; however, these temporal methods are slower and require a projector, using DLP, LCD, or CRT technology, which is bulky and costly.

The most popular commercially available structured light system is the Microsoft Kinect, which is used in gaming to map a person's pose and movements [209]. Structured light has also been demonstrated as a robust method to produce 3D images of skin topography [210].

Further analysis reveals that the setup should be simplified with a fixed-pattern projector. A gobo is a mechanism that is often used as a fixed-pattern projector for theatrical lighting. A gobo, or go-between, is a physical stencil mask that is placed in front of a light source and focused with a lens. A gobo provides the benefits of structured light, without the bulkiness and cost of projectors.

Fixed-pattern projectors are only able to provide sparse reconstruction, but Nyquist sampling theory can be used to justify this decision. Nyquist sampling theory states that a signal can be accurately described as long as the sampling frequency is greater than twice the frequency of the signal. Skin has low spatial frequency since it is fairly continuous without sharp changes in profile so sparse reconstruction should sufficiently describe the scene.

After evaluating the concepts against the functional requirements, constraints, and prior art, structured light and a negative pressure suction were selected as the displacement measurement and force application methods, respectively. Structured light is ideal because of its non-invasiveness, low cost, low power, accuracy, robustness, and ability to still take standard clinical images of the lesion for morphology analysis, without additional hardware. A negative pressure vacuum works best with structured light because it doesn't obstruct the view of the lesion and suction acts as a self-help mechanism. Once the device is preloaded against the skin, the suction will ensure that it stays held in place. Both concepts can be easily implemented on a portable platform like a smartphone, with only minor hardware additions.

Chapter 5

LesionAir

The previous chapter established the principle design goals for a portable medical device to diagnose cancer. This chapter presents a functional prototype, LesionAir, that embodies these requirements. LesionAir (Fig. 5-1) is built around the two components selected to apply force and measure deflection of tissue: a small vacuum pump and pressure sensor to create and maintain controllable negative pressure; and a simple, low-cost structured light system to create a deflection map of tissue. This initial prototype is tethered to a computer using USB, which controls these systems, collects data, and formulates patient results. These components are housed in a plastic, light-tight, air-tight housing that provides a self-contained, pressurized environment. An overview of the design is shown in Fig. 5-2.

5.1 Vision System

LesionAir's vision system comprises a ring light, projector, and camera. The ring light evenly illuminates the scene to provide adequate lighting for the camera to capture standard visible-light images. The projector is responsible for shining a fixed structured light pattern onto the tissue that the camera needs to build depth maps of the scene. The camera captures both standard visible-light clinical images, as well as structured light images used to create depth maps (and, consequently, deflection maps).
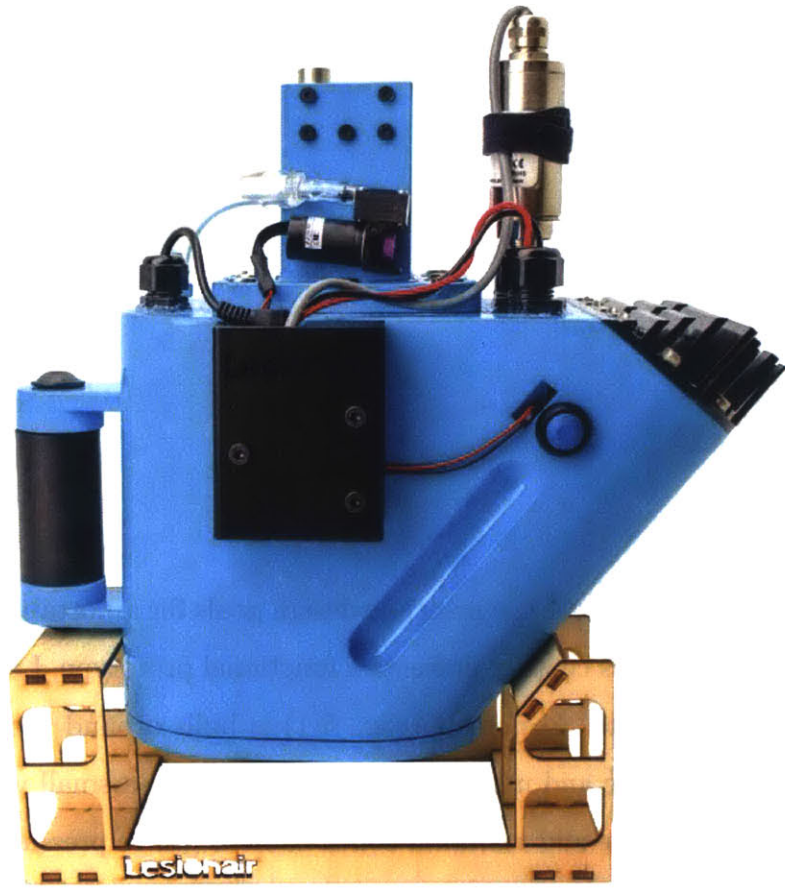
Figure 5-1: The final LesionAir prototype
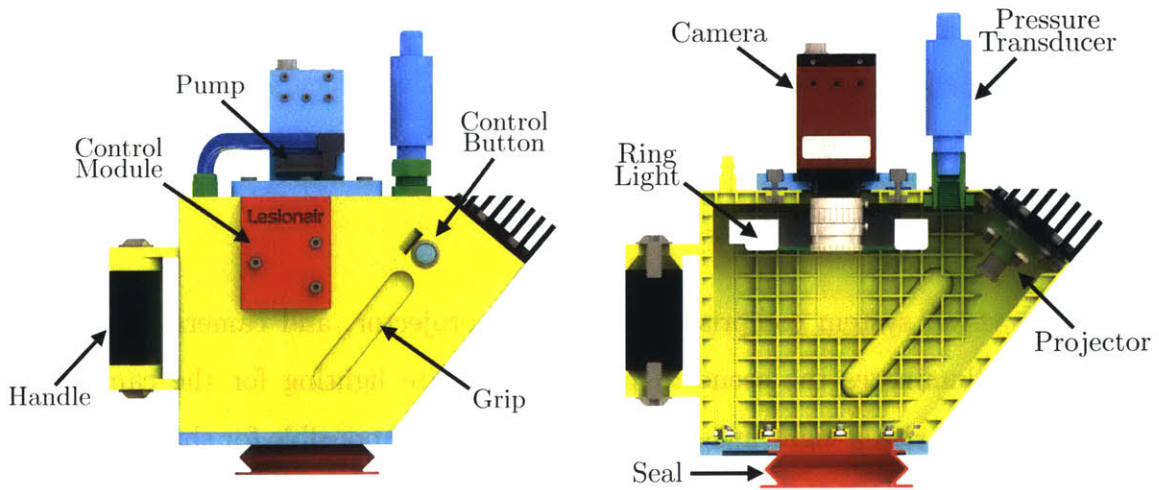
Figure 5-2: Side view rendering of LesionAir with labeled components
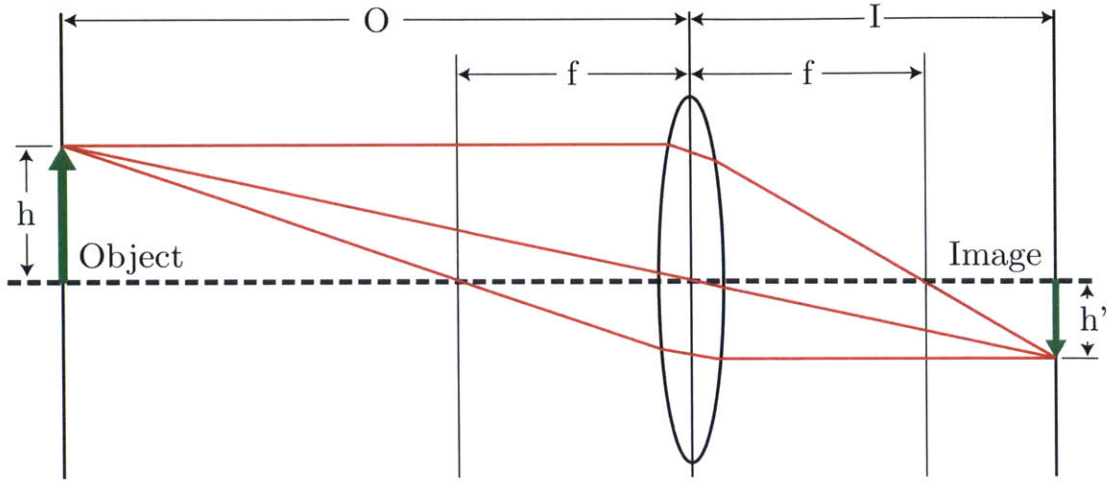
Figure 5-3: Optical geometry of a thin lens

5.1.1 Basic Optics Principles

An understanding of basic optics principles is required to specify a lens for a camera or projector. A lens focuses light based on its shape and material properties. Focal length, f, is the intrinsic parameter used to describe how a lens modulates light. Lenses also cause effects like distortion, chromatic aberration, and vignetting, however, these effects are complicated to model and don't significantly affect image quality when using professional optics, so they can be safely ignored for simplicity.

5.1.1.1 Lens Equation

The lens equation is a geometric relationship describing the distance between corresponding points in front of, and behind, the optical lens:

$$\frac{1}{o} + \frac{1}{i} = \frac{1}{f} \tag{5.1}$$

Image magnification can also be determined using Eqn. 5.2. A negative sign is used to designate that the image is always flipped on the imaging sensor.

$$M = \frac{-i}{o} = \frac{h'}{h} \tag{5.2}$$

89

Even though most practical lenses are actually comprised of several lenses — called *elements* — the lens equation is a simplification of a single thin lens that is used to approximate the focal plane of an image. This relationship is extremely useful in lens design.

5.1.1.2 Imaging Device

Digital cameras capture images using either a CCD (charge-coupled device) or a CMOS (complimentary metal-oxide-semiconductor) image sensor. Common sensor sizes are 1/4", 1/3", 1/2", 2/3" and 1". When comparing sensors with the same resolution, larger sensors are capable of producing images with a better dynamic range, less noise and improved low light performance, due to the increased pixel size. Larger sensors also have more room for increased resolution.

5.1.1.3 Field of View

Field of view (FOV) is the area of a scene that is visible to the camera. Field of view is usually expressed using angle of view (AOV). Angle of view describes the angular range of a scene that can be imaged by a camera.

Angle of view can be determined by the imager size and the focal length of the lens:

$$AOV = 2\tan^{-1}\left(\frac{h}{2f}\right) \qquad (5.3)$$

The relationship of field of view to angle of view is:

$$FOV = 2i \times \tan\left(\frac{AOV}{2}\right) \qquad (5.4)$$

Field of view calculations can be used to select a lens that maximizes the number of pixels on the region of interest.

5.1.1.4 Depth of Field

Depth of field describes the range between the nearest and furthest objects in a scene that appear in focus at any given time. When a point is out of focus, light rays

emanating from it will no longer converge to a single point on the image sensor and it will begin to look blurry. Lens focal length, focus distance, and aperture control depth of field. In optics, an aperture is a mechanically-controlled hole that controls the amount of light that passes through.

5.1.2 Optomechanical Design

These basic optics principles helped select a camera, lens, and projector. In this case, there are a lot of unknowns about the surface being measured. The magnitude of difference in stiffness between healthy and cancerous can vary significantly. The required spatial resolution is unknown. Even the skin tone of the patient being measured will vary. Approximations were used to help guide the selection process, but ultimately, trial-and-error was used to make the final decision.

5.1.2.1 Camera

The prototype device captures visible and structured light images using Allied Vision's Manta G-145B camera. This camera is ideal for prototyping machine vision applications because of its plug and play MATLAB support. This monochrome 1.4 MP camera can capture images at 30 fps. Other relevant parameters for the Manta G-145 can be found in Table 5.1.

A 16 mm f/1.4 fixed focal lens (Fujinon, HF16HA-1B) provides the necessary optics to focus and maximize pixels on the region of interest. The lens has a locking iris and focus so that the settings do not change and the calibration stays valid through vibration or any other bumps that may occur during normal use.

This lens is suitable for this application because it has a narrow field of view (17° horizontal, 12° vertical), which maximizes the number of camera pixels on the region of interest, ensuring that as few pixels as possible are wasted. Given the camera image sensor size (2/3"), the focal length of the lens (16 mm), and the approximate distance to the object (13 cm), the field of view is 6.4 × 5.3 cm.

Table 5.1: Relevant parameters for Allied Vision's Manta G-145B-30fps camera

Parameter	Specification
Interface	GigE Vision
Sensor type	Sony ICX285 CCD
Resolution	1388 × 1038
Sensor size	2/3"
Cell size	6.45 µm × 6.45 µm
Frame rate	30.1 fps
ADC	12 Bit

For visible light images, a generic 48 LED macro ring light evenly illuminates the scene. The ring light, along with LesionAir's light-tight enclosure, will ensure that all of the images taken will have standardized lighting and no shadows.

5.1.2.2 Projector

As presented at the end of Ch.4, a fixed-pattern projector creates the structured light pattern. A fixed-pattern projector can be created many ways, but the most cost-effective is a gobo setup. A gobo projector requires only a light source, a mask (called a *gobo*), and a lens. Light rays emitted from the source are scattered in all directions. Just placing a gobo over the light source will not produce a crisp pattern projected out into space. The added lens focuses the light that passes through the pin holes in the gobo to a point out in space, as determined by the lens equation of this projection lens.

The designed projector includes a high-brightness LED, gobo plate with dot pattern, and focusing optics. A Bridgelux Vero 10 ultra-bright LED is the light source. This LED emits a cool white (5000K) color, with a nominal forward voltage of 26.7 V at a rated operating current of 350 mA. At full power, the LED will output 1120 lumens. The LED must be mounted to a heat sink to dissipate thermal energy and prevent the LED from overheating.
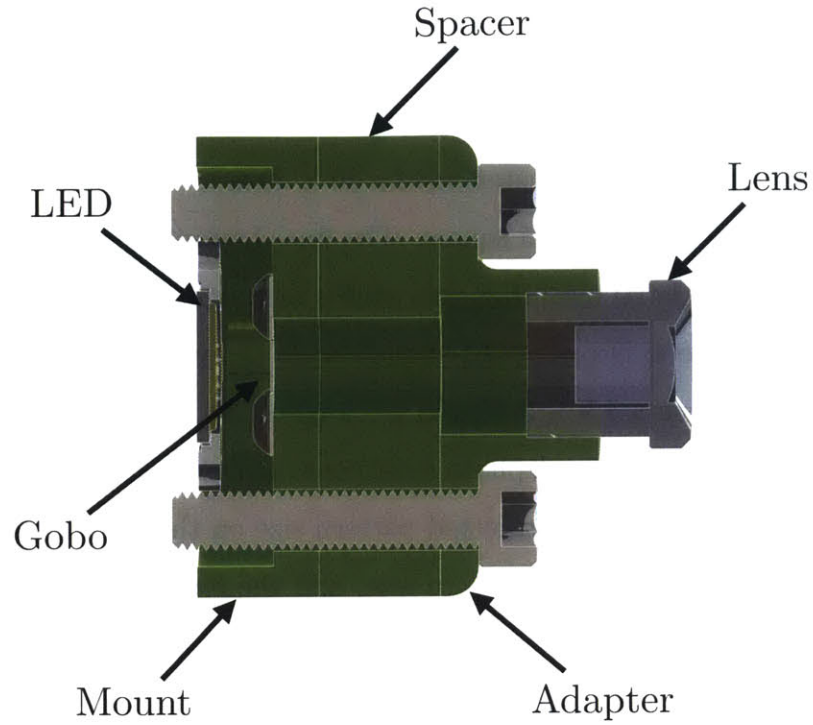
Figure 5-4: Schematic of the projector design

This LED provides more than enough light for the given application, but was selected because of its large output range that can be varied to experimentally determine the optimum value. After testing, an output of 110 lumens was chosen, requiring only 23.8 V at 50 mA.
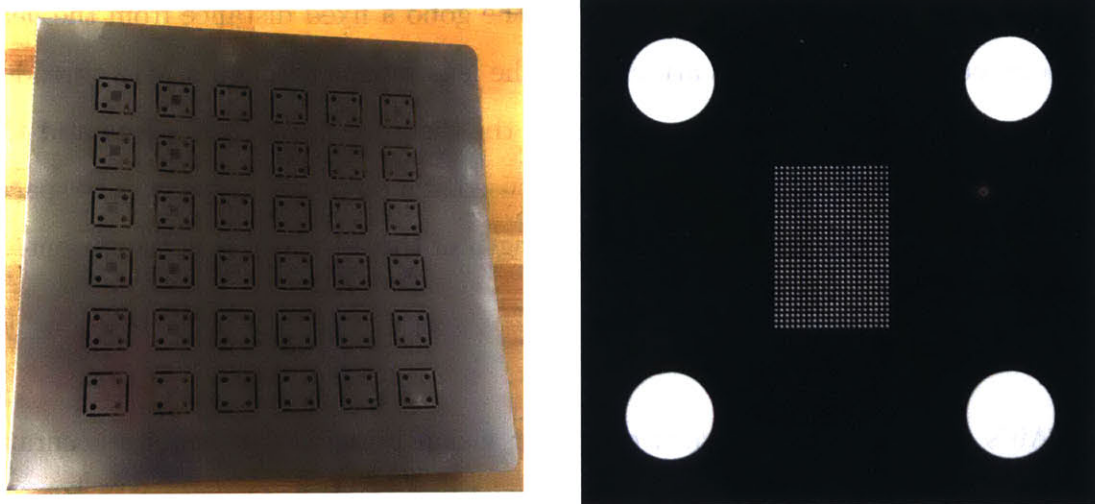
Figure 5-5: Gobo stencil pattern

The gobo was fabricated from a sheet of 0.1 mm thick 304 stainless steel using a precision laser cutter. All of the dots were approximately 40 micron in diameter. As shown in Fig. 5-5, several different patterns were created and tested. Initial benchtop validation of the structured light system used a 20 × 20 array with 0.1125 mm spacing between the dots to form a 4.5 mm square. The final LesionAir design increased the dot density for better spatial resolution and used a rectangular array to better fill the 6 cm aperture. This gobo is comprised of a 40 × 28 array with 0.1125 mm spacing between the dots to form a 4.5 × 3.15 mm rectangle.

A 16mm focal length, f/2.5 telephoto mini board camera lens focuses the pattern onto the region of interest. The projected pattern size on the skin can be estimated using the lens equation, the gobo pattern size, and the focal length of the lens. At 13.5 cm away, the 4.5 mm square pattern will be magnified by 7.5x, resulting in a 3.4 cm projection. However, this estimation does not take into account for the keystone effect that occurs since the projector is not normal to the surface. Because the light strikes the measured surface at a 45° angle, the pattern on a flat surface will not appear square, but instead like a isosceles trapezoid, as shown in Fig. 5-6, with the small side closest to the projector. This occurs because the light rays do not travel the same distance, and therefore, are not magnified the same amount.

The LED, gobo, and lens are rigidly held together by the base, spacer, and lens mount adapters. These parts were CNC (computer numerical control) machined from 6061-T6 aluminum. The base adapter holds the gobo a fixed distance from the heat sink mounted LED. The lens is attached to the lens mount through a M12 threaded interface so that it can translate, modifying the distance between the lens and the gobo so the structured light pattern can be focused at a point out in space. The spacer adapter was added for instances when the length of thread travel is not sufficient.

5.1.3   Structured Light

LesionAir's design uses established computer vision principles to acquire accurate, high resolution measurements of the topology of human skin. Computer vision is a powerful research area used widely across engineering and biology fields that allows

94
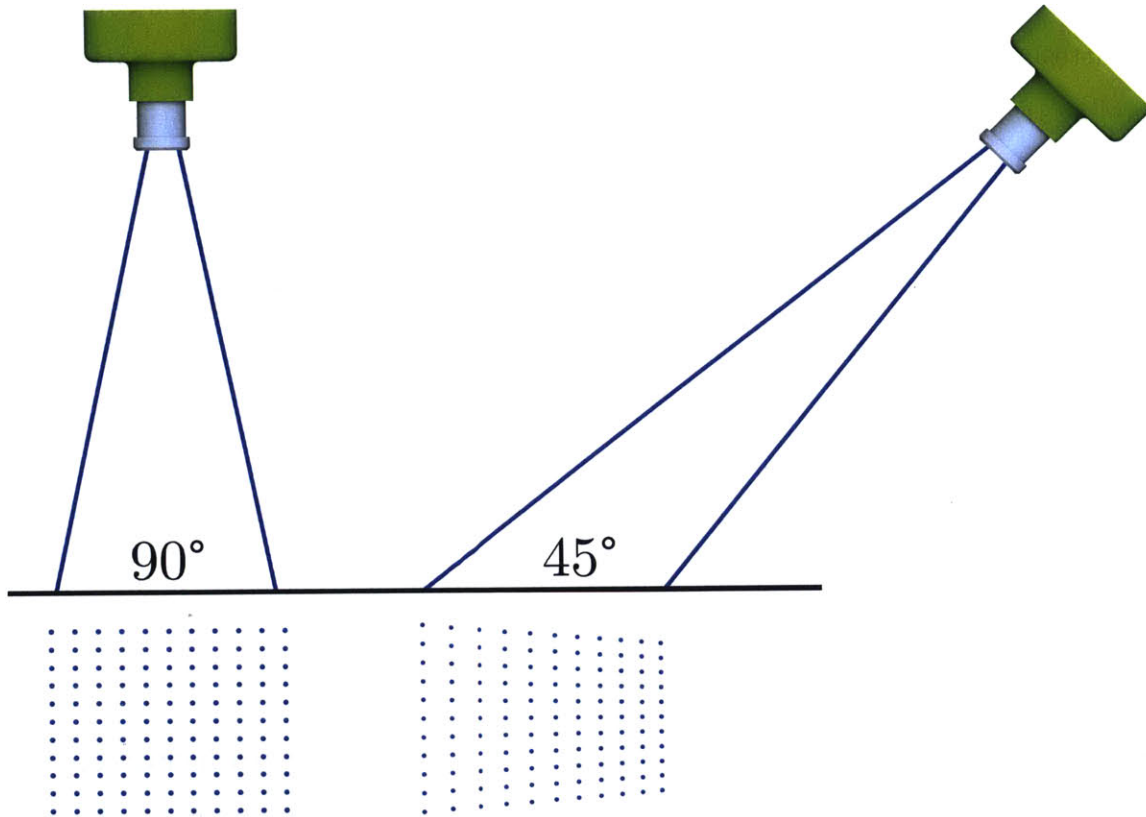
Figure 5-6: Schematic demonstrating the change in shape of the projected pattern as the angle changes

a machine to mimic human visual perception. It transforms a real world scene into digital data that can be analyzed to inform a specific action.

5.1.3.1 Multi-View Geometry

Multiple-view geometry describes how a 3D scene is projected onto a 2D plane like an image sensor. Basic multi-view geometry principles will now be discussed to explain how structured light is used to reconstruct a 3D scene, but first, some preliminary topics will be covered.

Homogeneous Coordinates   Homogeneous coordinates are useful for representing 2D and 3D points in projective geometry applications due to their ability to represent points, even those at infinity, as finite coordinates. Additionally, homogeneous coor-

dinates represent points, lines, and planes using the same notation. When compared to Cartesian coordinates, homogeneous coordinates also simplify transformations by enabling translations inside matrix transforms. All projective transformations can be represented as a linear operation with a transformation matrix.

A point in 2D space can be represented by a pair of coordinates, $(x, y) \in \mathbb{R}^2$. A line defined by $ax + by + c = 0$ can be made to pass through this point by choosing an appropriate a, b, and c. In this case, the triplet (a, b, c) is the homogenous representation of (x, y). The selection of a, b, and c is not unique; in fact, any ka, kb, and kc will work provided $k \neq 0$, thus a single point can be represented by infinitely many homogenous coordinates. Points at infinity are defined when $k = 0$. Typically, ka, kb, and kc are represented as $[x, y, w]^\mathsf{T}$ for a 2D point. For a 3D point, this is extended to $[x, y, z, w]^\mathsf{T}$.

Projective Transforms Any point defined using homogenous coordinates can easily be transformed using transformation matrices. These transformations can include translation, rotation, scaling. All transforms on 2D homogenous coordinates are represented by a 3 × 3 matrix.

A translation transform, shown in Eqn. 5.5, moves a point in the x-direction by a value of t_x and in the y-direction by a value of t_y.

$$x' = \begin{bmatrix} 1 & 0 & t_x \\ 0 & 1 & t_y \\ 0 & 0 & 1 \end{bmatrix} x \tag{5.5}$$

A rotation transform, as seen in Eqn. 5.6, rotates a point by an angle of θ.

$$x' = \begin{bmatrix} \cos(\theta) & -\sin(\theta) & 0 \\ \sin(\theta) & \cos(\theta) & 0 \\ 0 & 0 & 1 \end{bmatrix} x \tag{5.6}$$

A scaling transform, shown in Eqn. 5.7, scales a point in the x-direction by a value of s_x and in the y-direction by a value of s_y.

$$x' = \begin{bmatrix} s_x & 0 & 0 \\ 0 & s_y & 0 \\ 0 & 0 & 1 \end{bmatrix} x \tag{5.7}$$

Translation, rotation, and scaling transforms can be combined. All three are known as similarity transformations because angles are preserved through the transformation.

An affine transform, as seen in Eqn. 5.8, preserves parallel lines. While this transform resembles a combined rotation and translation transform, it differs as it is not constrained by θ.

$$x' = \begin{bmatrix} a_{00} & a_{01} & a_{02} \\ a_{10} & a_{11} & a_{12} \\ 0 & 0 & 1 \end{bmatrix} x \tag{5.8}$$

The projective transform is the most versatile due to its lack of constraints. This type of transformation, shown in Eqn. 5.9, preserves straight lines but allows everything else to be modified.

$$x' = \begin{bmatrix} h_{00} & h_{01} & h_{02} \\ h_{10} & h_{11} & h_{12} \\ h_{20} & h_{21} & h_{22} \end{bmatrix} x \tag{5.9}$$

2D transforms for homogeneous coordinates can be extended to the 3D case. All transforms on 3D homogenous coordinates are represented by a 4 × 4 matrix to account for the additional dimension.

Pinhole Camera Model   To simplify the calculations required for computer vision, a real-world camera with its complex and irregular lens setup, is simplified to what is known as a pin-hole camera model. This model, as seen in Fig. 5-7, assumes that the camera views the real world through an infinitely small pinhole rather than a lens. Every point in space is transferred to the image plane via a single ray of light,
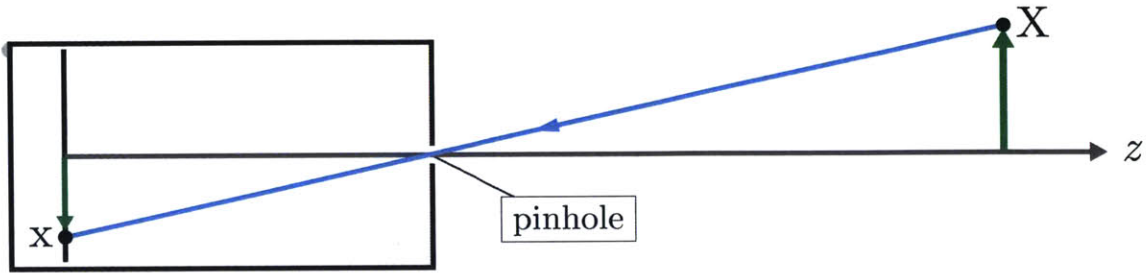
Figure 5-7: Pinhole camera model

such that everything is in focus and there are no optical distortion effects. Through this model, 3D points in space are mapped onto the image plane as 2D points. This mapping is expressed as:

$$\tilde{x} = \boldsymbol{P}\widetilde{X} \qquad (5.10)$$

where $\widetilde{X}$ is a 3D world point, $\tilde{x}$ is the point's 2D projection on an image plane, and $\boldsymbol{P}$ is a 3×4 camera projection matrix.
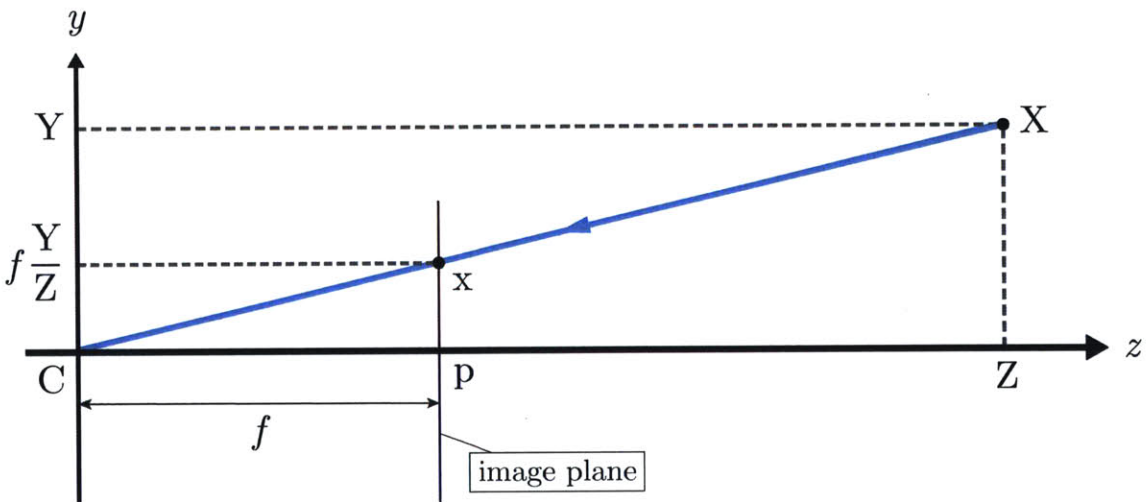
Figure 5-8: Central projection pinhole camera model

Additional simplification of this model results in the central projection pinhole model (Fig. 5-8). In the case of central projection, the pinhole or optical center, $\boldsymbol{C}$,

is located at the origin of the coordinate system and the optical axis is the z-axis. A virtual image plane is placed at $Z = f$, where f is the focal length of the camera. The principle point, p, is where the optical axis intersects the image plane. In an actual camera, the image plane is at $Z = -f$ and the image is inverted.

Through the use of similar triangles, the following relationship is derived:

$$\begin{bmatrix} f & & 0 \\ & f & 0 \\ & 1 & 0 \end{bmatrix} \begin{bmatrix} X \\ Y \\ Z \\ 1 \end{bmatrix} = \begin{bmatrix} fX \\ fY \\ Z \end{bmatrix} \sim \begin{bmatrix} f\frac{X}{Z} \\ f\frac{Y}{Z} \\ 1 \end{bmatrix} \tag{5.11}$$

Cameras are pixel-based and therefore, the origin is typically the top left of the image and not the center. To account for this, a principle offset is added to the projection matrix:

$$\begin{bmatrix} fX + Zp_x \\ fY + Zp_y \\ Z \end{bmatrix} = \begin{bmatrix} f & p_x & 0 \\ & f & p_y & 0 \\ & & 1 & 0 \end{bmatrix} \begin{bmatrix} X \\ Y \\ Z \\ 1 \end{bmatrix} \tag{5.12}$$

Thus, the projection matrix takes the following form:

$$\boldsymbol{P} = \boldsymbol{K}[\boldsymbol{I}|\boldsymbol{0}] \tag{5.13}$$

where K is the camera calibration matrix:

$$\boldsymbol{K} = \begin{bmatrix} f & & p_x \\ & f & p_y \\ & & 1 \end{bmatrix} \tag{5.14}$$

Eqn. 5.13 assumes that the camera is at the origin of the world coordinate system, however, this is not always the case, especially when multiple cameras are involved. An arbitrarily placed camera can be related to the world coordinate system using a rotation matrix, R, and translation vector, t.

$$P = K[R|t] \qquad (5.15)$$

Thus, using a pinhole camera model, 3D real world coordinates are mapped to 2D coordinates through the following general relationship:

$$\tilde{x} = K[R|t]\widetilde{X} \qquad (5.16)$$

5.1.3.2 Calibration

The perspective projection matrix, P, is comprised of the camera calibration matrix, K, rotation matrix, R, and translation vector, t. The camera calibration matrix is considered an intrinsic parameter, as it is based on internal parameters of the camera (focal length, pixel size, principle offset, etc.). The rotation matrix and translation vectors are extrinsic parameters, describing the relationship of the camera coordinate frame to the real world coordinate frame through three rotational and three translational degrees of freedom.

The intrinsic parameters could be set based on the given manufacturer specifications, however, this would not take into account the tolerances and defects. For more accurate results, it is better to compute the parameters by calibrating the actual camera with test images. The camera calibration matrix can be determined using a direct linear transform matrix solving algorithm on a series of images of an object with a known geometry, such as a checker pattern on a flat board.

Several calibration software toolboxes exist, but one of the most widely used is Bouguet's Camera Calibration Toolbox for MATLAB [211], based on a method introduced by Zhang [212]. This calibration toolbox also calculates the extrinsic parameters.

To determine the projection matrix of LesionAir's camera, a series of images of the calibration pattern were taken and input into the Camera Calibration Toolbox.

The intrinsic camera calibration for LesionAir, as determined by the Camera Calibration toolbox, is:

$$K_{cam} = \begin{bmatrix} 2681.56 & 0 & 561.47 \\ 0 & 2703.34 & 470.73 \\ 0 & 0 & 1 \end{bmatrix} \tag{5.17}$$

The camera's coordinate system origin is placed so that it coincides with the world coordinate system origin. This means the extrinsic rotation matrix is the identity matrix:

$$R_{cam} = \begin{bmatrix} 1 & 0 & 0 \\ 0 & 1 & 0 \\ 0 & 0 & 1 \end{bmatrix} \tag{5.18}$$

and the extrinsic translation vector is equal to zero:

$$t_{cam} = \begin{bmatrix} 0 \\ 0 \\ 0 \end{bmatrix} \tag{5.19}$$

For stereoscopy, multiple cameras can be calibrated using this toolbox, however, structured light replaces one of the cameras with a projector, requiring a slightly different method for calibration. A projector can be thought of as an inverted camera. Instead of capturing 3D points on a 2D image plane, a projector projects a 2D image out into 3D space. Thus, a projector still has intrinsic and extrinsic parameters.

Calibrating a projector is completed by projecting a pattern onto a plane with a known position and orientation. The plane can be a flat board with fiducials. A calibrated camera can image the board and use the fiducials to determine the board's position and orientation. The structured light pattern can be imaged simultaneously and then used to calibrate the projector. The ProCamCalib toolbox by Falcao [213] is an extension to Bouguet's toolbox that was used to determine the projector calibration matrix.

The intrinsic projector calibration for LesionAir, as determined by the ProCam-Calib toolbox, is:

$$K_{proj} = \begin{bmatrix} 141.13 & 0 & 29.74 \\ 0 & 136.84 & 19.92 \\ 0 & 0 & 1 \end{bmatrix} \tag{5.20}$$

The position of the projector with respect to the camera is given by the rotation matrix:

$$R_{proj} = \begin{bmatrix} 0.832 & 0.0127 & 0.555 \\ -0.0202 & 0.999 & 0.00739 \\ -0.555 & -0.0174 & 0.832 \end{bmatrix} \tag{5.21}$$

and the translation matrix:

$$t_{proj} = \begin{bmatrix} -94.26 \\ -2.38 \\ 13.62 \end{bmatrix} \tag{5.22}$$

Figure 5-9 illustrates a 3D model of the scene that was derived by the Camera Calibration toolbox and the ProCamCalib toolbox.

Interpreting calibration results, it can be seen that the camera and projector's lens focal length deviates from the manufacturer's specification. The camera has a focal length of approximately 2692.5 pixels (as determined by averaging the f_x and f_y focal lengths together). Converting this from pixels to millimeters results in a 17.4 mm focal length, slightly larger than the 16 mm specification. The projector has a focal length of approximately 139.0 pixels. Converting this from pixels to millimeters results in a 15.6 mm focal length, slightly smaller than the 16 mm specification.

The extrinsic relationship between the camera and projector was qualitatively validated, as it is difficult to determine where exactly the optical center is in the camera and projector CAD models. Additionally, the position of both the camera and projector will vary from the model due to 3D printing tolerances. The calibrated positions were reasonably close to the designed model.

Additional details from this calibration procedure can be found in Appendix A.
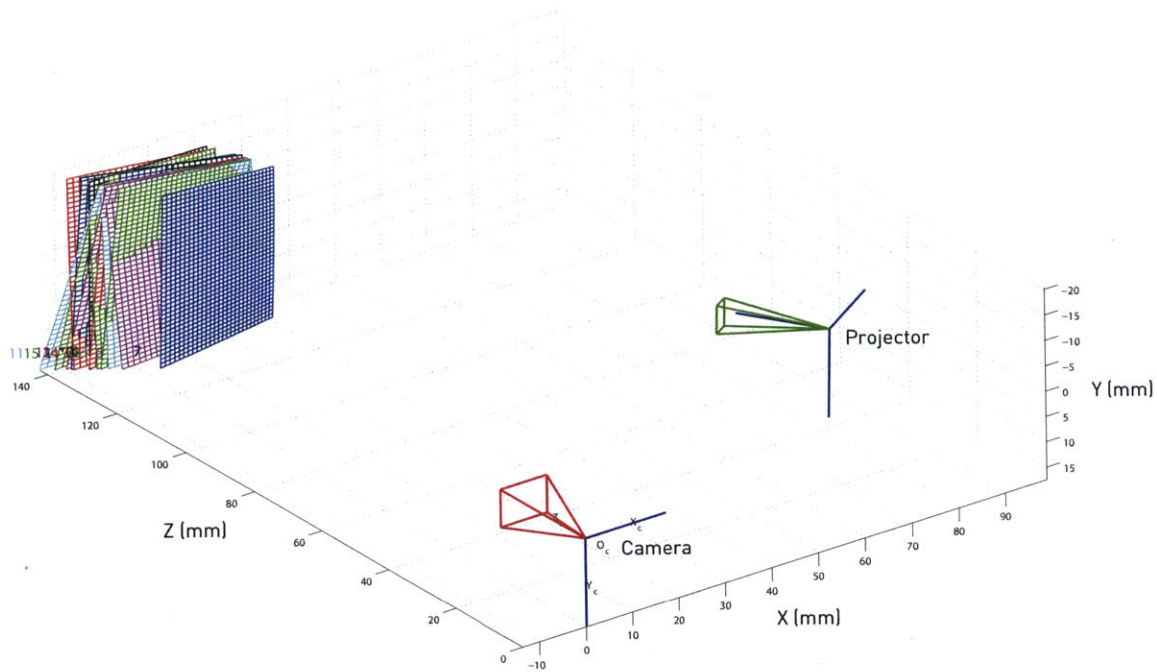
Figure 5-9: Calculated locations of each calibration image and the extrinsic relationship between the camera and projector

Blob Detection To identify where the structured light dots are in a given image, they must be identified through a process called blob detection. Blob detection locates the positions of the dots by detecting regions of the image that have different properties, such as brightness or color, and then separating these regions using segmentation. The centroids of each of the segmented blobs is used to identify the location of the dot on the image.

A typical segmentation process starts with pre-processing to accentuate the differences between the dots and the background. This is accomplished by increasing the contrast and sharpness of the image. The image is then thresholded using an intensity-based method. The image is a grayscale intensity map, so the bright structured light dots should have a higher intensity than the background. An intensity cutoff point is determined and the image is converted to binary, where pixels higher and lower than the intensity cutoff are represented by a 1 and 0, respectively.

To account for spatial variations in illumination, LesionAir uses a dynamic localized thresholding algorithm. Instead of specifying a single threshold cutoff for

the entire image, the Bradley adaptive thresholding method dynamically changes the threshold value based on the intensity of the surrounding local area [214]. This localized algorithm helps ensure a robust segmentation process.

Once the image was in a binary segmented format, any segmented connections between the dots were cleaned up using morphological operators such as dilation and erosion, and noise or additional artifacts were removed using a size filter.

The blob detection method that is described here, was implemented successfully and performed quite well. Segmentation parameters had to be tweaked for different skin tones. The method had the most difficulty with dots that were really close together and light that would strike the hair on the skin causing artifacts. A more advanced, dynamic method will need to be implemented before the device can become completely automated.

Structured Light Dot Ordering For both calibration and reconstruction using a structured light dot pattern, the dots from the projector must be correctly matched to the corresponding pixel in the image. To do so, the dots in the image must be automatically ordered.

When the dots are projected on a flat surface, they appear as a skewed square, which is simple to order using standard ordering algorithms. When the dots are projected on a curved surface, the pattern becomes highly distorted and the ordering becomes non-trivial. While this is intuitive for a human, it is quite difficult for a computer without a sophisticated algorithm. One such algorithm was presented by Entzinger [215].

Entzinger's algorithm begins by finding the corners of the structured light dot pattern. This is accomplished by wrapping a convex hull around a set of dots, such that those on the periphery are located. The corners are then located by evaluating the angles of the lines connecting each of the dots on the periphery. The four dots with angles closest to 90° are identified as the corners. Of the four corner dots, the starting point is found by identifying the two with the lowest horizontal index and further filtering to the one with the highest vertical index.

The algorithm then finds the next dot by finding the five objects closest to the current dot, removing those that have a higher vertical coordinate than the current dot, selecting the two leftmost dots, and then determining the angle between the current dot and the two leftmost dots. If the angle is small, the leftmost dot is selected, otherwise the other dot is selected. This process iterates until all the dots in a column are found, and then moves onto the next column, until all dots are ordered.

Entzinger's algorithm was implemented successfully for both calibration and reconstruction. It was extremely robust for the calibration procedure but occasionally had difficulty when ordering the structured light pattern for reconstruction. The method struggled with large curvature and would fail if any dots were missing from the segmentation process. Errors could be quickly caught through visual inspection of the reconstruction and manually fixed.

A more robust method is necessary and is proposed in Section 7.2.

5.1.3.3   Triangulation/Reconstruction

After the projection matrices are determined through calibration, two-view geometry can be used to triangulate the location of a point in space. Fig. 5-10 shows two cameras viewing a single point, p, in 3D space. Just as a projector is treated as an inverse camera for calibration, the same holds true for triangulation. All of the same math principles still apply. Point p gets mapped to the image planes as x_0 and x_1 via projection matrices P_0 and P_1, respectively.

$$P_0 = K_0[R_0|t_0] \tag{5.23}$$

$$P_1 = K_1[R_1|t_1] \tag{5.24}$$

A line can be ray-traced from the camera origin through the point on the image plane to the point p out in space by inverting this operation:

$$\hat{v}_0 = \mathcal{N}(R_0^{-1}K_0^{-1}x_0) \tag{5.25}$$

105
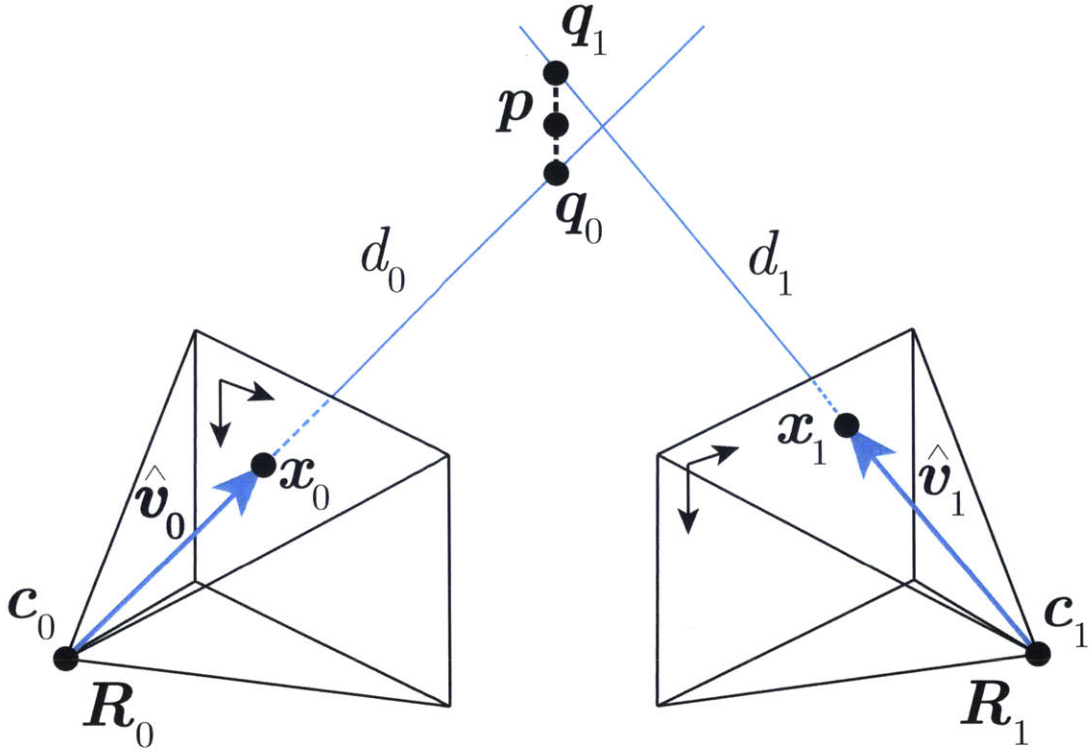
Figure 5-10: Two-view triangulation

$$\hat{v}_1 = \mathcal{N}(R_1^{-1} K_1^{-1} x_1) \tag{5.26}$$

Note that the magnitudes of $\hat{v}_0$ and $\hat{v}_1$ are arbitrary, so the values are normalized as only direction is necessary.

In an ideal world, doing so for both cameras would result in the lines crossing exactly at point p. Due to image sensor resolution constraints and optical distortion the lines do not usually intersect. To mitigate this issue, geometric distance minimization is used to find q_j, which is defined as the nearest point to p on ray $\hat{v}_j$. The geometric distance that is minimized is:

$$||C_j + d_j \hat{v}_j - p||^2 \tag{5.27}$$

The minimum occurs when the distance satisfies:

$$d_j = \hat{\boldsymbol{v}}_j \cdot (\boldsymbol{p} - \boldsymbol{C}_j) \qquad (5.28)$$

Substituting the distance into the equation for $\boldsymbol{q}_j = \boldsymbol{C}_j + d_j\hat{\boldsymbol{v}}_j$ yields:

$$\boldsymbol{q}_j = \boldsymbol{C}_j + (\boldsymbol{p} - \boldsymbol{C}_j) \qquad (5.29)$$

This gives an expression for $\boldsymbol{q}_j$ in terms of known $\hat{\boldsymbol{v}}_j$, $\boldsymbol{C}_j$, and unknown $\boldsymbol{p}$. To solve for $\boldsymbol{p}$, the sum of the squared distances given by:

$$E = \sum_j ||\boldsymbol{p} - \boldsymbol{q}_j||^2 \qquad (5.30)$$

is minimized by substituting 5.29 in for $\boldsymbol{q}_j$. Once this is minimized, the resulting $\boldsymbol{p}$ is the location of a particular point in three-dimensional space on the surface being reconstructed. This process is repeated for all other projected points, which forms a 3D point cloud representing the reconstructed scene.

5.1.3.4 Resolution

The spatial and depth resolution of a structured light system comprised of the camera and projector described in this section is extremely difficult to determine. A crude estimate of the resolution can be completed, but due to variability should not be trusted to guide the design. This example is only included to better understand the parameters that govern resolution, so that they may be used to scale the design at a later time.

Depth Resolution The depth resolution, which will be used to determine elasticity, is dependent on the camera pixel size and the angular offset of the projector, and the accuracy of the dot finding algorithm. Because the projector is offset at 45°, it can be assumed that the projected light rays strike the surface at 45°; however, only rays at the center of the projected pattern will actually have an incidence angle of 45°. Therefore, there is generally a 1:1 relationship between a unit change in depth and

a unit change in the horizontal direction. So the depth resolution is approximately equivalent to the size of the pixel that is magnified out in space.

For LesionAir, the 6.45 μm pixels are magnified to approximately 0.04 mm, so the depth resolution will be approximately 0.04 mm. This value is likely extremely conservative because it does not take into account the sub-pixel accuracy of the dot finding algorithm; however, this model assumes perfect optical sharpness and no distortion from the lens, and doesn't take into account the pixel magnification difference that occurs because the projector is off-axis.

Spatial Resolution Spatial resolution is even more difficult to determine. For a single structured light image, the spatial resolution is governed by the gobo design, the lens, and the distance to the surface being measured. A structured light dot pattern only provides exact depth information at each of the dots. Everything in between the dots has to be interpolated. So the spatial resolution is just the distance between the projected dots on the surface, which can be determined by calculating the magnification. Again, because the projector is offset at an angle, the spacing is not uniform throughout.

For the LesionAir design, the vertical resolution ranges from 1.25–1.5 mm, and the horizontal resolution ranges from 0.75–1 mm. The spatial resolution for a single image can be adjusted by changing the number of dots or dot spacing on the gobo, or by switching to a lens with a different focal length.

Spatial resolution for the displacement measurements that are created with a sequence of structured light images is even more difficult to determine. This resolution is determined by the spatial distance between corresponding dots from two images. It still has the same dependencies from a single image, and also depends on the material being measured. A smaller applied force or stiffer tissue will result in less displacement and a better spatial resolution. A smaller step size or increase frame rate will also result in improved spatial resolution. This spatial resolution also varies across the field of view — the further the projected light has to travel, the worse the resolution will be.
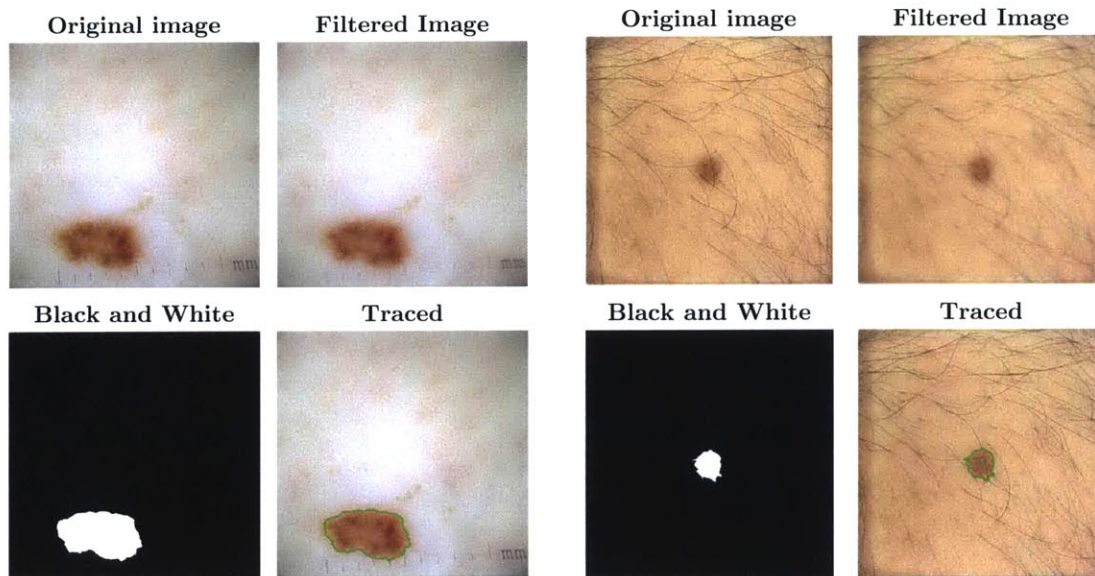
Figure 5-11: Lesion Segmentation Process

5.1.4 Image Analysis

To complete the functional requirement of capturing the lesion morphology, image processing and analysis techniques were employed. There is a large cross-over in the principles that are used in computer vision and image analysis. Both are used to extract meaningful information from an image. The novel contribution that is derived from this section is the implemented combination of lesion morphology measurement and tissue elasticity measurements to form a multi-modal approach to diagnosis.

5.1.4.1 Lesion Segmentation

Quantifying the morphologic properties of a lesion first requires that it be segmented so that it can be differentiated from the surrounding tissue. Lesion segmentation follows a similar process to the blob detection techniques that are discussed earlier in this chapter.

The image is pre-processed to accentuate differences in the lesion and surrounding tissue. A Gaussian blur is applied to the image to minimize noise and remove high spatial frequency areas that may cause oversegmentation, or the fracturing of the lesion segment into several smaller segments. The blur is minimal enough, such that
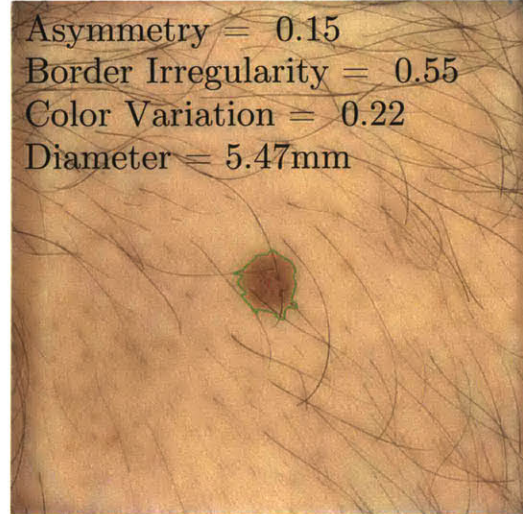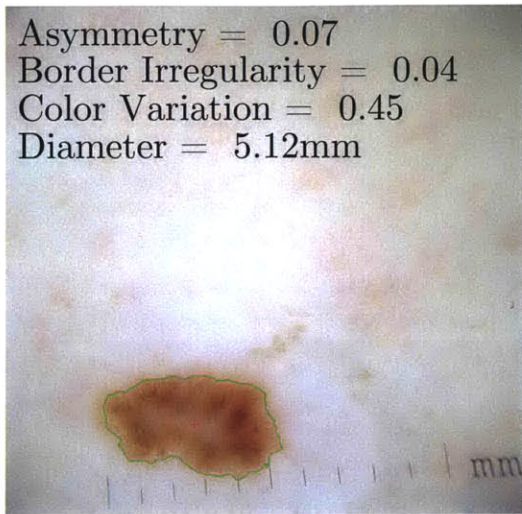
Figure 5-12: Examples of automated ABCD morphology quantification

the boundary edges of the lesion are not lost. Then an intensity thresholding is applied and a binary mask is created. The mask is then applied to the image so that the boundary can be identified. Examples of these steps are shown in Fig. 5-11.

The biggest issue in lesion segmentation is hairs. Hairs appear darker than the surrounding skin, similar to a melanocytic lesion, so they are commonly included in the segmentation. There are a few different ways to remove hairs; the most common is to evaluate the aspect ratio of the segmented region. Hairs are very long and thin so they have a large aspect ratio which can be used to filter them out of the segmentation. However, this method cannot be used on hairs that travel over the lesion, so additional advanced filtering techniques are required.

5.1.4.2 ABCD Algorithms

The following ABCD algorithms were used to quantify the morphological properties of a lesion. All of the algorithms are relatively simple for easy implementation. Each of the metrics has been normalized such that a value of zero correlates to a high probability of healthy tissue and as the value increases, the probability of cancer goes up. While these algorithms were not quantitatively compared to any other methods, it is expected that some of the more advanced techniques discussed in 3.2.3 would provide higher fidelity and robustness.

110

Asymmetry To determine asymmetry, the segmented lesion's centroid is determined and used to split the lesion horizontally and vertically so four quadrants are created. The area of each of these regions is measured. Then the top two quadrants are folded onto the bottom two quadrants, and the left two quadrants are folded onto the right two quadrants, and the area of the intersection regions is measured. Then the following algorithm is used to find the maximum difference in region area to intersecting area:

$$\text{Asymmetry} = \max\left(\frac{\max(A_{\text{Top}}, A_{\text{Bottom}})}{A_{\text{Top}\cap\text{Bottom}}}, \frac{\max(A_{\text{Left}}, A_{\text{Right}})}{A_{\text{Left}\cap\text{Right}}}\right) - 1 \qquad (5.31)$$

where A is the number of pixels that make up the area. A perfectly symmetric lesion will have an area ratio of one. Subtracting one normalizes it such that a perfectly symmetric lesion will have a value of zero.

Border Irregularity Border irregularity is quantified by computing the compactness of a lesion. The number of pixels on the boundary of the segmented lesion is compared to the number of pixels in the area.

$$\text{Border Irregularity} = \frac{P^2}{4\pi A} - 1 \qquad (5.32)$$

where P is the number of pixels on the border. If the lesion is a perfect circle that ratio will be equal to one, so one is subtracted so that a perfectly circular lesion with equal zero.

Color variation Color variation is difficult to measure using LesionAir because the camera is monochromatic, so all that is available is grayscale intensities (0–255). The intensity range of the lesion is calculated and then normalized such that a maximum color variation will be equal to one:

$$\text{Color Variation} = \frac{\text{Max Intensity} - \text{Min Intensity}}{255} \qquad (5.33)$$

111

While this calculation is sufficient, it lacks fidelity. A better solution would be to actually compute variance or standard deviation of the color within a lesion. Once a smartphone-based device is created, color variation will be straightforward to do.

Diameter The diameter of the lesion is calculated by finding the major diameter of the segmented lesion. This diameter is given in pixels so it needs to be converted to a real world distance. Most other algorithms are unable to do this because they lack a means to determine scale.

LesionAir is able to use the structured light images to determine scale. The structured light reconstruction provides the conversion 2D pixels to 3D real world coordinates. Once the pixels that make up the major diameter are identified, they can be converted to give a real-world diameter of the lesion.

5.2   Force Application System

LesionAir's force application system consists of a pneumatic pump, solid state pressure sensor, and a seal that acts as a junction between the device and the skin. Tissue models, from simple mathematical models to computer simulations and real-life phantoms, were developed to help guide the force application design and determine the required pressure and area of application.

5.2.1   Tissue Model

Simplifying the inherent complexities of tissue into a practical first-order model provides a robust method to quickly and accurately evaluate how different parameters affect the deformation response of tissue to a mechanical stimulus. The variability of tissue parameters, such as layer thickness or elasticity, results in a wide range of scenarios that may occur.

To simplify the model of skin, each layer is evaluated on a macroscopic scale such that it can be considered homogenous and isotropic, allowing the use of a 2D axisymmetric model. Skin is also assumed to be incompressible, so the Poisson's

ratio, ρ, is equal to 0.5. Finally, all loads will be applied statically, or quasi-statically, such that any time-dependencies from viscoelastic effects can be ignored.

The simplified tissue model was used to determine a starting point in design. A negative pressure will be applied to the skin and structured light will be used to measure the displacement. The design should be optimized such that, at a given pressure, a maximum difference in displacement occurs between tissue with a lesion and tissue without a lesion. The mechanical stimulus can be modulated by changing the negative pressure amount and the size of the area to which that pressure is being applied.

Initially, a first-order mathematical expression was derived to identify and understand the relationship of the parameters to the deformation response. Then, a finite element analysis (FEA) model was implemented to better understand the boundary conditions and optimize the design parameters. Finally, a skin mimicking phantom model was designed and fabricated to validate the the capabilities of the designed device.

5.2.1.1 Linear Approximation – Small Deflections

It is hypothesized that skin can be modeled as a beam or plate on an elastic foundation. The beam on an elastic foundation theory was appropriately described by Timeshenko [216], and has widely been applied in civil engineering to describe the behavior of a concrete slab on a soil foundation [217]. The epidermal layer of tissue is represented as a beam, whereas the dermal and hypodermal layers comprise the elastic foundation.

The elastic foundation is described by the foundation modulus:

$$k_0 = \frac{E}{t} \tag{5.34}$$

where E is Young's modulus and t is the thickness of the layer.

However, since tissue's elastic foundation has two layers with different stiffness values, a multi-layer model must be applied. The multi-layer models for soil cannot

113
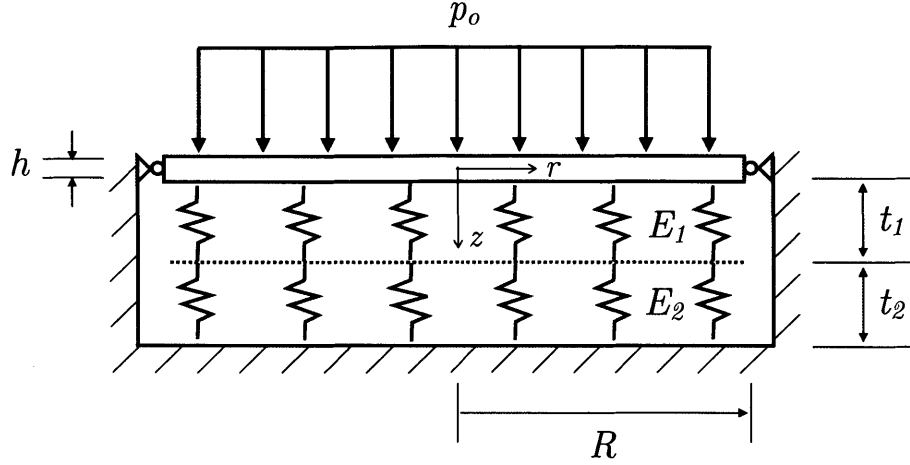
Figure 5-13: Structural schematic of skin, represented by a simply-supported circular plate on an elastic foundation

be applied because they assume a slip friction between the two layers. Tissue layers are bonded with no slip, so the elastic foundation can be approximated as two springs in series. To solve for the equivalent foundation modulus, the equation for the equivalent stiffness of two springs in series can be used:

$$k_{eq} = \frac{1}{\frac{1}{k_1} + \frac{1}{k_2}} \tag{5.35}$$

Substituting 5.34 into 5.35 yields:

$$k_0 = \frac{1}{\frac{t_1}{E_1} + \frac{t_2}{E_2}} \tag{5.36}$$

The schematic in Fig. 5-13 illustrates the structural model of tissue as a uniform pressure is applied to a given area. For these conditions, the deflection of a simply-supported circular plate subjected to uniformly distributed load and resting on an elastic foundation can be linearly approximated by the Raleigh-Ritz solution as given by [218]:

$$w(r) = \frac{p_0 R^4}{16D(1 + \nu) + \frac{2}{3}k_0 R^4} \left(1 - \frac{r^2}{R^2}\right) \tag{5.37}$$

114
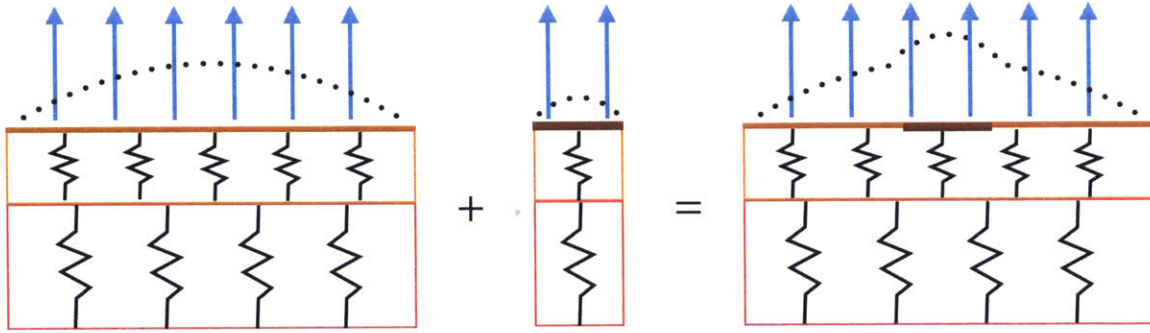
Figure 5-14: Schematic of superposition principle used to describe how tissue with a lesion deforms

where w is deflection, r is the radial distance from center, R is the radius of the plate, p_0 is the uniform pressure, D is the flexural rigidity, ν is Poisson's ratio which for incompressible materials like skin is equal to 0.5, and k_0 is the foundation modulus.

Maximum deflection occurs at the center of the plate:

$$w_{max} = w(0) = \frac{p_0 R^4}{16D(1 + \nu) + \frac{2}{3}k_0 R^4} \tag{5.38}$$

Flexural rigidity is defined as:

$$D = \frac{Eh^3}{12(1 - \nu^2)} \tag{5.39}$$

where h is the thickness of the plate.

Superposition is used to apply this approximation to skin with a lesion. The lesion is also treated as a plate on an elastic foundation. As shown in Fig. 5-14, the deflection of the lesion is added to the deflection of the epidermis to determine the total deflection.

This first-order approximation is linear and does not account for the additional effects that occur at large deformations. Since tissue is hyperelastic and has a relatively low stiffness, it will leave the linear small deformation region quickly. To better describe how tissue behaves at higher strain, a non-linear model is required.

115

5.2.1.2 Non-Linear Approximation – Large Deflections

A solution for the non-linear system of equations that describes the large deflections of a flat plate on an elastic foundation was proposed by [219]. The solution was derived by assuming the strain energy due to the second invariant of the middle surface strains may be neglected. A non-dimensionalized numerical solution is presented, but it does not provide the necessary information to solve the problem for the parameters given in this research.

The solution is:

$$
\frac{w}{t} = \left(\frac{qR^4}{Dt}\right)\left(\frac{1}{p_1^2 p_2^2 R^4}\right)
$$
$$
\left(1 - \frac{p_2\left(p_2 J_o(p_2 R) + \frac{\nu-1}{R}J_1(p_2 R)\right)J_o\left(p_1 J_o(p_1 R) + \frac{\nu-1}{R}J_1(p_1 R)\right)\left(J_o(p_2 r)\right)}{(p_2^2 - p_1^2)\,J_o(p_1 R)J_o(p_2 R) + \frac{\nu-1}{R}\left(p_2 J_o(p_1 R)J_1(p_2 R) - p_1 J_o(p_2 R)J_1(p_1 R)\right)}\right)
$$

$$(5.40)$$

where J_o and J_1 are zero order and first order Bessel functions of the first kind, respectively, q is the intensity of a uniform load, R is the radius of a circular plate, and w is deflection in the z-direction.

p_1 and p_2 are imaginary or complex constants equal to:

$$
p_1^2 + p_2^2 = -\alpha^2
$$

$$(5.41)$$

$$
p_1^2 p_2^2 = \frac{k_o}{D}
$$

$$(5.42)$$

A, B, and α are constants of integration:

$$
A = \frac{-\frac{q}{k_o}p_2\left(p_2 J_o(p_2 R) + \frac{\nu-1}{R}J_1(P_2 R)\right)}{(p_2^2 - p_1^2)\,J_o(p_1 R)J_o(p_2 R) + \frac{\nu-1}{R}\left(p_2 J_o(p_1 R)J_1(p_2 R) - p_1 J_o(p_2 R)J_1(p_1 R)\right)}
$$

$$(5.43)$$

$$
B = \frac{\frac{q}{k_o}p_1\left(p_1 J_o(p_1 R) + \frac{\nu-1}{R}J_1(P_1 R)\right)}{(p_2^2 - p_1^2)\,J_o(p_1 R)J_o(p_2 R) + \frac{\nu-1}{R}\left(p_2 J_o(p_1 R)J_1(p_2 R) - p_1 J_o(p_2 R)J_1(p_1 R)\right)}
$$

$$(5.44)$$

Table 5.2: FEA parameters for skin model

	Thickness (cm)	Diameter (cm)	Young's Modulus (kPa)	Mooney-Rivlin		Ogden	
				C_{10} (kPa)	C_{11} (kPa)	μ (kPa)	α
Epidermis	0.025	15	1000	9.4×10^3	8.2×10^4	8.2×10^4	2.98
Dermis	0.2	15	100	9.4	82	22.6	3.29
Hypodermis	3	15	15	3	0	10.4	13.6
Lesion	0.2	2	200/400	N/A	N/A	N/A	N/A

$$\frac{\alpha^2 t^2}{6} = A^2 p_1^2 \left(J_o^2(p_1 R) + J_1^2(p_1 R) - \frac{2}{p_1 R} J_o(p_1 R) J_1(p_1 R) \right)$$
$$+ B^2 p_2^2 \left(J_o^2(p_2 R) + J_1^2(p_2 R) - \frac{2}{p_2 R} J_o(p_2 R) J_1(p_2 R) \right)$$
$$+ \frac{4AB p_1 p_2}{R(p_1^2 - p_2^2)} \left(p_2 J_1(p_1 R) J_o(p_2 R) - p_1 J_o(p_1 R) J_1(p_2 R) \right) \quad (5.45)$$

This set of equations is hypothesized to describe the mechanics of tissue better than the first-order linear approximation presented in Section 5.2.1.1; however, due to the cyclic nature of the equations and the variables within Bessel functions, none of the attempted numerical solving techniques were successful. The development of a simplified non-linear model is a topic for future work.

5.2.1.3   Finite Element Analysis

ANSYS 16.0 was used to perform FEA and evaluate variations in geometry, boundary conditions, and elasticity models. Within ANSYS, a custom material was defined for each layer of skin and for the lesion. The definitions for each layer are given in Table 5.2. A 2D axisymmetric model was set up and each of the layers was bonded together. A 50 mbar vacuum pressure was applied to a 6 cm diameter area in the center of the model. FEA was performed to determine how the position of the lesion within the layers of tissue modifies the deflection. As seen in Fig. 5-15, the lesion was placed such that it was fully exposed through the epidermis, between the epidermis and dermis layers, and only in the dermis. In can be inferred through Table 5.3 that lesion position only slightly modifies deflection when tissue is modeled as a linear elastic

117

<div align="center">

Exposed   Dermal Junction   Dermis Only

</div>
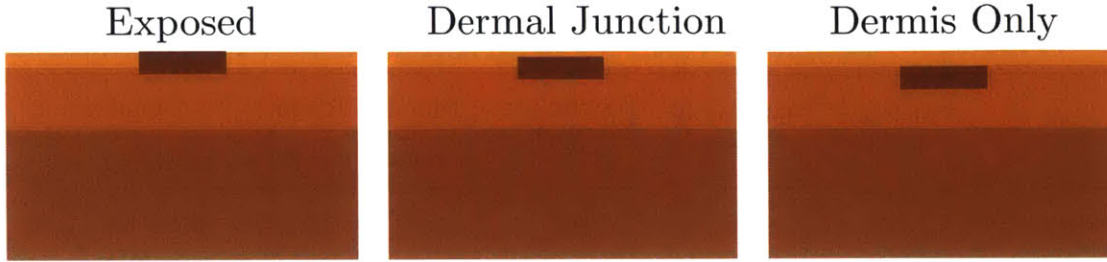
Figure 5-15: Schematic demonstrating the different lesion positions for FEA

Table 5.3: The FEA simulated effect of lesion location on maximum deformation

| | Maximum Displacement (mm) | | | |
| | Linear Elastic | | Mooney-Rivlin | |
	Lesion (200 kPa)	Lesion (400 kPa)	Lesion (200 kPa)	Lesion (400 kPa)
Exposed	7.85	7.85	4.72	4.69
Dermal Junction	7.84	7.84	4.07	4.07
Dermis Only	7.83	7.83	4.01	4.01

material; however, when a hyperelastic model is used, the difference in displacement becomes more substantial. A lesion positioned at the epidermal-dermal junction is the most realistic and this position was used in all of the rest of the FEA studies. FEA was also performed to determine how various boundary conditions modify the deflection. As seen in Fig. 5-16, the boundary conditions were set such that the sides were fixed and the bottom was free, the bottom was fixed and the sides were free, and the bottom was elastically connected to ground. Finally, FEA was utilized to evaluate the linear elastic model against the two hyperelastic models. how various boundary conditions modify the deflection. The results in Table 5.5 demonstrate how the Mooney-Rivlin model was able to handle the large deformations better. It is unclear why the Ogden model did not produce reasonable results. Table 5.4 reveals that the boundary conditions are highly influential on the maximum displacement. The bottom elastic condition is the most realistic because the hypodermis is connected to the underlying muscle and bone by connective tissue that is highly compliant. All

<div align="center">

118

</div>
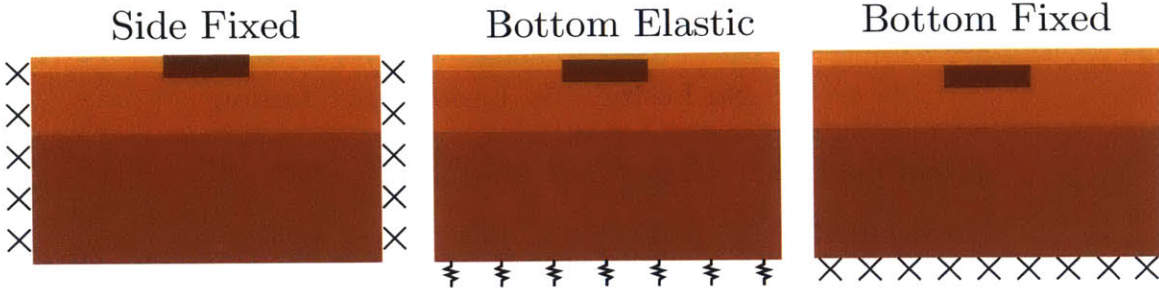
Figure 5-16: Schematic demonstrating the different boundary conditions for FEA

Table 5.4: The FEA simulated effect of boundary conditions on maximum deformation

	No Lesion	5x Lesion	10x Lesion
Side Fixed	9.75	9.92	9.74
Bottom Elastic	7.84	7.84	7.81
Bottom Fixed	5.94	5.84	5.82

remaining FEA studies modeled the tissue with a bottom elastic boundary condition. The elasticity of this boundary condition was estimated to be similar to that of the hypodermal layer.

A full-factorial parametric FEA study with 3000 design points was also performed. In this study, several parameters were varied. The variables and their values that were evaluated were:

- Epidermis thickness: 0.01, 0.025, 0.05 cm

- Dermis thickness: 0.1, 0.2, 0.3 cm

- Hypodermis thickness: 1, 2, 3 cm

- Lesion thickness: 0.1, 0.2 cm

- Lesion diameter: 1, 2 cm

- Diameter of the applied vaccum: 4, 5, 6, 7, 8, 9, 10, 11, 12 cm

- Pressure: 10, 50, 100 mbar

119

Table 5.5: The FEA simulated effect of material model type on maximum deformation

	No Lesion	5x Lesion	10x Lesion
Linear Elastic	7.84	7.84	7.81
Mooney-Rivlin	4.01	4.72	4.68
Ogden	0.64	0.64	0.64
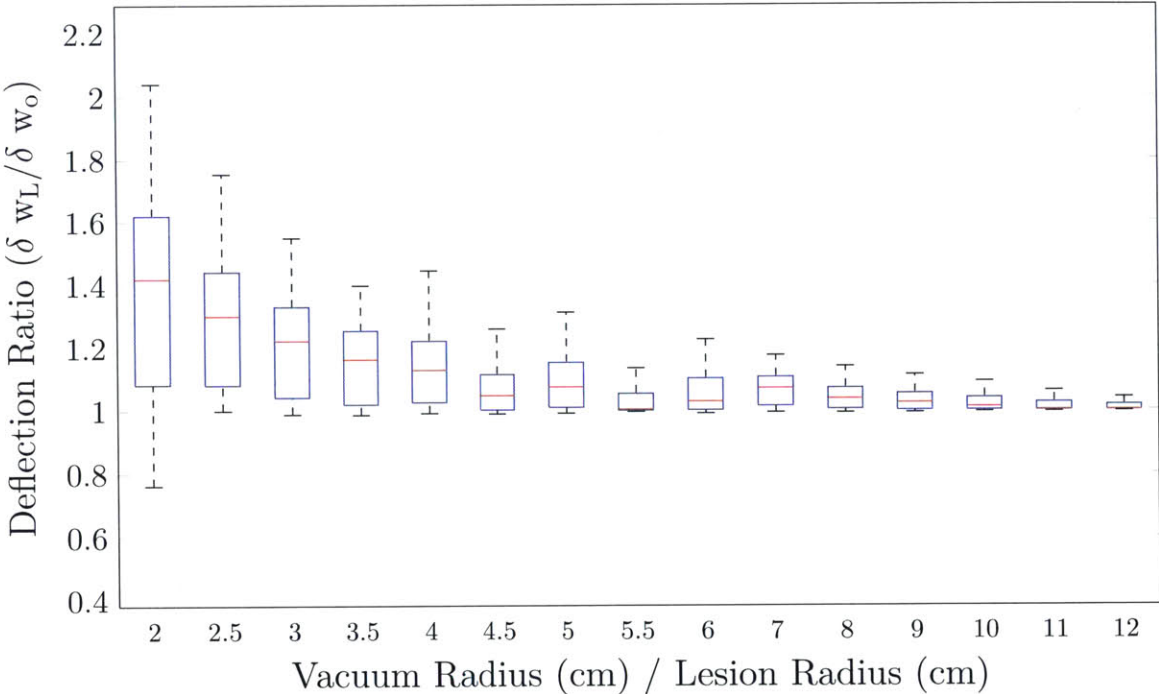
Figure 5-17: Full-factorial parametric study results

The output that was evaluated was the center deformation, which is equivalent to the maximum deformation. Mooney-Rivlin material constants were applied, along with a bottom elastic boundary condition and a lesion placement in the epidermal-dermal junction.

Stepwise regression was performed on the results. Vacuum diameter and pressure were the variables with the highest sensitivity. Lesion diameter as well as epidermal and hypodermal thickness were also important. Dermis and lesion thickness were not important.

No Lesion

Lesion
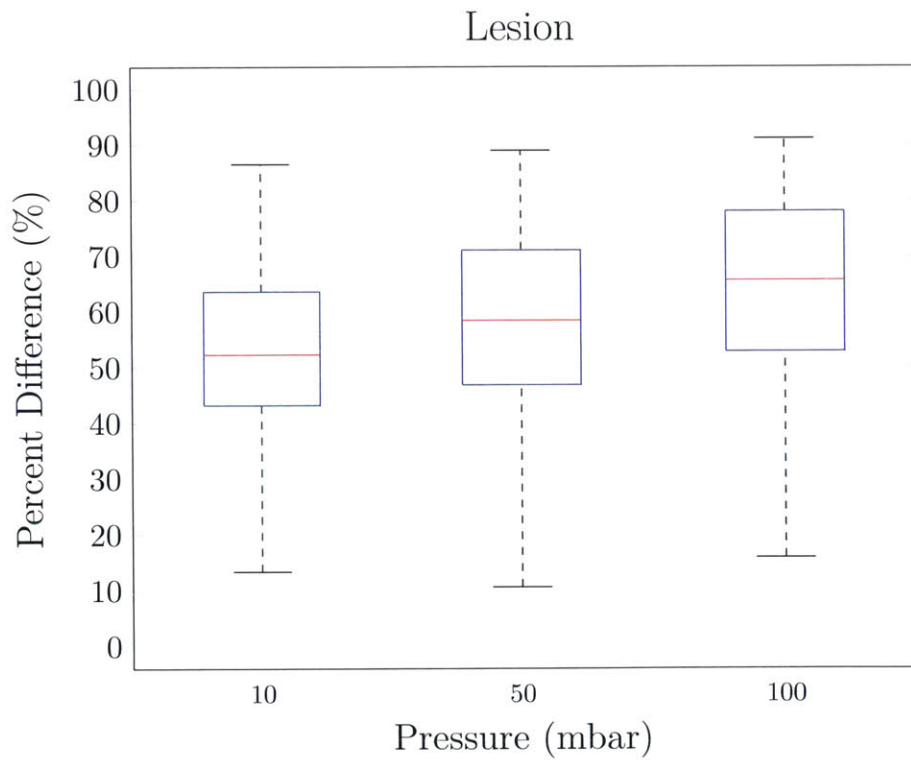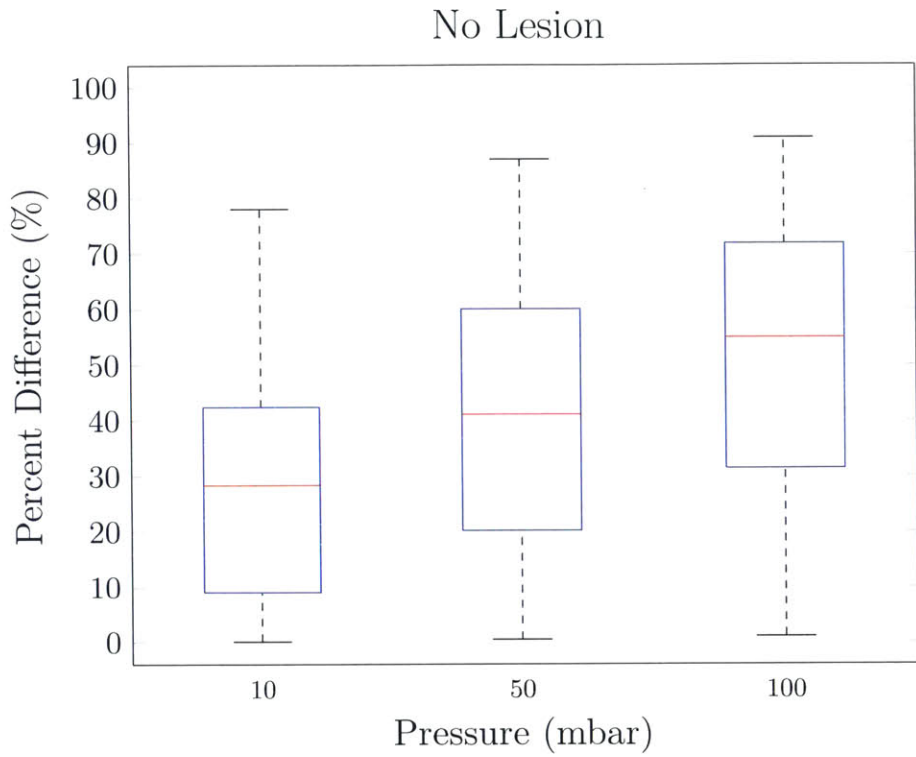
Figure 5-18: Evaluation of linear approximation model against FEA for different pressures
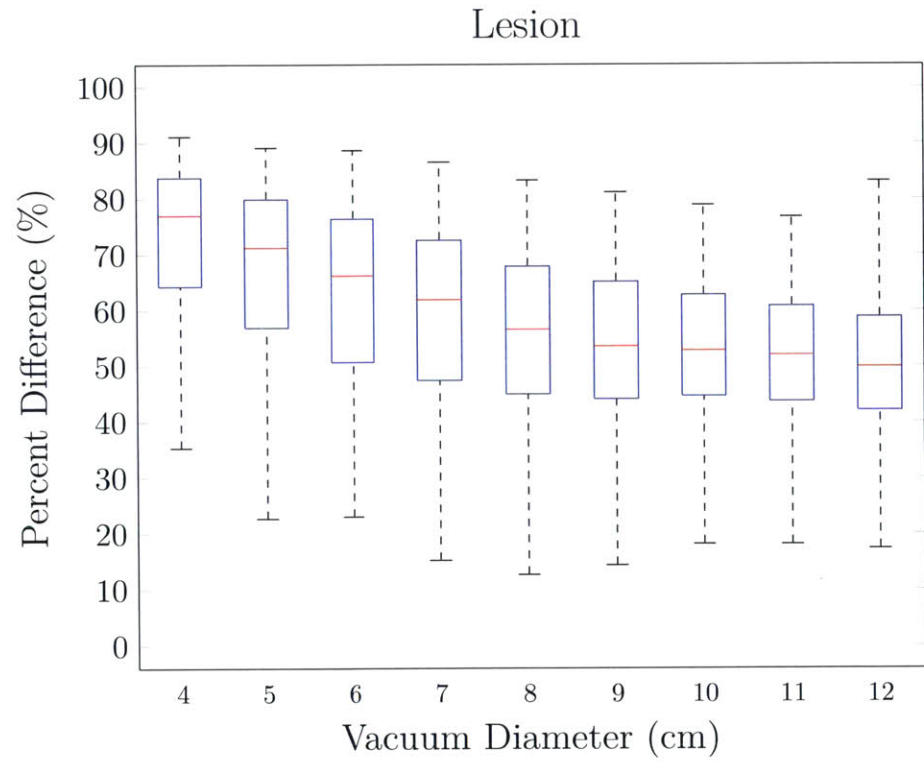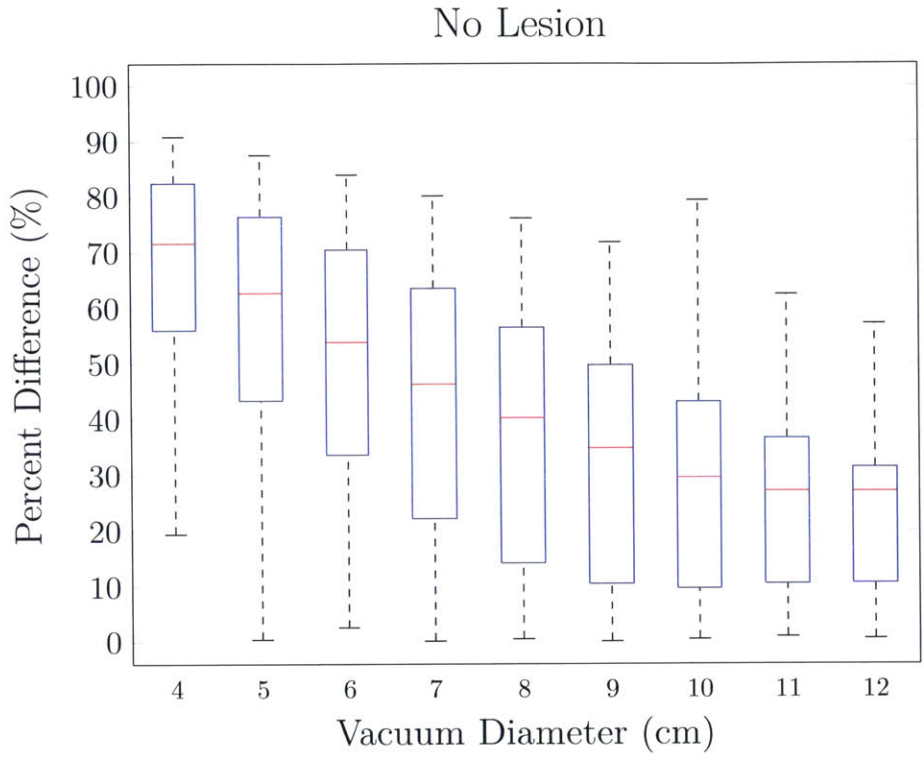
Figure 5-19: Evaluation of linear approximation model against FEA for different areas of application
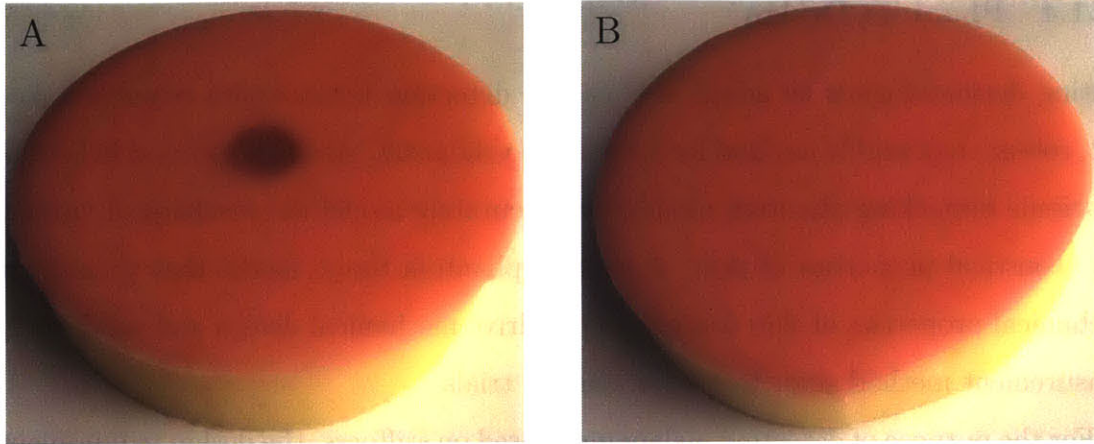
Figure 5-20: Fabricated phantom tissue models with (A) and without (B) a cancerous lesion

Fig. 5-17 is a plot of the lesion deflection ratio to the vacuum-lesion ratio. Lesion deflection ratio is the non-dimensionalized amount of displacement of a lesion to the amount of displacement without a lesion. Maximizing this amount will help to ensure that a cancerous lesion is differentiated from healthy tissue. It can be seen that the lesion deflection ratio is greatest when the negative pressure area is close to the same size of the lesion.

The full-factorial parametric study was also used to evaluate the linear first-order equation that was derived earlier in this section. The maximum deflection was calculated for each design point using the linear equation. The results were compared to the FEA results. Fig. 5-18 and 5-19 show how the linear model deviates from the FEA results for different pressures and vacuum diameters.

As expected, when pressure increases, the maximum deflection also increases. Large deflections are non-linear, so the FEA results deviate further from the linear approximation equation. The linear model is also less accurate for smaller vacuum diameters. This is caused by the boundary condition effects. This validates the quality of the approximation for small deflections; however the error will become significant for large deflections.

5.2.1.4 Phantom Design

Getting dermatologists to adopt new cancer detection technologies requires a low-cost, robust, repeatable method for large-scale validation. As demonstrated in Section 3.4, tissue mimicking phantom models can accurately model the mechanical, optical, and acoustical properties of skin. A custom phantom tissue model that mimics the mechanical properties of skin was created to drive mechanical design and validate the measurement method prior to human clinical trials.

For the purpose of detecting melanomas based on stiffness, the design requirements of tissue-mimicking phantom models are two-fold: (1) achieving accurate thicknesses for each layer of the skin and (2) modeling the elasticity of normal skin relative to melanomas.

The elasticity and thickness of human skin is not constant, and varies significantly depending on several factors, most notably, location on the body. The phantom model prototypes, as seen in Fig. 5-20, were fabricated by Design Circle, Inc. [220], a medical product development firm, according to the design specifications for layer thickness, diameter, and stiffness shown in Table 5.6. These specifications are based on the values presented in Chapter 2.

Table 5.6: Phantom tissue model specifications

	Thickness (mm)	Diameter (cm)	Young's Modulus (kPa)	Durometer (Shore OO)
Epidermis	0.25	12	1000	87
Dermis	2	12	200	55
Hypodermis	30	12	50	15
Melanoma Lesion	1.5	1.5	400	73

Each individual layer was fabricated by pouring a proprietary synthetic rubber into a custom mold. Three phantom models were fabricated — one without a lesion, one with an lesion exposed through the epidermis, and one with an embedded lesion situated in between the epidermal and dermal layers.

The property specifications for the initial prototype phantom models reflected those for an average person's abdomen. While sufficient for an initial validation, future models will incorporate varying stiffness and thickness values to simulate other body regions. Due to the use of synthetic rubber for the material, Young's Modulus values were converted to durometer according to the method proposed by Mix and Giacomin [221].

After the phantom models were fabricated, the Young's modulus of each layer was quantified to determine how close the final model matched the proposed specifications. An Admet Universal Materials Testing system with a 1 N force transducer was used to determine the Young's modulus of each layer. Each layer was measured three times and the mean value was compared to the specification. The epidermis and hypodermis were well outside the target specifications. The epidermis was 74.4% stiffer than the specification with a 1744 kPa mean measurement and the hypodermis was 63.8% less stiff with a mean measured value of 18.1 kPa. However, the dermis and lesion were within 15% at 221 kPa and 343 kPa, respectively.

Table 5.7: Comparison of specified phantom tissue model stiffness with measured results

Young's Modulus (kPa)	Test 1	Test 2	Test 3	Average	Specification	Percent Difference
Epidermis	1712	1780	1740	1744	1000	74.4%
Dermis	223	223	216	221	200	10.3%
Hypodermis	19.5	17.9	17.0	18.1	50	-63.8%
Lesion	350	344	336	343	400	-14.2%

Differences in the measured stiffness of the individual layers of the phantom versus the specifications are likely due to the conversion between Young's Modulus and durometer. Durometer is a non-linear hardness measurement from zero to 100, with 100 being equivalent to a material with infinite hardness. There are several durometer scales, each using a different measurement method. The two scales discussed in this thesis are Shore OO and A.

The epidermis was at the higher end of the Shore OO scale so it was more sensitive to error. Since the phantom model is used to validate a prototype diagnostic device with finite element analysis results, a stiffer epidermis is adequate as long as the increased stiffness is taken into account. The hypodermis was well below the specified stiffness value, however, this was advantageous. The lowest possible stiffness of the synthetic rubber was thought to be 50 kPa and therefore, slightly above the acceptable range for the hypodermis. The measured value of 18.1 kPa fits within the actual range.

This novel phantom tissue model has shown initial promise as a viable solution to mimic human skin as it provides a low cost, robust, and repeatable method to enable validation of a prototype device that diagnoses skin cancer through the quantification of tissue stiffness. The model adequately validated the prototype system as the measured results were within 20% of the FEA results. While sufficient for initial validation, future models will incorporate varying stiffness and thickness values to simulate other body regions. Further tuning is required to consistently reduce the difference between the specified and measured elasticity.

5.2.2 Vacuum Pump

The force application system is used to apply the mechanical stimulus, in this case, a negative pressure vacuum force. Based on analysis of the FEA results, a 6 cm diameter aperture was chosen as the initial starting point for the pressure area size. This area is small enough such that the lesion displacement ratio is maximized, yet large enough so that the boundary effects from the seal-to-skin interface will not heavily influence the measurement results.

A negative pressure of 100 mbar was chosen to be applied in 20 mbar increments. 100 mbar over a 6 cm diameter results in an approximate 30 N force. This is estimated to be larger than the force that is applied during manual palpation, but greater forces should amplify the non-linearity differences. The pressure can be scaled back if lower pressures are sufficient in differentiating cancerous lesions from healthy tissue.

It is necessary that this pressure does not cause any pain or discomfort. The reported pain threshold and pain tolerance levels for humans is 4 bar and 5–11 bar,

Table 5.8: Relevant parameters for KNF Neuberger's NMP 05 B pneumatic pump

Parameter	Specification
Motor type	Brushless
Operating voltage	5 VDC
Flow rate	0.3 L/min
Maximum vaccuum pressure	500 mbar

respectively [222]. A 100 mbar pressure is significantly below these values. The pressure is also low enough that the device can be rapidly removed if necessary.

Initially, a hand-powered ball pump with button release valve was specified to evacuate air from the enclosure, creating the required negative pressure. This was implemented in the design and later discarded as it took too long to reach the desired pressure and caused the enclosure to wobble around.

To address this issue, a KNF Neuberger NMP 05 B micro-diaphragm gas sampling pump was selected to reduce the air pressure within the enclosure. This small pump is powered by a 5 V brushless DC motor with integrated electronics. A brushless motor was specifically chosen to minimize vibration and noise. It is extremely dynamic and durable and can pull up to a 500 mbar absolute vacuum at a flow rate of 0.3 L/min.

Boyle's law can be used to determine the amount of time the pump will take to create a 100 mbar vacuum pressure. Boyle's law states that for a constant temperature, the volume of a fixed amount of gas is inversely proportional to the pressure. This relationship is commonly presented as:

$$P_1 V_1 = P_2 V_2 \tag{5.46}$$

where P and V are the pressure and volume, respectively, at two different states.

To calculate the volume of air that needs to be removed from the enclosure to reach an internal vacuum pressure of 100 mbar, Boyle's law can be rewritten as:

$$\frac{P_1 V_1}{P_2} = V_2 = V_1 + V_p \tag{5.47}$$

where V_p is the volume of air removed.

To create a 100 mbar vacuum in a 2000 cm^3, or 2 L, enclosure, requires the evacuation of 220 mL of air. The flow rate of the pump is rated at 300 mL/min. With no leaks, the pump could reduce the pressure by 100 mbar in 44 seconds. If this process were broken up into 20 mbar steps, each iteration would require approximately 9 seconds.

The pump is the bottleneck to the data acquisition cycle. Under a minute is an adequate cycle time for the initial prototype evaluation. The designed enclosure is larger so that the commercial off the shelf components can be modularly swapped in and out. Shrinking the size of the enclosure will reduce the internal volume and therefore, reduce the amount of time to reach the required pressure.

5.2.3 Pressure Sensor

The internal pressure is monitored by an Omega PX209-30VAC5V solid state pressure transducer with a range of 0 to -1000 mbar. The sensor requires 7 to 35 VDC power to operate and outputs 0 to 5 VDC — 5 V at ambient pressure and 0 V at full vacuum. The pressure transducer is accurate and very reliable, backed by a 5-point NIST-traceable calibration. Accuracy is within 2.5 mbar, or 0.25% of the full scale range. The output is not sensitive to thermal or vibration effects.

5.2.4 Seal

The design of a seal was extremely important as this is the interface between the device and the patient. The design must be able to conform to a range of contours on the human body while still keeping an airtight seal. The geometry of a traditional lip seal was used as a starting point. FEA was then used to guide the geometry

Table 5.9: Relevant parameters for Omega's PX209-30VAC5V pressure sensor

Parameter	Specification
Negative pressure range	0 – 1000 mbar
Operating voltage	7 – 35 VDC
Output voltage	0 – 5 VDC
Accuracy	0.25% of full-scale range
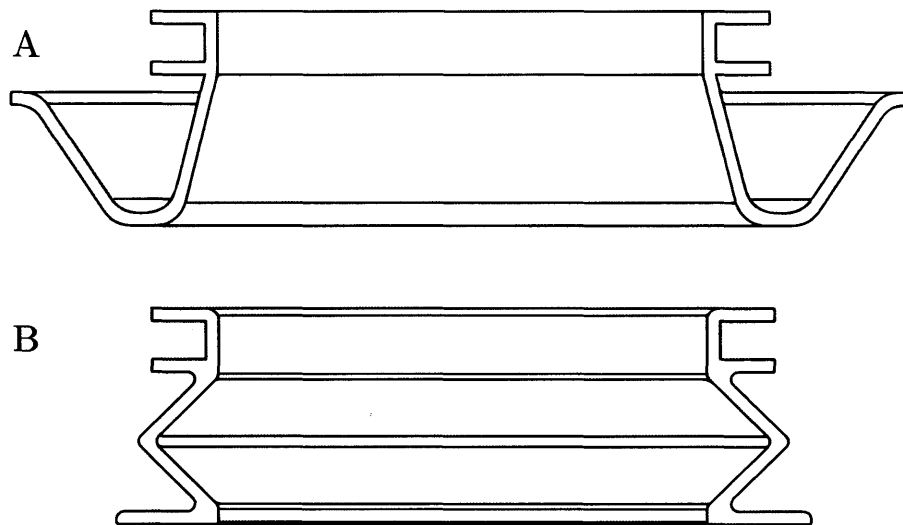
Figure 5-21: Cross-sections of tested seal geometries: (A) U-shaped seal, and (B) Bellows shaped seal

modifications. The first attempted geometry, shown as (A) in Fig. 5-21, was modeled in the shape of a U. This shape was rejected after FEA revealed that, when applied to highly contoured surfaces, the edges of the seal will actually pull up and away from the surface.

The final selected geometry, shown as (B) in Fig. 5-21, resembles a bellows profile. This profile was able to form a seal on a variety of contours. The ANSYS contact tool was used to determine 8.21 N of force is required to form a complete seal on an average forearm contour. This is a reasonable force to preload the device against the skin.
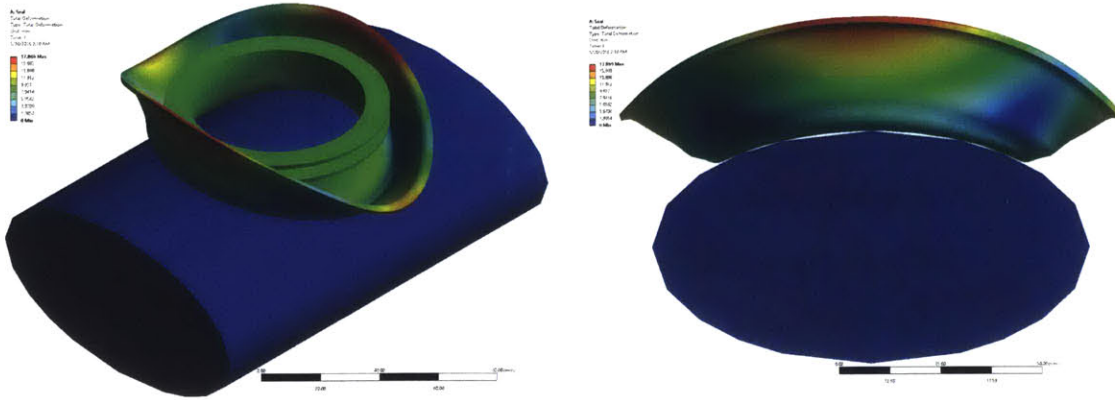
Figure 5-22: Initial seal FEA
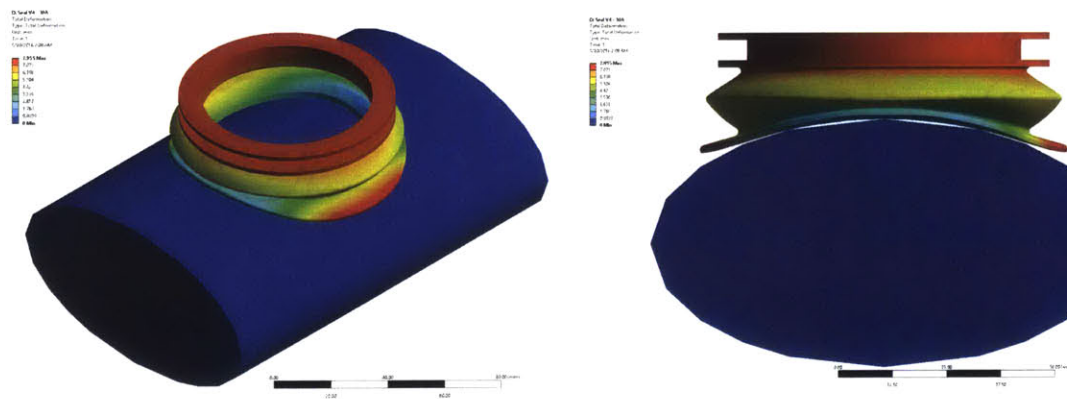
Figure 5-23: Final seal FEA

Several seals were fabricated for experimental use. A three-part mold was designed and 3D printed using a stereolithography process. SmoothOn Mold Star 30 silicone was chosen as the casted material because it has a low viscosity and vacuum degassing is not required, resulting in a quick and easy molding procedure. Mold Star 30 has a Shore 30A hardness and is tear resistant with low shrinkage. It is also a biocompatible material that will not irritate the skin. Oil- or water-based lubricants can be applied to the sealing interface to help prevent any air leaks. The seal can be easily sterilized by applying alcohol.

5.3 System Integration

The measurement and force application subsystems are combined with an enclosure and interface module to complete the device. The enclosure provides structural sup-
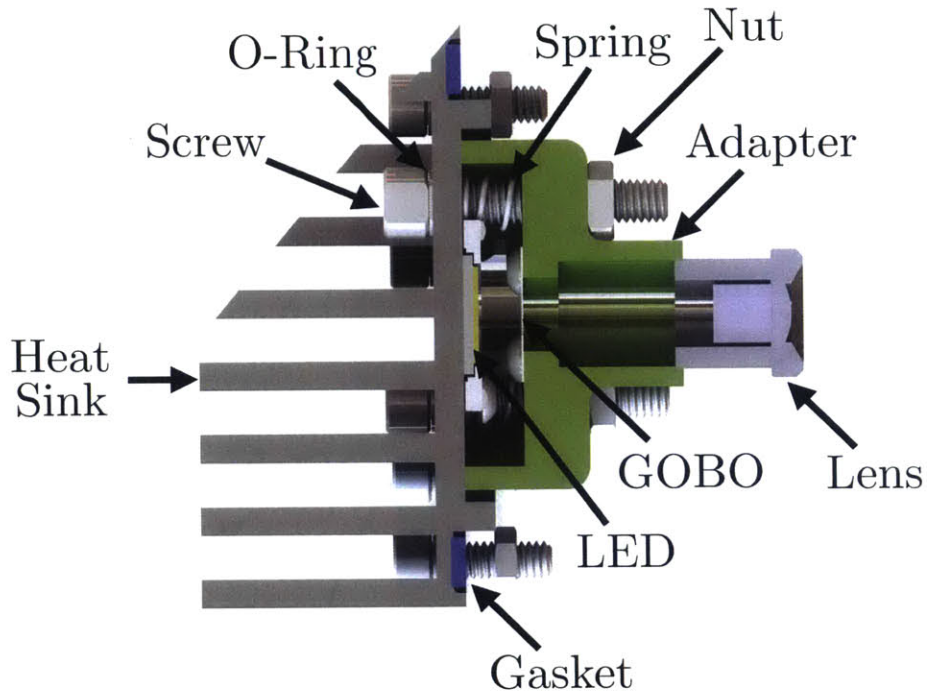
Figure 5-24: Cross-section of projector mount

port and creates a controlled environment, while the interface module controls all of the peripherals. A functional flow map of a typical use case is presented and the steps for data acquisition and data processing will be explained.

5.3.1 Enclosure

The enclosure serves several purposes. It rigidly holds the camera and projector systems relative to each other and the tissue, enabling a single calibration procedure that can be used for all subsequent measurements. It provides a pressure-regulated, self-contained internal chamber that is light-tight so that all recorded images are standardized. It also acts as a modular platform, so that components can be swapped out if necessary. The enclosure is 3D printed from a high-impact ABS-like material (Somos NeXt). Without any attachments, the enclosure measures $14 \times 11 \times 25$ cm. In its final form with everything attached, the device is $26 \times 13 \times 26$ cm and weighs approximately 1.5 kg. The projector is offset to the side of the camera by approximately 8.4 cm and tilted at a 45 degree angle to maximize depth resolution.

131
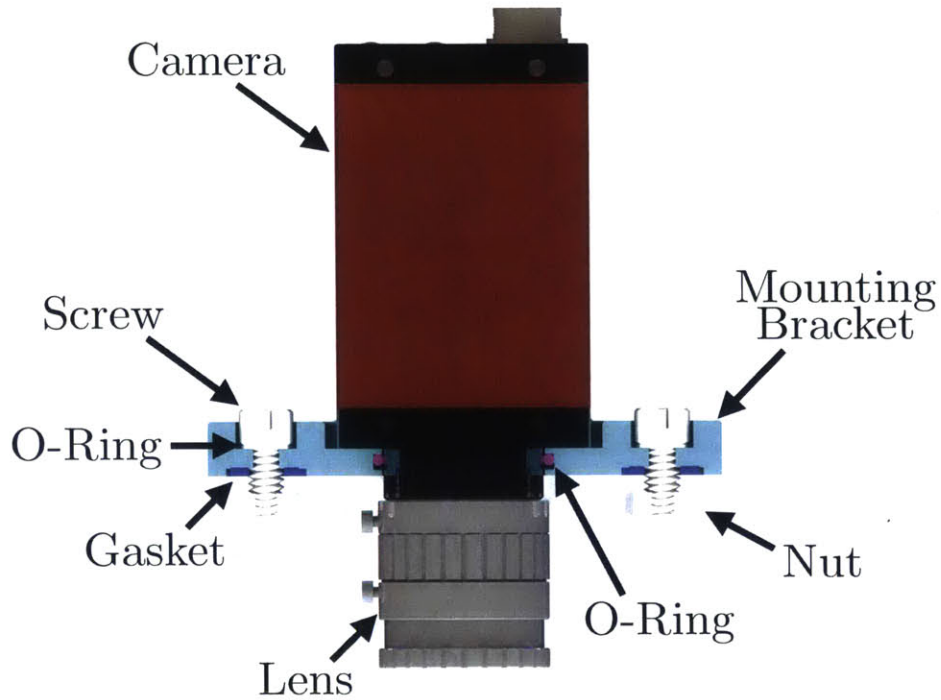
Figure 5-25: Cross-section of camera mount

This size, while still portable, is larger than the ideal diagnostic tool, but acceptable for an initial prototype. Starting with a larger size provides the ability to ignore miniaturization issues while the core technology is worked out. The walls are 1.5 mm thick, with internal ribs to provide an optimized strength to material volume ratio. Nut captures were also designed into the printed enclosure to ease assembly. All through-wall connections are sealed using gaskets and O-rings. Compact liquid and air tight cord grips were used as vias for the wiring. A miniature through-wall fitting with a 1/4" NPT pipe connection was used for the inlet to the pressure sensor.

Three flanges were designed to mount the projector (Fig. 5-24), camera (Fig. 5-25), and seal (Fig. 5-26) to the enclosure. The camera and seal flanges were 3D printed, while the projector flange served a dual purpose as a heat sink and mounting bracket, so it was CNC'd from 6061-T6 aluminum. Custom gaskets for each of the flanges were water jet from 1/16" compressible nitrile rubber.
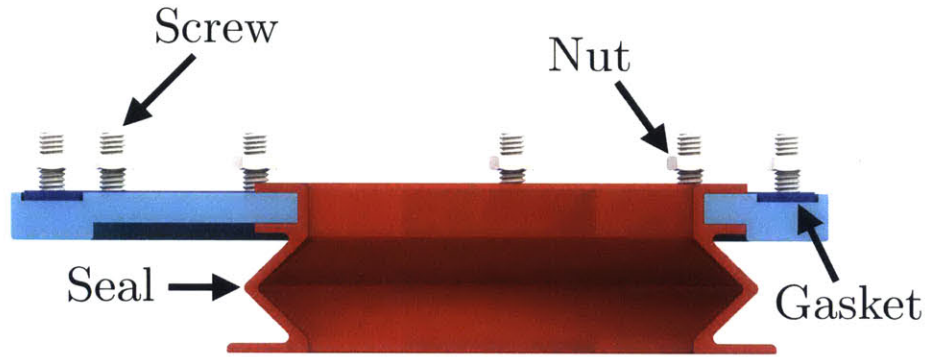
Figure 5-26: Cross-section of seal mount

Ten 18-8 stainless steel 8-32 screws with built-in silicone o-rings are used to mate the projector flange to the enclosure. Three additional 18-8 stainless steel 10-32 screws, equidistantly circumferentially spaced, are used to attach the projector to the flange. These screws are preloaded with a spring to allow for a slight angular adjustment of the projector lens direction once it is mounted to the enclosure, while still maintaining an airtight seal. Eight 18-8 stainless steel 1/4"-20 screws with built-in silicone o-rings hold the camera flange. Twelve 18-8 stainless steel 8-32 screws with built-in silicone o-rings hold the seal flange.

Additionally, a PCB cover was 3D printed to protect the exposed electronics. All wiring was fixed to the enclosure to provide strain relief. Silicone sealant was applied to all of the interfaces to ensure the junctions were airtight, while not permanently fixing the device allowing it to be taken back apart. The ring light is fixed concentric to the camera using magnets and the handle is a simple threaded spacer stock with neoprene rubber cover.

After complete assembly, the ability of the enclosure to maintain a constant pressure was evaluated by sealing the aperture, running the pump for twenty seconds and then sampling the pressure every 0.1 seconds for another twenty seconds. Under these conditions, the enclosure is able to hold a constant pressure moderately well, losing approximately 0.25 mbar every second. This is acceptable because the data

133
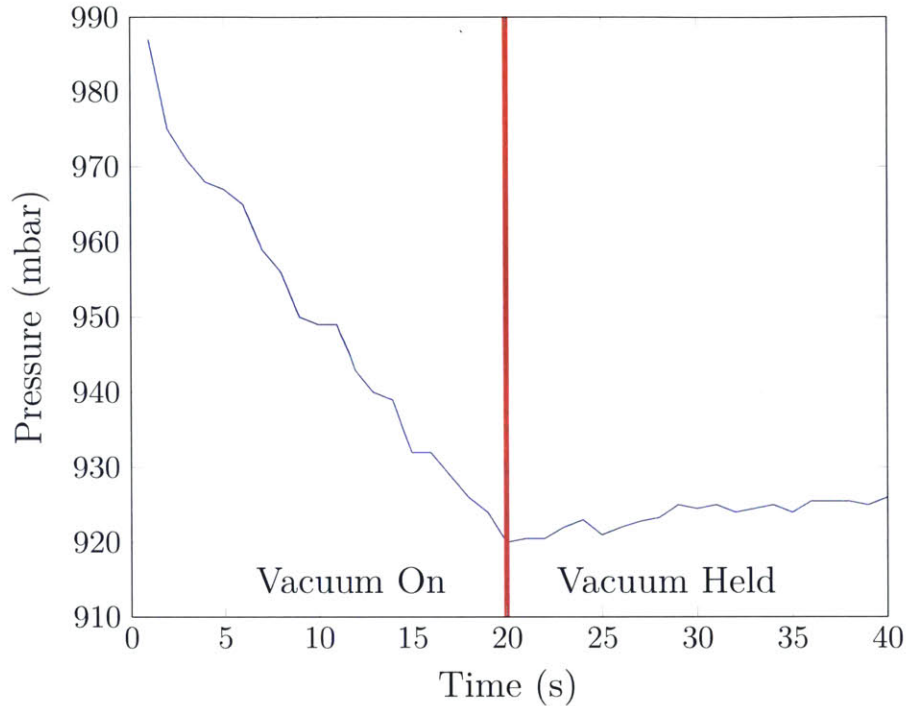
Figure 5-27: The enclosure is able to hold a constant pressure moderately well, losing approximately 0.25 mbar every second

acquisition at a given pressure will happen in less than a second, resulting in minimal error.

5.3.2 System Controller

The lighting system, vacuum pump, and pressure sensor communicate with a PC using Treehopper, a USB-based open-source platform for connecting computers, smartphones, and tablets to electronics for signal acquisition, control, and interfacing [223]. Running treehopper firmware allows MATLAB to directly control the microcontroller. This was advantageous as the rest of the data processing is also performed using MATLAB.

A custom circuit board was designed to integrate the Treehopper platform with a constant-current high-brightness LED driver and power control electronics for the vacuum pump and ring light. The custom circuit board, referred to as the interface
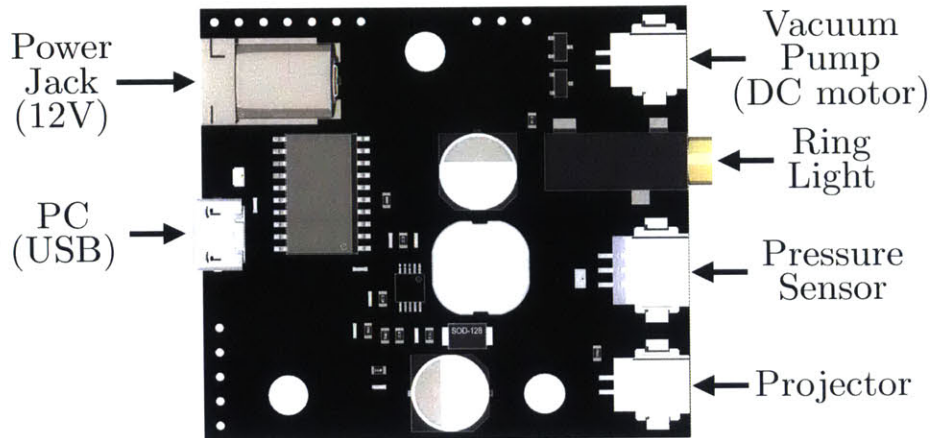
Figure 5-28: PCB connections

module, can be seen in Fig. 5-28. A schematic of the control loop between the interface module, PC, and peripherals is shown in Fig. 5-29.

The primary integrated circuit on the interface module is a PIC16F1459 microcontroller. This microcontroller was selected to communicate with PC using USB to control the vacuum pump, projector, and ring light as well as read the button and pressure sensor inputs. A PIC16F can only source or sink 25 mA of current, so the high-current vacuum pump and ring light are controlled through a low-side switch MOSFET. A constant-current boost converter is used to drive the 350 mA projector LED (with an approximate forward voltage of 26.7 V) from a 12 V wall wart supply.

Additional features were added to the design to ensure the pressure readings are accurate and repeatable. The internal 10-bit ADC of the microcontroller is referenced to the 5 V USB supply rail, which can vary between 4.75 – 5.25 V and still be compliant with USB specifications. The ADC will also clip in V_{in} exceeds V_{supply}, therefore, the ADC's value is formulated as:

$$\text{ADC} = \min\left(\frac{V_{in}}{V_{supply}}, 1\right) \times 1024 \qquad (5.48)$$

The pressure sensor, however, outputs absolute voltages that are always relative to its internal 5V precision reference. It has a pressure P range of 0 to 1 bar, corre-

135
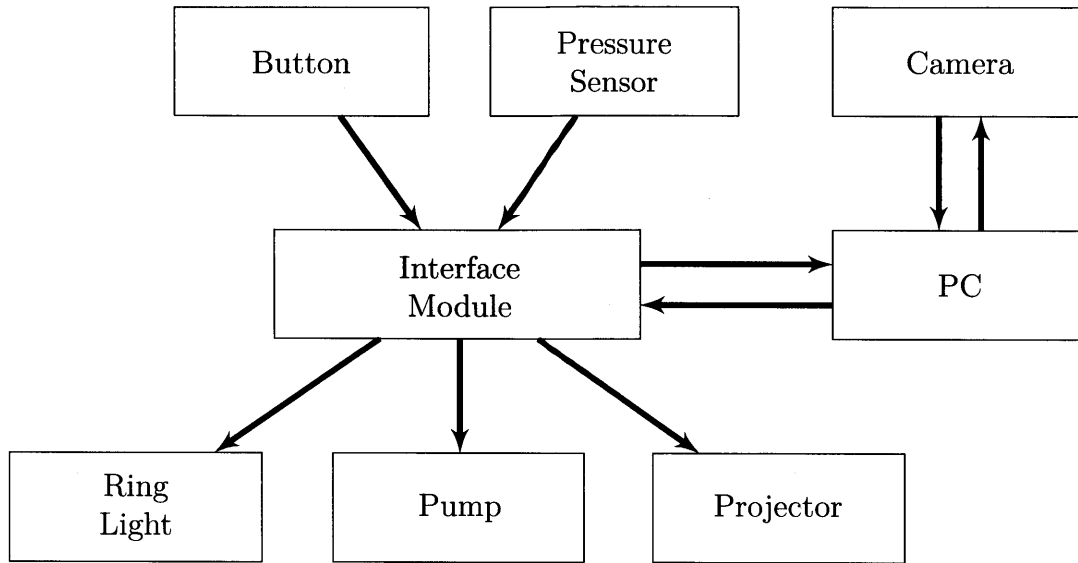
Figure 5-29: Interface module control loop

sponding to a 0–5 volt output, i.e.:

$$V_{\text{pressure}} = 5P \qquad (5.49)$$

Therefore, the ADC value obtained for a given P (in bar) is:

$$\text{ADC}_{\text{pressure}} = \min\left(\frac{5P}{V_{\text{supply}}}, 1\right) \times 1024 \qquad (5.50)$$

As can be seen, the ADC reading relies not only on P (pressure, in bar), but also on V_{supply}; however, V_{supply} is unknown. Also note that if V_{supply} is less than 5 V, the ADC can clip for values of P close to ambient pressure. Both problems must be addressed to minimize variability in the pressure readings.

To address the first problem, V_{supply} must be determined. The control board measures V_{supply} indirectly by obtaining an ADC reading of a precision 3.3V Zener reference. That is:

$$\text{ADC}_{\text{zener}} = \min\left(\frac{3.3}{V_{\text{supply}}}, 1\right) \times 1024 \qquad (5.51)$$

136

Since it is assumed that $V_{\text{supply}} > 3.3$, then:

$$\text{ADC}_{\text{zener}} = \frac{3.3}{V_{\text{supply}}} \times 1024 \tag{5.52}$$

$$V_{\text{supply}} = \frac{3.3}{\text{ADC}_{\text{zener}}} \times 1024 \tag{5.53}$$

The measured V_{supply} is substituted back into the original equation to correct for supply voltage inaccuracies.

To address the problem of clipping, a voltage divider is introduced between the pressure sensor and the ADC pin to scale down the pressure sensor's output to a value safely less than V_{supply}. The output of a voltage divider is:

$$V_{\text{out}} = \frac{R_2}{R_1 + R_2} V_{\text{in}} \tag{5.54}$$

so, integrating both of these into the original equation yields:

$$\text{ADC}_{\text{pressure}} = \min\left(\frac{R_2}{R_1 + R_2} \frac{5P}{\frac{3.3}{\text{ADC}_{\text{zener}}} \times 1024}, 1 \right) \times 1024 \tag{5.55}$$

R_1 and R_2 can be selected to guarantee the voltage from the pressure sensor never exceeds V_{supply} (which has a minimum of 4.75 V), so that the ADC never clips, thus:

$$\text{ADC}_{\text{pressure}} = \frac{R_2}{R_1 + R_2} \frac{5P \times \text{ADC}_{\text{zener}}}{3.3} \tag{5.56}$$

5.3.3   System Flow

The procedural flow for a typical use case of LesionAir will now be presented. The high level physical steps that occur are shown in Fig. 5-30.

For preparation, a suspect lesion must be identified and the region to be measured is sanitized. Initial patient demographics and lesion data are recorded. A timestamp along with patient information (patient identification code, age, sex, ethnicity, skin tone) and lesion information (location, type) are all recorded. For a clinical trial, the

137

patient information is associated with an anonymous patient identification code so the patient cannot be personally identified.

The device is then placed against the skin, centered over the region of interest. The device acquires data and is then removed. This data acquisition process is completed twice — once for the lesion and once for assumed healthy tissue on a region of the body symmetric to the location of the lesion. The lesion and no lesion regions will be compared for a relative stiffness measurement. A relative measurement removes the boundary condition effects that are caused by the seal. After data acquisition, the results are analyzed with the demographic data to produce a diagnosis and elasticity mapping of the lesion.

Both the data acquisition and data processing function blocks are processes that are implemented in software using MATLAB scripts. MATLAB is able to control the hardware according to the software architecture diagram shown in Fig. 5-31.

5.3.3.1   Data Acquisition

A flow map of the data acquisition process is shown in Fig. 5-32. This process is implemented using a graphical user interface (GUI) so the user can view the camera view, as well as the stage of operation.

Acquisition begins with an initialization of the camera and interface control module, along with setup of a directory where the data will be saved. Once completed, the ring light is turned on so the user can see the view of the camera. The GUI asks the user to center the device over the region of interest and to press the button when ready. The script waits until the button is pressed.

Once the button is pressed, the ring light turns off and an image capture sequence begins. For each image capture sequence, the current pressure is recorded, then the projector is turned on, a structured light image is recorded, the projector is turned off. Then the ring light is turned on, a visible light image is recorded, and the ring light is turned off.

LesionAir is set to capture images for the pressures of 0–100 mbar in 20 mbar increments. After image acquisition the pump is turned on until the pressure is

138

decreased 20 mbar and the image acquisition cycle begins again. This is repeated until data is captured for all pressure levels.

When finished, the data is saved and all images are presented for review. If any errors in the images are located by the user, the data acquisition process can be repeated.

5.3.3.2 Data Processing

The data is processed according to the flow map shown in Fig. 5-33. The initial visible light image is segmented to differentiate the lesion from surrounding tissue using filtering and dynamic localized thresholding. The ABCDs are quantified using the algorithms described in Section 5.1.4.2.

Next, the tissue stiffness map is generated. For each set of structured light images, the projected pattern is differentiated from the background tissue using filtering and dynamic localized thresholding. The keypoints of the light pattern is ordered using the algorithm described in Section 5.1.3.2. The camera and projector calibration matrices are then used to triangulate and create sparse reconstructions of the scene. The sparse reconstruction point clouds are then bicubically interpolated to surfaces. Because bicubic interpolation does not handle discontinuous, limited-domain data, the surfaces must be carefully cropped in to provide accurate data.

Once the structured light images are converted into surfaces, the stiffness quantification process can begin. The ambient pressure surface for the lesion and symmetric healthy region are loaded and used as a reference for the other measurements. The next surfaces and corresponding pressure are then loaded and the pressure differential is calculated.

The script determines the overlapping data region between all of the images and crops any data outside of this region. The surfaces can only be compared where there the data is known. At high pressures, and consequently high strains, the tissue is deformed significantly, so only a small part of the high pressure surface overlaps with the original undeflected surface, causing the map to shrink.

139

Stiffness is determined by dividing the pressure differential by the calculated surface displacement. The pressure differential for the lesion and non-lesion images will be slightly different, so this conversion normalizes the values so they can be compared. While not a true Young's modulus value, the normalized stiffness is a relative metric created specifically for this study. Tissue elasticity is proportional to the normalized stiffness. The stiffness is further normalized to remove boundary condition effects by comparing the lesion stiffness map to the non-lesion stiffness map.

The elasticity of the lesion can be qualitatively compared with the healthy surrounding tissue through analysis of the normalized stiffness map. ABCDs, stiffness, and demographics can all be input into a classification algorithm for diagnostic information. This information can be used instantly to assist with diagnosis. Or it can be stored and compared to a later measurement to determine if the lesion is evolving, and therefore, potentially cancerous.

Preparation	Lesion is located and region is sanitized
Data Input	Initial patient and lesion data is recorded
Device Placement	Device is centered over the region of interest and preloaded against the skin
Data Acquisition	Data collection details in Fig. 5-32
Data Processing	Data processing details in Fig. 5-33
Device Removal	Device is removed
Skin and device contact pad are sanitized
Review Results	Output = diagnostic information from classification algorithm and mapping information from normalized stiffness maps

Figure 5-30: Procedural flow chart

```
┌─────────────────────────────────────────────────────┐
│                      MATLAB                          │
│                    user code                         │
└─────────────────────────────────────────────────────┘

┌──────────────────────┐      ┌──────────────────────┐
│      Treehopper       │      │    MATLAB Image       │
│    MEX interface      │      │  Acquisition toolbox  │
└──────────────────────┘      └──────────────────────┘

┌──────────────────────┐      ┌──────────────────────┐
│      Treehopper       │      │  GigE Vision hardware │
│    C/C++ library      │      │    support package    │
└──────────────────────┘      └──────────────────────┘

┌──────────────────────┐      ┌──────────────────────┐
│    LibUSB userspace   │      │        GigE           │
│      USB driver       │      │   ethernet driver     │
└──────────────────────┘      └──────────────────────┘

┌──────────────────────┐      ┌──────────────────────┐
│   Treehopper firmware │      │   Manta G-145 GigE    │
│  running on PIC16F1454 │      │    camera firmware    │
└──────────────────────┘      └──────────────────────┘
```
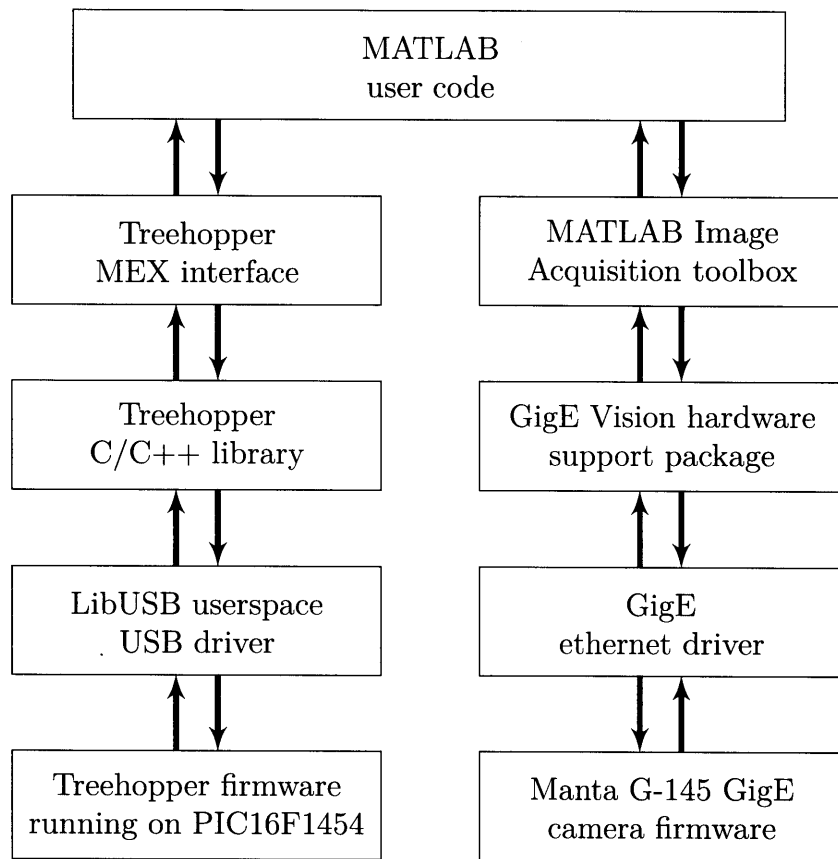
Figure 5-31: Software architecture diagram

Initialization

```
┌──────────────┐     ┌──────────────┐     ┌──────────────┐
│    Input     │────▶│    Setup     │────▶│ Initialize & │
│   user ID    │     │   file I/O   │     │  configure   │
│              │     │              │     │  Treehopper  │
└──────────────┘     └──────────────┘     └──────────────┘
                                                  │
                                                  ▼
┌──────────────┐     ┌──────────────┐     ┌──────────────┐
│ Tell user to │     │   Turn ON    │     │ Initialize & │
│ center device│◀────│  ring light  │◀────│  configure   │
│   over ROI   │     │              │     │    camera    │
└──────────────┘     └──────────────┘     └──────────────┘
        │
        ▼
   ◇ Button
No ◀ Pressed?
        │ Yes
        ▼
┌──────────────┐
│   Turn OFF   │
│  ring light  │
└──────────────┘
```

Image Acquisition

```
┌──────────────┐     ┌──────────────┐     ┌──────────────┐     ┌──────────────┐
│  Begin new   │────▶│    Record    │────▶│  Structured  │────▶│Structured light│
│ acquisition  │     │   pressure   │     │  light ON    │     │image capture │
│  iteration   │     │              │     │              │     │              │
└──────────────┘     └──────────────┘     └──────────────┘     └──────────────┘
                                                                      │
┌──────────────┐     ┌──────────────┐     ┌──────────────┐     ┌──────────────┐
│     Ring     │     │ Visible light│     │     Ring     │     │  Structured  │
│  light OFF   │◀────│image capture │◀────│   light ON   │◀────│  light OFF   │
└──────────────┘     └──────────────┘     └──────────────┘     └──────────────┘
```

```
   ◇ Done
   with all ──Yes──▶ ┌──────────┐ ───▶ ┌──────────────┐
   iterations?       │   Save   │      │ Present images│
        │            │ all data │      │  for review  │
        │ No         └──────────┘      └──────────────┘
        ▼
┌──────────────┐
│   Turn ON    │
│    pump      │
└──────────────┘
        │
        ▼
   ◇ Pressure
No ◀ decreased
   20 mbar?
        │ Yes
        ▼
┌──────────────┐
│   Turn OFF   │
│    pump      │
└──────────────┘
```

Figure 5-32: Computational flow chart – Data acquisition

143

Morphology Quantification

Load initial visible light image → Segment image → Determine ABCD metrics

Scene Reconstruction

Load structured light images → Segment images → Order keypoint centroids

Point cloud to bicubic interpolated surface ← 3D Reconstruction ← Establish point correspondences

Load ambient pressure lesion & no lesion surface

Stiffness Quantification

Begin next pressure iteration → Load next pressure lesion & no lesion surface → Calculate ambient & current pressure difference

Normalize stiffness $\left(\frac{Lesion}{No\,Lesion}\right)$ ← Determine stiffness $\left(\frac{\Delta P}{\Delta z}\right)$ ← Determine overlapping data region & crop

Adjust data for angular bias

Plot normalized stiffness map
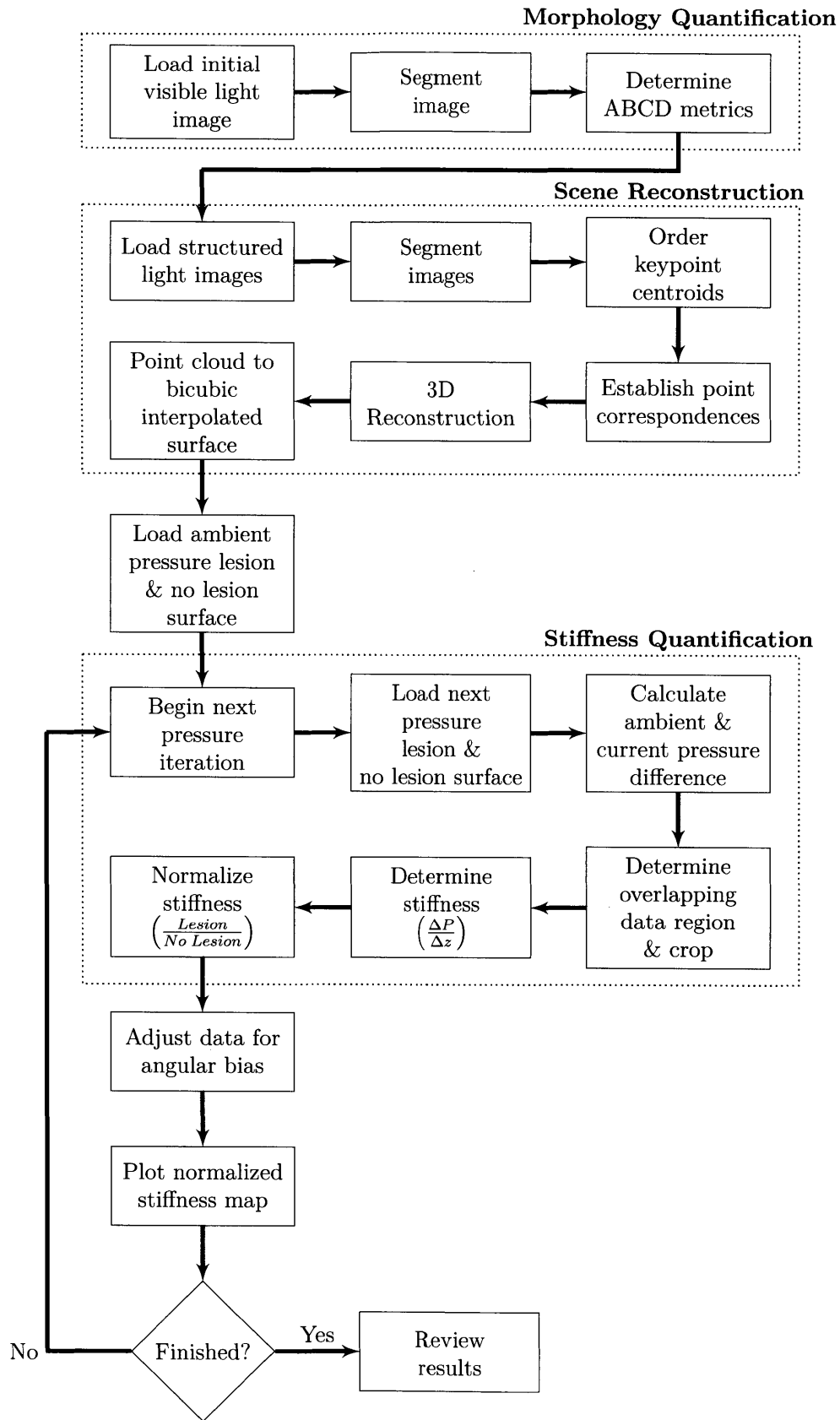
Finished? — Yes → Review results

No

Figure 5-33: Computational flow chart – Data Processing

144

Chapter 6

Design Evaluation

To investigate the efficacy of LesionAir, a series of tests were performed. Benchtop experiments were used to evaluate the measurement accuracy, then the system accuracy was quantified on a characterized object. Finally, an initial validation of the prototype was completed in a human clinical trial.

6.1 Structured Light Performance

To determine the accuracy and repeatability of the structured light reconstruction, the surfaces of a billiards ball and precision ground flat plate were measured using a benchtop experimental setup.

6.1.1 Accuracy

Accuracy was determined by comparing the results of the reprojection depth map to Coordinate Measuring Machine (CMM) results. A precise curved surface (billiard ball) and a precise flat surface were both measured to gauge the extremes. The results of the structured light billiards ball and precision ground flat plate measurements are shown in Table 6.1. It can be seen that the curved surface has slightly more error than the flat surface, but both values are still extremely accurate, especially considering the low cost of implementation.

Table 6.1: Structured light accuracy on a billiard ball and a precision ground flat plate

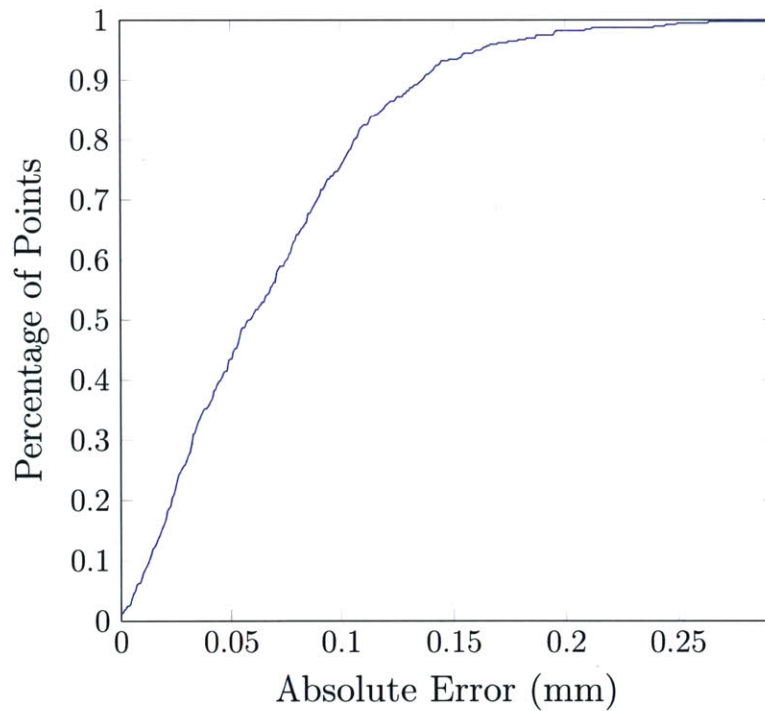| Accuracy	Billiard Ball	Precision Ground Flat Plate
Maximum error (mm)	0.293	0.282
Mean absolute error (mm)	0.068	0.047
RMS error (mm)	0.085	0.062
Standard deviation (mm)	0.051	0.041

Figure 6-1: Cumulative distribution function of a billiard ball

A billiard ball was chosen as a precise curved reference surface. Billiard balls are manufactured according the World Pool Billiards Association standard [224], with a diameter of 57.15 mm, plus or minus 0.127 mm. This roundness was verified by a Zeiss CMM to not deviate by more than 0.025 mm.

The results of the structured light billiard ball measurement are visualized in Fig. 6-1 and 6-2. The maximum measured error was 0.293 mm, RMS error was 0.085 mm, and standard deviation was 0.051 mm. The cumulative distribution function of these
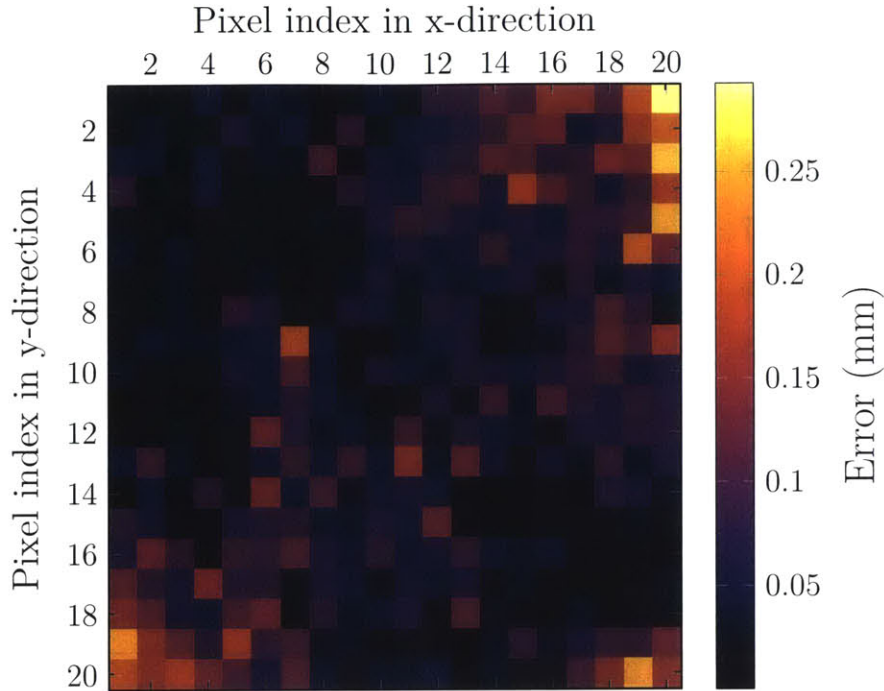
Figure 6-2: Error heat map for structured light on a billiard ball

results reveals that approximately 50% of the data points have less than 0.05 mm error and 90% of the points have less than 0.15 mm of error.

The heat map highlights the areas in the measured region that are more prone to error. The bottom left and top right of the mapping are localized regions of increased error. This is likely due to the distortion effects of the lens. The calibration procedure that was used is able to quantify lens distortion, but the distortion values were not accounted for in the reconstruction.

An aluminum plate, that is precision ground and parallel to within 0.127 mm, was used as the flat surface. The maximum measured error was 0.282mm, RMS error was 0.062mm, and standard deviation was 0.041mm. The cumulative distribution function of these results is better than the billiard ball, with approximately 90% of the points with less than 0.1 mm of error.

The heat map of the measurement accuracy of the flat plate is similar to the billiard ball, with less pronounced localized regions of increased error in the bottom left and top right. This provides further evidence that the error is likely due to the lens distortion and can be amplified depending on the measured surface contour.
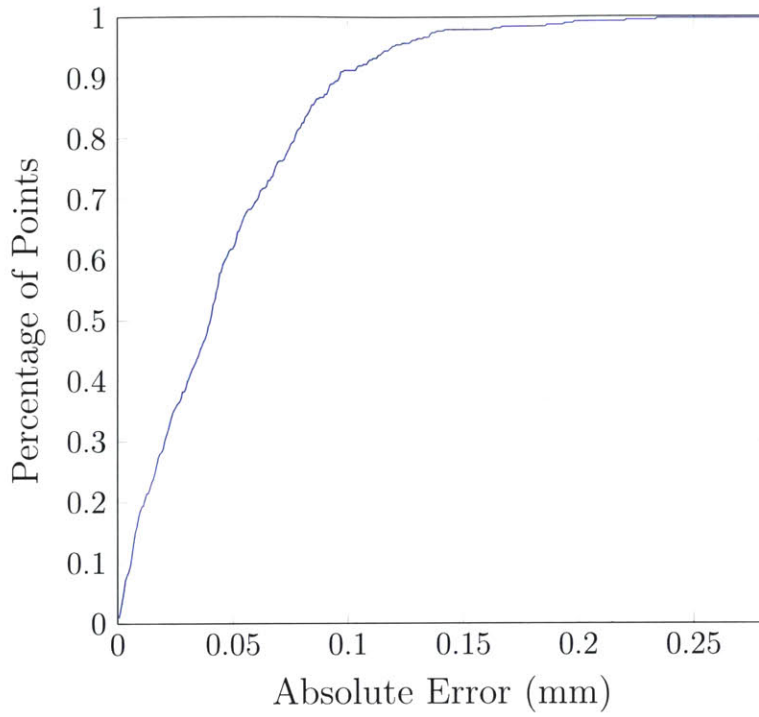
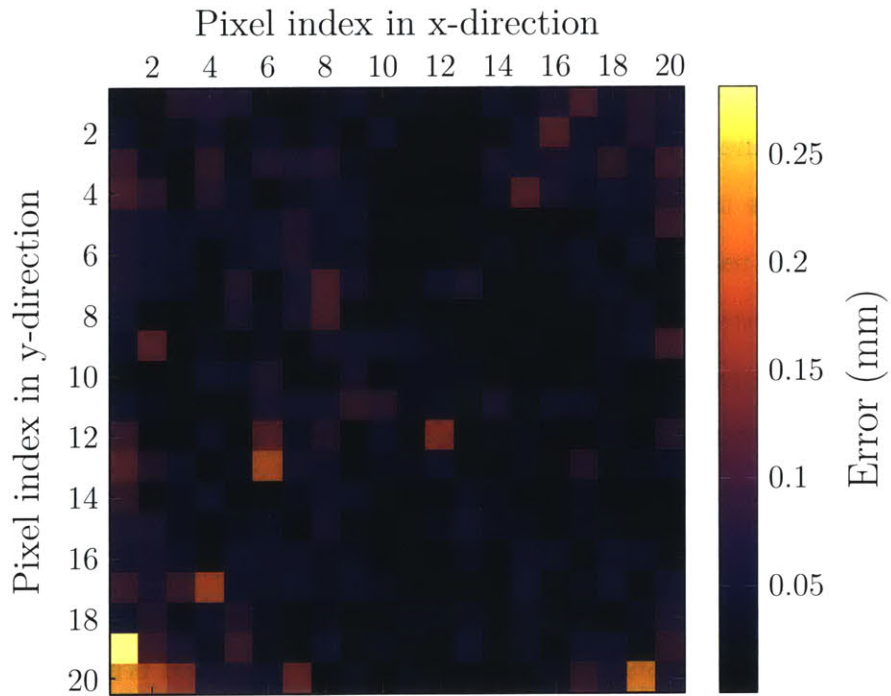Figure 6-3: Cumulative distribution function of a precision ground flat plate

Figure 6-4: Error heat map for structured light on a precision ground flat plate

Table 6.2: Structured light repeatability

Repeatability	X	Y	Z	Magnitude
Maximum deviation (mm)	0.023	0.034	0.026	0.027
Average deviation (mm)	0.009	0.017	0.011	0.011
Standard deviation (mm)	0.004	0.004	0.004	0.004

6.1.2 Repeatability

Repeatability was quantified by measuring the same surface ten different times with a delay between the measurements. The device and measured object were rigidly fixed so they wouldn't move between measurements. The measured object was again the precision ground flat plate. The time delay between all ten measurements was ten seconds.

The results of the repeatability experiment are shown in Table 6.2. The maximum and average deviation in the three principle Cartesian directions was quantified, along with the total magnitude of deviation. The total average deviation was 0.0112 mm with a maximum deviation of 0.0274 mm. Again, the results are determined to be extremely good and acceptable for the application.

6.2 Viscoelastic Response

Using the LesionAir setup, a typical viscoelastic response of tissue was quantified to validate the assumption that viscoelastic effects could be negated in the analysis.

For data collection, the device was placed on the abdomen of a patient, the pump was turned on and monitored until it reached the set point pressure, then the pump was turned off and the vacuum was held while the pressure was sampled every 0.1 seconds.

Two set point pressures were evaluated: 25 mbar (Fig. 6-5) and 50 mbar (Fig. 6-6). The structured light reconstruction was used to determine the maximum deflection
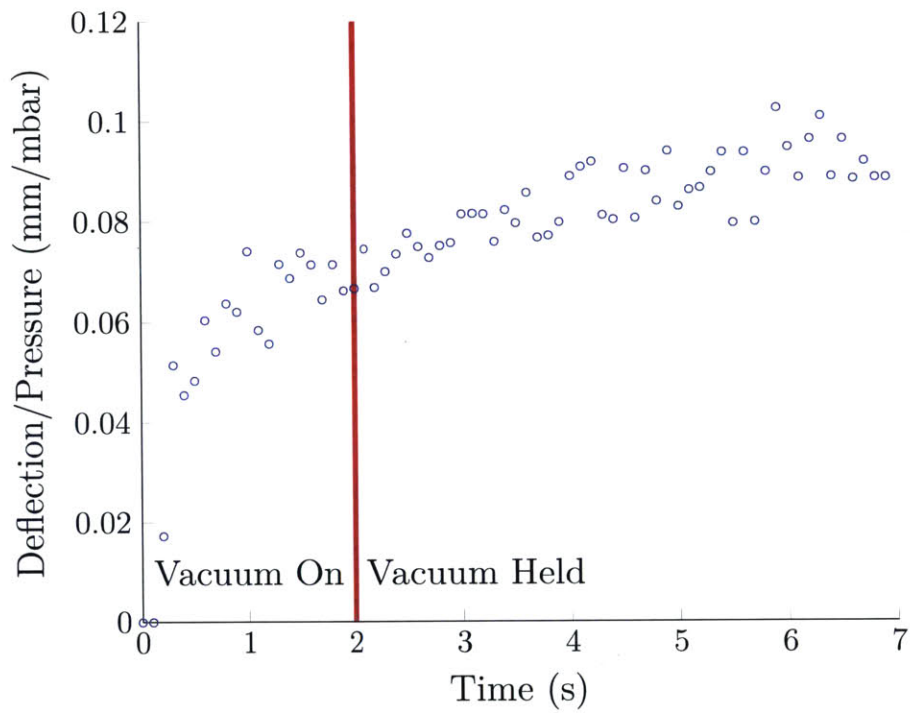
Figure 6-5: Viscoelastic response – tissue creep from 25 mbar negative pressure
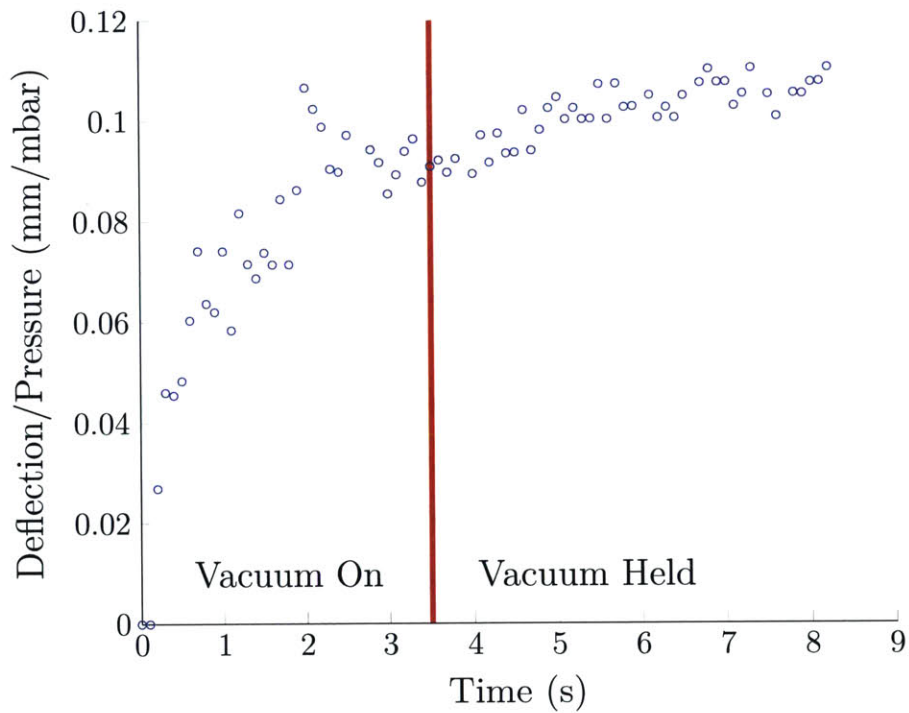

Figure 6-6: Viscoelastic response – tissue creep from 50 mbar negative pressure

(at the center). Deflection was normalized with pressure to account for any leakage that may occur.

As expected, the tissue exhibits characteristic viscoelastic effects; as the pressure is held, the tissue starts to creep, such that deflection increases for a given pressure. As the tissue relaxes over five seconds, the amount of deflection per unit of pressure increases approximately 0.02 mm/mbar, equating to 0.004 mm/mbar/sec. At the maximum applied pressure of 100 mbar, this equates to 0.4 mm of creep per second.

LesionAir is able to nullify this effect by minimizing the time required to take the series of visible and structured light images. As soon as the pressure set point is reached, the device takes both images, starting with the structured light images since the measurements derived from these images are tied directly to the pressure value.

6.3 Phantom Simulation

FEA was performed to predict how the phantom model would deform. The measured properties (Table 5.7) and dimensions (Table 5.6) were used to form custom materials within ANSYS 16.0. A pressure ramped from 0 to 100 mbar was applied to a 6 cm diameter area, replicating the conditions used with the experimental measurement device, LesionAir.

The FEA provided an evaluation of the difference in deflection for a model with and without a lesion, as shown in Table 6.3. The center deflection at full pressure for a phantom model with an exposed and embedded lesion is 10.67 and 9.97 mm, respectively, versus a model without a lesion at 9.98 mm, resulting in a 6.9% and 0.79% difference. The reduced deflection for the embedded case is unexpected, but likely caused by the overly stiff epidermis model.

The phantom models were also measured five times using LesionAir. The average device measurement deviated from the FEA results by 10.0%, 57.8%, and 18.6% for the models with an exposed lesion, embedded lesion, and without a lesion, respectively. The larger error for the embedded phantom model is likely due to a couple of factors. The FEA measured deflection for the embedded case was much lower than

151

Table 6.3: Maximum deflection percent difference for lesion vs. no lesion of phantom models

Pressure (mbar)	No Lesion Max Deflection (mm)	Exposed Lesion Max Deflection (mm)	Percent Difference	Embedded Lesion Max Deflection (mm)	Percent Difference
20	2.71	2.78	2.66%	2.69	-0.79%
40	5.07	5.29	4.44%	5.04	-0.47%
60	7.00	7.39	5.64%	6.98	-0.30%
80	8.61	9.16	6.39%	8.59	-0.22%
100	9.98	10.67	6.91%	9.97	-0.17%

Table 6.4: Average difference between experimentally measured results and FEA of phantom models

	Average Difference (%)
No Lesion	18.6
Exposed Lesion	10.0
Embedded Lesion	57.8

expected and the fabrication process did not securely bond the embedded lesion to the epidermal and dermal layers surrounding it, causing an increase in error.

Full-field normalized stiffness maps were also created for the exposed and embedded phantom models. Qualitative analysis of the stiffness maps clearly shows a stiffer mass in the center of the image. The mass has an approximate diameter of 1.5 cm, matching the specification.

These results verify that the device is able to successfully map variations in stiffness and that the stiffness map can be used to identify the boundaries of a lesion.
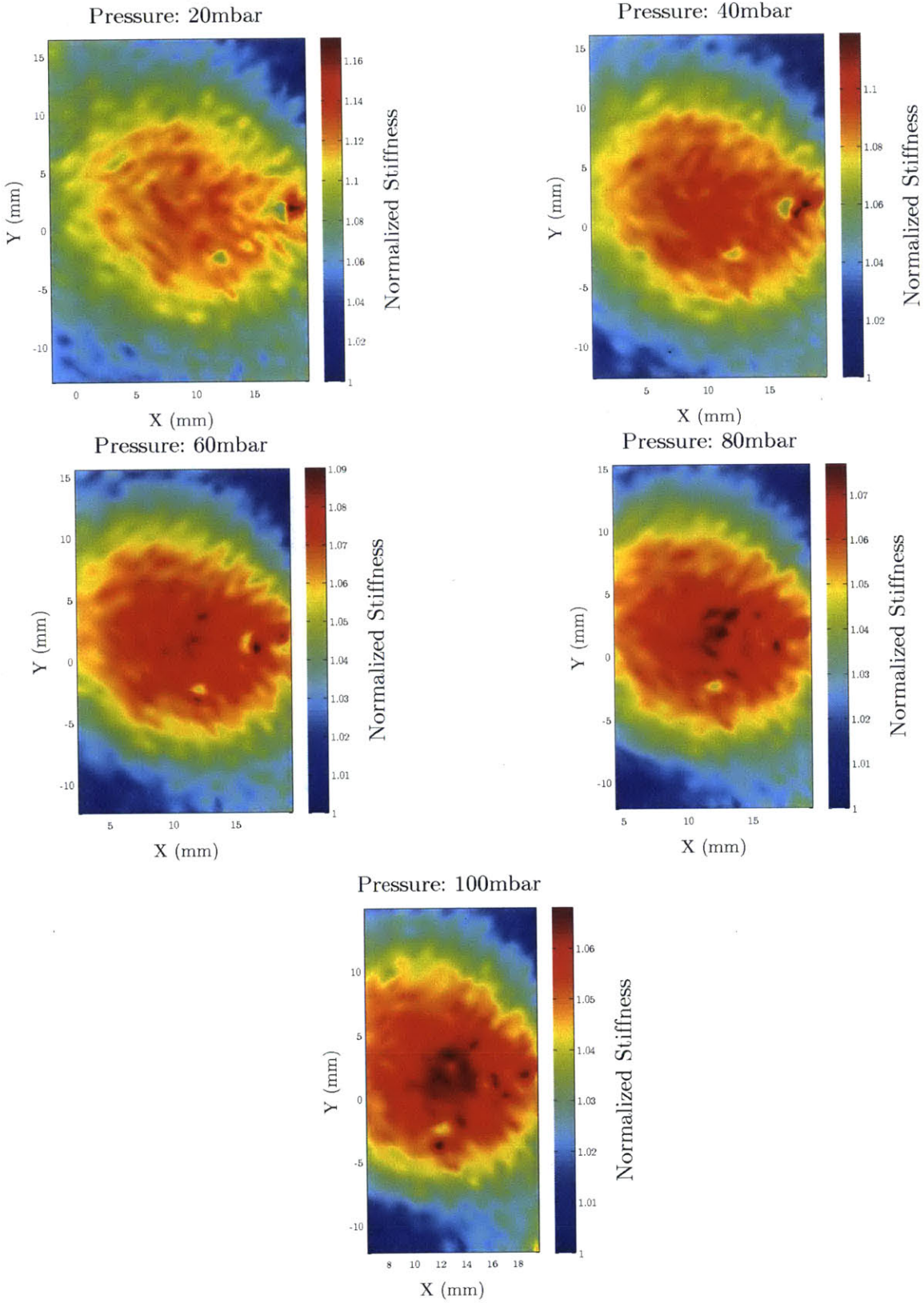
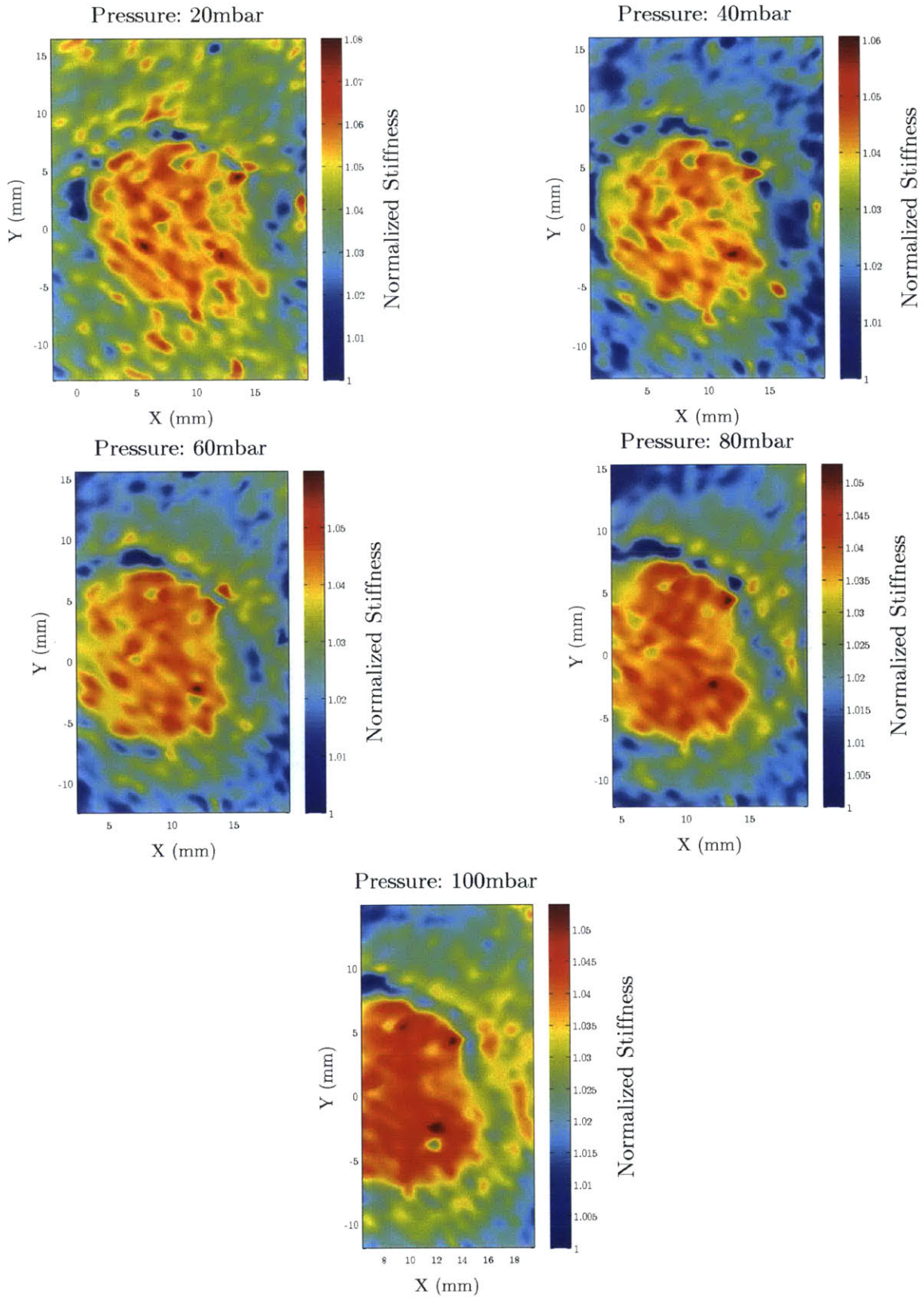Figure 6-7: Normalized stiffness maps of the phantom tissue model with an embedded lesion

153

Figure 6-8: Normalized stiffness maps of the phantom tissue model with an exposed lesion

154

6.4 LesionAir Proof of Concept in Human Studies

LesionAir was clinically tested with ten patients over the course of two separate weeks in a proof of concept study at the Dermatology Laser Center in San Marcos, Texas. The general design of the study was to identify patients with potentially malignant lesions and to assess those lesions prior to biopsy or excision. Along with the standard of care, excised lesions were subjected to histopathological review by generating hematoxylin/eosin slides and having a diagnosis rendered by a dermatopathologist.

Additionally, the histological sections of excised lesions were further evaluated by comparing them to the results produced LesionAir. Half of the patients tested were chosen specifically for having benign lesions. The benign lesions were also examined using LesionAir, but in keeping with the medical standard of care, these patients were not subjected to lesion excision and histopathological analysis.

6.4.1 Human Study Overview

The clinical protocol used to perform testing with LesionAir was approved by the Committee on the Use of Humans as Experimental Subjects (COUHES) at the Massachusetts Institute of Technology. The study was approved under COUHES Protocol No. 1511310864 and the device was determined to be a non-significant risk. The protocol approval and consent form can be found in Appendix B.

All participants were properly trained and validated to ethically and professionally work with human subjects in medical research. A trained dermatologist working in a high-volume general medical and surgical dermatology clinic would identified potential patients to participate in the study. Patients were selected from those individuals who presented for routine dermatologic visits. During the clinical visit, patients with potentially cancerous skin lesions were offered the opportunity to participate in the clinical study. The patients who elected to participate were properly informed, and those wishing to participate were properly consented prior to initiation of LesionAir device use.

Table 6.5: Clinical trial patient synopsis

ID #	Date	Age	Sex	Ethnicity	Skin Type	Diagnosed Lesion Type	Lesion Location	Pathology Results
001	1/14/16	86	F	White	II	SCC/AK	R Top Forearm	Squamous Cell Carcinoma
002	1/15/16	60	M	White	I-II	BCC	R Jaw	Malignant Melanoma 3 mm Breslow's Depth
003	1/15/16	86	M	White	I-II	BCC	R Medial Mid-Back	Basal Cell Carcinoma
004	1/15/16	62	M	White	II-III	SCC/AK	R Top Wrist	Squamous Cell Carcinoma
005	3/1/16	25	F	Hispanic	IV	Intradermal Nevus	R Lateral Torso	N/A
006	3/2/16	72	M	White	II	Seborrheic Keratosis	R Medial Knee	N/A
007	3/2/16	21	M	White	II	Macular Congenital Nevus	R Upper Back	N/A
008	3/3/16	82	M	White	I-II	Intradermal Nevus	R Medial Mid-Back	Intradermal Nevus
009	3/3/16	50	F	White	I-II	AK	R Upper Back	N/A
010	3/4/16	29	M	White	II	Intradermal Nevus	R Medial Upper Abdomen	N/A

In general, a single trial attempt, using the process described in Section 5.3.3, was made for each lesion. A comparison of data acquired from the lesion was performed on normal skin on the corresponding contralateral side of the patient. Clinical photographs were obtained for each lesion. The normal standard of clinical care was pursued afterwards. This consisted of local anesthesia (1% lidocaine) and sterile excision of the entire malignant lesion with subsequent surgical closure. Specimens were processed with hematoxylin/eosin histological staining for definitive microscopic diagnosis to inform patient management subsequent to surgery.

Lesion analysis was also performed on patients with lesions that were not deemed malignant. Again, owing to the standard of care there was no need for surgical excision of those lesions. Thus, histologic comparison to the data acquired from LesionAir was not possible. A synopsis of patient demographics and lesion information are shown in Table 6.5.

6.4.2   Clinical Testing Results

Ten patients elected to participate in the study. The patients ranged from 21 to 86 years of age. Seven patients were male and three were female. All but one patient was Caucasian. The single non-Caucasian patient was Hispanic. Skin type ranged from Fitzpatrick type I to type III, with the single Hispanic patient being skin type IV.

Seven patients were able to complete the study under the full device cycle. Patient ID 001, 004, and 006 did not complete the full data acquisition process due to a loss of pressure. Table 6.6 presents those patients who completed the full device testing cycle. Included in Appendix C are the comprehensive data sets for all ten patients including: clinical photograph, structured and visible light images, normalized stiffness maps, and strain stiffening plots. Three patients — patient ID 002, 003, and 006 — will now be presented in greater detail.

6.4.2.1   Clinical Presentation and Assessed Stiffness

Patient 002   Patient 002 was a 60-year-old Caucasian male with Fitzpatrick type I-II skin. This patient was new to the clinic and presented for a full skin examination. It was noted that the patient had a lesion along the right jawline measuring approximately 8 to 10 mm in diameter. From the patient history, the patient reported that this lesion was relatively new over the last year.

Clinical examination of the lesion revealed it to be a skin-colored papule with some hyperkeratosis over the center. The lesion felt fairly indurated throughout

Table 6.6: Clinical testing results for fully completed test cycles

ID #	Clinical Diagnosis	Lesion Description	Histological Diagnosis	Strain Stiffening	Calculated Asymmetry	Calculated Border Irregularity	Calculated Color Variation	Calculated Diameter (mm)
002	Basal Cell Carcinoma	Skin-colored dome-shaped papule with hyperkeratosis and mild induration	Amelanotic Malignant Melanoma	+	0.84	0.92	0.12	11.55
003	Basal Cell Carcinoma	Pink, pearly flat plaque with mild induration	Multifocal Nodular Basal Cell Carcinoma	+	N/A	N/A	N/A	N/A
005	Intradermal Nevus	Evenly hyperpigmented thin papule with well-defined borders, soft	No biopsy	-	0.11	0.32	0.18	5.29
007	Congenital Nevus	Evenly hyperpigmented macule with mild border irregularity, normal feel	No biopsy	-	0.17	0.69	0.16	5.55
008	Intradermal Nevus	Skin color elevated papule with well-defined borders, soft	Intradermal Nevus	-	0.35	0.12	0.26	8.48
009	Actinic Keratosis	White sandpaper-like ill-defined papule without underlying induration	No biopsy	-	N/A	N/A	N/A	N/A
010	Recurrent Nevus	Evenly hyperpigmented dome-shaped papule with well-defined borders, mild induration	No biopsy	+	0.17	0.11	0.22	3.31
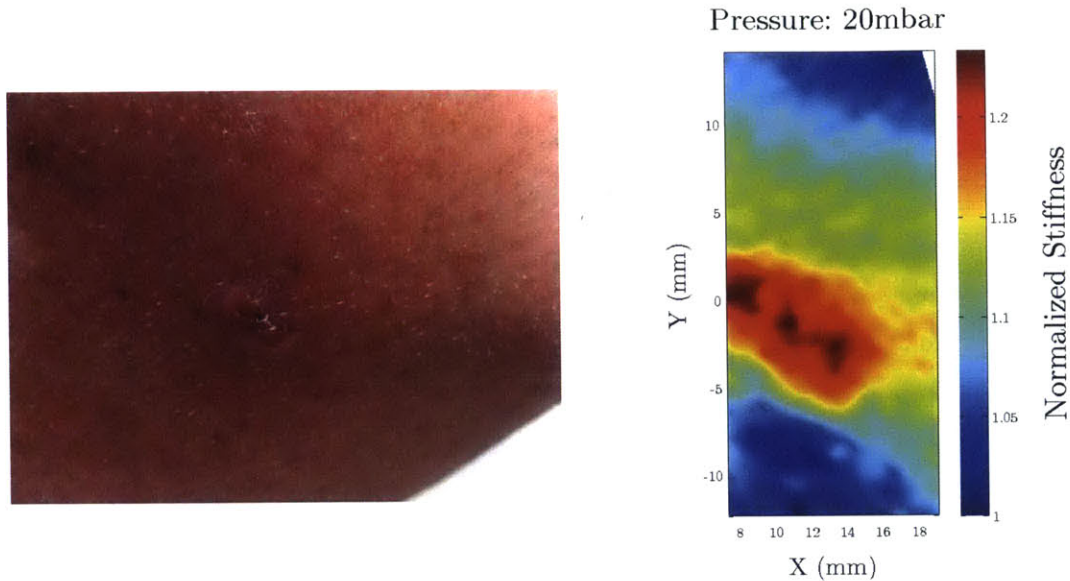
Figure 6-9: Patient 002 – Comparison of the clinical presentation and normalized stiffness map at 20 mbar

without any evidence of hyperpigmentation. The clinical presentation of this lesion was consistent with a basal cell carcinoma.

A comparison of the clinical presentation and the computed normalized stiffness map can be seen in Figure 6-9. The clinical appearance of the lesion is well-defined as shown in the clinical photograph. The normalized stiffness mapping indicates a well-defined region of increased relative stiffness. This increased stiffness is virtually uniform throughout the entire lesion.

Patient 003 Patient 003 was an 86-year-old Caucasian male with Fitzpatrick type I-II skin. The subject was a returning patient to the clinic with a history of numerous basal cell carcinomas. A large lesion was noted on the patient's right back as highly suspect for basal cell carcinoma. The lesion was a plaque of approximately 15 mm in diameter, with a pink pearly color surrounded by slightly tanned skin. The lesion felt significantly indurated with respect to the surrounding normal skin.

In comparison to the clinical photograph, a stiffness map is shown in Figure 6-10. The normalized stiffness map shows a pattern of isolated pockets of relative increased stiffness, with intervening less stiff areas visible within the bulk of the lesion.
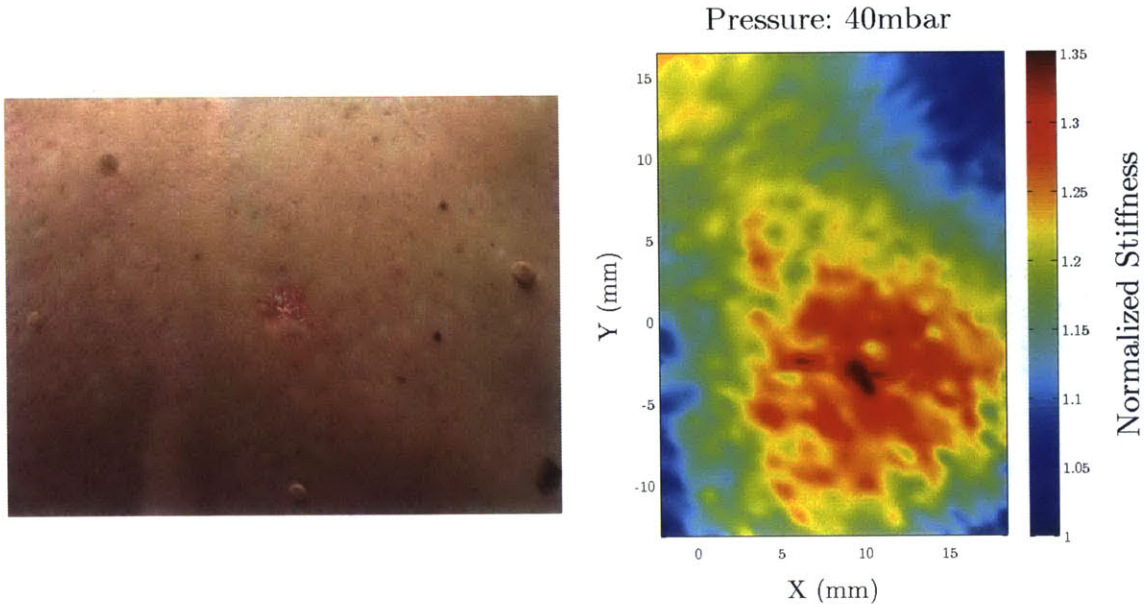
159

Figure 6-10: Patient 003 – Comparison of the clinical presentation and normalized stiffness map at 40 mbar

Patient 005 Patient 005 was a 25-year-old Hispanic female with Fitzpatrick type IV skin. This patient presented with a melanocytic nevus on the right flank. The lesion clinically appeared as a well-defined area of hyperpigmentation. The slightly dome-shaped papule showed significant compliance in comparison with the surrounding skin. This lesion was deemed clinically benign being an intradermal nevus. The comparison of the clinical presentation and normalized stiffness map are shown in Figure 6-11. The stiffness mapping seen on the computer-generated surface surface shows a well-defined area of laxity and compliance.

As can be seen in these three patients, the clinical assessment of lesion palpation was directly reproduced in the computer-generated images of stiffness. In this gross determination of lesion location, LesionAir was able to quantitatively generate the mechanical characteristics perceived by the clinician. Perceptibly harder lesions appeared stiffer and perceptibly softer lesions appeared as less stiff. In addition, analysis of the lesion on patient 003 provided mechanical detail not perceived by palpation (i.e. pockets of stiffness).

160
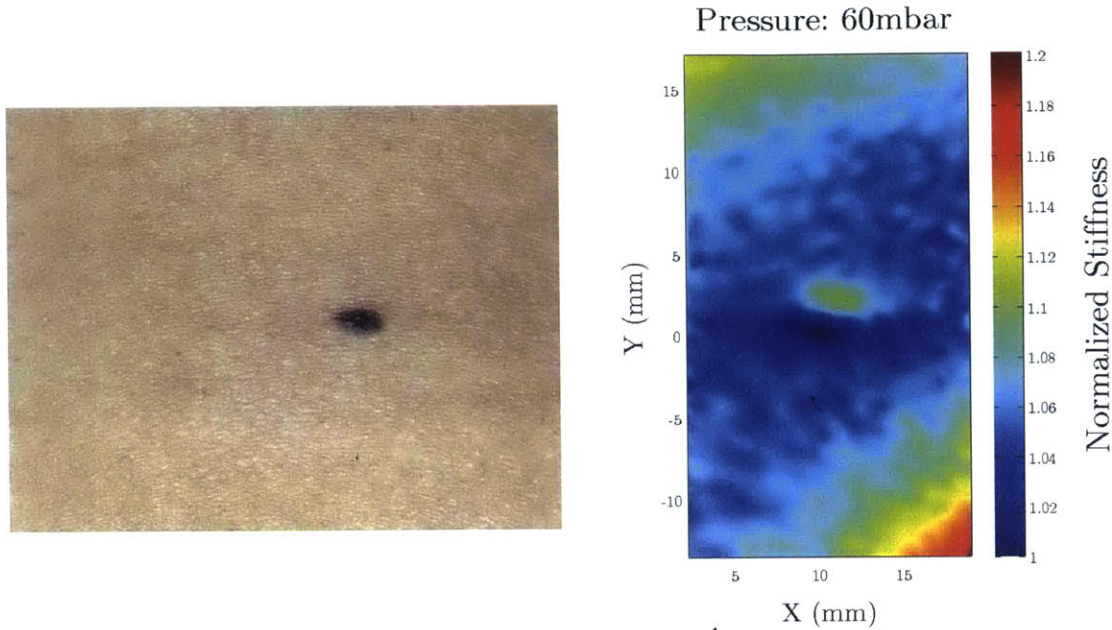
Figure 6-11: Patient 005 – Comparison of the clinical presentation and normalized stiffness map at 60 mbar

6.4.2.2 Excised Lesion Histology, Normalized Stiffness Maps, and ABCD Morphological Assessment

Patient 002   The cancerous lesion from patient 002 provided an interesting nuance to these proof of concept studies. Although the clinical determination correctly identified the lesion as a malignancy, this particular lesion did not have the gross clinical appearance of a melanoma. Clinical suspicion of the pink dome-shaped lesion was most consistent with a clinical diagnosis of basal cell carcinoma.

An examination of the low-power (4X magnification) view of a cross-section through the bulk of the melanoma shown in Fig. 6-12 reveals a large nodular aggregate of malignant melanocytes in the papillary and mid-dermis. Below the epidermis, there are nests, cords, and strands of atypical melanocytes (appearing as dark purple dots) producing sheets of malignant cells that extend deep into the reticular dermis. As with any malignancy, adnexal structures (terminal hair follicles, sweat glands, and oil glands) have been destroyed by the tumor mass.

Fig. 6-13 shows a medium-power view (10X magnification) of the border of the malignancy and the peripheral normal tissue. This image shows the newly formed

Figure 6-12: Patient 002 – Histological cross-section of a large malignant melanoma lesion
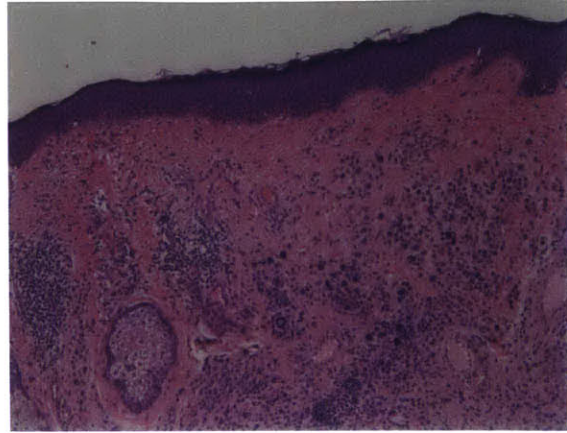

Figure 6-13: Patient 002 – Histological view of malignant melanocytes surrounded by an over-expression of collagen
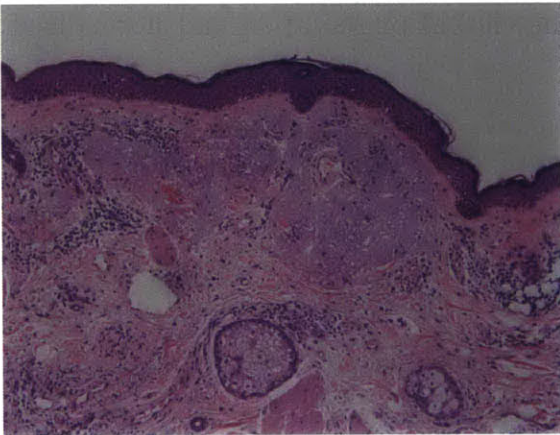

Figure 6-14: Patient 002 – Histological view of solar elastosis in the healthy tissue next to the lesion, demonstrating what typical sun-damaged collagen should look like
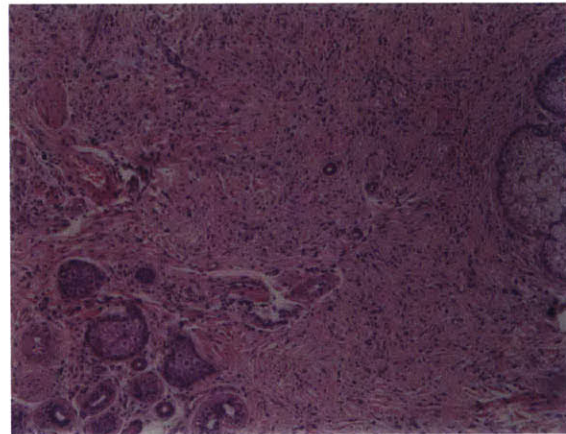

Figure 6-15: Patient 002 – Histological view of a solid mass of sclerosis and spindly invasive melanoma cells

collagen surrounding individual and groups of malignant melanocytes. The over-expression of collagen is identified as the bright pink and red area surrounding the cells.

As a comparison, Fig. 6-14 shows what normal skin looks like in this type I skin individual. The pale blue nodules of solar elastotic collagen can be seen in the center of the photomicrograph along with adnexal structures (sebaceous glands, pilar muscles,

and normal telangiectatic vessels). Fig. 6-15 shows a high-power (20X magnification) photomicrograph of the spindle-shaped invasive malignant melanoma cells in a thick fibrotic stroma.

Normalized stiffness maps, as shown in Fig. 6-17, were created from the acquired data and overlaid onto the visible light images for qualitative evaluation. The images consistently show the lesion as being stiff throughout. This is completely consistent with the clinical assessment of induration of lesion and the histologic confirmation of a solid nodule of fibrotic tumor mass. While the lesion position was not quantitatively verified, the mapping appears to match up very well with the lesion position.

The results of the automated ABCD morphology quantification are shown in Fig. 6-16. The segmentation algorithm had difficulty correctly segmenting the lesion, since its appearance was not that of a typical melanoma. The diameter, boundary, and symmetry values were all large, signifying a high cancer probability.
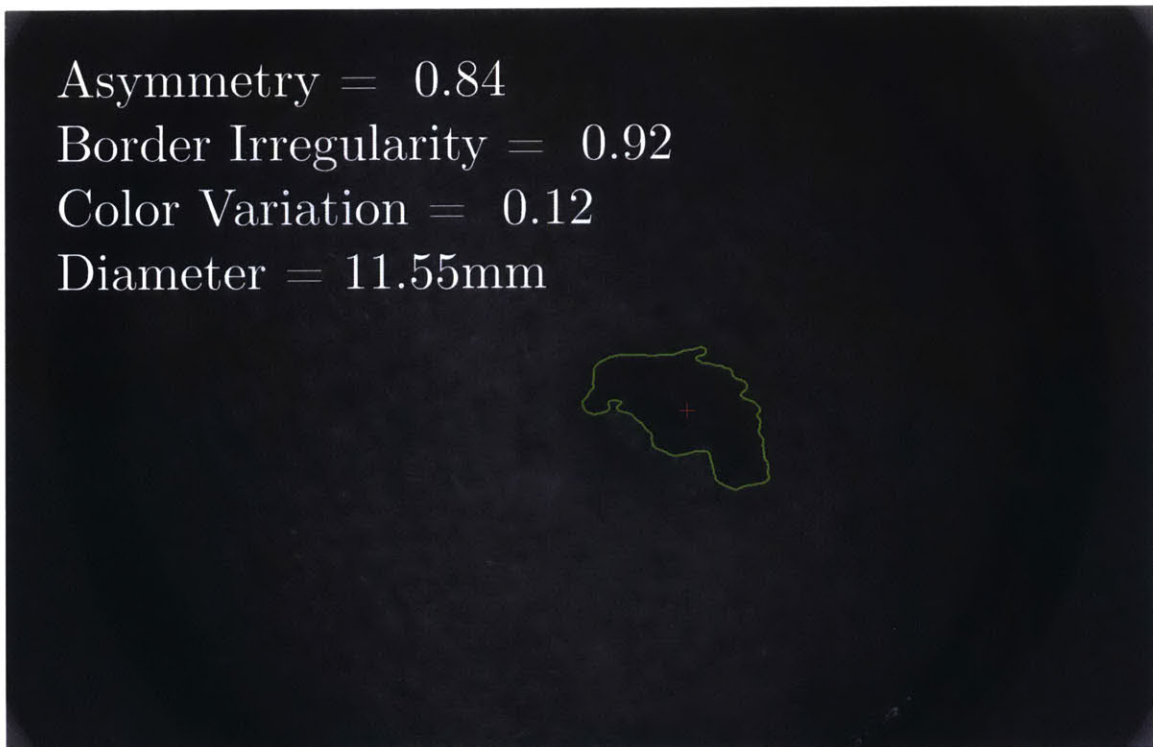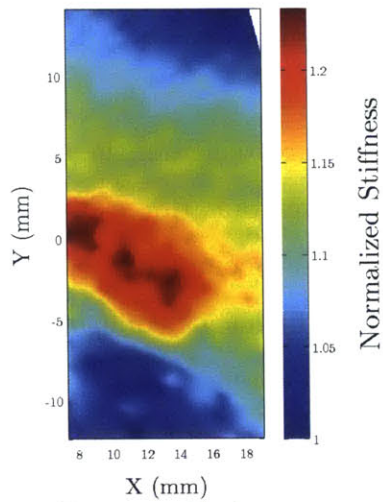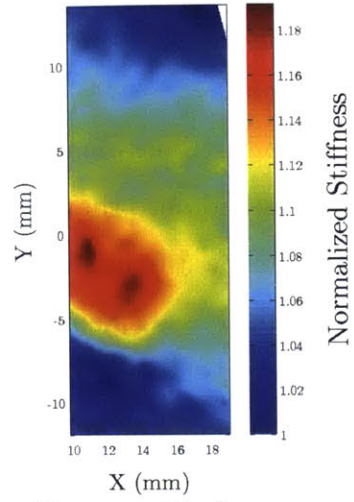

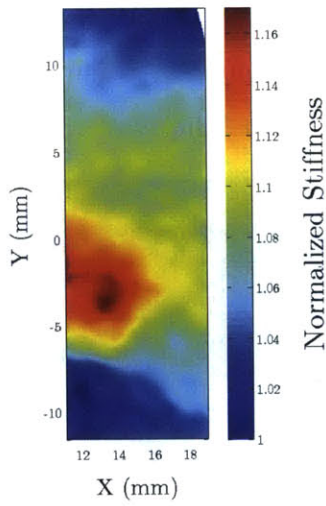Figure 6-16: Patient 002 – Automated ABCD results
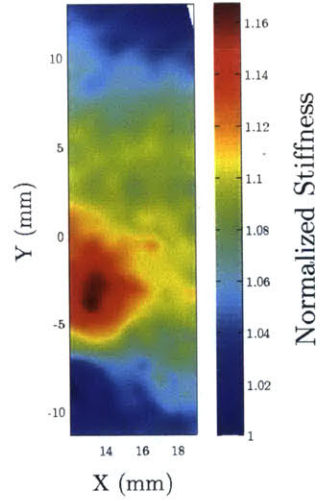
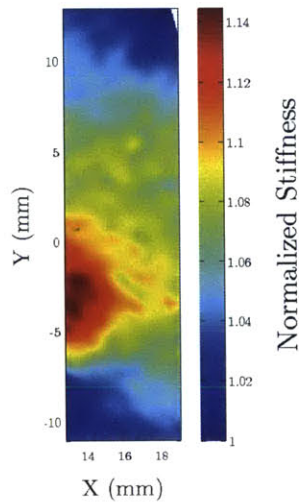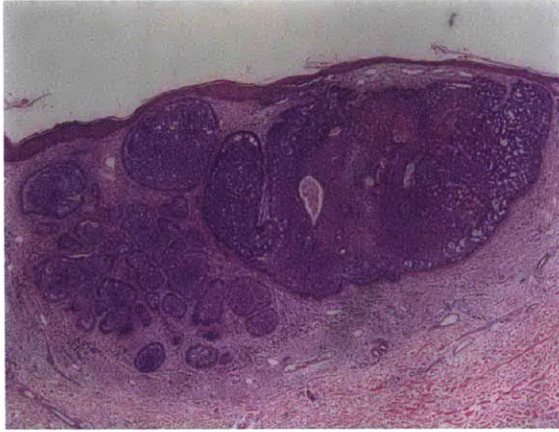Figure 6-17: Patient 002 – Normalized stiffness maps for all pressures

Figure 6-18: Patient 003 – Histological cross-section of a large nodular basal cell carcinoma
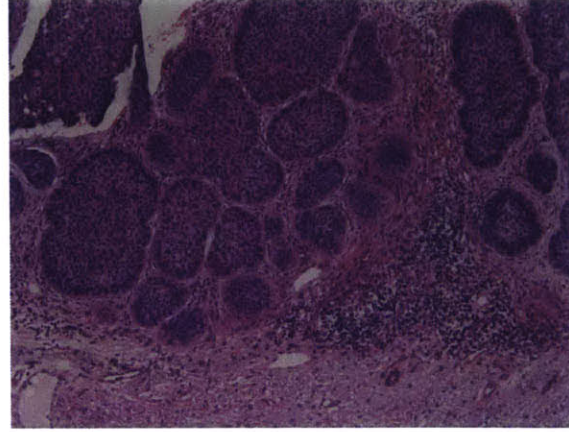

Figure 6-19: Patient 003 – Histological view of nodular basal cell carcinoma with sclerotic capsule

Patient 003 Histopathological review confirmed that the lesion excised from patient 003 was a basal cell carcinoma. In the center of the excised specimen there is an ulceration or fibrosing granulation tissue in the upper portion of the dermis. In the surrounding dermis there are aggregates of basaloid cells.

A closer look at the histology (Fig. 6-18) shows sheets of basophilic cells, appearing as blue dots, with a palisading perimeter of basal cell carcinoma cells. The basal cell carcinoma extends from the epidermis in nodules and micro-nodules. The small, white pocket in the middle of the lesion is an area of necrotic tissue. Necrosis occurs because the diffusion of nutrients is limited into the center of a large, dense lesion.

Fig. 6-19 shows a medium-power (10X magnification) view of these nodules of basal cell carcinoma being encased in a shell of fibrotic stroma. This is can be visualized by examining the eosinophilic (pink) newly produced collagenous stroma. Again, this overexpression of collagen is what causes the noticeable change in stiffness.

Fig. 6-20 shows a low-power (4X magnification) view of the basal cell carcinoma. In this panoramic view, nodules extending from the basal layer of the epidermis are visualized with intervening non-affected papillary dermis. It follows that this intervening tissue should be more compliant than the fibrotic stroma that surrounds and encapsulates the cancerous tissue.
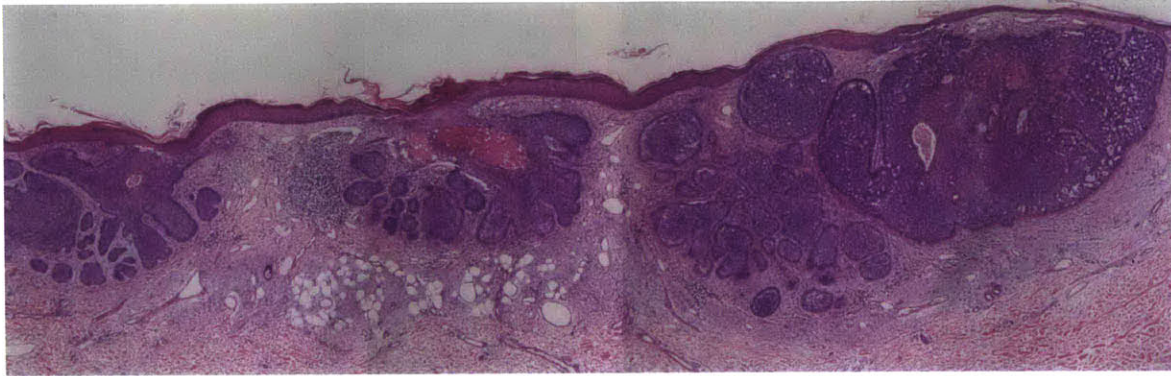
Figure 6-20: Patient 003 – Macro histological view showing gaps of healthy tissue between basal cell carcinoma nodules

In Fig. 6-21, the computed normalized stiffness maps show a clear increase in stiffness where the lesion is located. The boundaries of the entire lesion can be distinguished, and within the map itself there appears to be intervening pockets of more compliant tissue that surround islands of stiffer tissue. This is consistent with the histology. The ability of LesionAir to discriminate these micro-anatomic structures and map those structures on the skin surface provides a compelling feature of the device's utility.
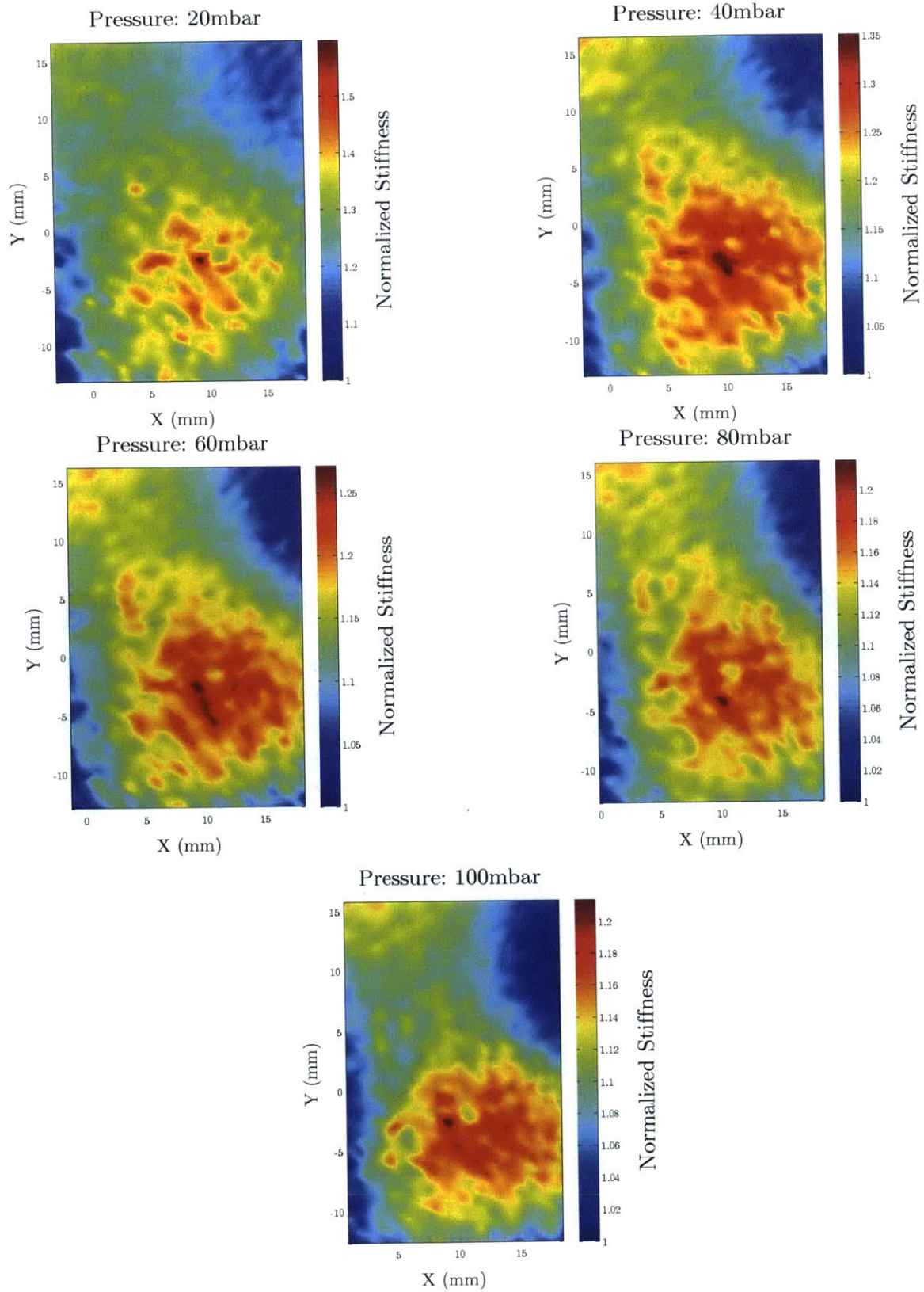
Figure 6-21: Patient 003 – Normalized stiffness maps for all pressures

Patient 005 The benign lesion found on the right flank of patient 005 was suspected to be an intradermal nevus. This lesion was simply assessed by gross clinical observation and no biopsy was performed. The lesion itself was a well-demarcated, hyperpigmented oval that was slightly elevated as a dome-shaped papule. It felt significantly softer when compared to the surrounding tissue.

The resulting normalized stiffness maps, shown in Fig. 6-23, agree with the clinical stiffness assessment that the lesion is much more compliant than the surrounding tissue. This particular patient specimen demonstrates the capability of the device to discriminate softer skin. Characteristically older intradermal nevi such as this can be composed of normal melanocyte nests in either a soft myxoid or fatty tissue stroma.

The automated ABCD morphology quantification results, shown in Fig. 6-22, appear quite normal. The algorithm accurately segmented the lesion, and the ABCD metrics are quite small, signifying a low probability of cancer.
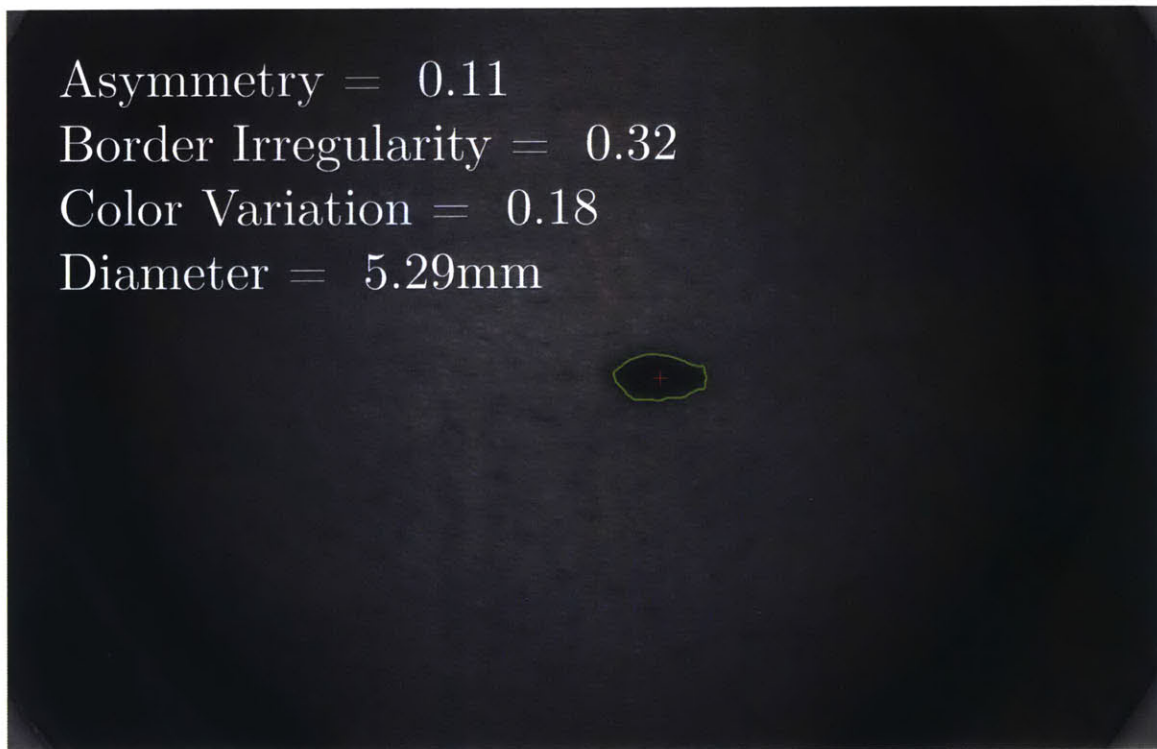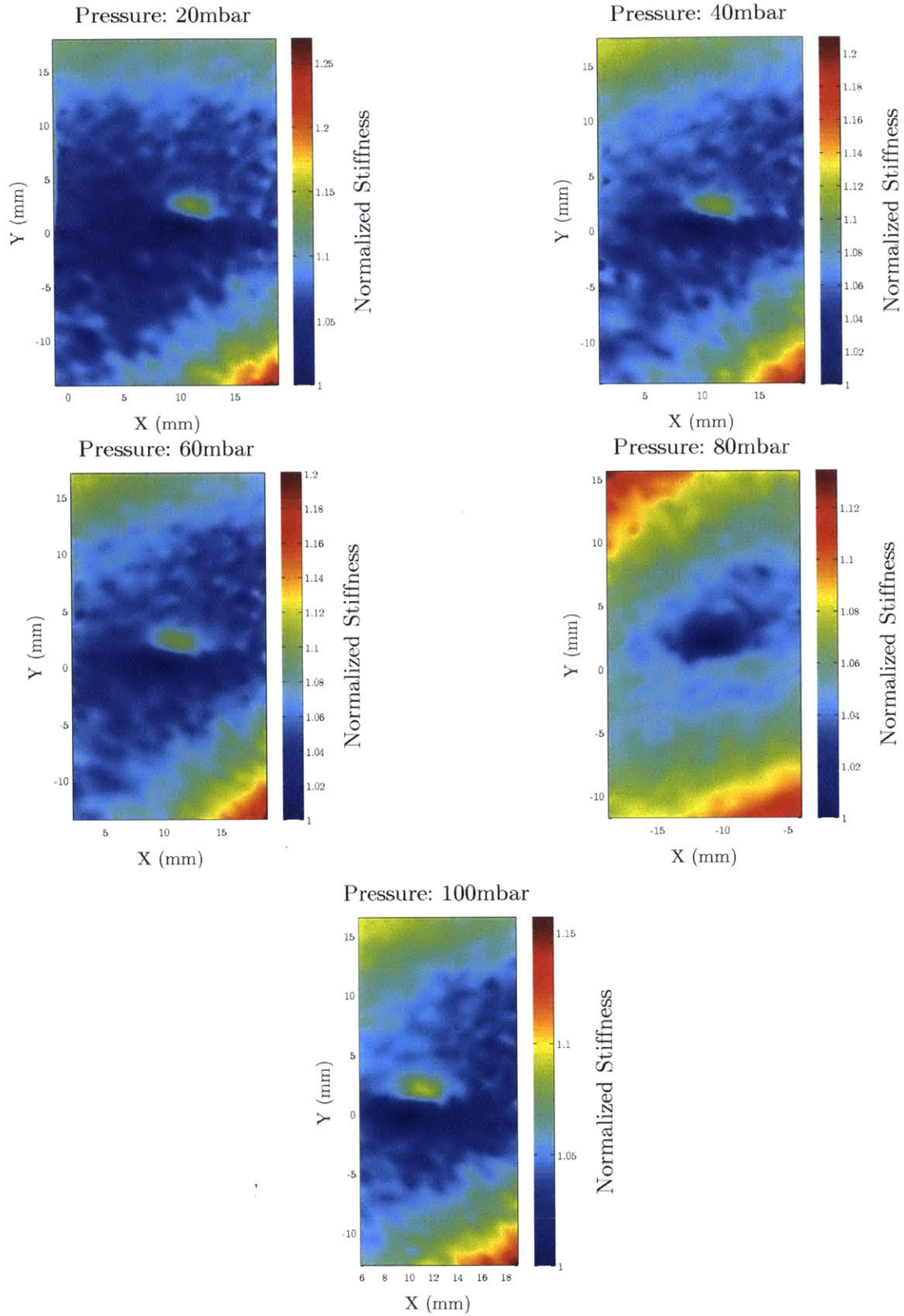

Figure 6-22: Patient 005 – Automated ABCD results

Pressure: 20mbar

Pressure: 40mbar

Pressure: 60mbar

Pressure: 80mbar

Pressure: 100mbar

Figure 6-23: Patient 005 – Normalized stiffness maps for all pressures

169

Table 6.7: Failure modes for incomplete test cycles

ID #	Lesion Location	Failure Mode
001	Distal Right Forearm	Suction loss due to curvature of forearm
004	Distal Right Wrist	Suction loss due to curvature of wrist
006	Medial Right Knee	Suction loss due to curvature of inner knee

6.4.3 Patient Testing Failures

As mentioned previously, LesionAir was unable to complete a full data acquisition process on three of the ten patients. Table 6.7 presents those three patients who experienced the device failure. All three failures occurred on areas of the body with highly variable and significantly curved surface contours. All three failures also occurred on aging patients with inelastic skin.

Chapter 7

Conclusion

Skin cancer is a dangerous disease that affects millions of people every year. Early stage identification is critical to successful treatment. Expert observation lacks sensitivity and specificity, and nearly all of the existing and newly developed *in vivo*, non-invasive technologies for detection are limited in their deployment due to high costs and complexity.

LesionAir is a fully automated, non-invasive tissue characterization device using low-cost hardware that will better enable dermatologists and non-specialists to effectively diagnose skin diseases, such as skin cancer. While still in the early stages of development, the presented method and instrument have shown promise as an assessment tool.

LesionAir accomplished the goals of the research by converting palpation into an automated, repeatable, objective process. LesionAir also has increased spatial resolution and sensitivity over a physicians finger. The method is also advantageous over other diagnostic technologies. The presented platform is simple, low-cost, and portable, while still providing accurate results, different from any other product available.

Based on the results of the pilot study, the device was shown to provide compelling evidence that the proposed method is capable of differentiating between stiff cancerous tissue and normal healthy tissue. Additionally, the spatial resolution appears to be sufficient to map out the extents of the lesion for precision excision. The sample

size of this trial was too small to achieve results with statistical significance, but the results are very promising and warrant a continued investigation of the efficacy of the device and method. Subsequent studies will help determine if the device is able to definitively confirm a cancer diagnosis, or if the device just provides additional information about a lesion that a specialist can use to make a diagnostic decision.

There are three primary improvements that are necessary based on field use. First, the amount of deflection was too large, causing the structured light pattern to shift substantially and not cover the entire lesion, losing information in the process. There are several ways to address this issue. Reducing both the pressure and the aperture size will lessen the amount of deflection. The study revealed that lower pressures were sufficient enough to differentiate changes in tissue stiffness. The structured light pattern could also be optimized to cover more of the aperture, or the angle of the light could be reduced, although this would diminish the depth resolution.

A second necessary upgrade is an improved structured light dot ordering algorithm. The ordering algorithm that was used was unable to handle highly curved surfaces and any errors had to be fixed manually. This hindrance prevents the device from being fully automated. A new algorithm has been devised but not implemented yet. Rectifying the structured light image through a transformation can warp the dots so they are in horizontal lines, then the ordering algorithm can just search linearly down the lines. Once the dots are ordered, the image can be warped back to it's original shape.

Finally, the current size of the device creates limitations. The device is unable to reach certain areas of the body and the large aperture occasionally makes it difficult to seal on a highly contoured portion of the body. Shrinking the device and aperture will address most of these issues; however, there will always be areas of the body that must be excluded. The proposed method won't work for lesions under nails (subungual), on small, highly curved areas (acral), or in places it can't reach (mucosal).

172

7.1 Broader Impact

The technology presented in this thesis has broad applications outside skin cancer diagnosis and mapping. Similar to cancerous tissue, other diseased tissues also demonstrate a modulation of elasticity that is commonly used for diagnosis. Scar tissue, psoriasis, edema, and scleroderma are all examples of clinical conditions that exhibit an increase in elasticity.

For example, assessment of the severity of edema employs similar palpation techniques to those previously described for cancer detection. An edema is caused by blocked or malfunctioning veins that allow fluid to leak into the interstitial space. The fluid-filled tissue has different mechanical properties than surrounding tissue. Currently, the severity of an edema is diagnosed by applying momentary pressure and evaluating the restoration of the skin to its original form before pressure was applied. The method that LesionAir employs could be used to automate the quantification of this elasticity.

Other medical applications for the low-cost structured light measurement system are non-invasive wound depth measurement and tuberculosis skin tests. Large wounds, such as pressure ulcers, are measured to assess the healing progress and to inform treatment. Currently, the length, width, and depth of a wound are simply measured using a ruler. Specifically, the depth is measured using an archaic process where a cotton-tip applicator is placed into the deepest part of the wound bed and grasped near the base of the wound so the distance can be measured with a ruler. The structured light method used by LesionAir would be able to quickly and easily make non-contact length, width, and depth measurements, preventing any irritation to the wound.

In another possible application, patients are tested for tuberculosis by injecting a small amount of the tuberculin protein under the top layer of skin. A few days later, the reaction, which presents as a red, raised, hardened area, is quantified for diagnosis. LesionAIR could accurately measure the size of the reaction, providing increased objectivity to the diagnostic test.

The auxiliary technology developed in this thesis will also have a broad impact outside of biomedical applications; a low-cost structured light system will provide an avenue for smartphone developers to add depth-sensing to many non-medical measurement applications.

7.2   Future Work

The method described in this research has shown great promise as a diagnostic tool, but additional development and testing is required before the research goal is fully realized. Most importantly, a larger scale, longitudinal test is required. The initial intent of the method was not to evaluate the relative stiffness of a lesion versus an area of healthy tissue, but instead to look at the evolution of a lesion.

Significant changes in stiffness and morphology over time correlate directly with an increased chance of skin cancer. This multi-year study would require lesions to be measured daily, weekly, or monthly to verify how fast the evolve and how soon this change can be identified.

A large dataset from a longitudinal study would also be beneficial in creating a robust classification algorithm. It is hypothesized that a machine learning neural network classifier would be ideal for this application. The neural network could be trained using the ABCD metrics and normalized stiffness maps as inputs. This process would provide an algorithm to give all subsequent measured lesions a score on how likely they are to be cancerous.

The mapping feature of the method also needs to be quantitatively evaluated. Qualitative evaluation of the pilot study showed the maps matched up quite well, but a testing method will have to be developed to determine how closely the mapping actually matches the lesion profile.

Additionally, there needs to be a transition from a relative stiffness measurement to an absolute stiffness measurement. A method has been devised, but not yet implemented, to determine the actual stiffness value. Through a system of loosely coupled

equations and a finite difference matrix, it is hypothesized that the data currently collected by LesionAir is sufficient to calculate absolute stiffness.

Finally, the method needs to be miniaturized to the initially proposed smartphone form factor with real-time processing capabilities. The device was designed with miniaturization in mind, such that all of the components necessary are already included on the phone, or easy to add through a hardware attachment.

Appendix A

Camera/Projector Calibration
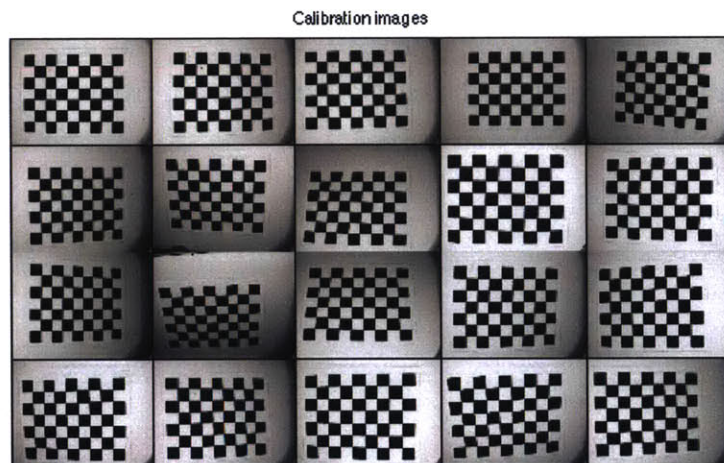
A.1 Camera Calibration

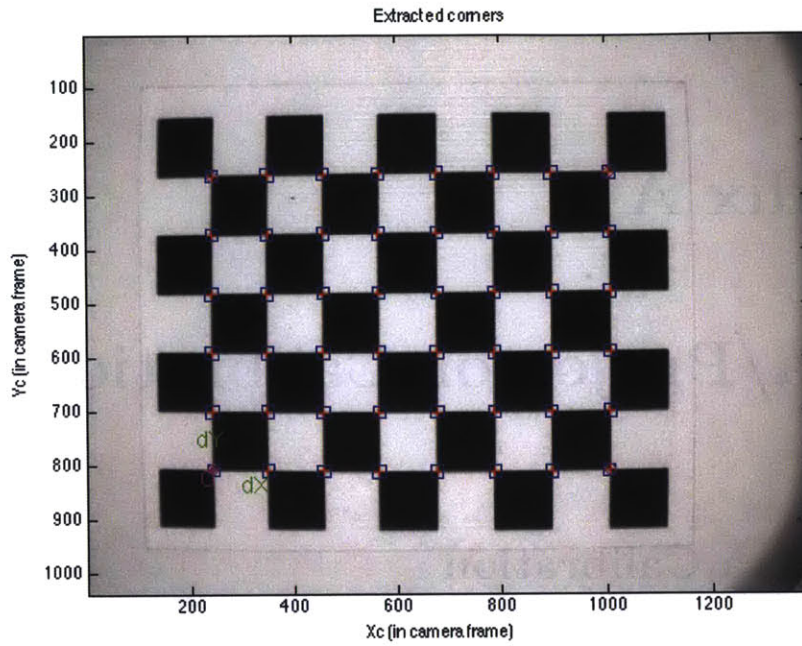Figure A-1: All twenty camera calibration images

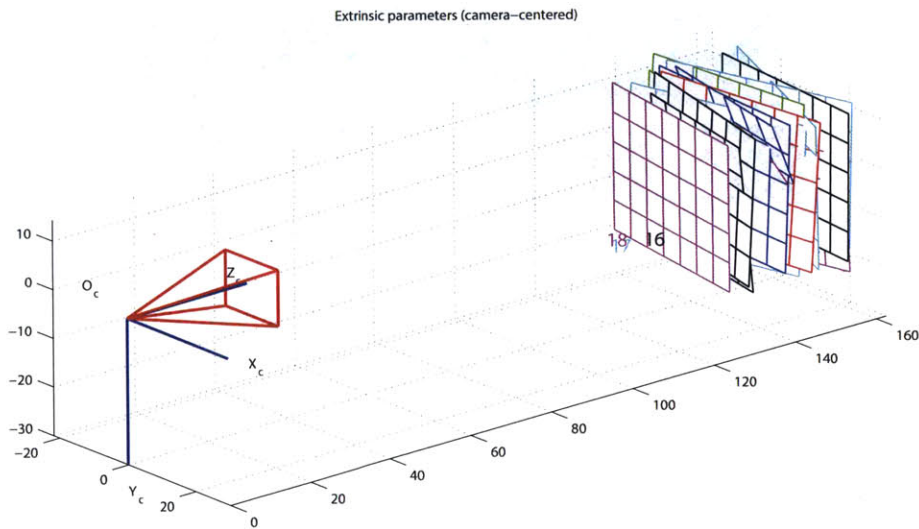Figure A-2: Extracted corners of the checkboard pattern from one calibration image

Figure A-3: Extrinsic relationship of camera to all twenty images as determined by calibration procedure

```
Calibration results after optimization (with uncertainties):

Focal Length:      fc = [ 2712.27886    2733.44335 ] ± [ 25.39361    25.26755 ]
Principal point:   cc = [ 558.88560    465.93905 ] ± [ 17.98298    14.97182 ]
Skew:         alpha_c = [ 0.00000 ] ± [ 0.00000  ]    => angle of pixel axes = 90.00000 ± 0.00000 degrees
Distortion:        kc = [ -0.49646    1.37378    -0.00637    0.00411   0.00000 ] ± [ 0.04875    0.91302    0.00130
Pixel error:      err = [ 0.53093    0.43132 ]
```

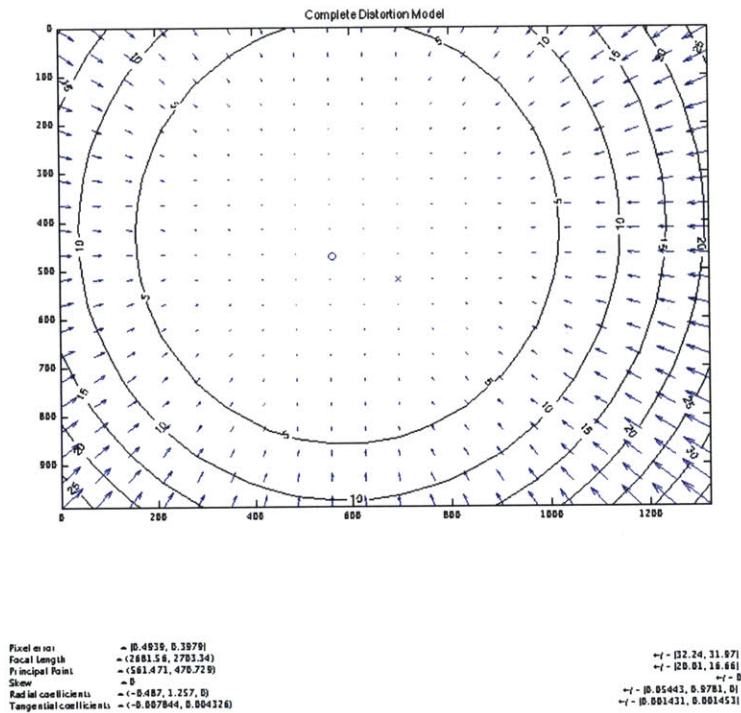Figure A-4: Camera calibration results after optimization

Figure A-5: Complete distortion model of lens

Figure A-6: Radial distortion model of lens

Figure A-7: Tangential distortion model of lens

180
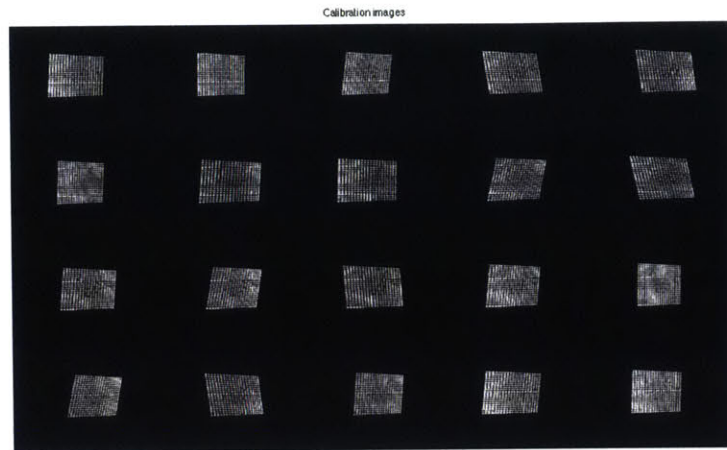
A.2 Projector Calibration

Figure A-8: All twenty projector calibration images
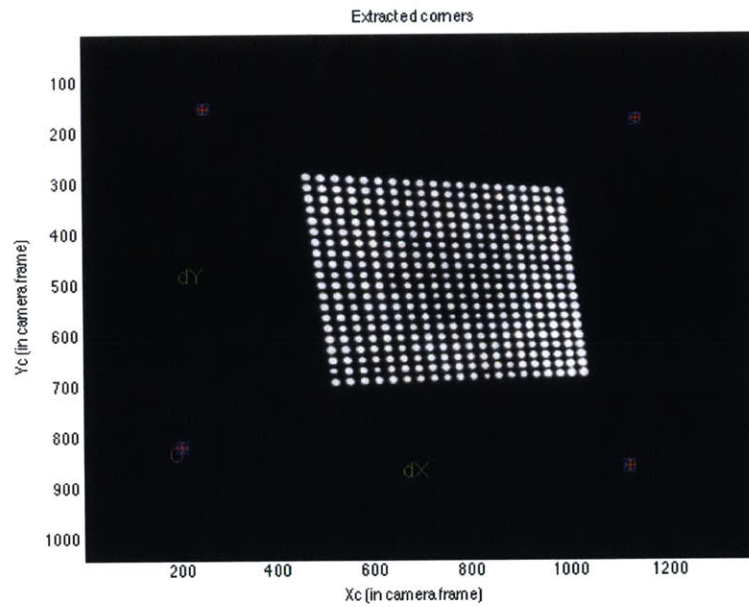

Figure A-9: Extracted corners of the fiducials on the calibration board from one calibration image
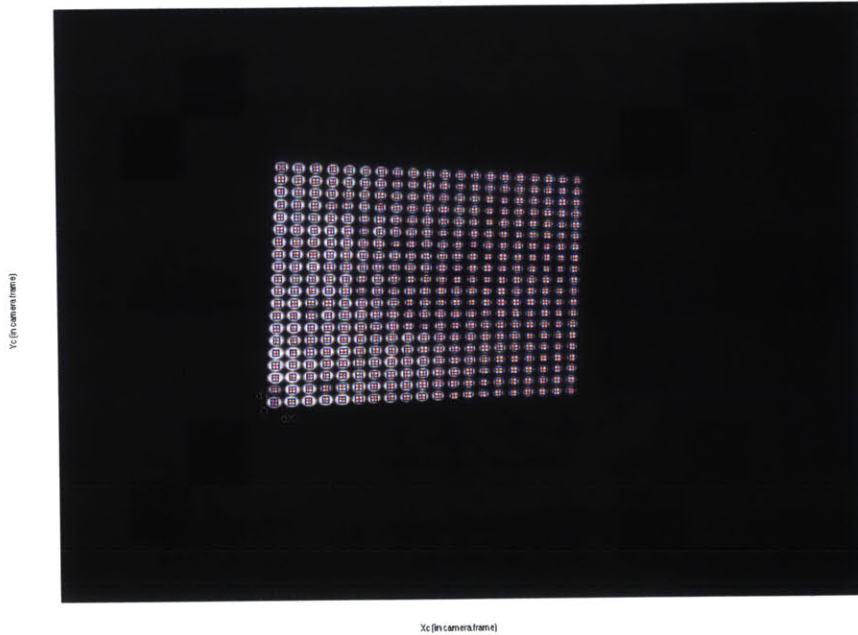
Figure A-10: Extracted projection dots on the calibration board from one calibration image

```
Calibration results after optimization (with uncertainties):

Focal Length:       fc = [ 123.07548   126.73012 ] ± [ 0.68290   0.95271 ]
Principal point:    cc = [ 1.42152   3.66501 ] ± [ 1.07607   0.68394 ]
Skew:          alpha_c = [ 0.00000 ] ± [ 0.00000  ]  => angle of pixel axes = 90.00000 ± 0.00000 degrees
Distortion:         kc = [ 0.44965   -6.10016   -0.02245   -0.01537 0.00000 ] ± [ 0.04559   1.27565   0.00318
Pixel error:       err = [ 0.01703   0.01775 ]

Note: The numerical errors are approximately three times the standard deviations (for reference).
```

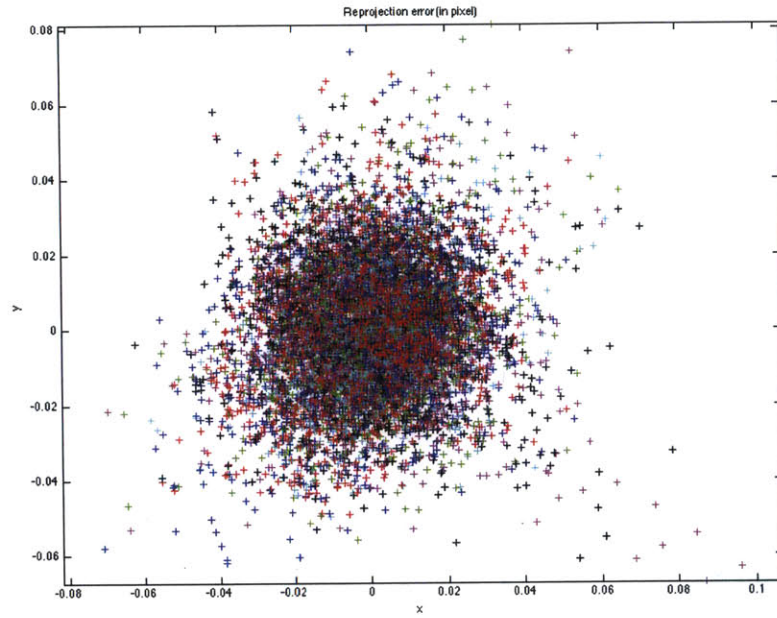Figure A-11: Projector calibration results after optimization

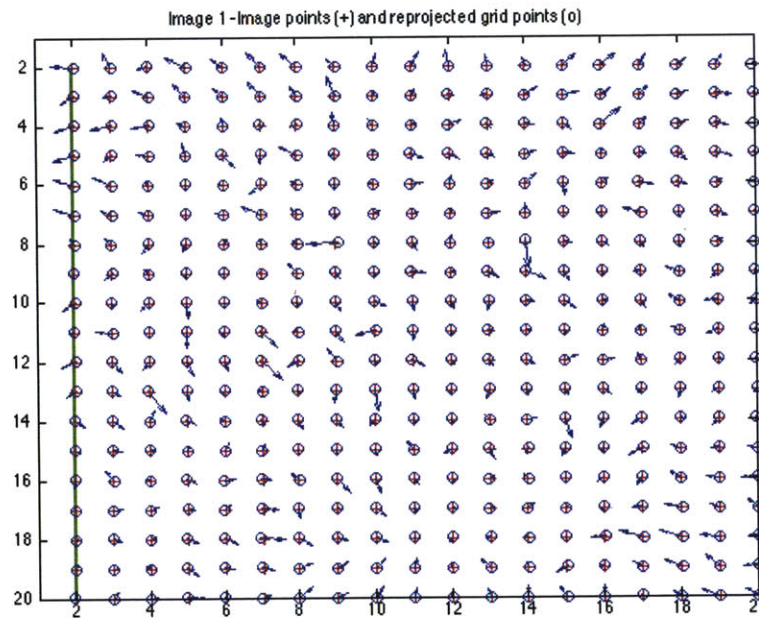Figure A-12: Projector reprojection error for all twenty images

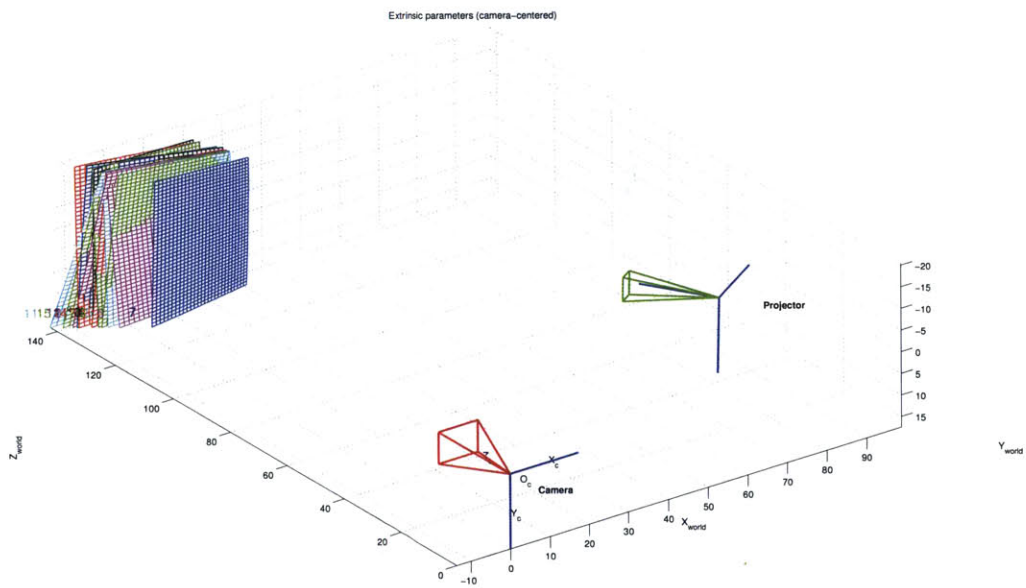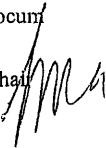Figure A-13: Projector reprojection error for a single calibration image

Figure A-14: Extrinsic relationship of projector to the camera and all twenty images as determined by calibration procedure

Appendix B

COUHES IRB Documents

To:	Alexander Slocum 3-445
From:	Leigh Firn, Chair COUHES
Date:	12/17/2015
Committee Action:	Approval
Committee Action Date	12/17/2015
COUHES Protocol #	1511310864
Study Title	Tissue Stiffness Quantification for Diagnosis and Mapping
Expiration Date	12/16/2016 FDA Determination: Non Significant Risk Device (21 CFR 812)

The above-referenced protocol has been APPROVED following Full Board Review by the Committee on the Use of Humans as Experimental Subjects (COUHES).

If the research involves collaboration with another institution then the research cannot commence until COUHES receives written notification of approval from the collaborating institution's IRB.

It is the Principal Investigator's responsibility to obtain review and continued approval before the expiration date. Please allow sufficient time for continued approval. You may not continue any research activity beyond the expiration date without COUHES approval. Failure to receive approval for continuation before the expiration date will result in the automatic suspension of the approval of this protocol.

Information collected following suspension is unapproved research and cannot be reported or published as research data. If you do not wish continued approval, please notify the Committee of the study termination.

Adverse Events: Any serious or unexpected adverse event must be reported to COUHES within 48 hours. All other adverse events should be reported in writing within 10 working days.

Amendments: Any changes to the protocol that impact human subjects, including changes in experimental design, equipment, personnel or funding, must be approved by COUHES before they can be initiated.

Prospective new study personnel must, where applicable, complete training in human subjects research and in the HIPAA Privacy Rule before participating in the study.

You must maintain a research file for at least 3 years after completion of the study. This file should include all correspondence with COUHES, original signed consent forms, and study data.

CONSENT TO PARTICIPATE IN
BIOMEDICAL RESEARCH

Tissue Stiffness Quantification for Diagnosis and Mapping

You are asked to participate in a research study conducted by Prof. Alex Slocum and Tyler Wortman, from the Mechanical Engineering Department at the Massachusetts Institute of Technology (M.I.T.). You have been asked to participate in this study because you are visiting this clinic with a potentially cancerous skin lesion. This study involves the use of a non-invasive, investigational device that will collect images of your skin in the area of the lesion, in order to help further develop a potential diagnostic technology. The collection of this data will have no influence on your treatment and your patient confidentiality will be maintained. You should read the information below, and ask questions about anything you do not understand, before deciding whether or not to participate.

- **PARTICIPATION AND WITHDRAWAL**

Your participation in this research is completely VOLUNTARY. If you choose to participate you may subsequently withdraw from the study at any time without penalty or consequences of any kind. If you choose not to participate, that will not affect your relationship with M.I.T. or Dermatology Laser Center and Spa or your right to health care or other services to which you are otherwise entitled.

- **PURPOSE OF THE STUDY**

The purpose of this study is to evaluate a new medical device to assist in the diagnosis and mapping of cancerous skin lesions by non-invasively measuring optical and mechanical properties of tissue. This will facilitate device development and a longer-term study to measure how lesions evolve over time.

- **PROCEDURES**

If you volunteer to participate in this study, after your standard clinical examination, but before a biopsy or any other treatment, the following procedure will be carried out:

1. Your clinician will swab the suspect lesion and surrounding area with alcohol
2. The investigator will place the device on your skin over the lesion
3. The device will project a visible light pattern onto your shin
4. A light vacuum will be applied to mimic manual examination
5. A sequence of images and pressure readings will be recorded
6. The vacuum will be released and the device removed

This procedure will last less than a minute and, afterwards, your clinician will proceed with your visit.

As part of this study, select characteristics including your age, gender, ethnicity, skin tone and your clinician's perceptions regarding the lesion will be recorded. Your information will be associated with an anonymous code. This code will be placed in your patient record and used to connect the pathology results of your biopsy with the images and other information collected. No personally identifying information will be stored with the data.

- **POTENTIAL RISKS AND DISCOMFORTS**

The device will apply a light vacuum to your skin, similar to the same level of pressure as a clinician would apply during normal palpitation. You may feel minor, temporary discomfort and your skin may be red afterwards.

The treatment or procedure may involve risks that are currently unforeseeable.

- **ANTICIPATED BENEFITS TO SUBJECTS**

This device only collects additional information about your skin, and is not used to diagnose, treat, or cure. The data collected will not be used to influence your diagnosis or treatment.

- **ANTICIPATED BENEFITS TO SOCIETY**

The goal of this study is to characterize tissue so that skin cancer and other skin diseases may be identified faster and more efficiently. This technology also has the potential to better map lesions so that they may be better excised, removing the need for additional excisions of the same lesion.

- **ALTERNATIVES TO PARTICIPATION**

If you choose not to participate, your doctor will still perform all standard screening and treatment procedures.

- **PAYMENT FOR PARTICIPATION**

There will be no pay or other benefits offered for participating in this study.

- **FINANCIAL OBLIGATION**

Neither you nor your insurance company will be billed for your participation in this research. All costs will be covered by the investigators.

- **PRIVACY AND CONFIDENTIALITY**

The only people who will know that you are a research subject are members of the research team and, if appropriate, your physicians and nurses. No information about you, or provided by you during the research will be disclosed to others without your written permission, except: if necessary to protect your rights or welfare, or if required by law.

All images collected will only show small areas of your skin that will not be able to be used to distinguish you. You have the right to view the images as they are taken. Data will be anonymized and when the results of the research are published or discussed in conferences, no information will be included that could reveal your identity.

•WITHDRAWAL OF PARTICIPATION BY THE INVESTIGATOR

The investigator may withdraw you from participating in this research if circumstances arise which warrant doing so. You will be informed why it is not possible for you to continue.

• EMERGENCY CARE AND COMPENSATION FOR INJURY

If you feel you have suffered an injury, which may include emotional trauma, as a result of participating in this study, please contact the person in charge of the study as soon as possible.

In the event you suffer such an injury, M.I.T. may provide itself, or arrange for the provision of, emergency transport or medical treatment, including emergency treatment and follow-up care, as needed, or reimbursement for such medical services. M.I.T. does not provide any other form of compensation for injury. In any case, neither the offer to provide medical assistance, nor the actual provision of medical services shall be considered an admission of fault or acceptance of liability. Questions regarding this policy may be directed to MIT's Insurance Office, (617) 253-2823. Your insurance carrier may be billed for the cost of emergency transport or medical treatment, if such services are determined not to be directly related to your participation in this study.

• IDENTIFICATION OF INVESTIGATORS

In the event of a research related injury or if you experience an adverse reaction, please immediately contact one of the investigators listed below. If you have any questions about the research, please feel free to contact:

Dr. Alex Slocum (Principle Investigator) – 617-253-0012 | slocum@mit.edu
Tyler Wortman (Primary Researcher) – 308-383-3395 | wortman@mit.edu

• RIGHTS OF RESEARCH SUBJECTS

You are not waiving any legal claims, rights or remedies because of your participation in this research study. If you feel you have been treated unfairly, or you have questions regarding your rights as a research subject, you may contact the Chairman of the Committee on the Use of Humans as Experimental Subjects, M.I.T., Room E25-143B, 77 Massachusetts Ave, Cambridge, MA 02139, phone 1-617-253 6787.

SIGNATURE OF RESEARCH SUBJECT OR LEGAL REPRESENTATIVE

I have read (or someone has read to me) the information provided above. I have been given an opportunity to ask questions and all of my questions have been answered to my satisfaction. I have been given a copy of this form.

BY SIGNING THIS FORM, I WILLINGLY AGREE TO PARTICIPATE IN THE RESEARCH IT DESCRIBES.

_____

Name of Subject

_____

Name of Legal Representative (if applicable)

_____   _____

Signature of Subject or Legal Representative   Date

SIGNATURE OF INVESTIGATOR

I have explained the research to the subject or his/her legal representative, and answered all of his/her questions. I believe that he/she understands the information described in this document and freely consents to participate.

_____

Name of Investigator

_____   _____

Signature of Investigator   Date (must be the same as subject's)

SIGNATURE OF WITNESS (If required by COUHES)

My signature as witness certified that the subject or his/her legal representative signed this consent form in my presence as his/her voluntary act and deed.

_____

Name of Witness

_____   _____

Appendix C

Detailed Clinical Results

C.1   Patient 001 - Squamous Cell Carcinoma

Patient 001 was an 86 year old female with a suspected squamous cell carcinoma or actinic keratosis on the top distal part of her right forearm. The clinical presentation of the lesion is shown in Fig. C-1. The lesion was completely excised after clinical evaluation and data acquisition from LesionAir.

Pathology confirmed that the excised lesion was a squamous cell carcinoma. In the specimen there was an ulceration or zone of altered epidermis with fibrosing granulation tissue in the underlying dermis. Beneath and to the side of the zone of fibrosis there are islands of atypical keratinocytes lying free in the dermis. It is expected that the fibrosis will be seen on the stiffness map.

LesionAir was unable to complete the full test for patient 001. The seal was lost at higher pressures due to the small wrist with large curvature and the aging inelastic skin. A full set of measurements were acquired for the lesion, but not for the healthy symmetric region.

The series of visible and structured light images of the lesion with corresponding pressure is shown in Fig. C-2.

Normalized stiffness maps were created for the pressures that had completed data sets. The normalized stiffness maps were overlaid onto the visible light images for qualitative evaluation. The regions of stiffer tissue appear as striations across the

Figure C-1: Patient 001 – Clinical presentation of suspected squamous cell carcinoma

Vacuum Pressure = 0.0 mbar   **Vacuum Pressure = 17.2 mbar**

Vacuum Pressure = 37.5 mbar   **Vacuum Pressure = 58.8 mbar**

Vacuum Pressure = 75.1 mbar   **Vacuum Pressure = 98.4 mbar**
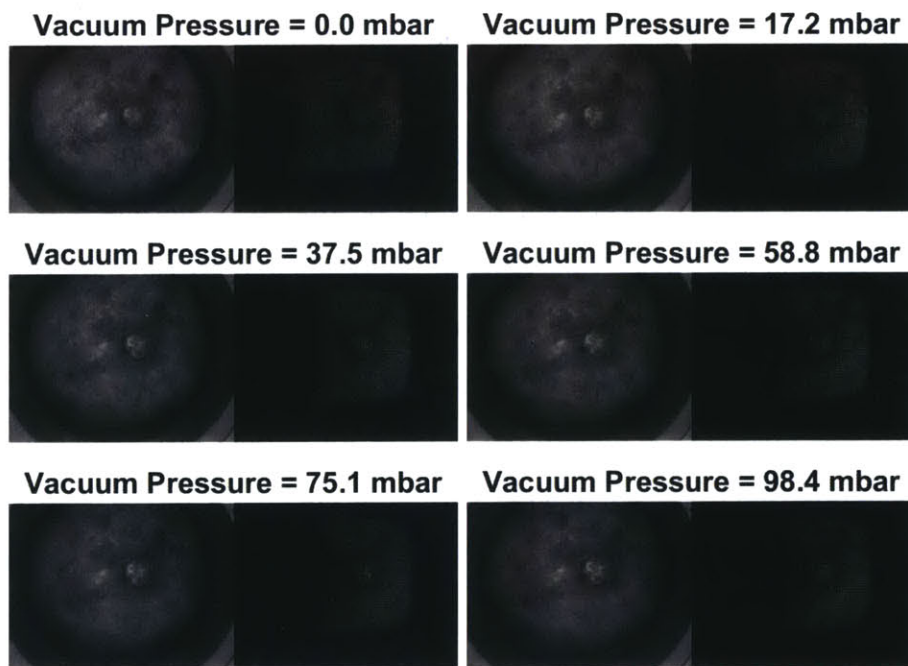

Figure C-2: Patient 001 – Series of structured and visible light images taken during data acquisition cycle
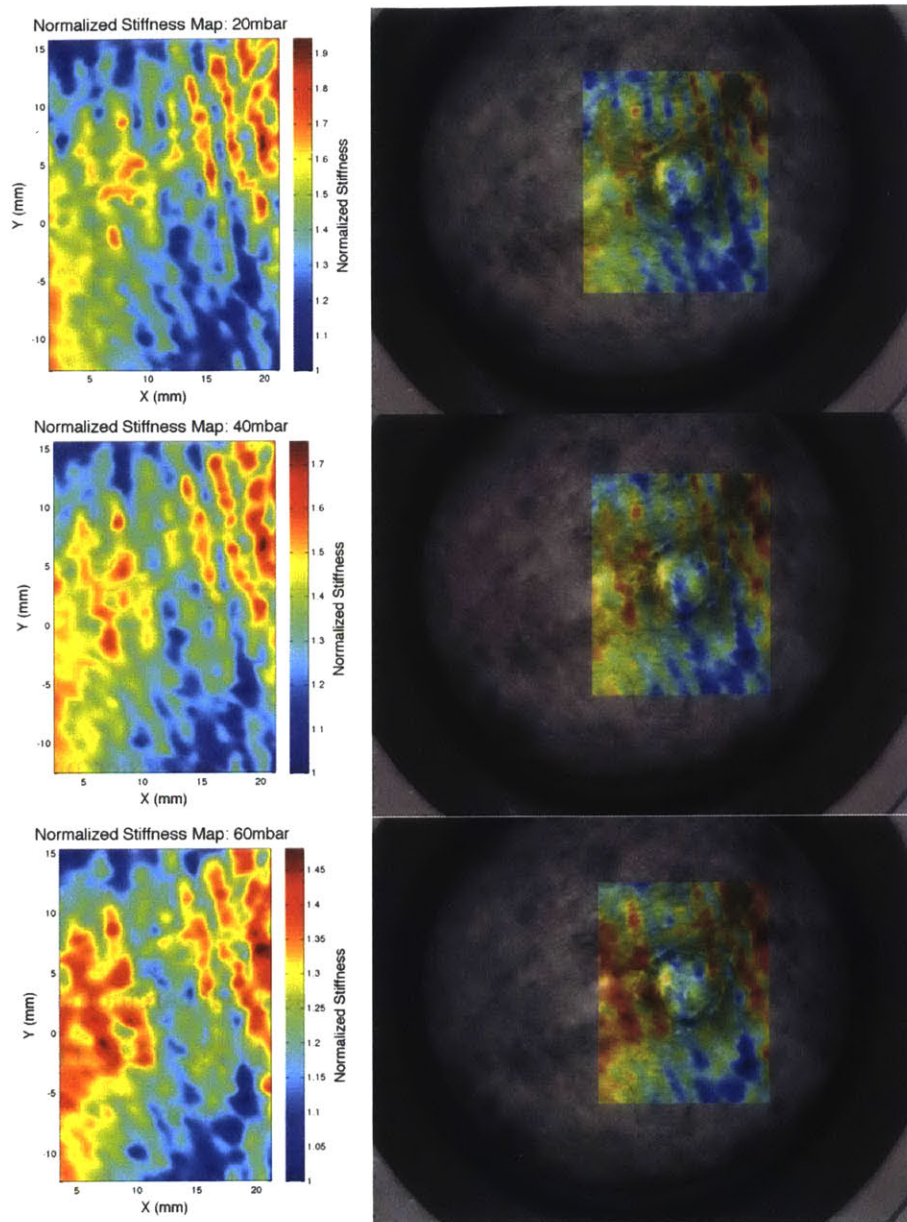
Figure C-3: Patient 001 – Normalized stiffness maps

image. The cause of this is unclear, as the pattern does not seem to be associated with with any visible features.

The strain stiffening feature of skin was also evaluated by creating a box-and-whisker plot of all of the measured stiffness values at a given pressure. As expected, as the pressure increases, the amount of strain increases, and the tissue gets even more stiff. This is due to the straightening of the collagen molecules.
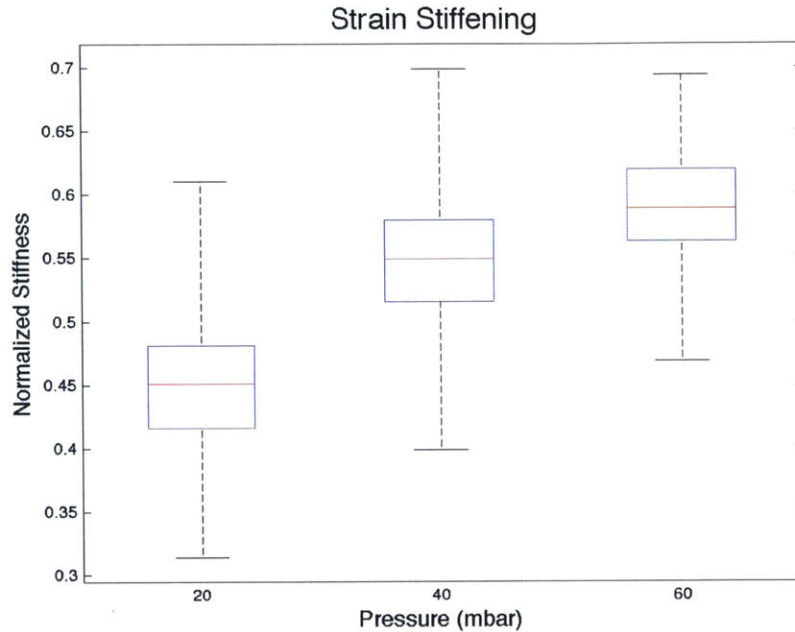
Figure C-4: Patient 001 – Strain stiffening that occurs at higher pressures

C.2   Patient 002 - Melanoma

Patient 002 was a 60 year old male with a suspected basal cell carcinoma on his right jaw line. The clinical presentation of the lesion is shown in Fig. C-5. The lesion was excised after clinical examination and LesionAir data acquisition.

Pathology corrected the clinical diagnosis and determined that the excised lesion was actually a stage T3a malignant melanoma, with a Breslow's depth of approximately 3.0 mm. The specific subtype was a melanoma in situ or superficial spreading melanoma. This was a surprising result, since the lesion does not exhibit the features typical to a melanoma in situ. The lesion was determined to be within 1 mm of the peripheral margins of the excision so it will require an additional excision process with wider and deeper margins. Since it was so deep in the dermis, the patient will need a lymph node biopsy.

In the excisional biopsy specimen from sun-damaged skin of the right jawline, the histology shows a large, asymmetric, and poorly circumscribed melanocytic lesion

196

Figure C-5: Patient 002 – Clinical presentation of suspected basal cell carcinoma

characterized by focal confluence of moderately atypical melanocytes distributed as solitary units and a rare small nest along the dermal-epidermal junction.

A low power view of the cross-section through the bulk of the melanoma is shown in Fig. C-6. Below the epidermis, there are nests, cords, and strands of atypical melanocytes (appearing as dark purple dots) producing sheets of malignant cells that extend deep into the reticular dermis. There is an obvious marked absence of adnexal structures, such as sweat or oil glands, as they have probably been destroyed by the invasive malignancy.

Fig. C-7 shows a medium power view of a cross-section just at the edge of the bulk of the lesion. This image shows the newly laid down collagen surrounding individual and groups of malignant melanocytes. The newly formed, over-expression of collagen is identified as the bright pink and red area surrounding the cells.

Fig. C-8 shows a solid mass of sclerosis mixed with invasive malignant melanoma cells extending deep into the dermis.

The cross-section shown in Fig. C-9 is a region of healthy tissue from patient 002 that is representative of the skin that would normally be in a type I skin individual who has spent a lot of time in the sun. This view shows normal collagen, normal adnexal structures, and the accumulation of sun damage (solar elastosis). Solar elastosis is seen close to the epidermis where aged collagen is plainly visible as a light sky blue material beneath the epidermis.

LesionAir was able to complete the entire data acquisition process for both the lesion and healthy symmetric region, even though the lesion was located on the jaw line, which has a sharp contour. The series of visible and structured light images of the lesion with corresponding pressure is shown in Fig. C-10.

Normalized stiffness maps were created from the acquired data and overlaid onto the visible light images for qualitative evaluation. The histology shows an increase in collagen in and around the bulk of the lesion, which is clearly shown as a stiffer mass in the normalized stiffness maps. While the lesion position was not quantitatively verified, the mapping appears to match up very well with the lesion position.

As expected, Fig. C-12 demonstrates the strain stiffening of the tissue. The results of the ABCD morphology quantification are shown in Fig. C-13. The segmentation algorithm had difficulty correctly segmenting the lesion, since its appearance was not that of a typical melanoma. The diameter, boundary, and symmetry values were all large, signifying a high cancer probability.
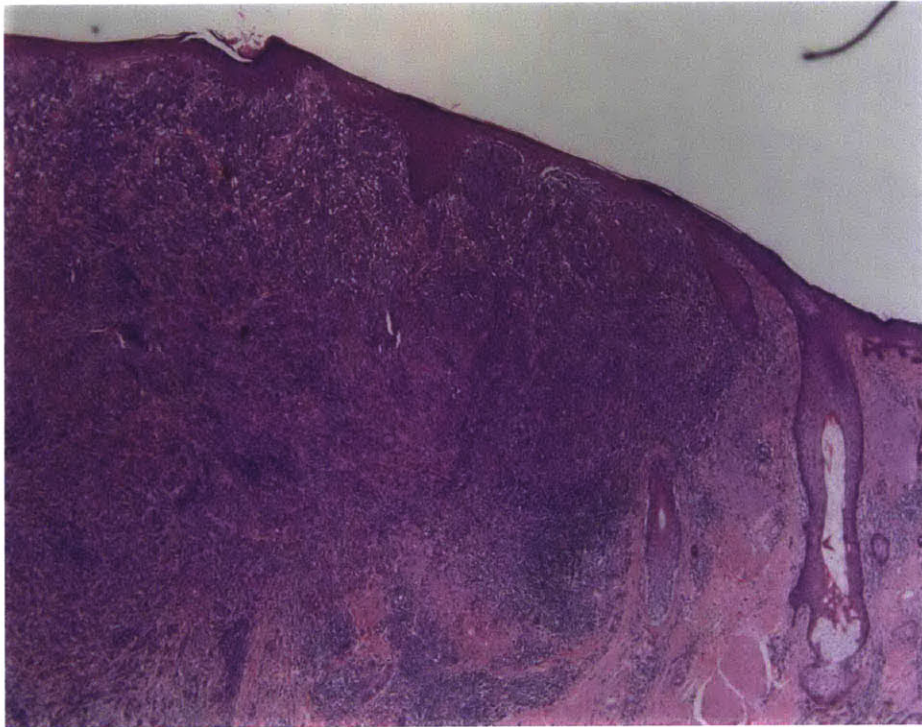
Figure C-6: Patient 002 – Histological cross-section of a large malignant melanoma lesion
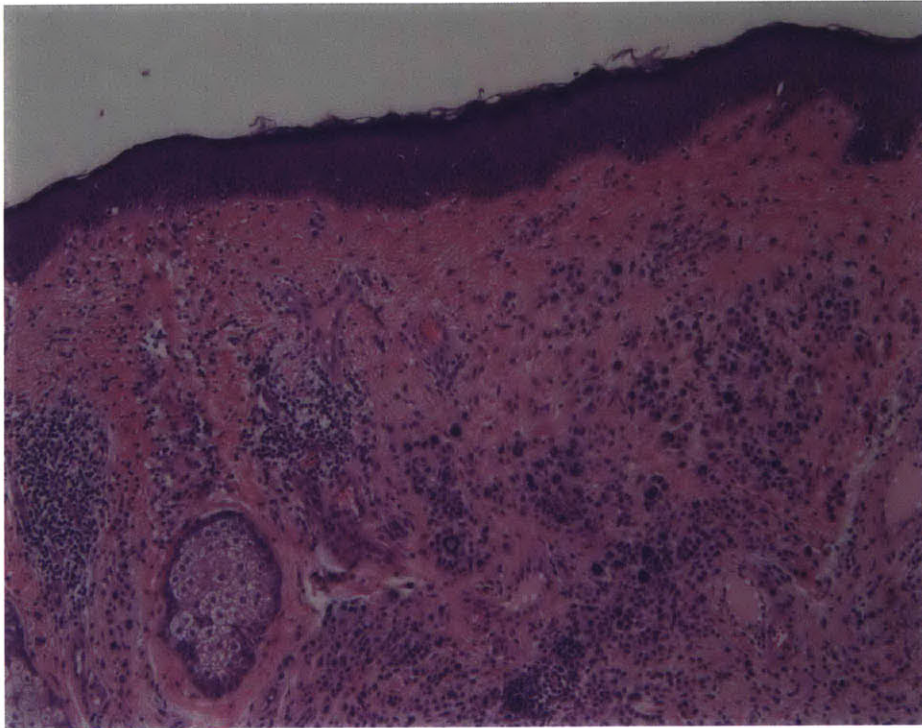
Figure C-7: Patient 002 – Histological view of malignant melanocytes surrounded by an over-expression of collagen
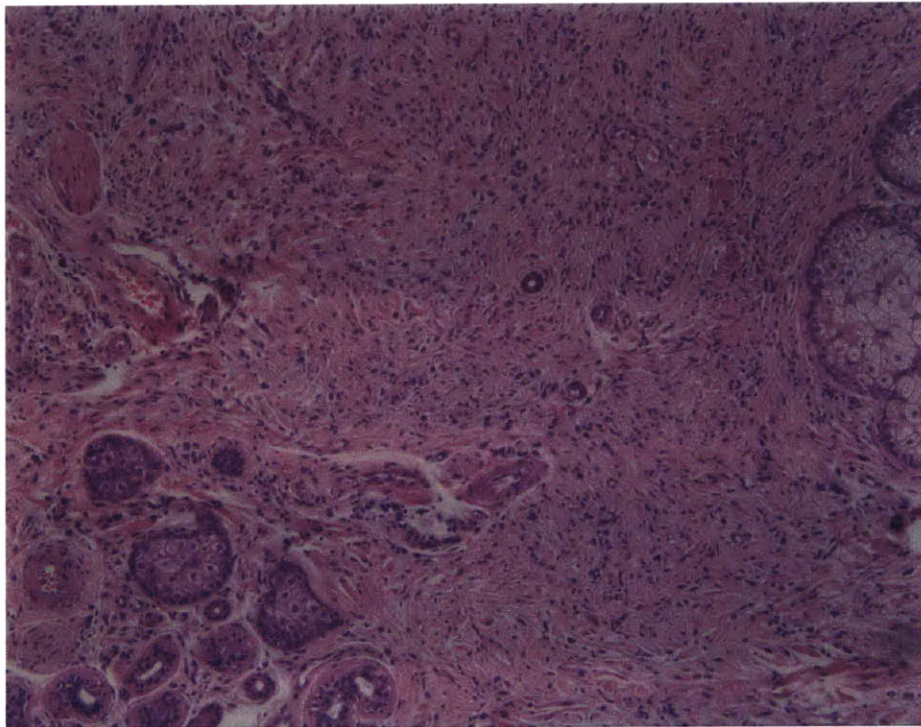
Figure C-8: Patient 002 – Histological view of a solid mass of sclerosis and spindly invasive melanoma cells
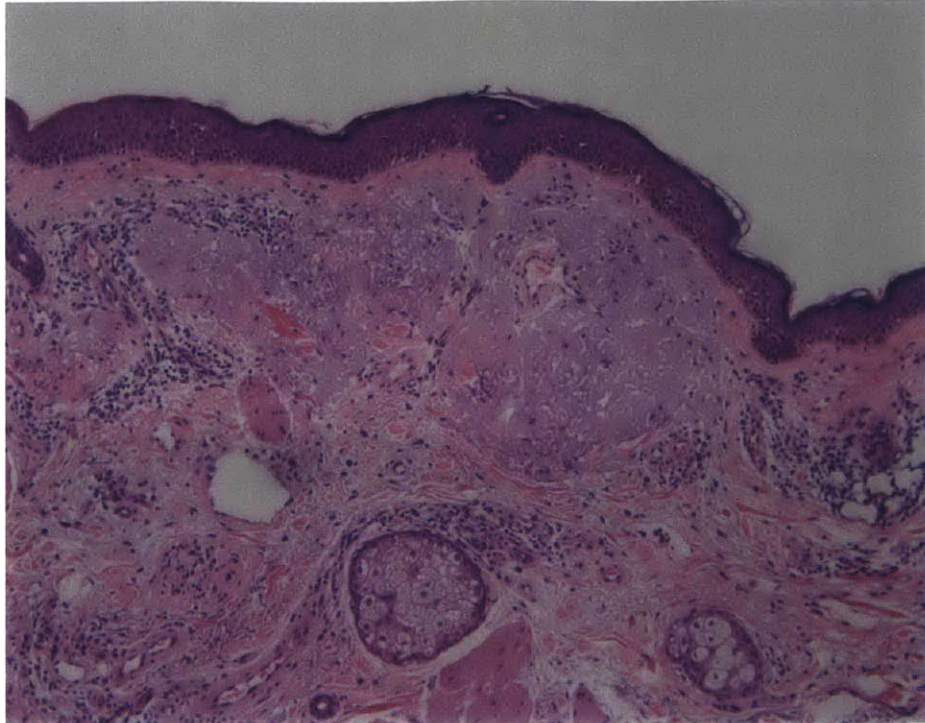
Figure C-9: Patient 002 – Histological view of solar elastosis in the healthy tissue next to the lesion – what typical sun-damaged collagen should look like

Vacuum Pressure = 0.0 mbar   **Vacuum Pressure = 19.2 mbar**

Vacuum Pressure = 37.5 mbar   **Vacuum Pressure = 54.7 mbar**

Vacuum Pressure = 77.0 mbar   **Vacuum Pressure = 96.2 mbar**

Figure C-10: Patient 002 – Series of structured and visible light images taken during data acquisition cycle

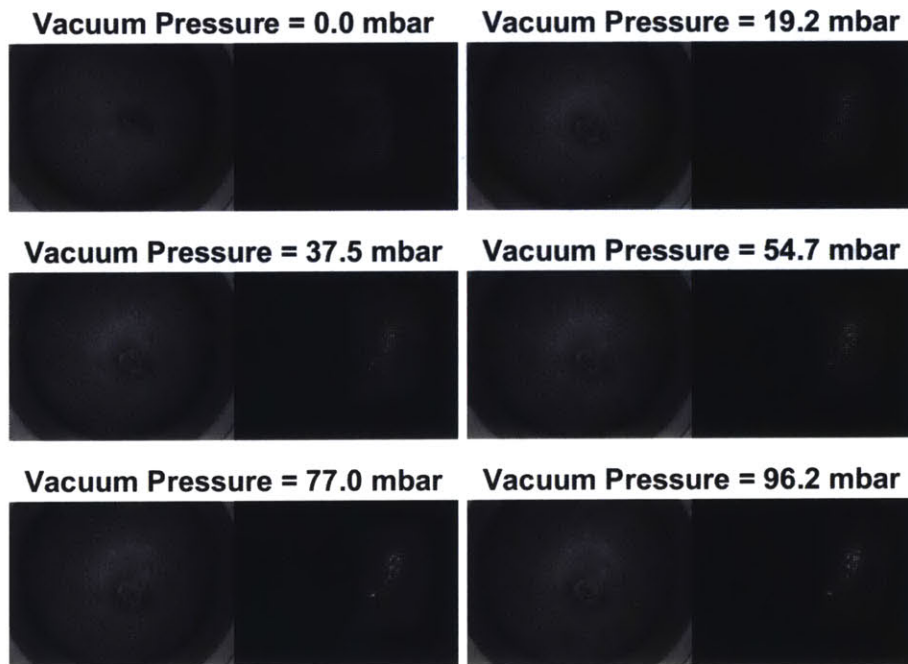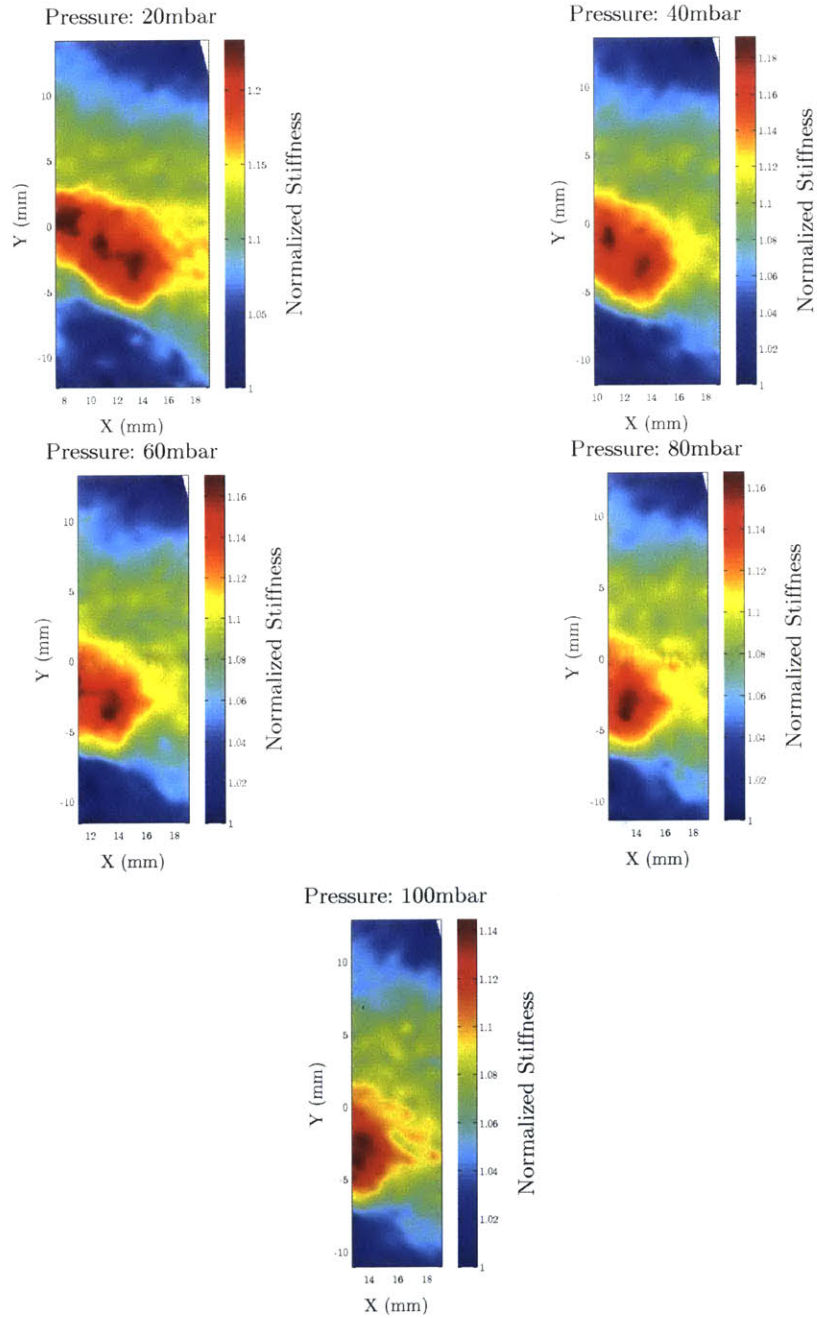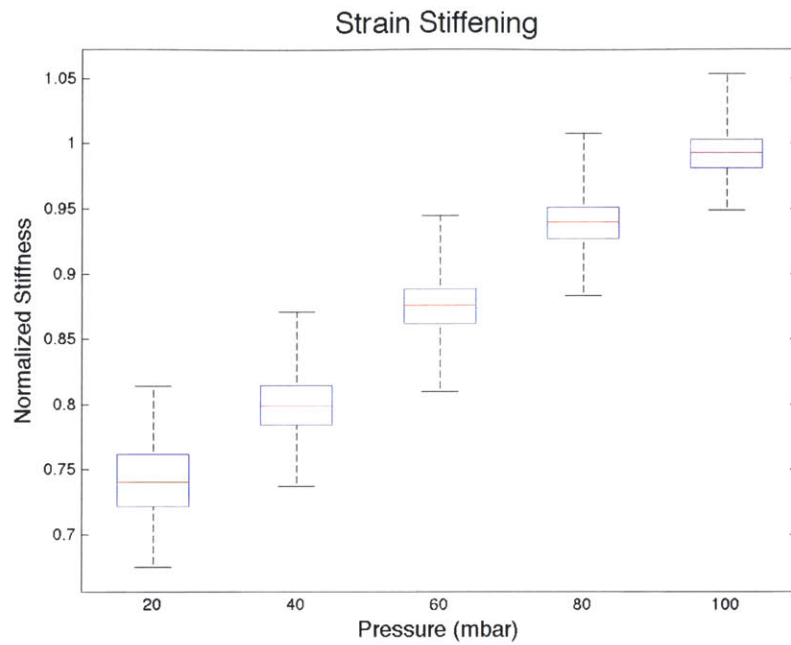Figure C-11: Patient 002 – Normalized stiffness maps

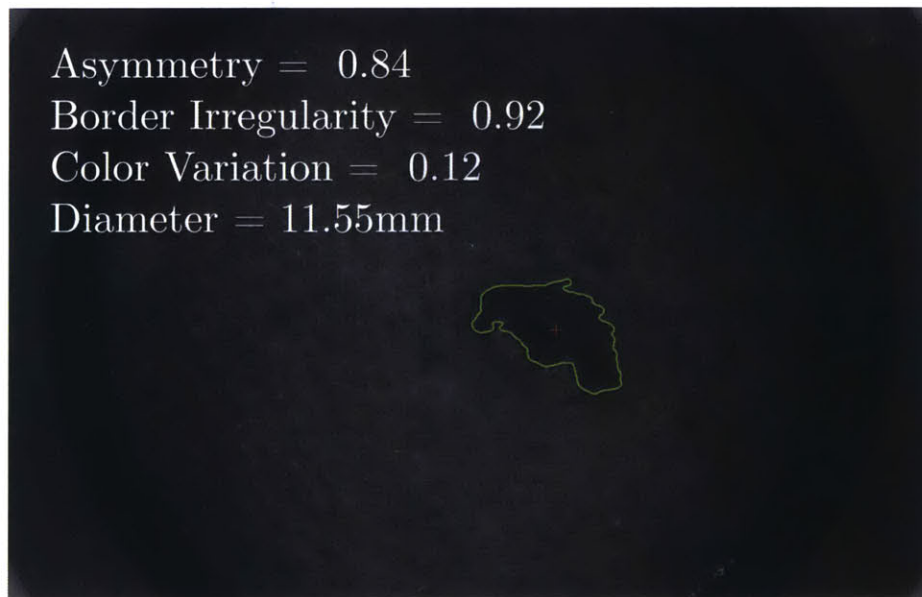Figure C-12: Patient 002 – Strain stiffening that occurs at higher pressures

Asymmetry = 0.84
Border Irregularity = 0.92
Color Variation = 0.12
Diameter = 11.55mm

Figure C-13: Patient 002 – Computed ABCD results

C.3 Patient 003 - Basal Cell Carcinoma

Patient 0033 was an 86 year old male with a suspected basal cell carcinoma in the middle of his back. A clinical image of the lesion is shown in Fig. C-14.

Figure C-14: Patient 003 – Clinical presentation of suspected basal cell carcinoma

Pathology confirmed that the lesion was a residual basal cell carcinoma with biopsy site changes. In the center of the excised specimen there is an ulceration or fibrosing granulation tissue in the upper portion of the dermis. In the surrounding dermis there are aggregates of basaloid cells.

A closer look at the histology (Fig. C-15 shows sheets of basophilic cells, appearing as blue dots, with a palisading perimeter of basal cell carcinoma cells. The basal cell carcinoma is extending from the epidermis in nodules and micro nodules. The small, white pocket in the middle of the lesion is an area of necrotic tissue. Necrosis occurs because the diffusion of nutrients is limited into the center of a large lesion. The higher power image, shown in Fig. C-16, reveals a close up picture of the aggregated

Figure C-15: Patient 003 – Histological cross-section of a large nodular basal cell carcinoma

nodules encased in a shell of fibrotic stroma. The darker pink area is an overexpression of collagen that will cause a noticeable change in stiffness.

Fig. C-17 is multiple histological views stitched together, such that the larger nodules of basal cell carcinoma can be seen, with micro nodules extending down from the epidermis. The stiffer fibrotic stroma that surrounds these nodules, acting as a shell, can also be seen. In between the large nodules of basal cell carcinoma is normal looking tissue. It is likely that this tissue is more compliant than the fibrotic stroma surrounding the cancerous tissue.

LesionAir was easily able to complete the entire data acquisition process for both the lesion and healthy symmetric region since the lesion was located on the flat portion of the back. The series of visible and structured light images of the lesion with corresponding pressure is shown in Fig. C-18. The normalized stiffness maps and corresponding overlaid images, shown in Fig. C-19, The maps show a clear increase in stiffness where the lesion is located, distinguishing the boundaries of the lesion.
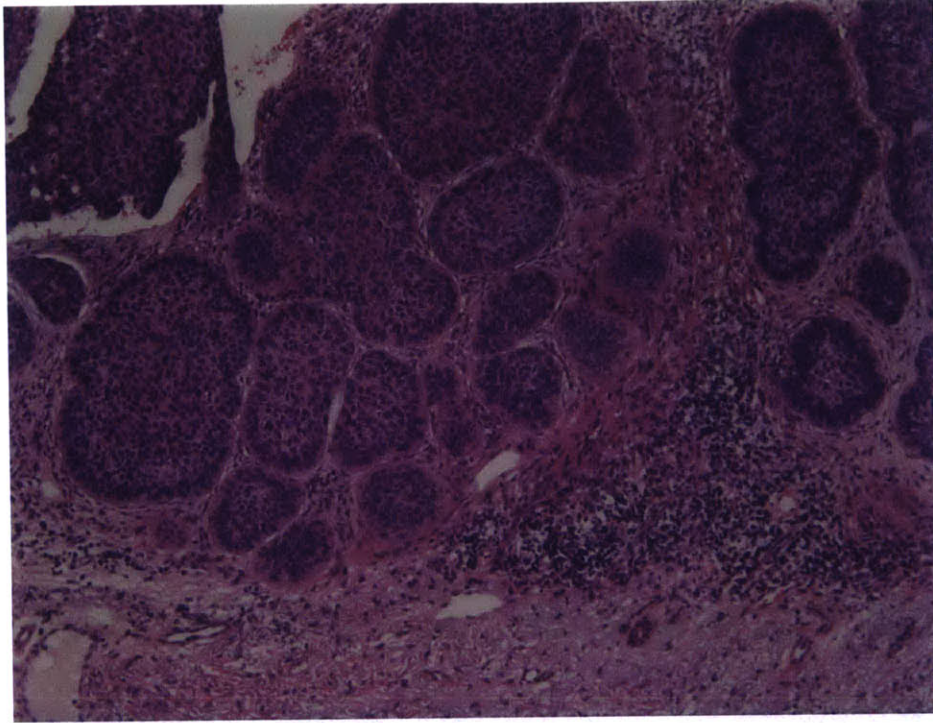
Figure C-16: Patient 003 – Histological view of nodular basal cell carcinoma with sclerotic capsule
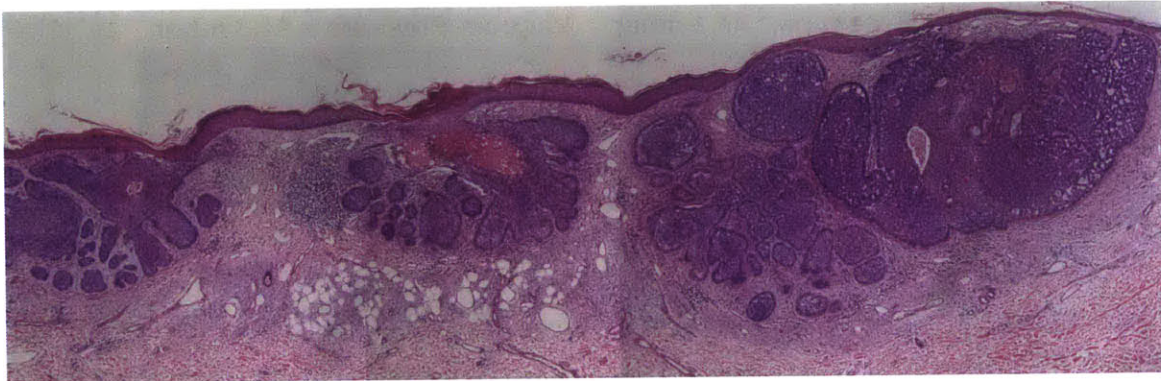
Figure C-17: Patient 003 – Macro histological view showing gaps of healthy tissue between basal cell carcinoma nodules

As predicted by the histology, there are pockets of more compliant tissue within the lesion, illustrating the devices ability to distinguish stiffness changes within the lesion. The strain stiffening of the tissue behaves as expected, increasing before plateauing.

Vacuum Pressure = 0.0 mbar   **Vacuum Pressure = 16.2 mbar**

Vacuum Pressure = 37.5 mbar   **Vacuum Pressure = 54.8 mbar**

Vacuum Pressure = 77.1 mbar   **Vacuum Pressure = 94.3 mbar**

Figure C-18: Patient 003 – Series of structured and visible light images taken during data acquisition cycle

Figure C-19: Patient 003 – Normalized stiffness maps

Figure C-20: Patient 003 – Strain stiffening that occurs at higher pressures

C.4 Patient 004 - Squamous Cell Carcinoma

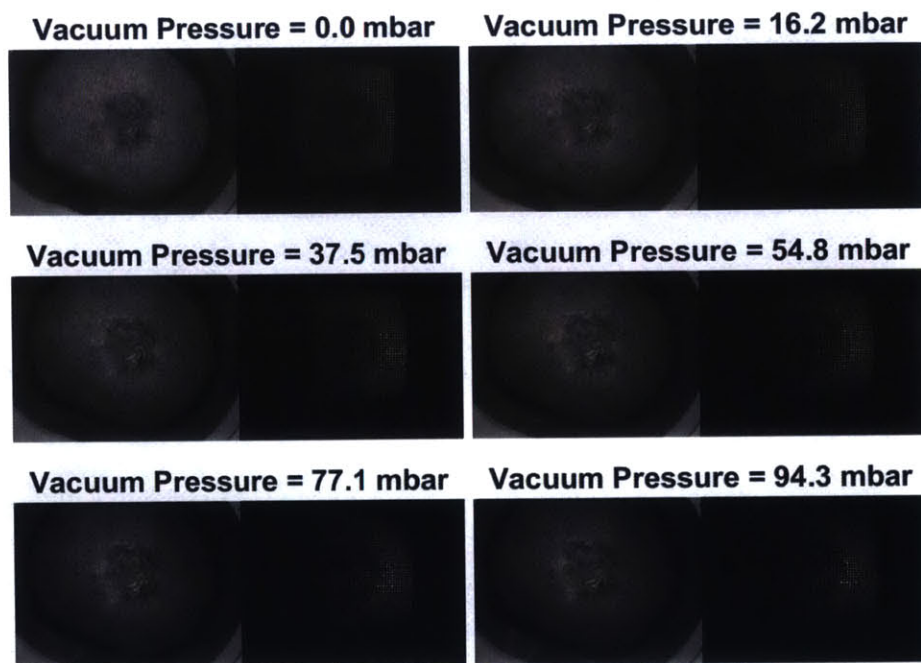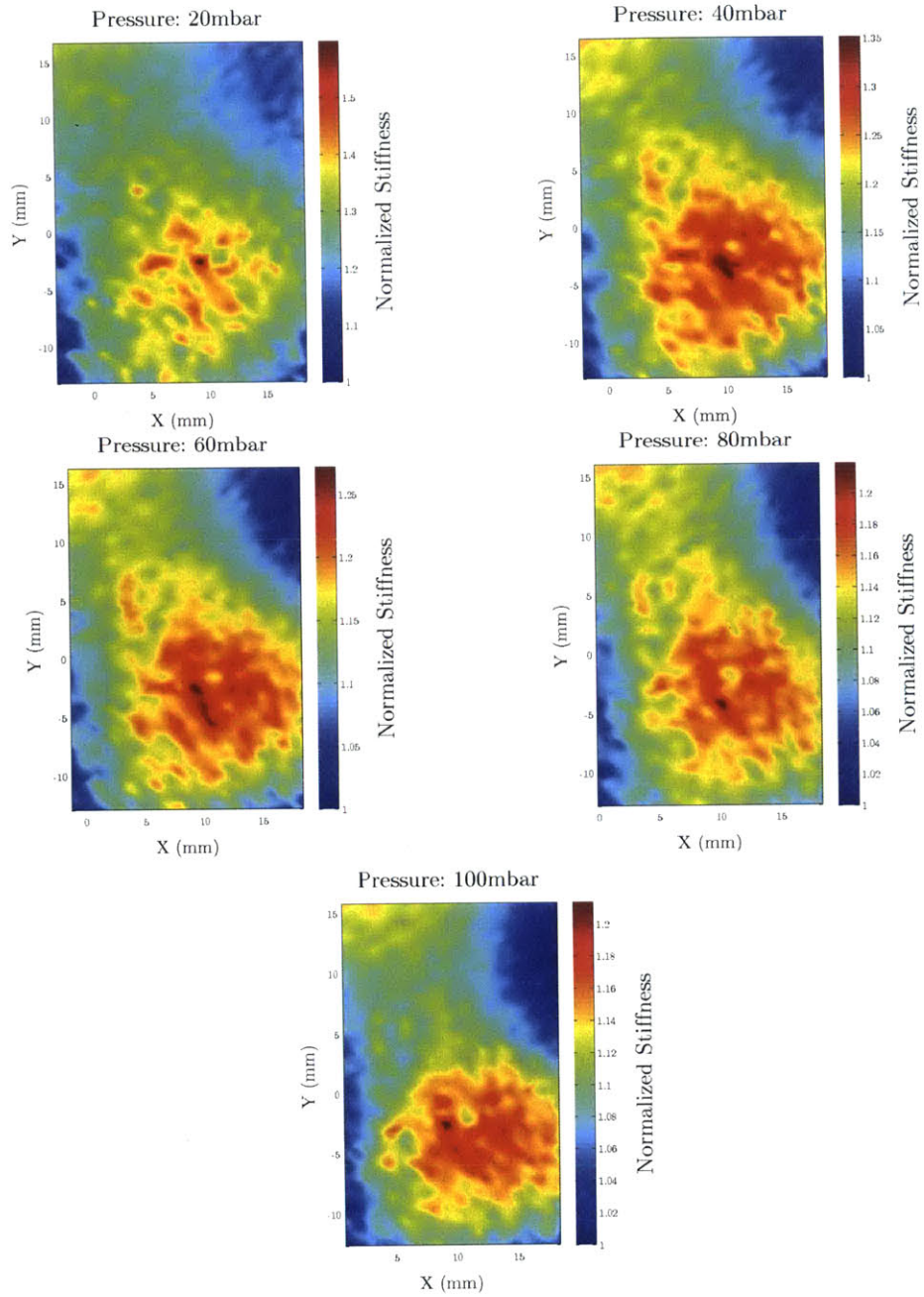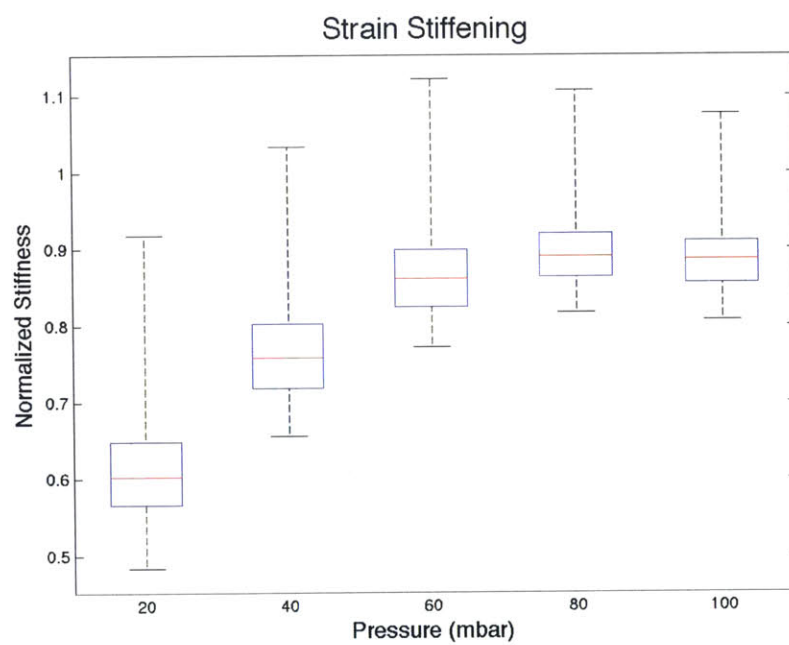Patient 004 is a 62 year old male with a suspected squamous cell carcinoma or actinic keratosis on the top of his right wrist. The clinical presentation of the lesion is shown in Fig. C-21. This lesion was also completely excised after clinical evaluation and data acquisition from LesionAir.

Figure C-21: Patient 004 – Clinical presentation of suspected squamous cell carcinoma

Pathology confirmed that the excised lesion was a superficial, inflamed squamous cell carcinoma. In the specimen there was large buds and cords of atypical keratinocytes emanating from the undersurface of the epidermis and extending into the upper portion of the reticular dermis.

As with patient 001, LesionAir was unable to complete the full set of tests. The seal was unable to hold the higher pressures on the wrist's curvature, so the tests were stopped prematurely. LesionAir was unable to acquire a full set of measurements were acquired for both the lesion and the healthy symmetric region.

The series of visible and structured light images of the lesion with corresponding pressure is shown in Fig. C-22.

211

Vacuum Pressure = 0.0 mbar **Vacuum Pressure = 16.5 mbar**

Vacuum Pressure = 34.7 mbar **Vacuum Pressure = 52.3 mbar**

Figure C-22: Patient 004 – Series of structured and visible light images taken during data acquisition cycle

Two normalized stiffness maps were created from the partial data sets and overlaid onto the visible light images for qualitative evaluation. Approximately half of the lesion appears to be stiffer than surrounding tissue, while the other half is compliant. Additionally, the partial dataset did not show any noticeable strain stiffening C-24.

Figure C-23: Patient 004 – Normalized stiffness maps
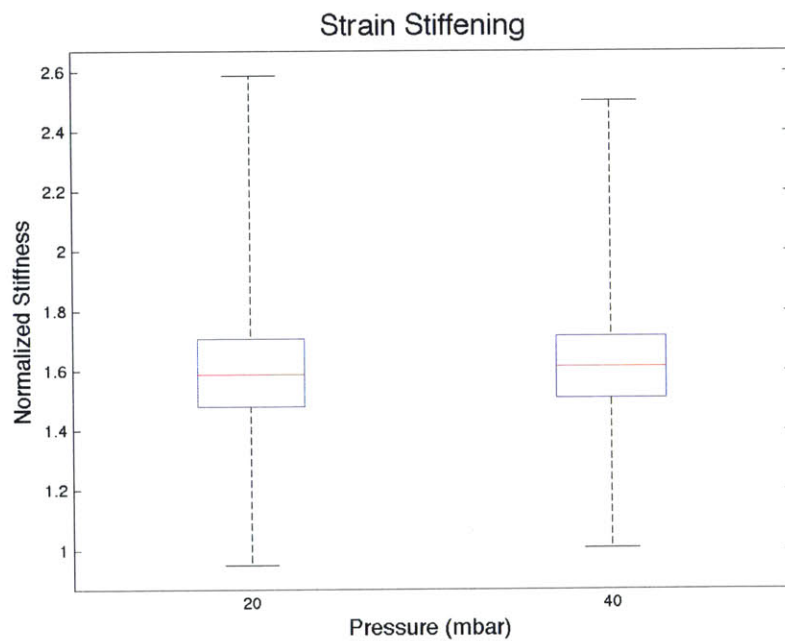
Figure C-24: Patient 004 – Strain stiffening that occurs at higher pressures

C.5 Patient 005 - Intradermal Nevus

Patient 005 was a 25 year old female with a suspected intradermal nevus on her right lateral torso. Fig. C-25 shows the clinical presentation of the nevus. This lesion was not biopsied, but was confirmed by the dermatologist to not be cancerous. The dermatologist commented that the lesion felt very soft compared to surrounding tissue.

Figure C-25: Patient 005 – Clinical presentation of suspected intradermal nevus

LesionAir completed a full testing cycle on the lesion and symmetric healthy tissue. An array of the visible and structured light images that were acquired is shown in Fig. C-26.

The resulting normalized stiffness maps (Fig. C-27) illustrate exactly what the dermatologist described. The lesion is much more compliant than surrounding tissue.

214

Vacuum Pressure = 0.0 mbar   **Vacuum Pressure = 12.2 mbar**

Vacuum Pressure = 35.5 mbar   **Vacuum Pressure = 47.7 mbar**

Vacuum Pressure = 69.0 mbar   **Vacuum Pressure = 84.2 mbar**
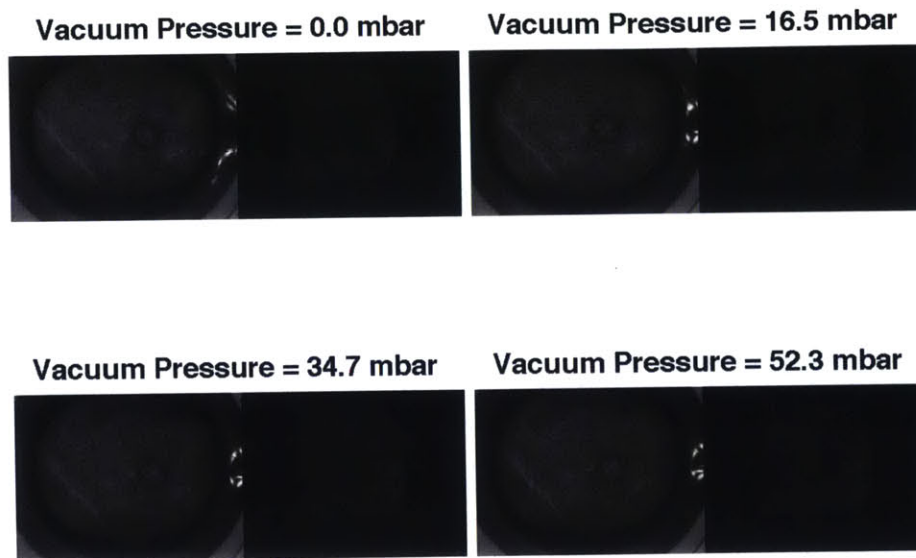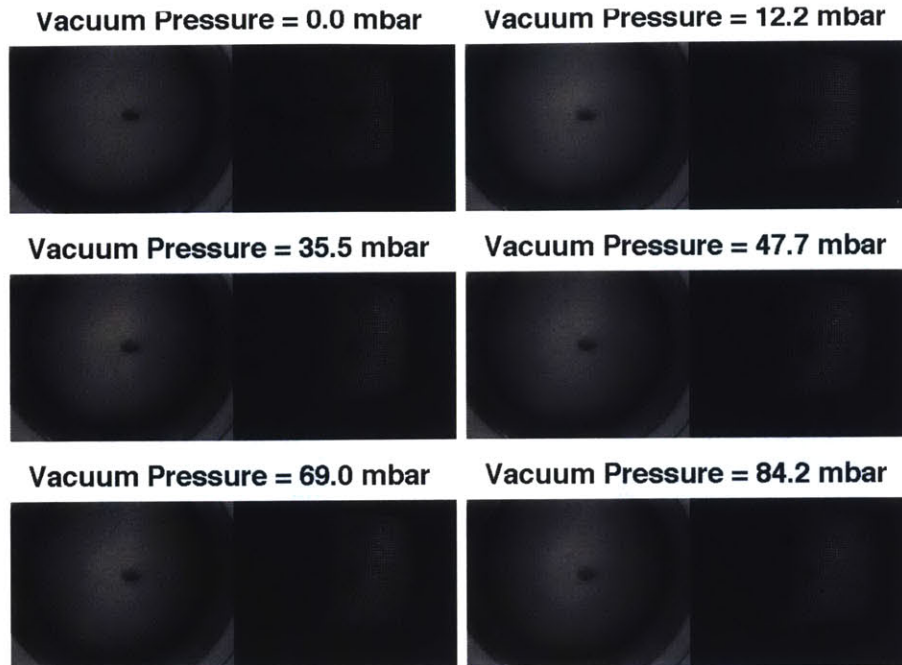

Figure C-26: Patient 005 – Series of structured and visible light images taken during data acquisition cycle

The analysis of the strain stiffening of the tissue was inconclusive. The 80 mbar data appears to be much more compliant than the other data sets, which could have been caused by a faulty measurement.

The ABCD morphology quantification, shown in Fig. C-29, appears quite normal. The algorithm accurately segmented the lesion, and the ABCD metrics are quite small, signifying a low probability of cancer.
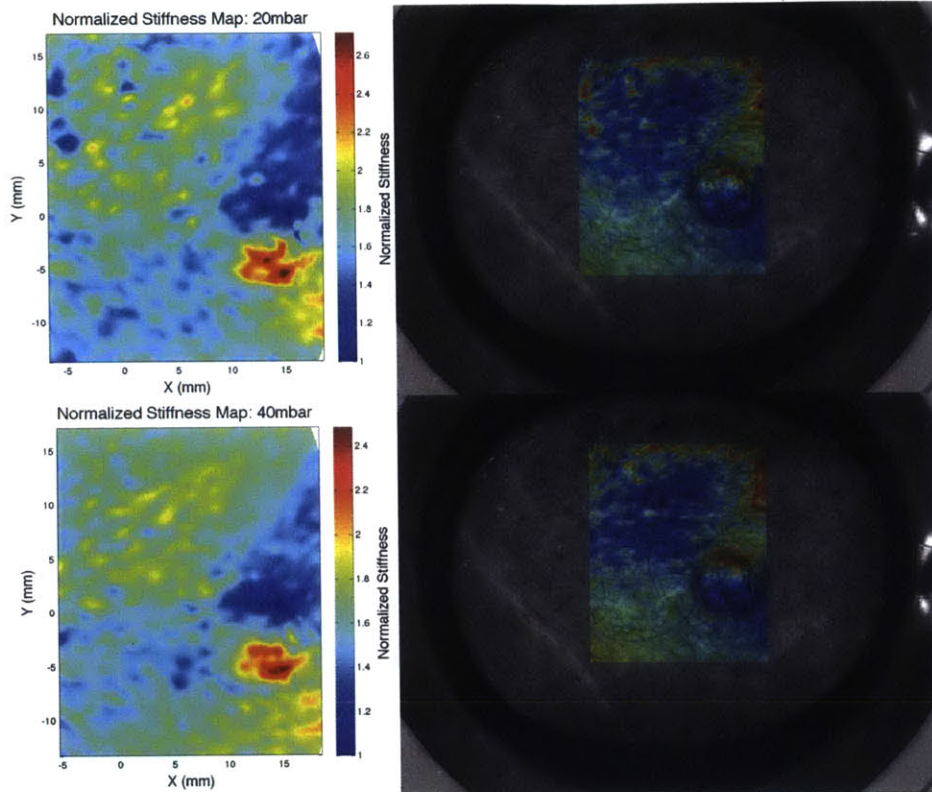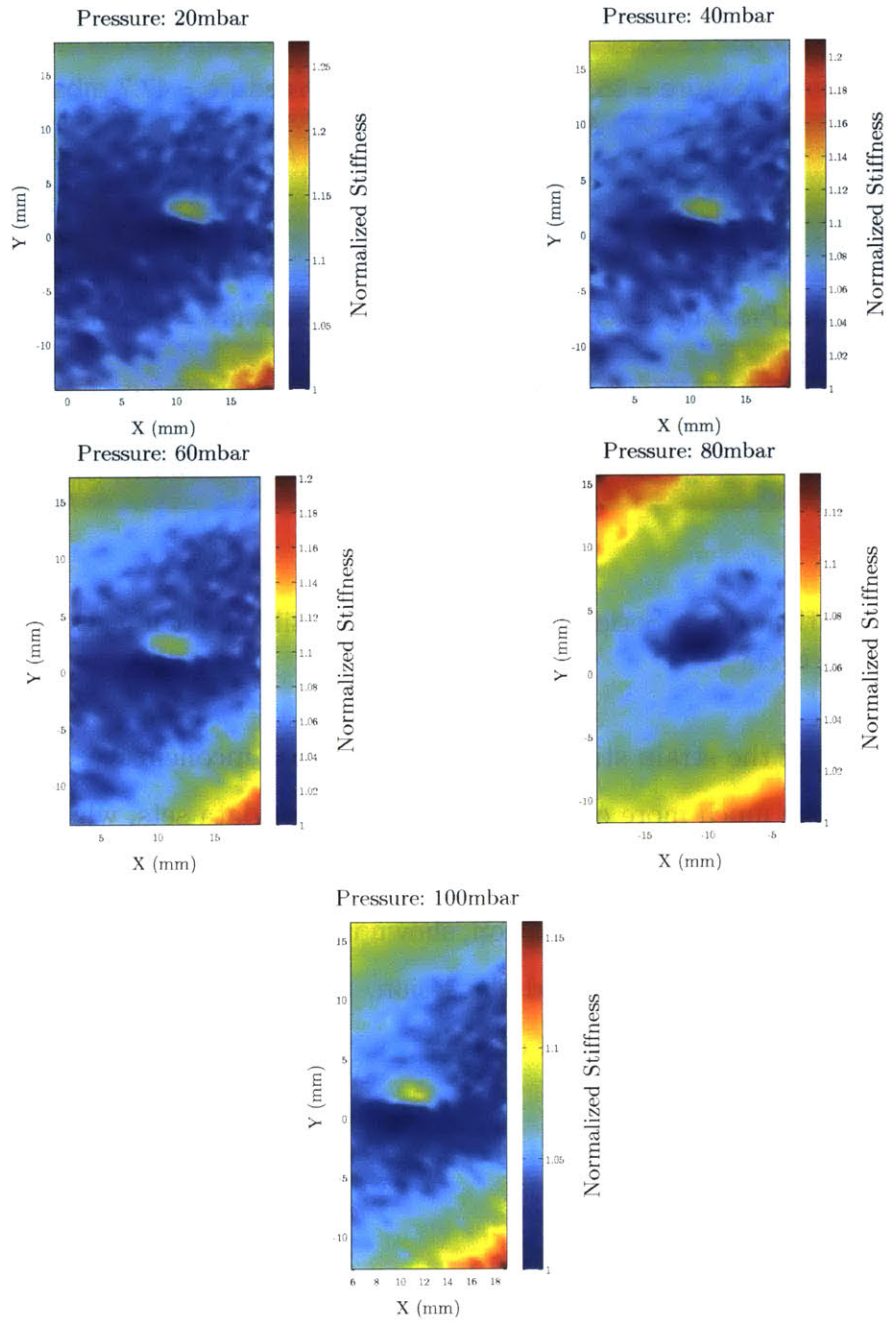
Figure C-27: Patient 005 – Normalized stiffness maps
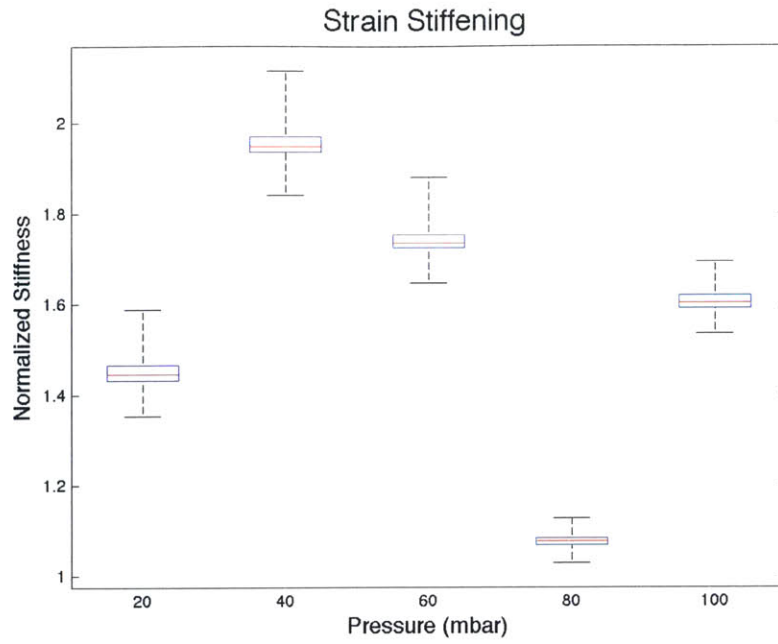
Figure C-28: Patient 005 – Strain stiffening that occurs at higher pressures
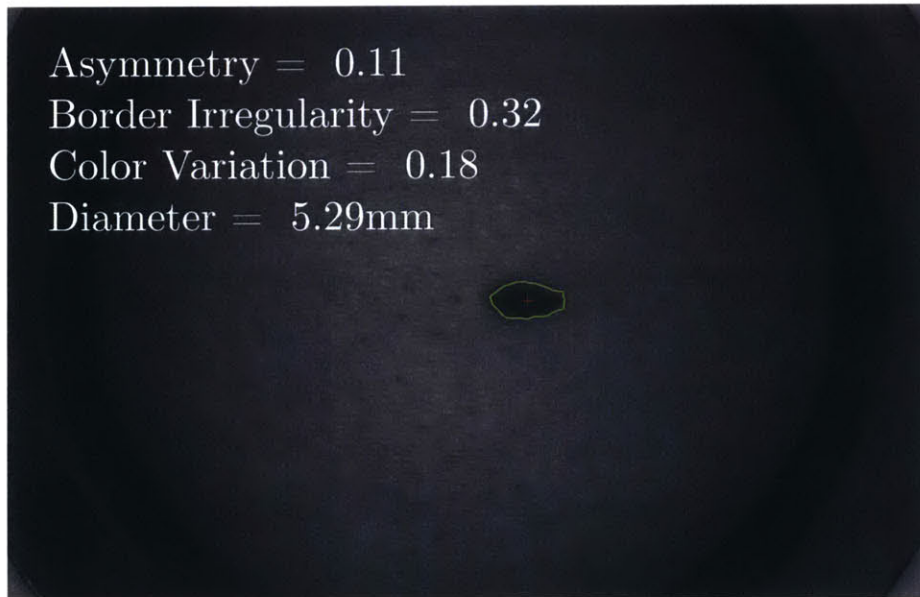
Figure C-29: Patient 005 – Computed ABCD results

C.6 Patient 006 - Seborrheic Keratosis

Patient 006 was a 72 year old male with a seborrheic keratosis, as seen in Fig. C-30, on the medial side of his right knee. The lesion was not biopsied, but the dermatologist commented that the lesion felt scaly, but similar in stiffness to the surrounding tissue.

Figure C-30: Patient 006 – Clinical presentation of suspected seborrheic keratosis

LesionAir was able to collect all but one image from the data acquisition cycle. The 100 mbar pressure on the healthy symmetric tests was too great for the seal so the test was killed prematurely. The irregular contour of the inner knee made the placement of the seal very finicky.

The normalized stiffness maps and associated overlaid images, shown in Fig. C-32, display a fairly consistent stiffness across the bulk of the image. The top and bottom of the images show an increase in stiffness that is likely attributed to the interpolation error at the edges of the data set.

The tissue strain stiffening for patient 006 is mostly consistent, with a noticeable increase for the 80 mbar measurement.

Vacuum Pressure = 0.0 mbar   **Vacuum Pressure = 11.2 mbar**

Vacuum Pressure = 30.4 mbar   **Vacuum Pressure = 52.8 mbar**

Vacuum Pressure = 69.0 mbar   **Vacuum Pressure = 84.2 mbar**

Figure C-31: Patient 006 – Series of structured and visible light images taken during data acquisition cycle

Figure C-32: Patient 006 – Normalized stiffness maps

Figure C-33: Patient 006 – Strain stiffening that occurs at higher pressures

C.7 Patient 007 - Congenital Nevus

Patient 007 is a 21 year old male with a macular congenital nevus, shown in Fig. C-34, on his right upper back. The patient had several similar lesions all over his body, and the lesion was clinically evaluated to be non-cancerous, so it was not biopsied.

Figure C-34: Patient 007 – Clinical presentation of suspected macular congenital nevus

A full data acquisition procedure was performed by LesionAir. The captured images can be seen in Fig. C-35.

Fig. C-36 shows the normalized stiffness maps and corresponding overlaid images. The top and bottom of the image show reduced stiffness compared to the consistent band stretching across the middle. The stiffness pattern does not appear to be associated with with any visible features.

The ABCD morphology analysis results can be seen in Fig. C-38. The segmentation and border identification matches the lesion and the metric values are quite low, implying a low risk of cancer.

Vacuum Pressure = 0.0 mbar　　　**Vacuum Pressure = 9.1 mbar**

Vacuum Pressure = 27.4 mbar　　**Vacuum Pressure = 47.7 mbar**

Vacuum Pressure = 65.0 mbar　　**Vacuum Pressure = 78.2 mbar**
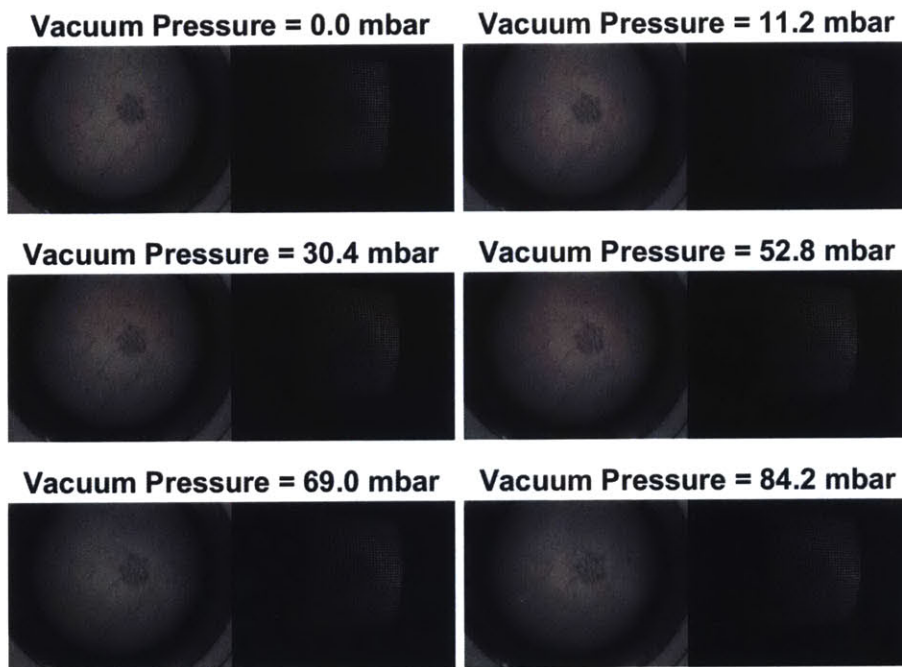
Figure C-35: Patient 007 – Series of structured and visible light images taken during data acquisition
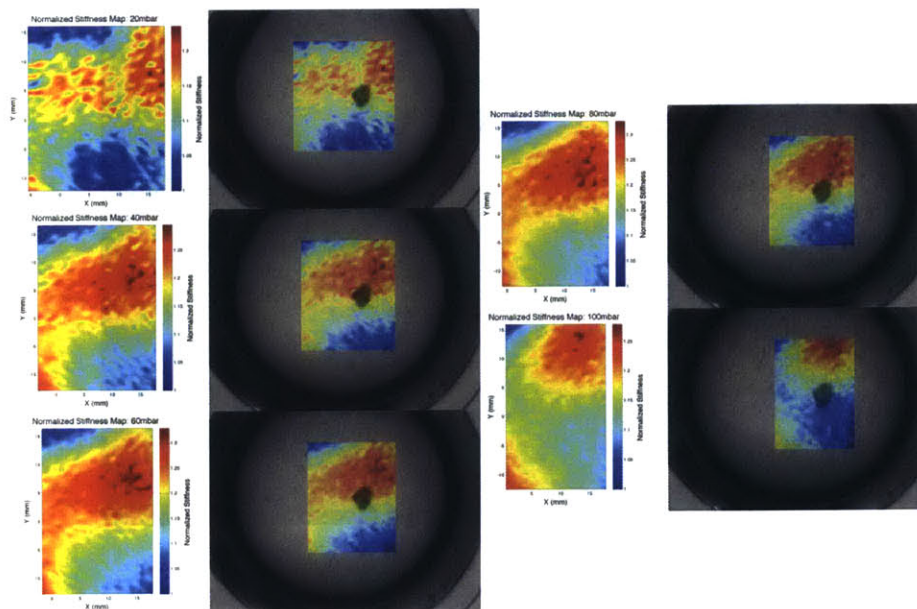
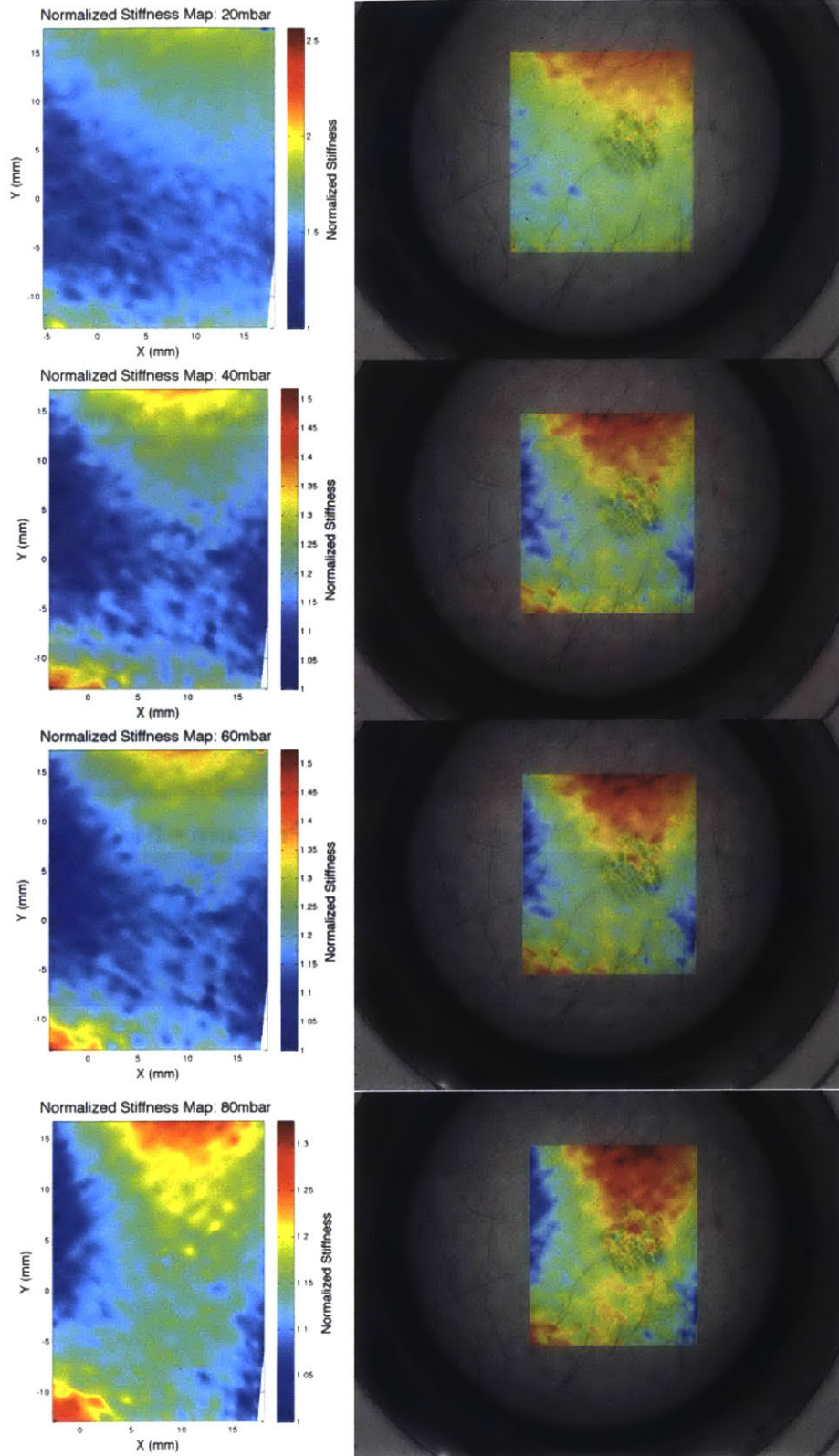Figure C-36: Patient 007 – Normalized stiffness maps

223
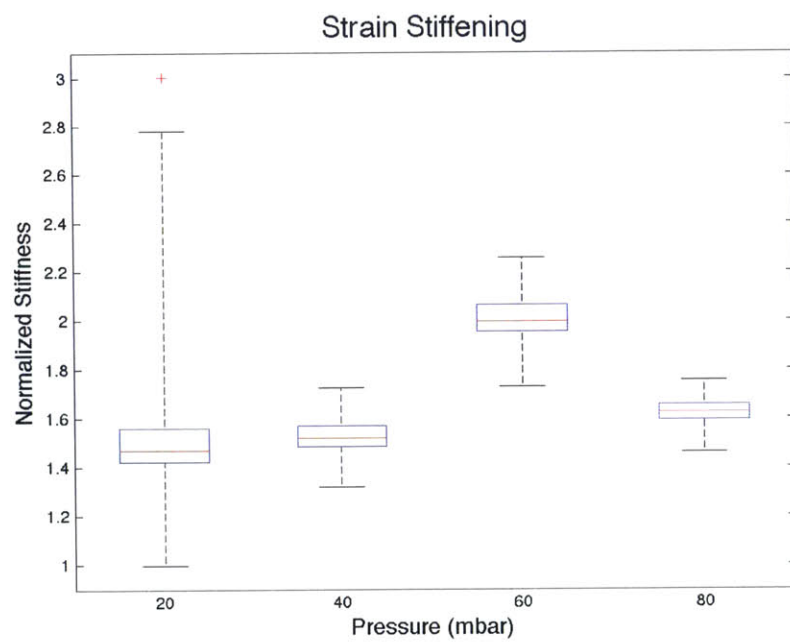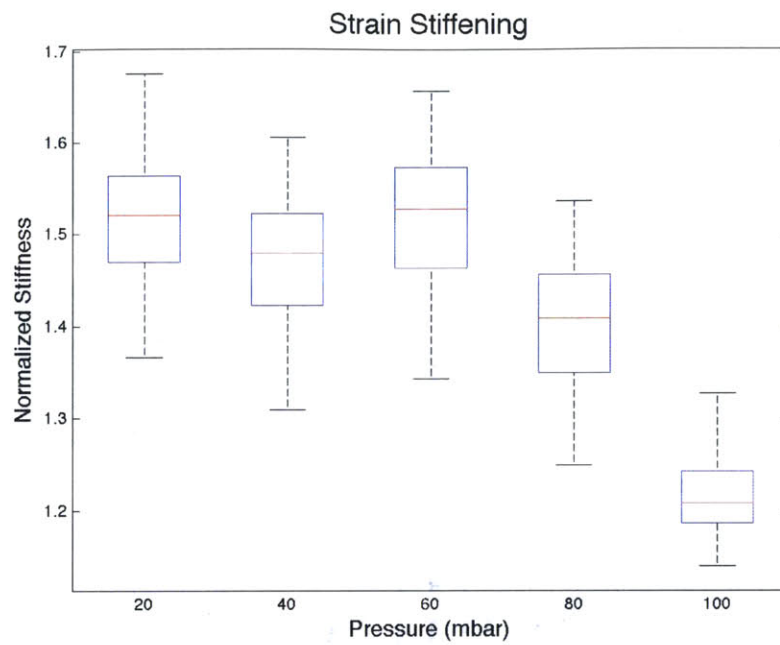
Figure C-37: Patient 007 – Strain stiffening that occurs at higher pressures
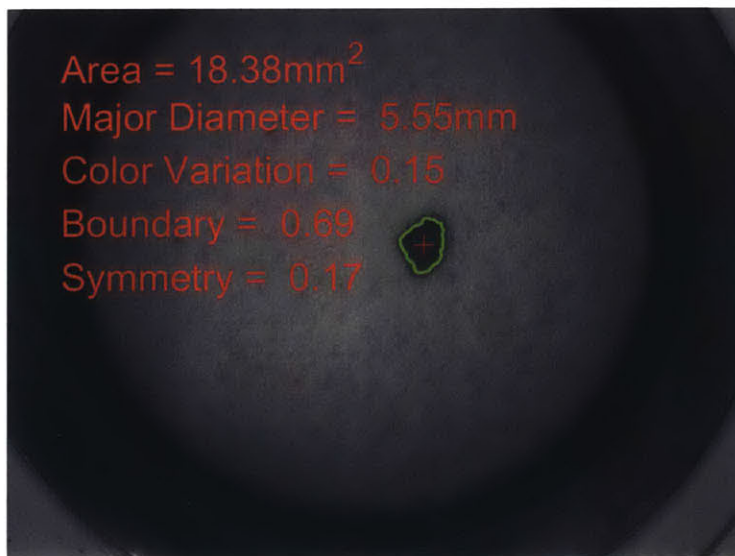
Figure C-38: Patient 007 – computed ABCD results

C.8   Patient 008 - Intradermal Nevus

Patient 008 is an 82 year old male with an intradermal nevus on on the right side of his mid-back with an appearance as shown in Fig. C-39. The lesion was diagnosed as an intradermal nevus, but it was still biopsied because of its atypical appearance.

Figure C-39: Patient 008 – Clinical presentation of suspected intradermal nevus

Pathology confirmed the lesion as an intradermal melanocytic nevus. The biopsy specimen showed orderly nests, cords and strands of uniform nevus cells within the dermis.

LesionAir was able to complete a full test, without losing a seal on the flat area on the back. The normalized stiffness maps show a uniform stiffness across the field of view with the stiffer regions not corresponding to any visible structures on the surface of the tissue.

The stiffness of the tissue was consistent for the lower pressures, but increased for the higher pressures, demonstrating the strain stiffening effect.

Vacuum Pressure = 0.0 mbar   **Vacuum Pressure = 12.2 mbar**

Vacuum Pressure = 32.5 mbar   **Vacuum Pressure = 48.7 mbar**

Vacuum Pressure = 67.0 mbar   **Vacuum Pressure = 82.2 mbar**
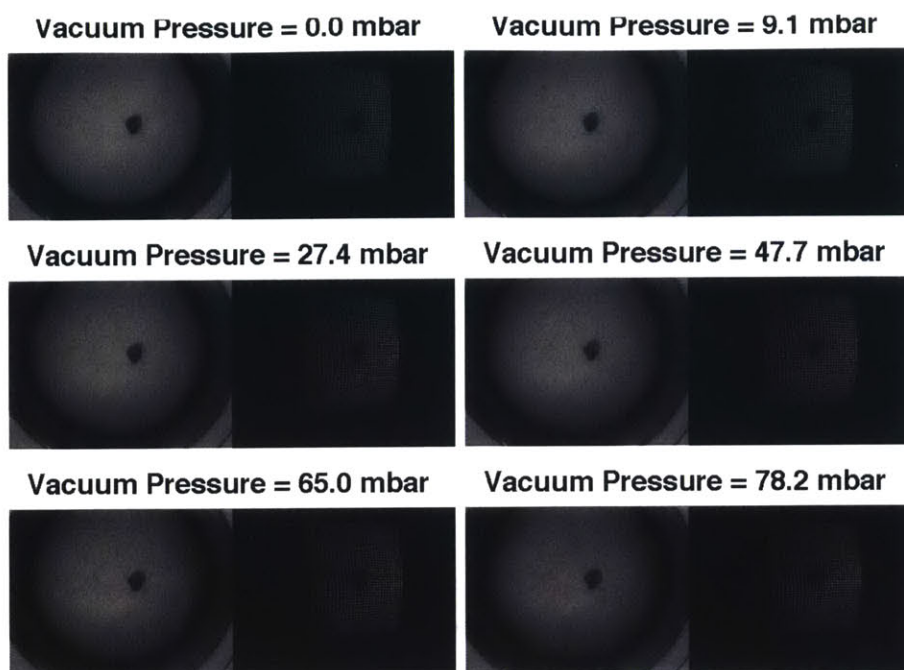
Figure C-40: Patient 008 – Series of structured and visible light images taken during data acquisition cycle
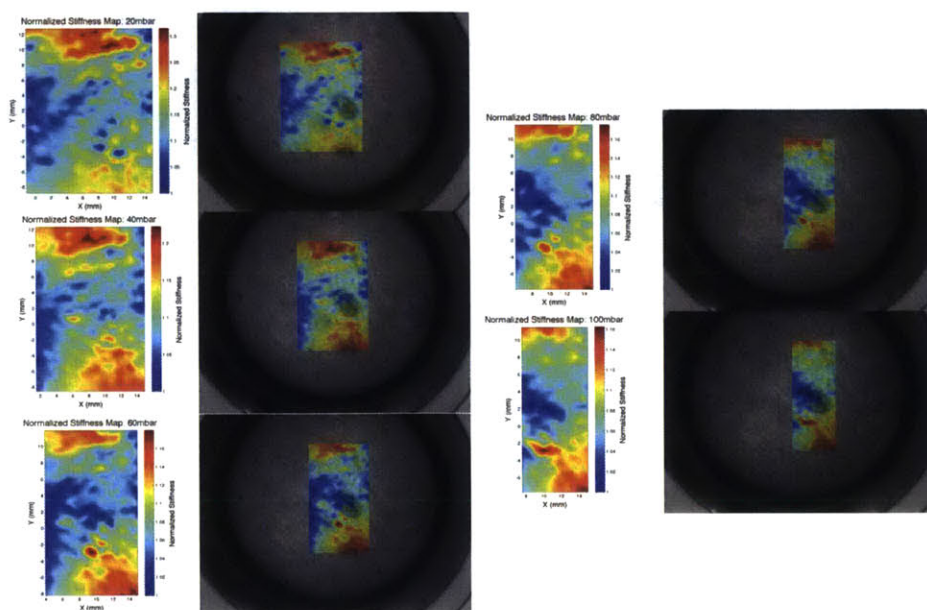
Figure C-41: Patient 008 – Normalized stiffness maps

The ABCD morphology quantification, shown in Fig. C-43, appears quite normal. The algorithm accurately segmented the lesion, and the ABCD metrics are quite small, suggesting a low probability of cancer.
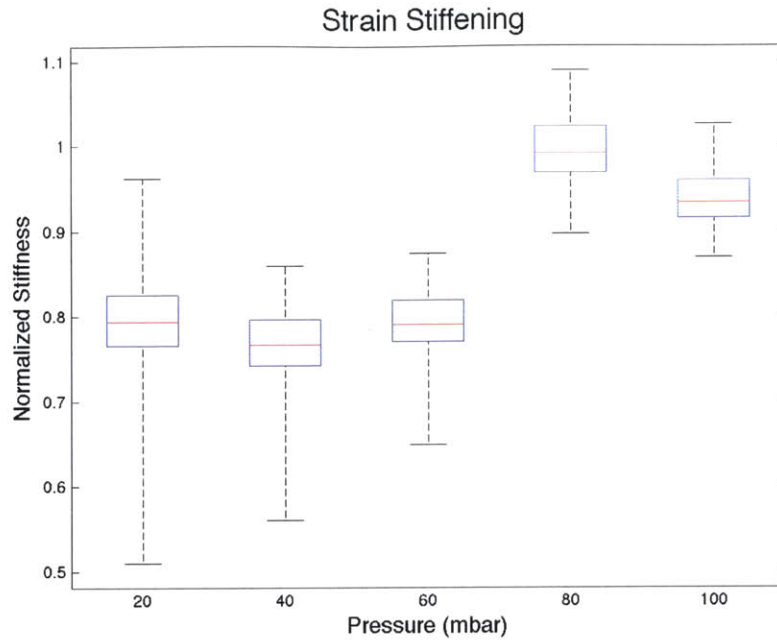
Figure C-42: Patient 008 – Strain stiffening that occurs at higher pressures
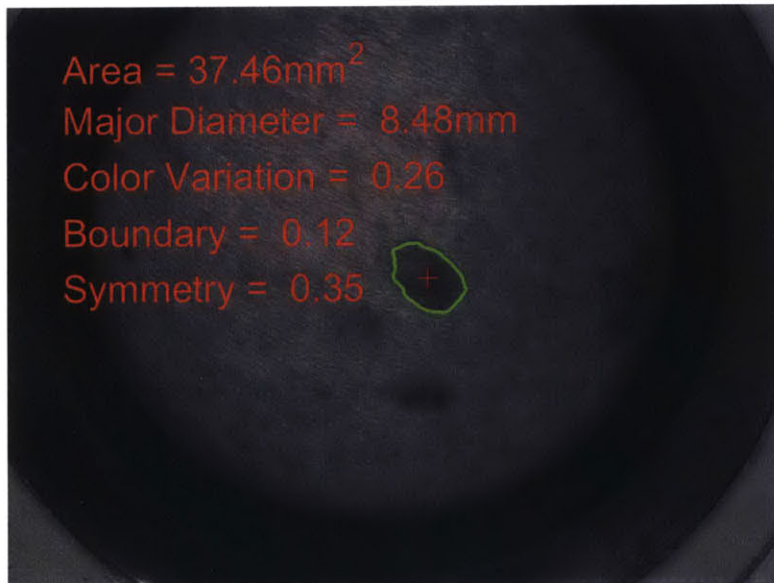
Figure C-43: Patient 008 – Computed ABCD results

C.9 Patient 009 - Actinic Keratosis

Patient 009 is a 50 year old female with a suspected actinic keratosis on her right upper back. The patient opted to not have a biopsy performed.

Figure C-44: Patient 009 – Clinical presentation of suspected actinic keratosis

LesionAir completed a full testing cycle on the lesion and symmetric healthy tissue. An array of the visible and structured light images that were acquired is shown in Fig. C-45.

The normalized stiffness maps and associated overlaid images, shown in Fig. C-46, display a consistent stiffness across the bulk of the image. The top and bottom of the images show a slight increase in stiffness that is likely attributed to the interpolation error at the edges of the data set.

The resulting maps display a peculiar reduction in stiffness as the pressure is increased. It is unknown why this occurred.

Vacuum Pressure = 0.0 mbar   **Vacuum Pressure = 12.2 mbar**

Vacuum Pressure = 32.5 mbar   **Vacuum Pressure = 47.7 mbar**

Vacuum Pressure = 64.9 mbar   **Vacuum Pressure = 83.2 mbar**
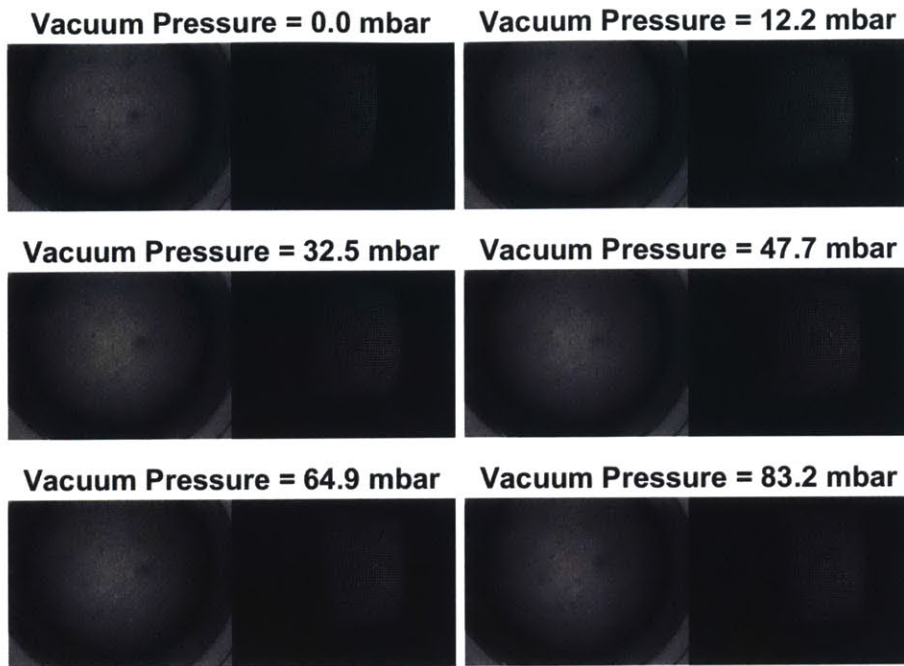
Figure C-45: Patient 009 – Series of structured and visible light images taken during data acquisition cycle
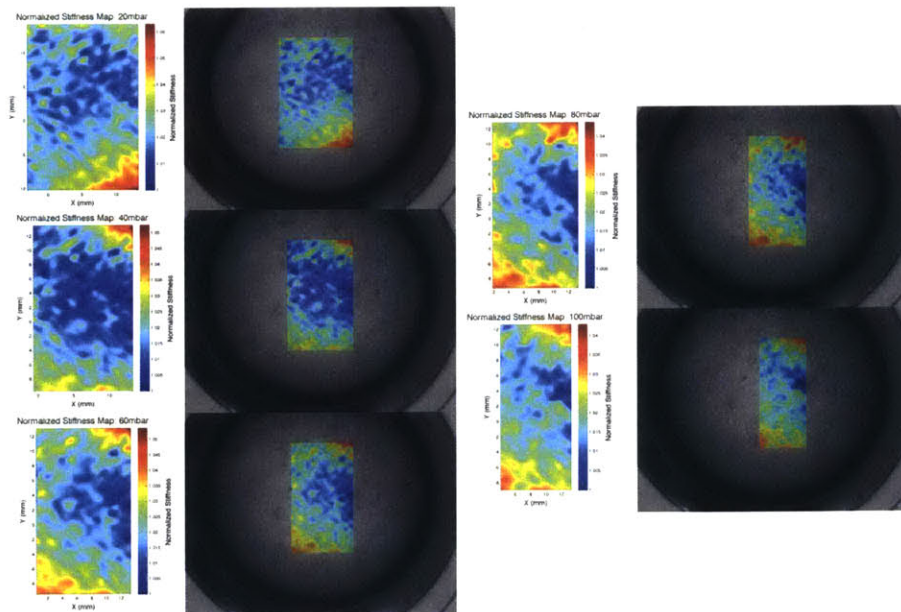
Figure C-46: Patient 009 – Normalized stiffness maps
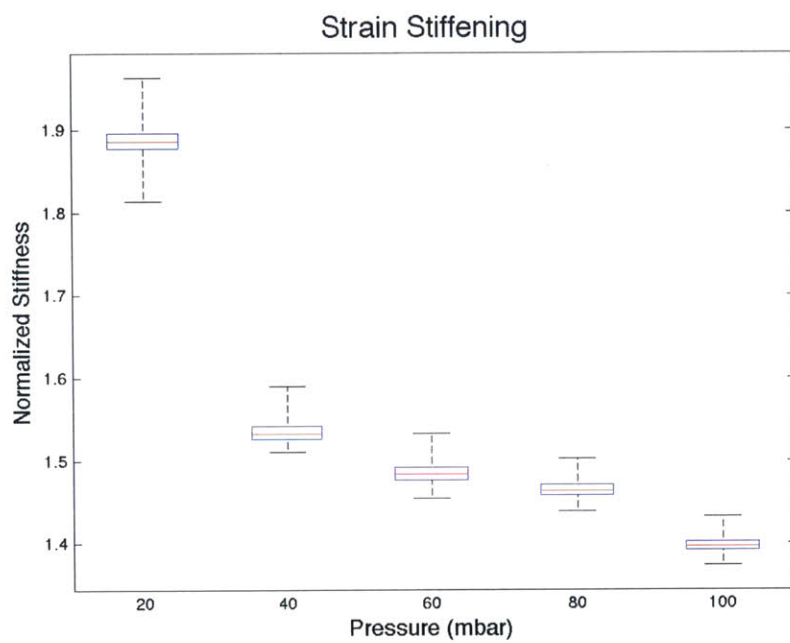
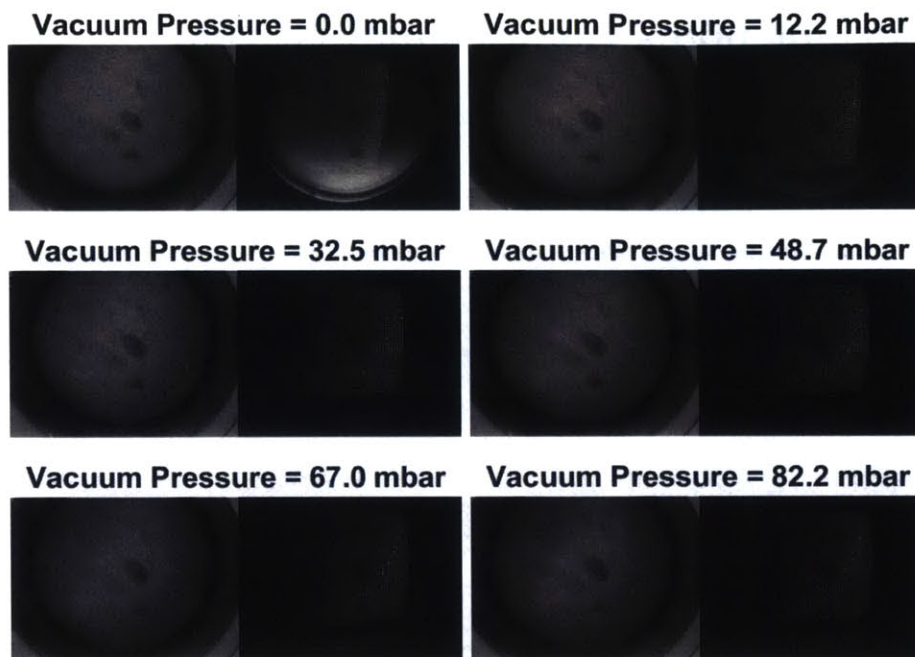Figure C-47: Patient 009 – Strain stiffening that occurs at higher pressures

C.10 Patient 010 - Intradermal Nevus

Patient 010 is a 29 year old male with an intradermal nevus, shown in Fig C-48, on the middle of his upper abdomen. The lesion was deemed not cancerous by the dermatologist due to its small symmetric shape and uniform color. Palpation of the lesion revealed it was slightly stiffer than surrounding tissue, but the patient commented that it had received trauma before, causing a likely increase in fibrotic tissue.

Figure C-48: Patient 010 – Clinical presentation of a intradermal nevus

The array of LesionAir captured images and associated pressures is shown in Fig. C-49.

The normalized stiffness maps and associated overlaid images show a regular stiffness pattern across the field of view, with increased localized regions of stiffness and compliance on the lesion.

As expected, Fig. C-51 demonstrates an increase in tissue stiffness as the pressure is increased.

Vacuum Pressure = 0.0 mbar **Vacuum Pressure = 10.1 mbar**

Vacuum Pressure = 29.4 mbar **Vacuum Pressure = 46.6 mbar**

Vacuum Pressure = 64.8 mbar **Vacuum Pressure = 79.0 mbar**
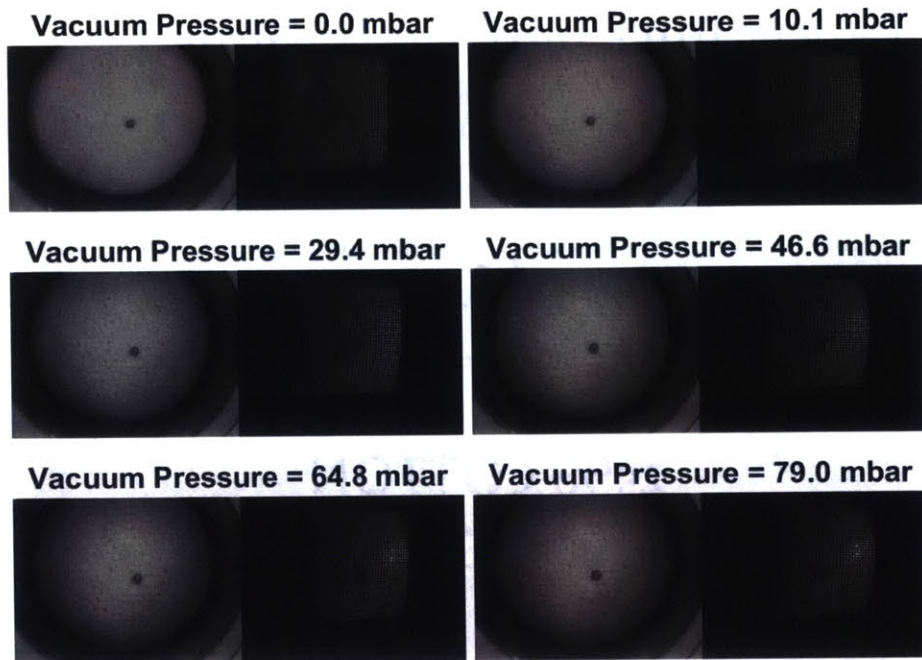
Figure C-49: Patient 010 – Series of structured and visible light images taken during data acquisition cycle
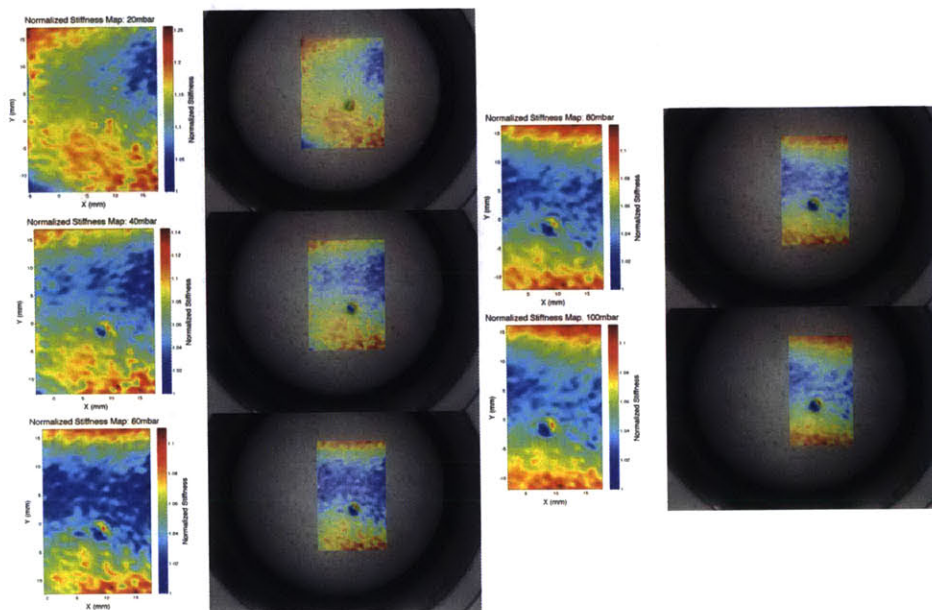
Figure C-50: Patient 010 – Normalized stiffness maps

The results of the ABCD morphology quantification are shown in Fig. C-52. The segmentation algorithm accurately segmented the lesion. The diameter, boundary, and symmetry values were all small, signifying a low cancer probability.

232
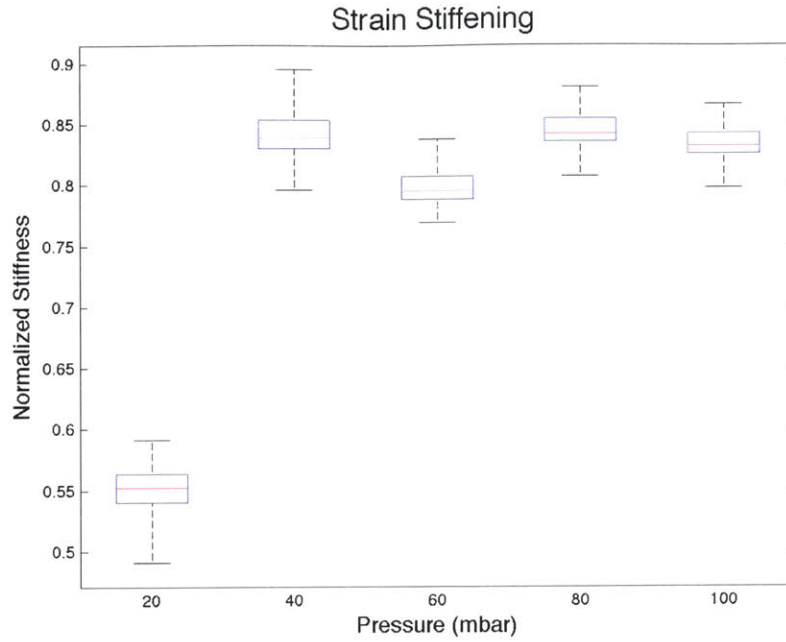
Figure C-51: Patient 010 – Strain stiffening that occurs at higher pressures
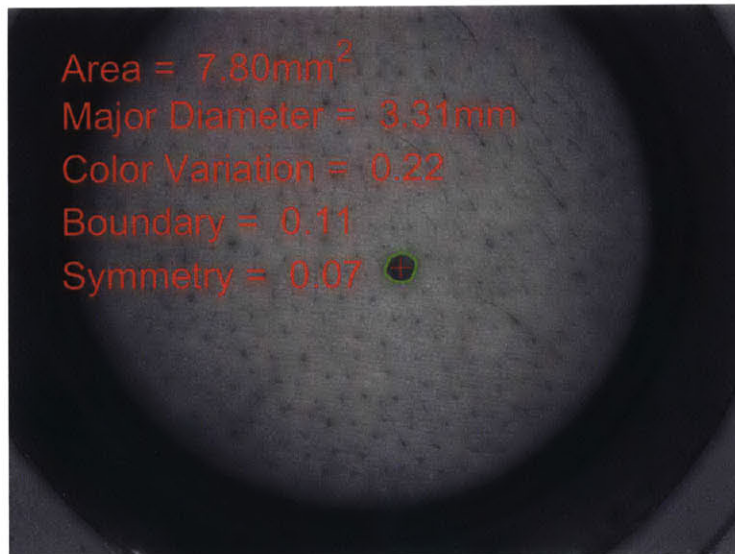
Figure C-52: Patient 010 – Computed ABCD results

233

Bibliography

[1] H. W. Rogers, M. A. Weinstock, S. R. Feldman, and B. M. Coldiron, "Incidence estimate of nonmelanoma skin cancer (keratinocyte carcinomas) in the u.s. population, 2012," *JAMA Dermatol*, vol. 151, no. 10, pp. 1081–6, 2015.

[2] "Cancer facts & figures 2016," American Cancer Society, Tech. Rep., 2016.

[3] U. C. S. W. Group, "United states cancer statistics: 1999–2010 incidence and mortality web-based report," *Atlanta: US Department of Health and Human Services, Centers for Disease Control and Prevention and National Cancer Institute*, 2013.

[4] J. K. Robinson, "Sun exposure, sun protection, and vitamin d," *Jama*, vol. 294, no. 12, pp. 1541–1543, 2005.

[5] R. L. Siegel, K. D. Miller, and A. Jemal, "Cancer statistics, 2016," *CA: A cancer journal for clinicians*, 2015.

[6] R. Siegel, C. DeSantis, K. Virgo, K. Stein, A. Mariotto, T. Smith, D. Cooper, T. Gansler, C. Lerro, S. Fedewa, C. Lin, C. Leach, R. S. Cannady, H. Cho, S. Scoppa, M. Hachey, R. Kirch, A. Jemal, and E. Ward, "Cancer treatment and survivorship statistics, 2012," *CA: A Cancer Journal for Clinicians*, vol. 62, no. 4, pp. 220–241, 2012.

[7] T. Diepgen and V. Mahler, "The epidemiology of skin cancer," *British Journal of Dermatology*, vol. 146, no. 61, pp. 1–6, 2002.

[8] J. Gloster, H. M. and D. G. Brodland, "The epidemiology of skin cancer," *Dermatologic Surgery*, vol. 22, no. 3, pp. 217–26, 1996.

[9] H. G. Welch, S. Woloshin, and L. M. Schwartz, "Skin biopsy rates and incidence of melanoma: population based ecological study," *British Medical Journal*, vol. 331, no. 7515, p. 481, 2005.

[10] H. I. Hall, P. Jamison, J. P. Fulton, G. Clutter, S. Roffers, and P. Parrish, "Reporting cutaneous melanoma to cancer registries in the united states," *Journal of the American Academy of Dermatology*, vol. 49, no. 4, pp. 624–630, 2003.

[11] E. Linos, S. M. Swetter, M. G. Cockburn, G. A. Colditz, and C. A. Clarke, "Increasing burden of melanoma in the united states," *J Invest Dermatol*, vol. 129, no. 7, pp. 1666–74, 2009.

[12] D. S. Rigel and J. A. Carucci, "Malignant melanoma: prevention, early detection, and treatment in the 21st century," *CA Cancer J Clin*, vol. 50, no. 4, pp. 215–36; quiz 237–40, 2000.

[13] S. Sahin, B. Rao, A. W. Kopf, E. Lee, D. S. Rigel, R. Nossa, I. J. Rahman, H. Wortzel, A. A. Marghoob, and R. S. Bart, "Predicting ten-year survival of patients with primary cutaneous melanoma: corroboration of a prognostic model," *Cancer*, vol. 80, no. 8, pp. 1426–31, 1997.

[14] E. L. Psaty and A. C. Halpern, "Current and emerging technologies in melanoma diagnosis: the state of the art," *Clin Dermatol*, vol. 27, no. 1, pp. 35–45, 2009.

[15] U. P. S. T. Force, "Counseling to prevent skin cancer: recommendations and rationale of the u.s. preventive services task force," *MMWR Recomm Rep*, vol. 52, no. RR-15, pp. 13–7, 2003.

[16] A. F. Jerant, J. T. Johnson, C. D. Sheridan, and T. J. Caffrey, "Early detection and treatment of skin cancer," *Am Fam Physician*, vol. 62, no. 2, pp. 357–68, 375–6, 381–2, 2000.

[17] M. Elbaum, "Computer-aided melanoma diagnosis," *Dermatol Clin*, vol. 20, no. 4, pp. 735–47, x–xi, 2002.

[18] J. D. Whited and J. M. Grichnik, "The rational clinical examination. does this patient have a mole or a melanoma?" *JAMA*, vol. 279, no. 9, pp. 696–701, 1998.

[19] L. K. Ferris and R. J. Harris, "New diagnostic aids for melanoma," *Dermatol Clin*, vol. 30, no. 3, pp. 535–45, 2012.

[20] I. H. Wolf, J. Smolle, H. P. Soyer, and H. Kerl, "Sensitivity in the clinical diagnosis of malignant melanoma," *Melanoma Res*, vol. 8, no. 5, pp. 425–9, 1998.

[21] A. H. Slocum, *Precision machine design*. Society of Manufacturing Engineers, 1992.

[22] J. Kanitakis, "Anatomy, histology and immunohistochemistry of normal human skin," *European journal of dermatology: EJD*, vol. 12, no. 4, pp. 390–9; quiz 400–1, 2001.

[23] C.-A. Butnaru and J. Kanitakis, "Structure of normal human skin," *EJD. European journal of dermatology*, vol. 12, no. 6, pp. II–IV, 2002.

[24] R. Warwick, P. L. Williams *et al.*, *Gray's anatomy*. Longman Edinburgh, 1973, vol. 1302.

[25] C. Soutor and M. K. Hordinsky, *Clinical dermatology*. Lange Medical Books/McGraw-Hill, 2013.

[26] L. Rodrigues, "Eemco guidance to the in vivo assessment of tensile functional properties of the skin. part 2: instrumentation and test modes," *Skin Pharmacol Appl Skin Physiol*, vol. 14, no. 1, pp. 52–67, 2001.

[27] G. N. Stamatas, B. Z. Zmudzka, N. Kollias, and J. Z. Beer, "Non-invasive measurements of skin pigmentation in situ," *Pigment Cell Research*, vol. 17, no. 6, pp. 618–626, 2004.

[28] T. Winslow, "Schematic representation of normal human skin," April 2016. [Online]. Available: http://www.cancer.gov/images/cdr/live/CDR624959.jpg

[29] T. B. Fitzpatrick, "The validity and practicality of sun-reactive skin types i through vi," *Archives of dermatology*, vol. 124, no. 6, p. 869, 1988.

[30] H. Zahouani, C. Pailler-Mattei, B. Sohm, R. Vargiolu, V. Cenizo, and R. Debret, "Characterization of the mechanical properties of a dermal equivalent compared with human skin in vivo by indentation and static friction tests," *Skin Res Technol*, vol. 15, no. 1, pp. 68–76, 2009.

[31] C. Pailler-Mattei, S. Bec, and H. Zahouani, "In vivo measurements of the elastic mechanical properties of human skin by indentation tests," *Med Eng Phys*, vol. 30, no. 5, pp. 599–606, 2008.

[32] P. G. Agache, C. Monneur, J. L. Leveque, and J. De Rigal, "Mechanical properties and young's modulus of human skin in vivo," *Arch Dermatol Res*, vol. 269, no. 3, pp. 221–32, 1980.

[33] A. B. Cua, K. P. Wilhelm, and H. I. Maibach, "Elastic properties of human skin: relation to age, sex, and anatomical region," *Arch Dermatol Res*, vol. 282, no. 5, pp. 283–8, 1990.

[34] T. Burns and S. Breathnach, *Rook's Textbook of dermatology Vol 4*. London: Blackwell Scientific Publications, 1992, 1992.

[35] G. A. Holzapfel, "Biomechanics of soft tissue," *The handbook of materials behavior models*, vol. 3, pp. 1049–1063, 2001.

[36] Y. Lanir, "Skin mechanics," *Handbook of Bioengineering*, p. 11, 1987.

[37] Y. Lee and K. Hwang, "Skin thickness of korean adults," *Surgical and Radiologic Anatomy*, vol. 24, no. 3-4, pp. 183–189, 2002.

[38] F. H. Silver, J. W. Freeman, and D. DeVore, "Viscoelastic properties of human skin and processed dermis." *Skin Res Technol*, vol. 7, no. 1, pp. 18–23, Feb 2001.

[39] D. S. Rigel, J. K. Robinson, M. I. Ross, R. Friedman, C. J. Cockerell, H. Lim, and E. Stockfleth, *Cancer of the Skin: Expert Consult.* Elsevier Health Sciences, 2011.

[40] B. Mason, J. Califano, and C. Reinhart-King, *Matrix Stiffness: A Regulator of Cellular Behavior and Tissue Formation.* Springer New York, 2012, ch. 2, pp. 19–37.

[41] M. E. Fallowfield and M. G. Cook, "The vascularity of primary cutaneous melanoma," *J Pathol*, vol. 164, no. 3, pp. 241–4, 1991.

[42] R. L. Barnhill, K. Fandrey, M. A. Levy, J. Mihm, M. C., and B. Hyman, "Angiogenesis and tumor progression of melanoma. quantification of vascularity in melanocytic nevi and cutaneous malignant melanoma," *Lab Invest*, vol. 67, no. 3, pp. 331–7, 1992.

[43] W. Liu, J. P. Dowling, W. K. Murray, G. A. McArthur, J. F. Thompson, R. Wolfe, and J. W. Kelly, "Rate of growth in melanomas: characteristics and associations of rapidly growing melanomas," *Archives of Dermatology*, vol. 142, no. 12, pp. 1551–1558, 2006.

[44] D. S. Rigel, J. Russak, and R. Friedman, "The evolution of melanoma diagnosis: 25 years beyond the abcds," *CA Cancer J Clin*, vol. 60, no. 5, pp. 301–16, 2010.

[45] A. R. Rhodes, M. A. Weinstock, T. B. Fitzpatrick, J. Mihm, M. C., and A. J. Sober, "Risk factors for cutaneous melanoma. a practical method of recognizing predisposed individuals," *JAMA*, vol. 258, no. 21, pp. 3146–54, 1987.

[46] M. S. Brady, S. A. Oliveria, P. J. Christos, M. Berwick, D. G. Coit, J. Katz, and A. C. Halpern, "Patterns of detection in patients with cutaneous melanoma," *Cancer*, vol. 89, no. 2, pp. 342–7, 2000.

[47] R. L. Ferrini, M. Perlman, and L. Hill, "American college of preventive medicine policy statement: screening for skin cancer," *American journal of preventive medicine*, vol. 14, no. 1, pp. 80–82, 1998.

[48] E. W. Breitbart, A. Waldmann, S. Nolte, M. Capellaro, R. Greinert, B. Volkmer, and A. Katalinic, "Systematic skin cancer screening in northern germany," *Journal of the American Academy of Dermatology*, vol. 66, no. 2, pp. 201–211, 2012.

[49] M. R. Wickenheiser, J. S. Bordeaux, and J. K. Robinson, "Melanoma screening by physicians: time for a policy change in the united states," *JAMA dermatology*, vol. 150, no. 10, pp. 1045–1046, 2014.

[50] A. Breslow, "Thickness, cross-sectional areas and depth of invasion in the prognosis of cutaneous melanoma." *Annals of surgery*, vol. 172, no. 5, p. 902, 1970.

[51] L. Frederick, D. L. Page, I. D. Fleming, A. G. Fritz, C. M. Balch, D. G. Haller, M. Morrow *et al.*, *AJCC cancer staging manual.* Springer Science & Business Media, 2002, vol. 1.

[52] C. G. Ethun and K. A. Delman, "The importance of surgical margins in melanoma," *Journal of surgical oncology*, 2015.

[53] A. M. Hui, M. Jacobson, O. Markowitz, N. A. Brooks, and D. M. Siegel, "Mohs micrographic surgery for the treatment of melanoma." *Dermatol Clin*, vol. 30, no. 3, pp. 503–515, Jul 2012.

[54] Y. G. Patel, K. S. Nehal, I. Aranda, Y. Li, A. C. Halpern, and M. Rajadhyaksha, "Confocal reflectance mosaicing of basal cell carcinomas in mohs surgical skin excisions," *Journal of Biomedical Optics*, vol. 12, no. 3, p. 034027, 2007.

[55] S. A. Gandhi and J. Kampp, "Skin cancer epidemiology, detection, and management," *Medical Clinics of North America*, vol. 99, no. 6, pp. 1323–1335, 2015.

[56] N. T. Program, "Ntp 12th report on carcinogens." *Report on carcinogens: carcinogen profiles*, vol. 12, 2011.

[57] M. R. Wehner, M.-M. Chren, D. Nameth, A. Choudhry, M. Gaskins, K. T. Nead, W. J. Boscardin, and E. Linos, "International prevalence of indoor tanning: a systematic review and meta-analysis." *JAMA Dermatol*, vol. 150, no. 4, pp. 390–400, Apr 2014.

[58] M. Watson, C. J. Johnson, V. W. Chen, C. C. Thomas, H. K. Weir, R. Sherman, M. Cockburn, J. Jackson-Thompson, and M. Saraiya, "Melanoma surveillance in the united states: overview of methods," *J Am Acad Dermatol*, vol. 65, no. 5 Suppl 1, pp. S6–16, 2011.

[59] D. S. Rigel, "Epidemiology and prognostic factors in malignant melanoma," *Ann Plast Surg*, vol. 28, no. 1, pp. 7–8, 1992.

[60] G. P. Guy, S. R. Machlin, D. U. Ekwueme, and K. R. Yabroff, "Prevalence and costs of skin cancer treatment in the us, 2002- 2006 and 2007- 2011," *American journal of preventive medicine*, vol. 48, no. 2, pp. 183–187, 2015.

[61] D. T. Alexandrescu, "Melanoma costs: a dynamic model comparing estimated overall costs of various clinical stages," *Dermatology online journal*, vol. 15, no. 11, 2009.

[62] G. P. Guy Jr and D. U. Ekwueme, "Years of potential life lost and indirect costs of melanoma and non-melanoma skin cancer," *Pharmacoeconomics*, vol. 29, no. 10, pp. 863–874, 2011.

[63] S. V. Mohan and A. L. S. Chang, "Advanced basal cell carcinoma: Epidemiology and therapeutic innovations." *Curr Dermatol Rep*, vol. 3, pp. 40–45, 2014.

[64] National Cancer Institute, "Squamous cell carcinoma," 1985. [Online]. Available: https://visualsonline.cancer.gov/details.cfm?imageid=2165

[65] P. S. Karia, J. Han, and C. D. Schmults, "Cutaneous squamous cell carcinoma: estimated incidence of disease, nodal metastasis, and deaths from disease in the united states, 2012." *J Am Acad Dermatol*, vol. 68, no. 6, pp. 957–966, Jun 2013.

[66] R. C. Hibbeler, *Mechanics of materials.* Pearson, 2008.

[67] R. S. Rivlin and D. Saunders, "Large elastic deformations of isotropic materials. vii. experiments on the deformation of rubber," *Philosophical Transactions of the Royal Society of London A: Mathematical, Physical and Engineering Sciences*, vol. 243, no. 865, pp. 251–288, 1951.

[68] R. Rivlin, "Large elastic deformations of isotropic materials. i. fundamental concepts," *Philosophical Transactions of the Royal Society of London. Series A, Mathematical and Physical Sciences*, vol. 240, no. 822, pp. 459–490, 1948.

[69] M. Mooney, "A theory of large elastic deformation," *Journal of applied physics*, vol. 11, no. 9, pp. 582–592, 1940.

[70] R. Ogden, "Large deformation isotropic elasticity-on the correlation of theory and experiment for incompressible rubberlike solids," in *Proceedings of the Royal Society of London A: Mathematical, Physical and Engineering Sciences*, vol. 326, no. 1567. The Royal Society, 1972, pp. 565–584.

[71] T. A. Krouskop, T. M. Wheeler, F. Kallel, B. S. Garra, and T. Hall, "Elastic moduli of breast and prostate tissues under compression." *Ultrason Imaging*, vol. 20, no. 4, pp. 260–274, Oct 1998.

[72] G. Boyer, L. Laquieze, A. Le Bot, S. Laquieze, and H. Zahouani, "Dynamic indentation on human skin in vivo: ageing effects," *Skin Res Technol*, vol. 15, no. 1, pp. 55–67, 2009.

[73] G. Boyer, H. Zahouani, A. Le Bot, and L. Laquieze, "In vivo characterization of viscoelastic properties of human skin using dynamic micro-indentation," *Conf Proc IEEE Eng Med Biol Soc*, vol. 2007, pp. 4584–7, 2007.

[74] L. Coutts, J. Bamber, and N. Miller, "Multi-directional in vivo tensile skin stiffness measurement for the design of a reproducible tensile strain elastography protocol," *Skin Res Technol*, 2012.

[75] D. L. Bader and P. Bowker, "Mechanical characteristics of skin and underlying tissues in vivo," *Biomaterials*, vol. 4, no. 4, pp. 305–8, 1983.

[76] G. Boyer, C. Pailler Mattei, J. Molimard, M. Pericoi, S. Laquieze, and H. Zahouani, "Non contact method for in vivo assessment of skin mechanical properties for assessing effect of ageing," *Med Eng Phys*, vol. 34, no. 2, pp. 172–8, 2012.

[77] T. R. Tilleman, M. M. Tilleman, and M. H. Neumann, "The elastic properties of cancerous skin: Poisson's ratio and young's modulus," *Isr Med Assoc J*, vol. 6, no. 12, pp. 753–5, 2004.

[78] S. J. Kirkpatrick, R. K. Wang, D. D. Duncan, M. Kulesz-Martin, and K. Lee, "Imaging the mechanical stiffness of skin lesions by in vivo acousto-optical elastography," *Optics Express*, vol. 14, no. 21, 2006.

[79] M. Geerligs, L. van Breemen, G. Peters, P. Ackermans, F. Baaijens, and C. Oomens, "In vitro indentation to determine the mechanical properties of epidermis," *J Biomech*, vol. 44, no. 6, pp. 1176–81, 2011.

[80] C. Li, G. Guan, R. Reif, Z. Huang, and R. K. Wang, "Determining elastic properties of skin by measuring surface waves from an impulse mechanical stimulus using phase-sensitive optical coherence tomography," *J R Soc Interface*, vol. 9, no. 70, pp. 831–41, 2012.

[81] A. Hung, K. Mithraratne, M. Sagar, and P. Hunter, "Multilayer soft tissue continuum model: towards realistic simulation of facial expressions," *World Academy of Science, Engineering and Technology*, vol. 54, pp. 134–138, 2009.

[82] A. Marie-Angele, E. Feulvarch, H. Zahouani, and J.-M. Bergheau, "Numerical simulation of in vivo indentation tests: determination of the mechanical properties of human skin," *21ème Congrès Français de Mécanique, 26 au 30 août 2013, Bordeaux, France (FR)*, 2013.

[83] R. Groves, "Quantifying the mechanical properties of skin in vivo and ex vivo to optimise microneedle device design," Ph.D. dissertation, Cardiff University, 2012.

[84] S. Suresh, "Biomechanics and biophysics of cancer cells," *Acta Biomater*, vol. 3, no. 4, pp. 413–38, 2007.

[85] M. Lekka, K. Pogoda, J. Gostek, O. Klymenko, S. Prauzner-Bechcicki, J. Wiltowska-Zuber, J. Jaczewska, J. Lekki, and Z. Stachura, "Cancer cell recognition-mechanical phenotype," *Micron*, vol. 43, no. 12, pp. 1259–66, 2012.

[86] M. F. Coughlin, D. R. Bielenberg, G. Lenormand, M. Marinkovic, C. G. Waghorne, B. R. Zetter, and J. J. Fredberg, "Cytoskeletal stiffness, friction, and fluidity of cancer cell lines with different metastatic potential," *Clin Exp Metastasis*, vol. 30, no. 3, pp. 237–50, 2013.

[87] W. Xu, R. Mezencev, B. Kim, L. Wang, J. McDonald, and T. Sulchek, "Cell stiffness is a biomarker of the metastatic potential of ovarian cancer cells," *PLoS ONE*, vol. 7, no. 10, p. e46609, 2012.

[88] V. Swaminathan, K. Mythreye, E. T. O'Brien, A. Berchuck, G. C. Blobe, and R. Superfine, "Mechanical stiffness grades metastatic potential in patient tumor cells and in cancer cell lines," *Cancer Res*, vol. 71, no. 15, pp. 5075–80, 2011.

[89] K. R. Levental, H. Yu, L. Kass, J. N. Lakins, M. Egeblad, J. T. Erler, S. F. T. Fong, K. Csiszar, A. Giaccia, W. Weninger, M. Yamauchi, D. L. Gasser, and V. M. Weaver, "Matrix crosslinking forces tumor progression by enhancing integrin signaling," *Cell*, vol. 139, no. 5, pp. 891–906, 2009.

[90] P. Lu, V. M. Weaver, and Z. Werb, "The extracellular matrix: A dynamic niche in cancer progression," *The Journal of Cell Biology*, vol. 196, no. 4, pp. 395–406, 2012.

[91] S. Kumar and V. M. Weaver, "Mechanics, malignancy, and metastasis: the force journey of a tumor cell," *Cancer Metastasis Rev*, vol. 28, no. 1-2, pp. 113–27, 2009.

[92] M. Hawkins, "Physician appointment wait times and medicaid and medicare acceptance rates," *Report of Merritt Hawkins*, 2014.

[93] M. W. Tsang and J. Resneck, J. S., "Even patients with changing moles face long dermatology appointment wait-times: a study of simulated patient calls to dermatologists," *J Am Acad Dermatol*, vol. 55, no. 1, pp. 54–8, 2006.

[94] J. K. Patel, S. Konda, O. A. Perez, S. Amini, G. Elgart, and B. Berman, "Newer technologies/techniques and tools in the diagnosis of melanoma," *Eur J Dermatol*, vol. 18, no. 6, pp. 617–31, 2008.

[95] R. J. Friedman, D. S. Rigel, and A. W. Kopf, "Early detection of malignant melanoma: The role of physician examination and self-examination of the skin," *CA: a cancer journal for clinicians*, vol. 35, no. 3, pp. 130–151, 1985.

[96] J. W. Kelly, J. M. Yeatman, C. Regalia, G. Mason, and A. P. Henham, "A high incidence of melanoma found in patients with multiple dysplastic naevi by photographic surveillance," *Med J Aust*, vol. 167, no. 4, pp. 191–4, 1997.

[97] R. M. MacKie, P. McHenry, and D. Hole, "Accelerated detection with prospective surveillance for cutaneous malignant melanoma in high-risk groups," *Lancet*, vol. 341, no. 8861, pp. 1618–20, 1993.

[98] L. Thomas, P. Tranchand, F. Berard, T. Secchi, C. Colin, and G. Moulin, "Semiological value of abcde criteria in the diagnosis of cutaneous pigmented tumors," *Dermatology*, vol. 197, no. 1, pp. 11–17, 1998.

[99] A. A. Marghoob, L. D. Swindle, C. Z. Moricz, F. A. Sanchez Negron, B. Slue, A. C. Halpern, and A. W. Kopf, "Instruments and new technologies for the in vivo diagnosis of melanoma," *J Am Acad Dermatol*, vol. 49, no. 5, pp. 777–97; quiz 798–9, 2003.

[100] M. J. Lin, V. Mar, C. McLean, R. Wolfe, and J. W. Kelly, "Diagnostic accuracy of malignant melanoma according to subtype," *Australasian Journal of Dermatology*, vol. 55, no. 1, pp. 35–42, 2014. [Online]. Available: http://dx.doi.org/10.1111/ajd.12121

[101] C. A. Morton and R. M. Mackie, "Clinical accuracy of the diagnosis of cutaneous malignant melanoma," *Br J Dermatol*, vol. 138, no. 2, pp. 283–7, 1998.

[102] M. J. Martinka, R. I. Crawford, and S. Humphrey, "Clinical recognition of melanoma in dermatologists and nondermatologists." *J Cutan Med Surg*, Dec 2015.

[103] M. D. Corbo and J. Wismer, "Agreement between dermatologists and primary care practitioners in the diagnosis of malignant melanoma: review of the literature." *J Cutan Med Surg*, vol. 16, no. 5, pp. 306–310, Sep-Oct 2012.

[104] N. E. Feit, S. W. Dusza, and A. A. Marghoob, "Melanomas detected with the aid of total cutaneous photography," *Br J Dermatol*, vol. 150, no. 4, pp. 706–14, 2004.

[105] "Fotofinder bodystudio," 2016. [Online]. Available: http://www.fotofinder-systems.com/products/bodystudio-atbm/bodystudio-atbm/

[106] "Constellation," 2016. [Online]. Available: http://constellation.io/

[107] C. Benvenuto-Andrade, S. W. Dusza, A. L. Agero, A. Scope, M. Rajadhyaksha, A. C. Halpern, and A. A. Marghoob, "Differences between polarized light dermoscopy and immersion contact dermoscopy for the evaluation of skin lesions," *Arch Dermatol*, vol. 143, no. 3, pp. 329–38, 2007.

[108] C. Massone, A. Di Stefani, and H. P. Soyer, "Dermoscopy for skin cancer detection," *Curr Opin Oncol*, vol. 17, no. 2, pp. 147–53, 2005.

[109] "Dermlite dl1," 2016. [Online]. Available: http://dermlite.com/collections/home-skin-monitoring-products/products/dermlite-dl1-basic-smartphone-skin-magnifier

[110] G. Argenziano, I. Zalaudek, G. Ferrara, R. Hofmann-Wellenhof, and H. P. Soyer, "Proposal of a new classification system for melanocytic naevi," *Br J Dermatol*, vol. 157, no. 2, pp. 217–27, 2007.

[111] K. Wolff, M. Binder, and H. Pehamberger, "Epiluminescence microscopy: a new approach to the early detection of melanoma," *Adv Dermatol*, vol. 9, pp. 45–56; discussion 57, 1994.

[112] H. Skvara, L. Teban, M. Fiebiger, M. Binder, and H. Kittler, "Limitations of dermoscopy in the recognition of melanoma," *Arch Dermatol*, vol. 141, no. 2, pp. 155–60, 2005.

[113] V. Ahlgrimm-Siess, M. Laimer, E. Arzberger, and R. Hofmann-Wellenhof, "New diagnostics for melanoma detection: from artificial intelligence to rna microarrays," *Future Oncol*, vol. 8, no. 7, pp. 819–27, 2012.

[114] M. E. Vestergaard, P. Macaskill, P. E. Holt, and S. W. Menzies, "Dermoscopy compared with naked eye examination for the diagnosis of primary melanoma: a meta-analysis of studies performed in a clinical setting." *Br J Dermatol*, vol. 159, no. 3, pp. 669–676, Sep 2008.

[115] H. Kittler, H. Pehamberger, K. Wolff, and M. Binder, "Diagnostic accuracy of dermoscopy," *Lancet Oncol*, vol. 3, no. 3, pp. 159–65, 2002.

[116] D. Piccolo, A. Ferrari, K. Peris, R. Diadone, B. Ruggeri, and S. Chimenti, "Dermoscopic diagnosis by a trained clinician vs. a clinician with minimal dermoscopy training vs. computer-aided diagnosis of 341 pigmented skin lesions: a comparative study," *Br J Dermatol*, vol. 147, no. 3, pp. 481–6, 2002.

[117] L. Xu, M. Jackowski, A. Goshtasby, D. Roseman, S. Bines, C. Yu, A. Dhawan, and A. Huntley, "Segmentation of skin cancer images," *Image and Vision Computing*, vol. 17, no. 1, pp. 65–74, 1999.

[118] M. A. H. Bhuiyan, I. Azad, and M. K. Uddin, "Image processing for skin cancer features extraction," *International Journal of Scientific & Engineering Research*, vol. 4, no. 2, pp. 1–6, 2013.

[119] I. Maglogiannis and C. N. Doukas, "Overview of advanced computer vision systems for skin lesions characterization," *IEEE Transactions on Information Technology in Biomedicine*, vol. 13, no. 5, pp. 721–733, 2009.

[120] E. Claridge, P. Hall, M. Keefe, and J. Allen, "Shape analysis for classification of malignant melanoma," *Journal of biomedical engineering*, vol. 14, no. 3, pp. 229–234, 1992.

[121] J. H. Christensen, M. B. Soerensen, Z. Linghui, S. Chen, and M. O. Jensen, "PreâĂŘdiagnostic digital imaging prediction model to discriminate between malignant melanoma and benign pigmented skin lesion," *Skin Research and Technology*, vol. 16, no. 1, pp. 98–108, 2010.

[122] J. Breneman, "Towards early-stage malignant melanoma detection using consumer mobile devices," 2012.

[123] "First derm," 2016. [Online]. Available: https://www.firstderm.com/

[124] "3derm," 2016. [Online]. Available: https://www.3derm.com/

[125] "Molescope," 2016. [Online]. Available: https://molescope.com/

[126] M. J. A. O. Wolf Ja and et al., "Diagnostic inaccuracy of smartphone applications for melanoma detection," *JAMA Dermatology*, pp. 1–4, 2013, 10.1001/jamadermatol.2013.2382.

[127] F. T. Commission, "Ftc cracks down on marketers of "melanoma detection" apps," 2015.

[128] "Medx simsys-molemate," 2016. [Online]. Available: http://www.medxhealth.com/Our-Products/SIAscopytrade;/overview.aspx

[129] M. Michalska, G. Chodorowska, and D. Krasowska, "Siascopy–a new non-invasive technique of melanoma diagnosis," *Ann Univ Mariae Curie Sklodowska Med*, vol. 59, no. 2, pp. 421–31, 2004.

[130] J. March, M. Hand, and D. Grossman, "Practical application of new technologies for melanoma diagnosis: Part i. noninvasive approaches." *J Am Acad Dermatol*, vol. 72, no. 6, pp. 929–941, Jun 2015.

[131] "Melafind," 2016. [Online]. Available: http://www.melafind.com/

[132] D. Gutkowicz-Krusin, M. Elbaum, A. Jacobs, S. Keem, A. W. Kopf, H. Kamino, S. Wang, P. Rubin, H. Rabinovitz, and M. Oliviero, "Precision of automatic measurements of pigmented skin lesion parameters with a melafind(tm) multispectral digital dermoscope," *Melanoma Res*, vol. 10, no. 6, pp. 563–70, 2000.

[133] M. Elbaum, A. W. Kopf, H. S. Rabinovitz, R. G. Langley, H. Kamino, J. Mihm, M. C., A. J. Sober, G. L. Peck, A. Bogdan, D. Gutkowicz-Krusin, M. Greenebaum, S. Keem, M. Oliviero, and S. Wang, "Automatic differentiation of melanoma from melanocytic nevi with multispectral digital dermoscopy: a feasibility study," *J Am Acad Dermatol*, vol. 44, no. 2, pp. 207–18, 2001.

[134] K. G. Bergstrom, "Melafind is approved by the fda: where does it fit in dermatology?" *J Drugs Dermatol*, vol. 11, no. 3, pp. 420–2, 2012.

[135] R. Wells, D. Gutkowicz-Krusin, E. Veledar, A. Toledano, and S. C. Chen, "Comparison of diagnostic and management sensitivity to melanoma between dermatologists and melafind: A pilot study," *Arch Dermatol*, vol. 148, no. 9, pp. 1083–4, 2012.

[136] G. Monheit, A. B. Cognetta, L. Ferris, H. Rabinovitz, K. Gross, M. Martini, J. M. Grichnik, M. Mihm, V. G. Prieto, P. Googe, R. King, A. Toledano, N. Kabelev, M. Wojton, and D. Gutkowicz-Krusin, "The performance of melafind: a prospective multicenter study," *Arch Dermatol*, vol. 147, no. 2, pp. 188–94, 2011.

[137] E. Altman, "Melafind, an fda-approved device for melanoma detection: Pros and cons," 2011.

[138] N. Singer, "Dissent over a device to help find melanoma," *The New York Times*, 2013.

[139] T. Gambichler, P. Regeniter, F. G. Bechara, A. Orlikov, R. Vasa, G. Moussa, M. Stucker, P. Altmeyer, and K. Hoffmann, "Characterization of benign and malignant melanocytic skin lesions using optical coherence tomography in vivo," *J Am Acad Dermatol*, vol. 57, no. 4, pp. 629–37, 2007.

[140] T. Gambichler, V. Jaedicke, and S. Terras, "Optical coherence tomography in dermatology: technical and clinical aspects," *Arch Dermatol Res*, vol. 303, no. 7, pp. 457–73, 2011.

[141] "Michelson diagnostics vivosight," 2016. [Online]. Available: https://us.vivosight.com/

[142] A. Gerger, R. Hofmann-Wellenhof, H. Samonigg, and J. Smolle, "In vivo confocal laser scanning microscopy in the diagnosis of melanocytic skin tumours," *Br J Dermatol*, vol. 160, no. 3, pp. 475–81, 2009.

[143] G. Pellacani, P. Guitera, C. Longo, M. Avramidis, S. Seidenari, and S. Menzies, "The impact of in vivo reflectance confocal microscopy for the diagnostic accuracy of melanoma and equivocal melanocytic lesions," *J Invest Dermatol*, vol. 127, no. 12, pp. 2759–65, 2007.

[144] P. Guitera, G. Pellacani, C. Longo, S. Seidenari, M. Avramidis, and S. W. Menzies, "In vivo reflectance confocal microscopy enhances secondary evaluation of melanocytic lesions," *J Invest Dermatol*, vol. 129, no. 1, pp. 131–8, 2009.

[145] "Caliber i.d. vivascope," 2016. [Online]. Available: http://www.caliberid.com/vivascope3000-Overview.html

[146] M. A. Calin, S. V. Parasca, R. Savastru, M. R. Calin, and S. Dontu, "Optical techniques for the noninvasive diagnosis of skin cancer." *J Cancer Res Clin Oncol*, vol. 139, no. 7, pp. 1083–1104, Jul 2013.

[147] "Verisante aura," 2016. [Online]. Available: http://www.verisante.com/aura/

[148] M. Sharma, E. Marple, J. Reichenberg, and J. W. Tunnell, "Design and characterization of a novel multimodal fiber-optic probe and spectroscopy system for skin cancer applications," *Review of Scientific Instruments*, vol. 85, no. 8, 2014. [Online]. Available: http://scitation.aip.org/content/aip/journal/rsi/85/8/10.1063/1.4890199

[149] M. Stucker, I. Horstmann, C. Nuchel, A. Rochling, K. Hoffmann, and P. Altmeyer, "Blood flow compared in benign melanocytic naevi, malignant melanomas and basal cell carcinomas," *Clin Exp Dermatol*, vol. 24, no. 2, pp. 107–11, 1999.

246

[150] R. E. Hunger, R. Della Torre, A. Serov, and T. Hunziker, "Assessment of melanocytic skin lesions with a high-definition laser doppler imaging system." *Skin Res Technol*, vol. 18, no. 2, pp. 207–211, May 2012.

[151] F. Lacarrubba, M. Potenza, and G. Micali, "Enhanced videodermoscopic visualization of superficial vascular patterns on skin using a 390- to 410-nm light," *Archives of Dermatology*, vol. 148, no. 2, pp. 276–276, 2012.

[152] M. Takahashi and H. Kohda, "Diagnostic utility of magnetic resonance imaging in malignant melanoma," *J Am Acad Dermatol*, vol. 27, no. 1, pp. 51–4, 1992.

[153] D. Rallan, N. L. Bush, J. C. Bamber, and C. C. Harland, "Quantitative discrimination of pigmented lesions using three-dimensional high-resolution ultrasound reflex transmission imaging," *J Invest Dermatol*, vol. 127, no. 1, pp. 189–95, 2007.

[154] T. Hinz, T. Hoeller, J. Wenzel, T. Bieber, and M. H. Schmid-Wendtner, "Real-time tissue elastography as promising diagnostic tool for diagnosis of lymph node metastases in patients with malignant melanoma: a prospective single-center experience," *Dermatology*, vol. 226, no. 1, pp. 81–90, 2013.

[155] D. J. Rohrbach, D. Muffoletto, J. Huihui, R. Saager, K. Keymel, A. Paquette, J. Morgan, N. Zeitouni, and U. Sunar, "Preoperative mapping of nonmelanoma skin cancer using spatial frequency domain and ultrasound imaging." *Acad Radiol*, vol. 21, no. 2, pp. 263–270, Feb 2014.

[156] C. Herman and M. P. Cetingul, "Quantitative visualization and detection of skin cancer using dynamic thermal imaging," *J Vis Exp*, no. 51, 2011.

[157] M. P. Cetingul and C. Herman, "Identification of skin lesions from the transient thermal response using infrared imaging technique," in *IEEE International Symposium on Biomedical Imaging: From Macro to Nano*, ser. 2008 IEEE International Symposium on Biomedical Imaging: From Macro to Nano (ISBI '08). IEEE, 2008, pp. 1219–22.

[158] "Notouch breastscan," 2016. [Online]. Available: http://www.notouchbreastscan.com/thermography.html

[159] Y. Har-Shai, Y. A. Glickman, G. Siller, R. McLeod, M. Topaz, C. Howe, A. Ginzburg, B. Zamir, O. Filo, G. Kenan, and Y. Ullmann, "Electrical impedance scanning for melanoma diagnosis: a validation study," *Plast Reconstr Surg*, vol. 116, no. 3, pp. 782–90, 2005.

[160] "Nevisense," 2016. [Online]. Available: http://scibase.se/en/the-nevisense-product/

[161] "Dermtech," 2016. [Online]. Available: http://dermtech.com/

[162] P. Gerami, J. P. Alsobrook, T. J. Palmer, and H. S. Robin, "Development of a novel noninvasive adhesive patch test for the evaluation of pigmented lesions of the skin," *Journal of the American Academy of Dermatology*, vol. 71, no. 2, pp. 237–244, 2014.

[163] P. Rubegni, L. Feci, N. Nami, M. Burroni, P. Taddeucci, C. Miracco, M. A. M. Butorano, M. Fimiani, and G. Cevenini, "Computer-assisted melanoma diagnosis: a new integrated system," *Melanoma research*, vol. 25, no. 6, pp. 537–542, 2015.

[164] "Dermoscan moleexpertmicro," 2016. [Online]. Available: http://www.dermoscan.de/en/software-options/moleexpertmicro/

[165] H. Cheng and P. Guitera, "Systematic review of optical coherence tomography usage in the diagnosis and management of basal cell carcinoma," *British Journal of Dermatology*, vol. 173, no. 6, pp. 1371–1380, 2015.

[166] M. Mogensen, T. M. Joergensen, B. M. Nurnberg, H. A. Morsy, J. B. Thomsen, L. Thrane, and G. B. E. Jemec, "Assessment of optical coherence tomography imaging in the diagnosis of non-melanoma skin cancer and benign lesions versus normal skin: observer-blinded evaluation by dermatologists and pathologists." *Dermatol Surg*, vol. 35, no. 6, pp. 965–972, Jun 2009.

[167] C. Borchers, "Laser imaging device makes no-cut biopsies possible," *Boston Globe*, October 2013.

[168] H. Markert, J. Ring, N. Campbell, and K. Grates, "A comparison of four commercially available portable raman spectrometers," *National Forensic Science Technology Center*, vol. 727, pp. 1–8, 2011.

[169] "Fluxexplorer," 2016. [Online]. Available: http://www.fluxexplorer.com/

[170] "Siemens magnetom," 2016. [Online]. Available: http://usa.healthcare.siemens.com/magnetic-resonance-imaging

[171] "Cortex technologies dermascan c ultrasound," 2016. [Online]. Available: http://www.cortex.dk/skin-analysis-products/dermascan-ultrasound.aspx

[172] Ultrasound supply - equipment costs. [Online]. Available: http://www.ultrasoundsupply.com/ultrasound-equipment/

[173] "Siemens biograph truepoint pet/ct," 2016. [Online]. Available: http://www.healthcare.siemens.com/molecular-imaging/pet-ct/biograph-truepoint-petct

[174] "General electric logiq e9," 2016. [Online]. Available: http://www3.gehealthcare.com/en/products/categories/ultrasound/

[175] I. Lye, D. W. Edgar, F. M. Wood, and S. Carroll, "Tissue tonometry is a simple, objective measure for pliability of burn scar: is it reliable?" *J Burn Care Res*, vol. 27, no. 1, pp. 82–5, 2006.

[176] T. H. Bartell, W. W. Monafo, and T. A. Mustoe, "A new instrument for serial measurements of elasticity in hypertrophic scar," *J Burn Care Rehabil*, vol. 9, no. 6, pp. 657–60, 1988.

[177] S. Fong, L. Hung, and J. Cheng, "The cutometer and ultrasonography in the assessment of postburn hypertrophic scar—a preliminary study," *Burns*, vol. 23, pp. S12–S18, 1997.

[178] S. Es'haghian, K. M. Kennedy, P. Gong, D. D. Sampson, R. A. McLaughlin, and B. F. Kennedy, "Optical palpation in vivo: imaging human skin lesions using mechanical contrast," *Journal of biomedical optics*, vol. 20, no. 1, pp. 016013–016013, 2015.

[179] J. F. Greenleaf, M. Fatemi, and M. Insana, "Selected methods for imaging elastic properties of biological tissues," *Annual review of biomedical engineering*, vol. 5, no. 1, pp. 57–78, 2003.

[180] X. Liang and S. A. Boppart, "Biomechanical properties of in vivo human skin from dynamic optical coherence elastography," *IEEE Trans Biomed Eng*, vol. 57, no. 4, pp. 953–9, 2010.

[181] Y. Zhang, R. T. Brodell, E. N. Mostow, C. J. Vinyard, and H. Marie, "In vivo skin elastography with highâĂŘdefinition optical videos," *Skin Research and Technology*, vol. 15, no. 3, pp. 271–282, 2009.

[182] J. D. Krehbiel, J. Lambros, J. Viator, and N. Sottos, "Digital image correlation for improved detection of basal cell carcinoma," *Experimental Mechanics*, vol. 50, no. 6, pp. 813–824, 2010.

[183] K. A. Wright, "Systems and methods for noninvasive health monitoring," 2015.

[184] "ibreastexam," 2016. [Online]. Available: http://www.ibreastexam.com/

[185] S. McKinley, A. Garg, S. Sen, R. Kapadia, A. Murali, K. Nichols, S. Lim, S. Patil, P. Abbeel, and A. M. Okamura, "A disposable haptic palpation probe for locating subcutaneous blood vessels in robot-assisted minimally invasive surgery," *IEEE CASE*, 2015.

[186] T. Yamamoto, B. Vagvolgyi, K. Balaji, L. L. Whitcomb, and A. M. Okamura, "Tissue property estimation and graphical display for teleoperated robot-assisted surgery," in *IEEE International Conference on Robotics and Automation*. IEEE, 2009, pp. 4239–4245.

[187] B. W. Pogue and M. S. Patterson, "Review of tissue simulating phantoms for optical spectroscopy, imaging and dosimetry," *Journal of biomedical optics*, vol. 11, no. 4, pp. 041102–041102–16, 2006.

[188] M. O. Culjat, D. Goldenberg, P. Tewari, and R. S. Singh, "A review of tissue substitutes for ultrasound imaging," *Ultrasound in medicine & biology*, vol. 36, no. 6, pp. 861–873, 2010.

[189] T. Bergmann, S. Beer, U. Maeder, J. M. Burg, P. Schlupp, T. Schmidts, F. Runkel, and M. Fiebich, "Development of a skin phantom of the epidermis and evaluation by using fluorescence techniques," in *SPIE BiOS*. International Society for Optics and Photonics, 2011, pp. 79060T–79060T-9.

[190] R. Cao, Z. Huang, T. Varghese, and G. Nabi, "Tissue mimicking materials for the detection of prostate cancer using shear wave elastography: A validation study," *Medical physics*, vol. 40, no. 2, p. 022903, 2013.

[191] K. Manickam, R. R. Machireddy, and S. Seshadri, "Characterization of biomechanical properties of agar based tissue mimicking phantoms for ultrasound stiffness imaging techniques," *Journal of the mechanical behavior of Biomedical Materials*, vol. 35, pp. 132–143, 2014.

[192] T. J. Hall, M. Bilgen, M. F. Insana, and T. A. Krouskop, "Phantom materials for elastography," *IEEE Transactions on Ultrasonics, Ferroelectrics, and Frequency Control*, vol. 44, no. 6, pp. 1355–1365, 1997.

[193] P. Togni, J. Vrba, and L. Vannucci, "Microwave applicator for hyperthermia treatment on in vivo melanoma model," *Medical & biological engineering & computing*, vol. 48, no. 3, pp. 285–292, 2010.

[194] M. M. Doyley, J. B. Weaver, E. E. Van Houten, F. E. Kennedy, and K. D. Paulsen, "Thresholds for detecting and characterizing focal lesions using steady-state mr elastography," *Medical Physics*, vol. 30, no. 4, pp. 495–504, 2003.

[195] T. Wang, S. Mallidi, J. Qiu, L. L. Ma, A. S. Paranjape, J. Sun, R. V. Kuranov, K. P. Johnston, and T. E. Milner, "Comparison of pulsed photothermal radiometry, optical coherence tomography and ultrasound for melanoma thickness measurement in pdms tissue phantoms," *Journal of biophotonics*, vol. 4, no. 5, pp. 335–344, 2011.

[196] P. Fawkes, "Psfk future of health," *PSFK*, 2014.

[197] C. Herman, "Emerging technologies for the detection of melanoma: achieving better outcomes," *Clin Cosmet Investig Dermatol*, vol. 5, pp. 195–212, 2012.

[198] P. Guitera and S. W. Menzies, "State of the art of diagnostic technology for early-stage melanoma," *Expert Rev Anticancer Ther*, vol. 11, no. 5, pp. 715–23, 2011.

[199] D. Storie, "Mobile devices in medicine: a survey of how medical students, residents, and faculty use smartphones and other mobile devices to find information," *Journal of the Medical Library Association*, vol. 102, no. 1, p. 22, 2014.

[200] "Kito+," 2016. [Online]. Available: https://azoi.com/

[201] "ihealth wireless blood pressure wrist monitor," 2016. [Online]. Available: https://ihealthlabs.com/blood-pressure-monitors/ wireless-blood-pressure-wrist-monitor/

[202] "Kardia," 2016. [Online]. Available: http://www.alivecor.com/

[203] "Eyenetra," 2016. [Online]. Available: https://eyenetra.com/

[204] A. Slocum, *FUNdaMENTALS of Design*. Slocum, Alexander, 2007.

[205] E. Pritchard, M. Mahfouz, B. Evans III, S. Eliza, and M. Haider, "Flexible capacitive sensors for high resolution pressure measurement," in *IEEE Sensors*. IEEE, 2008, pp. 1484–1487.

[206] S. Lee, A. Reuveny, J. Reeder, S. Lee, H. Jin, Q. Liu, T. Yokota, T. Sekitani, T. Isoyama, Y. Abe, Z. Suo, and T. Someya, "A transparent bending-insensitive pressure sensor," *Nat Nano*, 01 2016. [Online]. Available: http://dx.doi.org/10.1038/nnano.2015.324

[207] P. J. Besl, "Active, optical range imaging sensors," *Machine vision and applications*, vol. 1, no. 2, pp. 127–152, 1988.

[208] J. Salvi, S. Fernandez, T. Pribanic, and X. Llado, "A state of the art in structured light patterns for surface profilometry," *Pattern recognition*, vol. 43, no. 8, pp. 2666–2680, 2010.

[209] J. Han, L. Shao, D. Xu, and J. Shotton, "Enhanced computer vision with microsoft kinect sensor: A review," *Cybernetics, IEEE Transactions on*, vol. 43, no. 5, pp. 1318–1334, 2013.

[210] M. C. Bloemen, M. S. van Gerven, M. B. van der Wal, P. D. Verhaegen, and E. Middelkoop, "An objective device for measuring surface roughness of skin and scars," *J Am Acad Dermatol*, vol. 64, no. 4, pp. 706–15, 2011.

[211] J.-Y. Bouguet, "Camera calibration toolbox for matlab," 2004.

[212] Z. Zhang, "A flexible new technique for camera calibration," *Pattern Analysis and Machine Intelligence, IEEE Transactions on*, vol. 22, no. 11, pp. 1330–1334, 2000.

[213] G. Falcao, N. Hurtos, J. Massich, and D. Fofi, "Projector-camera calibration toolbox," *Erasumus Mundus Masters in Vision and Robotics*, 2009.

[214] D. Bradley and G. Roth, "Adaptive thresholding using the integral image," *Journal of graphics, gpu, and game tools*, vol. 12, no. 2, pp. 13–21, 2007.

[215] J. Entzinger, "A flexible seam detection technique for robotic laser welding," Master's thesis, University of Twente, 2005.

[216] S. P. Timoshenko and S. Woinowsky-Krieger, *Theory of plates and shells.* McGraw-hill, 1959.

[217] J. E. Bowles, *Foundation analysis and design.* McGraw-Hill, 1988.

[218] H. Eschenauer, N. Olhoff, and W. Schnell, *Applied structural mechanics: fundamentals of elasticity, load-bearing structures, structural optimization: including exercises.* Springer Science & Business Media, 1997.

[219] S. Sinha, "Large deflections of plates on elastic foundations," *Journal of the Engineering Mechanics Division*, vol. 89, no. 1, pp. 1–24, 1963.

[220] "Design circle, inc." 2016. [Online]. Available: http://designcircleinc.com/

[221] A. Giacomin and A. Mix, "Standardized polymer durometry," *Journal of Testing and evaluation*, vol. 39, no. 4, pp. 1–10, 2011.

[222] G. Pickering, e. le, D. Jourdan, A. Eschalier, and C. Dubray, "Impact of age, gender and cognitive functioning on pain perception," *Gerontology*, vol. 48, no. 2, pp. 112–118, 2002.

[223] "Treehopper usb interface," 2016. [Online]. Available: http://www.treehopper.io

[224] Wpa tournament table & equipment specifications. [Online]. Available: http://www.wpa-pool.com/web/WPA_Tournament_Table_Equipment_Specifications